Engineering and evaluation of double magnetic tunnel junctions with a switchable assistance layer for high performance spin transfer torque magnetic memory

Daniel Sanchez Hazen

To cite this version:

Daniel Sanchez Hazen. Engineering and evaluation of double magnetic tunnel junctions with a switchable assistance layer for high performance spin transfer torque magnetic memory. Micro and nanotechnologies/Microelectronics. Université Grenoble Alpes [2020-..], 2022. English. NNT : 2022GRALT047 . tel-03828367

HAL Id: tel-03828367
https://theses.hal.science/tel-03828367v1

Submitted on 25 Oct 2022

THÈSE

Pour obtenir le grade de

DOCTEUR DE L’UNIVERSITÉ GRENOBLE ALPES

Spécialité : NANO ELECTRONIQUE ET NANO TECHNOLOGIES
Arrêté ministériel : 25 mai 2016

Présentée par

Daniel SANCHEZ HAZEN

Thèse dirigée par **Bernard DIENY**

préparée au sein du **Laboratoire Spintronique et Technologie des Composants**
dans **l'École Doctorale Electronique, Electrotechnique, Automatique, Traitement du Signal (EEATS)**

Double jonction tunnel magnétique avec couche d'assistance commutable pour une mémoire haute performance à écriture par transfert de spin

Engineering and evaluation of double magnetic tunnel junctions with a switchable assistance layer for high performance spin transfer torque magnetic memory

Thèse soutenue publiquement le **14 juin 2022**,
devant le jury composé de :

Monsieur Bernard DIENY
INGENIEUR HDR, Spintec CEA/Grenoble, Directeur de thèse
Monsieur Thibaut DEVOLDER
CHARGE DE RECHERCHE, CNRS , Rapporteur
Monsieur Ahmad BSIESY
PROFESSEUR DES UNIVERSITES, Université Grenoble Alpes, Examinateur
Monsieur Christophe THIRION
CHARGE DE RECHERCHE, CNRS, Examinateur
Madame Jullie GROLLIER
DIRECTEUR DE RECHERCHE, CNRS, Rapporteure
Monsieur François MONTAIGNE
PROFESSEUR DES UNIVERSITES, université de Lorraine, Examinateur

Abstract

The realization of energy-efficient perpendicular spin-transfer torque magnetic random access memory cells (p-STT-MRAM) is one of the main goals towards a wide adoption of MRAM technologies. MRAM combine a unique set of assets with their endurance, high speed, scalability, and non-volatility which could make them potentially usable at all levels in the memory hierarchy. This possibility triggered almost 30 years of MRAM development. However, nowadays industrial uses of p-STT-MRAM is limited to some specific applications in which its characteristics provide a significant processing simplification (e.g. eFlash replacement) or an important power consumption reduction of the integrated circuits. Another foreseen application of p-STT-MRAM is that of the cache memory levels which require high speed and large endurance. One important challenge while developing novel devices for high-performance p-STT-MRAM is to overcome the dilemma between increasing the thermal stability (Δ) while reducing the critical current (I_c) required to switch the storage layer magnetization between its parallel (P) or anti-parallel (AP) alignment with the reference layer. The trade-off between these properties is commonly expressed in terms of a figure of merit (Δ/I_c) which is used as a quantitative measurement of the memory cell writing efficiency. Double magnetic tunnel junctions (DMTJ) were the first stack design presenting a real improvement in STT efficiency. However, they present drawbacks in terms of difficulties of fabrication and of achieving symmetric properties in the "0" and "1" states. In this thesis, a simpler and thinner device, so-called double magnetic tunnel junction (ASL-DMTJ) with assistance layer, has been engineered and evaluated. The ASL-DMTJ relies on the use of a switchable top polarizer that acts as an assisting layer (ASL). The ASL is designed to switch its magnetic orientation during the write operation by the spin-polarized current from the storage layer (SL). The SL/ASL magnetic coupling and ASL thermal stability are finely adjusted so that the ASL always assist the switching of the SL magnetization by spin transfer torque while always ending in standby in parallel alignment with the SL thus increasing the SL thermal stability. Macrospin numerical simulations of the proposed concept set the basis for its correct operation and working principles under-voltage and field. The materials comprised in the full ASL-DMTJ were optimized at sheet film and on patterned devices till the required switching sequences were experimentally verified. Real-time observations of the devices resistance variations confirmed the expected operation mechanism in the fabricated cells. The SL writing efficiency was evaluated and compared to those of conventional single magnetic tunnel junction structures without the ASL. The ASL-DMTJ presents an average increase in thermal stability factor Δ of 5 to 10 with respect to single MTJ regardless of the memory size, while the critical current to switch by spin-transfer torque is decreased by 30% for the P-to-AP transition and conserved or reduced by 50% for the AP-to-P transition. These results represent a twofold increase in the figure of merit of the devices, which are in line with previously reported STT writting efficiency enhancements with conventional p-DMTJ cells but with a magnetic stack much simpler and easier to nano-fabricate.

Résumé

La réalisation de cellules de mémoire magnétique à accès aléatoire à écriture par couple de transfert de spin (p-STT-MRAM), économes en énergie, est l'un des principaux objectifs vers une large adoption des technologies MRAM. La MRAM combine un ensemble unique d'atouts avec leur endurance, leur haute vitesse, leur évolutivité et leur non-volatilité, ce qui pourrait les rendre potentiellement utilisables à tous les niveaux de la hiérarchie mémoire. Cependant, aujourd'hui, les utilisations industrielles de la p-STT-MRAM sont limitées à certaines applications spécifiques dans lesquelles ses caractéristiques permettent une simplification significative du procédé de fabrication (par exemple dans le cas du remplacement de l'eFlash) ou une réduction importante de la consommation d'énergie des circuits intégrés. Une autre application envisagée de la p-STT-MRAM est celle des niveaux de mémoire cache qui nécessitent une grande vitesse et une grande endurance. Un défi important dans la conception de p-STT-MRAM haute performance est de surmonter le dilemme entre augmentation de la stabilité thermique (Δ) et besoin de réduire le courant critique (Ic) nécessaire pour commuter l'aimantation de la couche de stockage entre l'état parallèle (P) ou anti-parallèle (AP) par rapport à l'aimantation de la couche de référence. Le compromis entre ces propriétés est couramment exprimé en termes de facteur de mérite (Δ/Ic) qui est utilisé comme mesure quantitative de l'efficacité d'écriture de la cellule mémoire. Les jonctions tunnel magnétiques doubles (DMTJ) ont constitué la première conception d'empilements présentant une réelle amélioration de l'efficacité du STT. Cependant, elles présentent des inconvénients en termes de difficultés de fabrication et d'obtention de propriétés symétriques dans les états 0 et 1 . Dans cette thèse, un dispositif plus simple et moins épais (donc plus facile à graver), appelé double jonction tunnel magnétique (ASL-DMTJ) avec couche d'assistance, a été conçu et évalué. L'ASL-DMTJ repose sur l'utilisation d'un polariseur supérieur commutable qui agit comme une couche d'assistance (ASL). L'ASL est conçu pour changer son orientation magnétique pendant l'opération d'écriture par le courant polarisé en spin provenant de la couche de stockage (SL). Le couplage magnétique SL/ASL et la stabilité thermique de l'ASL sont finement ajustés pour que l'ASL assiste toujours la commutation de l'aimantation du SL par le couple de transfert de spin tout en se terminant toujours à la fin de l'écriture en configuration parallèle avec le SL, augmentant ainsi la stabilité thermique du SL. Les simulations numériques Macrospin du concept proposé ont permis de déterminer les conditions pour son bon fonctionnement sous-tension et champ. Les matériaux compris dans l'ASL-DMTJ complet ont été optimisés sur les films en couches continues et sur les dispositifs gravés jusqu'à ce que les séquences de commutation requises soient vérifiées expérimentalement. Les observations en temps réel des variations de résistance des dispositifs ont confirmé le mécanisme de fonctionnement attendu dans les cellules fabriquées. L'efficacité d'écriture SL a été évaluée et comparée à celles des structures à jonction tunnel magnétique unique conventionnelles sans l'ASL. L'ASL-DMTJ présente une augmentation moyenne du facteur de stabilité thermique de 5 a 10 par rapport à une MTJ sans ASL, quelle que soit la taille de la mémoire, tandis que le courant critique pour commuter par le couple de transfert de spin est diminué 30% pour la transition P à AP et maintenu ou diminué 50% pour la transition de AP vers P. Ces résultats représentent un doublement du facteur de mérite des dispositifs, ce qui est conforme aux améliorations d'efficacité STT précédemment rapportées avec des cellules p-DMTJ conventionnelles mais avec ici, un empilement magnétique beaucoup plus simple et plus facile à nano-fabriquer.

Contents

Outline

This manuscript is organized into five chapters and a final concluding chapter. The chosen content of these chapters is arranged following the chronological development of the proposed stack design during the three years and four months of this thesis. The outline and a brief summary of the content that can be found in these chapters is as follows:

Chapter 1 - Introduction: Introduction to perpendicular-STT MRAM technologies and main working principles explaining the physical phenomena behind the reading, writing and retaining the information stored in this kind of magnetic memories. The conclusion of this chapter presents the main dilemma between critical current and retention time pointing to the strategies utilized in this thesis to brake with it using state of the art double magnetic tunnel junctions.

Chapter 2 - The ASL-DMTJ stack design: Introduction to the stack design developed during this thesis and the solutions it provides to the limitations of perpendicular-double Magnetic tunnel junctions, thus setting the main objectives of this thesis. Theoretical evaluation of the main working principles and reversal dynamics to enhance the thermal stability of the memories while decreasing the critical switching current. This chapter defines the magnetic properties of the layers comprised in our stack for a correct operation of the memory cell detailing the specific reversal orders and how to verify them experimentally.

Chapter 3 - Materials and experimental methods: Description of the experimental techniques to grow the material stack for both full sheet film level materials optimization or device nano-fabrication. The Measurement techniques, device fabrication steps and electrical characterization at patterned device level are detailed introducing as well the protocols for the extraction of the most important characteristics of the memory cells.

Chapter 4 - Materials optimization of the Assistance layer and Storage layer coupled system: Independent Materials development at wafer level for the assistance layer and storage layer magnetic properties and magnetic coupling between them. Material optimization at patterned device level, self-heating flaws encounter during the first realizations of our stack design and matching of the magnetic properties of the layers to comply with the required conditions for a correct operation and reversal schemes with voltage.

Chapter 5 - Experimental evaluation of device STT efficiency and writing dynamics: Evaluation of the device with the optimized material stacks performance and readability with respect to a control sample without the assistance layer influence. Experimental Real-time measurements confirming the reversal orders during the application of the writing voltage pulses. Prove of concept of the proposed stack design in terms of Spin transfer torque switching efficiency (Retention/Writability) and final evaluation with respect to conventional perpendicular-Double magnetic tunnel junctions.

Chapter 6- Conclusions: General summary of the main results obtained during this work and perspectives to further enhance the performance of our device.

List of Tables

List of Acronyms

ASL	Assistance layer
ASL-DMTJ	Assistance layer Double Magnetic Tunnel Junction
BEOL	Back End Of The Line
CMOS	Complementary Metal-Oxide semiconductor
CIPT	Current In-Plane Tunnel
DOS	Density Of States
DMTJ	Double Magnetic Tunnel Junction
DC	Direct Current
DRAM	Dynamic Random Acces Memory
FOM	Figure Of Merit
FL	Free layer
GMR	Giant Magneto-Resistance
IBE	Ion Beam Etching
LLGS	Landau-Lifshitz-Gilbert-Slonczewski
MOSFET	Metal-Oxide Semiconductor Field Effect Transistor
MTJ	Magnetic Tunnel Junction
MRAM	Magnetic-Random Access Memory
MOKE	Magneto-Optical Kerr Effect
OM	Optical Microscope
PMA	Perpendicular Magnetic Anisotropy
p-STT-MRAM	perpendicular STT-MRAM
p-DMTJ	perpendicular Double Magnetic Tunnel Junction
RH	Resistance Magnetic field loop
RV	Resistance Voltage loop
RIE	Reactive Ion Etching
RA	Resistance x Area product
RT	Room temperature
SRAM	Static Random Acces Memory
STT-MRAM	Spin-Transfer-Torque Magnetic-Random Access Memory
SOT-MRAM	Spin-Orbit-Torque Magnetic-Random Access Memory
SAF	Synthetic Anti-Ferromagnetic
SL	Storage layer
SEM	Scanning Electron Microscope
SIMS	Secondary Ion Mass Spectrometry
SFD	Switching Field Distribution
SCD	Switching Current Distribution
TMR	Tunnel Magneto-Resistance
UV	Ultra Violet

List of Symbols

A_{ex}	Exchange constant	J m^{-1}
α	Gilbert damping	
Δ_x	Thermal Stability factor	
ΔE_x	Energy barrier	J
E_{tot}	Total energy	J
$E_{exchange}$	Exchange energy	J
$E_{anisotropy}$	Anisotropy energy	J
$E_{demagnetizing}$	Demagnetizing energy	J
E_{Zeeman}	Zeeman energy	J
$E_{dipolar}$	Dipolar energy	J
e	Electron charge	$1.6 \times 10^{-19} As(C)$
η_x	Spin polarization efficiency	
γ	Gyromagnetic ratio	Hz T^{-1}
G_{MTJ}	Magnetic tunnel junction conductance	Ω^{-1}
$\hbar$	Planck constant	$1.05457182 \times 10^{-34} m^2 kg/s$
H_{ex}/H	Magnetic field amplitude	A m^{-1}
H_{eff}	Effective field amplitude	A m^{-1}
$H_{coupling}$	Coupling field amplitude	A m^{-1}
H_k	Anisotropy field amplitude	A m^{-1}
H_d	Demagnetizing field amplitude	A m^{-1}
I_c	Critical Current	A
J	Current density	A m^{-2}
J_c	Critical Current density	A m^{-2}
K_{eff}	Effective anisotropy constant	J m^{-3}
K_u	Uniaxial anisotropy constant	J m^{-3}
k_B	Boltzman constant	$1.380649 \times 10^{-23} m^2 kgs^-2K^-1$
m	Unitary magnetisation vector	
M_s	Saturation magnetisation	A m^{-1}
μ_0	Vacuum magnetic permeability	Chosen equal to $4\pi \times 10^{-7}$ T A^{-1} m
N	Demagnetizing tensor	
t_X	Thickness of material X	m
$\tau_\perp$	Field-like torque	s^{-1}
$\tau_\parallel$	Damping-like torque	s^{-1}
T	Temperature	K
T_B	Blocking temperature	K
T_c	Curie temperature	K
τ_0	Characteristic time	ns
V	Voltage amplitude	V
V_c	Critical switching voltage	V
Vol	Volume	m^2

Chapter 1

Introduction to perpendicular STT-MRAM

1.1 Basics of magnetic tunnel junctions

1.1.1 Brief introduction to spintronics : Spin-valves and GMR

The era of digital information needs technologies employing new physical phenomena to increase both storage capacity and processing speed while reducing power consumption. For the past 50 years, the information technology industry has doubled the digital electronics performance almost every two years while maintaining the cost, area, and power of the integrated circuits [1]. These advancements were described by an empirical law named after Gordon Moore during the sixties and are based on the miniaturization of the simplest transistor design, the metal-oxide-semiconductor field-effect transistor (MOSFET) [2] [3]. The MOSFET is a three-terminal electronic device, this implies that its working principles are based on controlling the mobility of charge carriers (either electrons or holes) between two terminals (source and drain of the charge carriers) applying a voltage on the third terminal (Gate). In general, these devices are used for multiple purposes in today's computer architectures, such as data processing (Logic gates), storing information (Random access memories), or signal amplification in RF circuits for telecommunications. All these examples and their related manufacturing processes are known as CMOS technologies. The development of more complex and precise lithographic techniques has been able to cope with the reduction of CMOS to the physical limits of transistors. The transistor is fundamentally an electric switch, opening or closing the current flow of charges. When scaling its size to a few atomic layers, the quantum tunneling of these charges is more probable to take place, thus causing an important increase in leakage currents. This problem leads to an increase as well in the standby power dissipation with important implications for volatile memories. Note that in this last case a constant supply of power is required to not lose the information stored. There are various solutions to still increase the performance of ICs without the need for scaling, these are summarized in three branches: development of new materials and devices (E.g Spintronic devices), new ways of computation (E.g neuromorphic and quantum computing), and more efficient architectures with tailored designs depending on the precise specifications (E.g processing-in-memory architectures) [1]. Spintronic devices are practically capable of being used in any of these solutions with zero standby leakage, no volatility of stored information, compatibility with current CMOS processes and, above all, scalability. For these reasons, this field has attracted attention from both industry and academic research generating fast and remarkable advancements in magnetic materials engineering, understanding of new spin transport phenomena to control the magnetization in the matter, and new device design concepts to open a vast number of opportunities beyond CMOS [4] [5] [6]. Spintronic devices uses the spin of the electron in combination with its charge to generate and control spin-polarized currents, and convert magnetic to electrical signals. An initial example of the potential of applied spintronics was the rocketing increase in the hard drive (HDD) storage density following the discovery of giant magnetoresistance in 1988 (GMR) and its application to spin-valves reading heads [7]. In fact, the GMR effect is considered the starting point of this field and its implications were so important that Albert Fert and Peter Grünberg won the Nobel Prize in Physics in 2007 for its discovery [8] [9]. Figure.1.1 illustrates the main mechanisms behind this effect. In a ferromagnetic material (Co,Ni,Fe and its alloys) there is an intrinsic asymmetry between the density of states (DOS) available for the conduction electrons with the spin in the same direction as the local magnetization (spin-up), to the ones with the opposite spin to the local magnetization (spin-down). This results in a significant majority of spin-up electrons below the Fermi energy (E_F). In a simple approximation with limited temperature, it can be considered that the electron spin is conserved in each scattering event. In this context, when a current is flowing through the ferromagnet, spin-down electrons will have more probability of scattering, thus presenting a higher resistivity than the spin-up electrons ($\rho_\downarrow > \rho_\uparrow$). The resulting difference in resistivity can be understood with a two-current model, in which each majority and minority currents will flow through two parallel conduction channels (Figure.1.1.(c)). Since most of the current flows through the channel with less resistivity, an important consequence is the spin polarization of the current. The spin polarization factor η, in this case, is defined as $\eta = (j_\uparrow - j_\downarrow)/(j_\uparrow + j_\downarrow)$ and is a measure of the efficiency of a ferromagnetic layer to generate a spin-polarized current.

(a) Density of states in a magnetized ferromagnet (b) Spin dependent scattering vs magnetic configuration

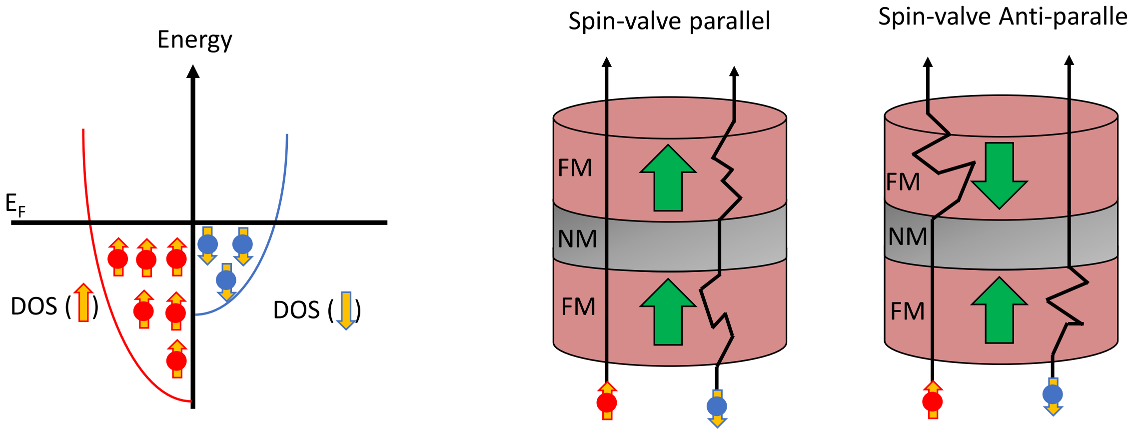

(c) Two current model in a ferromagnet (d) Two current model vs spin-valve magnetic configuration

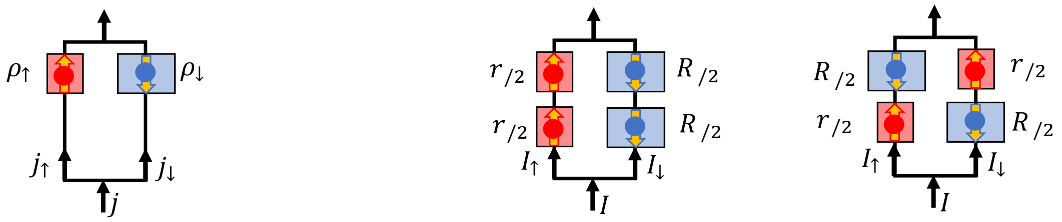

Figure. 1.1: (a) Simple schematic of the conduction electrons Density of states as a function of energy and spin polarization in a ferromagnetic material.(b) GMR based Spin-valve resistances states depending on the relative magnetic alignment of the ferromagnetic layers magnetization. (c) Two current model for a single ferromagnetic material.(d) Application of the two current model for a Spin-Valve between its two anti-parallel and parallel resistance states.

The GMR effect was first observed in Spin-Valve structures of the form Ferromagnetic/Non-magnetic/Ferromagnetic layers with in-plane magnetization. The same is applicable for the case of having ferromagnetic layers with magnetizations perpendicular to the plane as in figure.1.1.(b). In such structures, the electrical resistance depends on the relative parallel or anti-parallel magnetic configuration between the two ferromagnetic electrodes. The two current model can be applied then for the case of a current flowing through the full spin-valve as in figure.1.1.(d). For the case of a parallel configuration, the total parallel resistance of the FM/NM/FM can be written as R_P=rR/(r+R) with a free flow of the majority electrons through the less restive channels (low resistance). On the contrary, in an anti-parallel configuration, both spin-up and spin-down currents will suffer scattering when flowing through the Ferromagnet with opposite magnetization relative to the initial polarization. In this case, the resistance will be higher R_{AP}=(R+r)/4 and the GMR ratio between the two resistance states is derived as GMR= (R_{AP}-R_{AP})/R_P. Nowadays applications of GMR are mainly focused in sensors, it was primarily used as HDD reading heads till 2004 and was replaced due to the development of magnetic tunnel junctions with much higher magnetoresistance amplitudes.

1.1.2 The main MRAM building block : Magnetic tunnel junctions and TMR.

The magnetic tunnel junction (MTJ) is the most basic building block for magnetoresistive random access memory cells (MRAM) [10]. Similar to the spin-valve structure just introduced above, it is based on a multilayer structure comprising two ferromagnetic layers sandwiching a non-magnetic material, but at this time, this material is a really thin insulator. The first experimental demonstration of an MTJ and the tunnel magnetoresistance effect (TMR) was realized by Jullière in 1975 with an Fe/GeO/Co trilayer at really low temperatures (4.2 K) [11]. Contrary to the spin-valve based on the GMR effect, Jullière explained the change in magnetoresistance in the MTJ due to the differences in tunneling probability of the majority and minority spin-polarized currents between the parallel and anti-parallel alignments of the electrode's magnetization. Figure.1.2.(a) and (b) presents the basic schematics of the spin-dependent tunneling phenomena corresponding to the parallel and anti-parallel alignments between the M_1 and M_2 magnetization vectors. In this simple approach, the tunneling probability of a spin-polarized electron is provided by the available density of states and the number of occupied states at a given energy in the ferromagnetic metals at both sides of the tunnel barrier (ie.FM_1 and FM_2). If a bias voltage is applied, the Fermi energy of one of the ferromagnetic electrodes will decrease, thus causing a net tunneling current flowing from FM_1 to FM_2. The conductance of such current will be proportional to the product between the density of states in both electrodes at the same level of energy $G \propto DOS_1(E_{F-1})*DOS_2(E_{F-2}+eV)$, where $E_{F-1}=E_{F-2}+eV$. Then considering the ferromagnetic nature of each electrode, the spin polarization of the conduction electrons can be expressed as :

$$\eta_i = \frac{DOS_{\uparrow}(E_{F-i}) - DOS_{\uparrow}(E_{F-i})}{DOS_{\downarrow}(E_{F-i}) + DOS_{\downarrow}(E_{F-i})} \tag{1.1}$$

The TMR effect can be explained with the two current model considering the two conductance channels for each electron polarization (either spin-up of spin-down), and adding in parallel the two conductances:

$$G_{total} = DOS_1(\uparrow) * DOS_2(\uparrow) + DOS_1(\downarrow) * DOS_2(\downarrow) \tag{1.2}$$

When M_1 and M_2 are in parallel alignment, the majority spin-up electrons in FM_1 will tunnel towards the high number of available states in FM_2 (spin-up majority electrons with initial FM_1 polarization parallel to FM_2 local magnetization), a high current of majority electrons then is obtained with the corresponding low resistance state of the MTJ. On the other hand, if M_1 and M_2 are in anti-parallel alignment, the majority electrons in FM_1 now find a reduced number of available states in FM_2 (spin-up majority electrons with initial FM_1 polarization anti-parallel to FM_2 local magnetization), decreasing the current flow and resulting in a higher resistance state. In both cases, the minority electrons also tunnel but due to the lower number of occupied states in FM_1 the change is negligible. The TMR ratio is then defined as in equation 1.3, where η_1 and η_2 are the spin polarization efficiency of FM_1 and FM_2 electrodes.

$$TMR = \frac{R_{AP} - R_P}{R_P} = \frac{2\eta_1\eta_2}{1 - \eta_1\eta_2} \tag{1.3}$$

This last expression is known as Jullière's model and is a basic representation of the spin-dependent tunneling process. It neglects any spin-flip scattering during the tunneling process, Magnon generation in the ferromagnetic layer receiving the electrons, and all the band structures effects in both electrodes with the tunnel barrier.

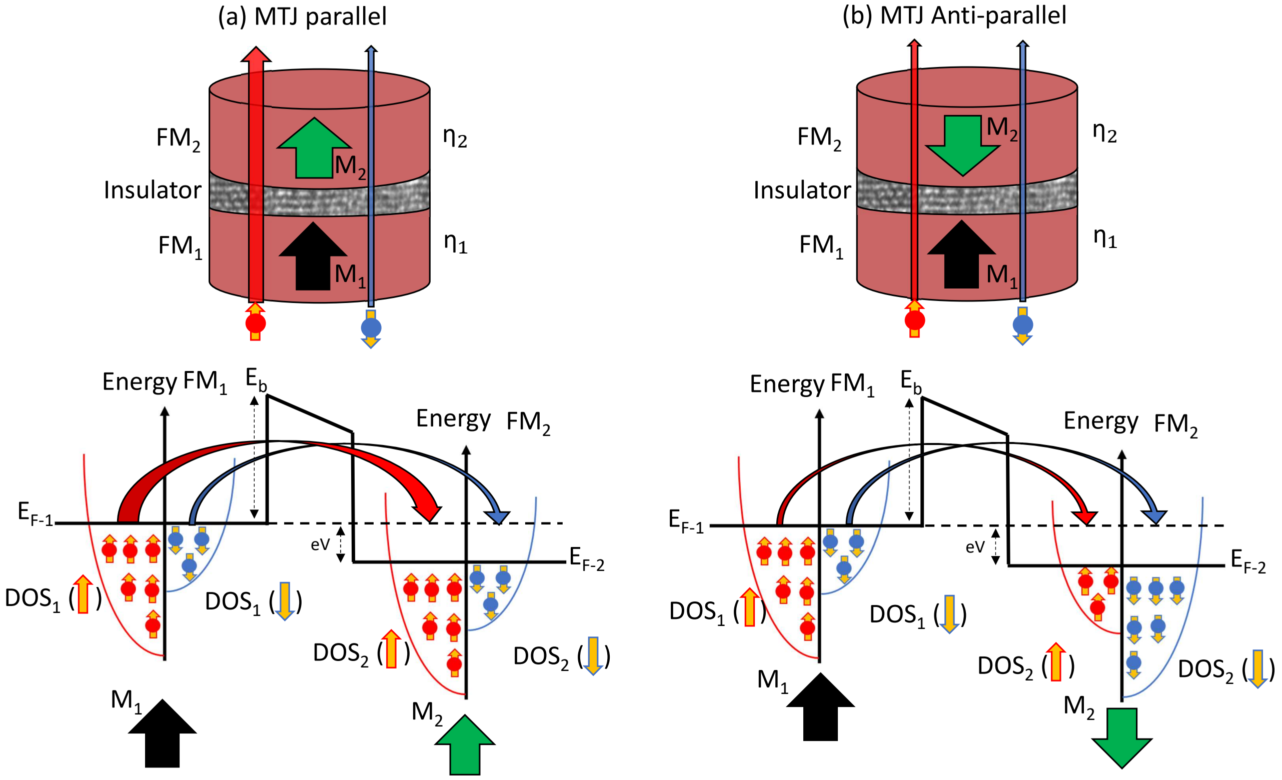

Figure. 1.2: Magnetic tunnel junction in parallel state (low resistance) (a) and anti-parallel state (high resistance) (b) and its associated spin-dependent tunneling mechanism through the tunnel barrier.

At its initial realization in 1975, the TMR effect did not attract much attention. It was later with the discovery of GMR and its potential applications that researchers started to rise the efforts to develop MTJ structures with TMR at room temperature. This was first attained with the work of Miyazaki et al.[12] and Moodera et al.[13] with insulating barriers based on amorphous aluminum oxides (AlOx). Following these results, the TMR ratios started to rise based on the optimization of the ferromagnetic electrodes composition and the crystal quality of the full MTJ structure. It all pointed out that not only the ferromagnetic electrodes were responsible for the spin polarization efficiency (controlling the final TMR ratio as in equation 1.3), but the crystallographic structure and epitaxial growth of the full trilayer itself. In 2001, more advanced model calculations were carried out by Butler [14] and Mathon [15] considering the impact in the tunneling probability of the different DOS for each type of electron in the trilayer band structure, predicting up to 1600% in TMR for Fe and Co epitaxially grown on MgO. The model was based on the so-called spin filtering effect. In a conductive crystalline material, the atoms in the cell structure hybridize their electronic orbitals generating several conduction bands of energy for the delocalized electrons. These energy bands are solutions to the electron's wave function when considering the periodic potential produced by the regular arrangement of the positive atomic nucleus in a crystal. Also known as Bloch states, these are quantum states controlling the required energy of the conduction electrons and are highly dependent on the interatomic distances in the crystal unit cell. In ferromagnetic metals with body-centered cubic structure, the Bloch states have specific symmetries (Δ_1 for spd hybridized orbitals,Δ_2 for d hybridized orbitals, and Δ_5 for pd hybridized orbitals). Then considering the spin polarization produced by the local magnetization, Bloch states with Δ_1 symmetry have a 100% spin-up population at the Fermi energy while for the Δ_2 and Δ_5 this polarization efficiency is lower. In an MTJ structure, when the insulating barrier and the ferromagnetic electrode crystal structure match, the same Bloch states will appear as evanescent wave function solutions in the barrier. Coherent tunneling of the polarized electrons can then be obtained as the Bloch states in the ferromagnetic crystal are coupled with the ones from the insulating barrier. This model also demonstrated that the exponential decay of the tunneling probability was faster for the Δ_2 and Δ_5 states with the spacer thickness. These results meant that only Δ_1 states with a spin polarization efficiency of $\eta_{\Delta_1} = 1$ are tunneling, thus filtering the tunneling current to be completely polarized and explaining the dramatic increase in TMR. The predictions made with this theoretical study was rapidly confirmed experimentally in epitaxial Fe/MgO/Fe structures [16] [17] and sputtered CofeB/MgO/CoFeB structures [18]. The highest TMR reported at room temperature is still 604% today [19] with resistance values in the kΩ range compatible with the impedance of the CMOS access transistor. For this reason, nowadays magnetic tunnel junctions comprising MgO tunnel barriers with the best epitaxial crystalline quality are the most used structure in magnetic random access memmories (MRAM). In our case, a detailed description of the critical materials parameters, barrier/electrodes growth, and annealing procedure to achieve these conditions are more detailed in chapter 3, sections 3.1 and 3.2.

1.1.3 Gibbs free energy of a nanomagnet

As introduced in the previous section concerning the first MTJ realizations and its spin-dependent transport properties, the simplest memory cell for MRAM consists of a series connection between an MTJ and the access MOSFET transistor. In real applications, the magnetic orientation of one of the electrodes must remain fixed while the other is free to reverse and thus retrieve the information stored as the resistance states in parallel or anti-parallel configurations of the MTJ. The MTJ resistance states R_P and R_{AP} are thus the logic "0" and "1" of the memory cell and are set by the relative magnetic orientation of the free layer with respect to the fixed layer. These two layers are also referred to as the storage layer (SL) and reference layer (RL). The main physical mechanism utilized to reverse the SL magnetization is the main characteristic defining the type of MRAM technology. The SL can be reversed by an external field as in Stoner Wolfarth MRAM [20] and toggle MRAM [21], with enough current passing through the junction (STT-MRAM [22]), or more recent, with the use of spin-orbit interactions (SOT-MRAM [23]). In the following sections, we will cover the main induced switching dynamics utilized in this thesis as well as a more detailed description of the full material stack for MRAM. The storage layer magnetization is the softest ferromagnetic layer in the stack and the height of the energy barrier between the two possible magnetic orientations at equilibrium is defines the retention of the information stored. In essence, under the application of an external perpendicular field (not produced by the magnetic volume itself) the free Gibbs energy of a nanomagnet of volume V consists of a balance of several energy contributions:

$$E_{total} = E_{exchange} + E_{anisotropy} + E_{demagnetizing} + E_{Zeeman} \tag{1.4}$$

This expression can be utilized in different models to find the magnetic configuration at equilibrium by minimizing the total energy of the system. In reality, a ferromagnetic system not magnetized in saturation consists of regions with uniform magnetization so-called domains separated by domain walls in which the local magnetization varies with position. Micromagnetic modeling of a ferromagnet is thus the description of the magnetization by means of continuous functions in which amplitude is the spontaneous magnetization (Ms) and varies in position and time $\vec{m}(\vec{r}$,t) [24]. This definition can be simplified with single-domain models (macrospin) in which the magnetization direction vector is taken to be uniform for the full volume of the magnetic system.

Exchange energy : Ferromagnets and antiferromagnets

The exchange interaction is one of the principal origins of spontaneous magnetization in materials, it arises from a quantum-mechanical effect originating between two neighboring spins. According to Pauli's exclusion principle, it results from the minimization of the interaction energy between the charges of the electrons in the same orbital when the spins are pointing in the same direction. this effect was described by Heisenberg [25] with the generalization of the Hamiltonian :

$$\hat{H}_{ex} = -\sum_{i,j} J_{i,j} \left\langle \vec{S}_i \cdot \vec{S}_j \right\rangle \tag{1.5}$$

Where $S_i \cdot S_j$ is the scalar product between the neighboring spins and $J_{i,j}$ is the exchange constant. The sign of the exchange constant determines the preference of the spins to be aligned either parallel (positive) or anti-parallel (negative) and is the reason behind ferromagnetism or antiferromagnetism in solids. Under the assumption of itinerant magnetism (applicable to transition metals such as Fe and Co and its alloys) the exchange energy is defined as:

$$E_{ex} = \int_V A_{ex} \left\{ (\nabla m_x(\vec{r}))^2 + (\nabla m_y(\vec{r}))^2 + (\nabla m_z(\vec{r}))^2 \right\} dr \tag{1.6}$$

Here, A_{ex} is the exchange stiffness constant and is dependent of the lattice parameter of the unit cell (For bcc $A_{ex} = KS^2/2$).

Zeeman energy

If there is a presence of an external magnetic field $\vec{H_{ex}}$, the local magnetization vector $\vec{M} = M_s\vec{m}(\vec{r}$,t) tends to be aligned with the field direction. The resulting Energy associated with the misalignment between the local magnetization vectors is defined by the Zeeman's expression (where μ_0 is the vacuum permeability):

$$E_{zeeman} = -\mu_0 \int_V \vec{M} \cdot \vec{H_{ex}} dV \tag{1.7}$$

Anisotropy energy

A non-infinite Ferromagnetic material will always present a preferential orientation of its magnetization. This direction is referred to as the easy axis of the magnetization and can be originated from the balance of several sources. In general, the anisotropy energy is usually expressed as $E_{anisotropy}=K_{eff}\sin^2(\theta)V$ for a single-domain approximation, where K_{eff} is the amplitude of the effective anisotropy, θ the angle of the magnetization $\vec{M}$ with respect to the prefered easy-axis orientation and V the volume of the ferromagnet. The various origins of anisotropy in a ferromagnetic material are described next:

Demagnetizing energy and shape anisotropy

As introduced with the exchange interaction energy in a ferromagnetic material, this interaction yields the parallel alignment of the atomic magnetic moments inside a domain or single magnetic nanoparticle. At the same time, each atomic magnetic moment will generate a localized magnetic field that will also be experienced by the neighboring magnetic moments (a.k.a magnetostatic interaction). These localized fields can be understood as magnetic dipoles with an energy minimum when the two magnetic moments are pointing in opposite directions. The exchange and magnetostatic interactions are thus in competition inside regions with uniform magnetization. Without the magnetostatic interactions, all the magnetic moments in the ferromagnet would be pointing in the same direction (due to the exchange interaction). In the boundaries of this uniform region of magnetization, the total number of neighboring magnetic moments is reduced, generating a localized unbalance between the dipolar and the exchange interactions. This unbalance has two effects; the uncompensated dipolar charges pointing at the surface normal will generate a distribution of fictitious positive and negative charges, at the same time, the reduction of the exchange interaction between magnetic moments at the surface will allow for the relaxation of the magnetic moments at the boundaries of the magnetic body. On one hand, the distribution of charges is responsible for the generation of the dipolar field or stray field outside the magnetic material. On the contrary, the misalignment caused by the reduced exchange interaction at the boundaries is mathematically expressed as a demagnetizing field inside the material. The demagnetizing energy quantifies the interaction of the magnetization $\vec{M}$ with this fictitious demagnetizing field generated by itself and is defined by :

$$E_{demagnetizing} = -\frac{1}{2}\mu_0 \int_V \vec{M} \cdot \vec{H}_d(\vec{r})dr \tag{1.8}$$

The demagnetizing energy is reduced when the magnetic charges are minimized, giving rise to the formation of domain structures with magnetization close paths and the shape anisotropy in nanomagnets and thin films. The demagnetizing field is defined as $\vec{H_d}=-N \cdot \vec{M}$, where N is the so-called demagnetizing tensor. This tensor depends on the geometry of the magnetic body and its diagonal values set the prefered direction imposed by the shape anisotropy that minimizes the generation of surface charges. For the case of thin films, $N_x=N_y=0$ while $N_z=1$ whose lateral size is much larger than its thickness.

Magnetocrystalline anisotropy

Depending on the crystal structure of a ferromagnetic material, the crystal lattice can favor certain directions of magnetization. The magnetocrystalline anisotropy originates when the ions in the crystal generate charge distributions with associated electro-static fields directions, this field then influences the orbital angular momentum of the electrons. This turns out to originate the preferable orientations in space of the spins and thus of the magnetization due to spin-orbit coupling. Depending on the unit cell, several easy axes can arise depending on the spacial ordering of the atoms (E.g cubic, hexagonal), the most common is the case of uniaxial anisotropy for which energy is expressed as :

$$E_{anisotropy} = \int_V K_u[1 - (\vec{u} \cdot \vec{m})]dV \tag{1.9}$$

Where $\vec{u}$ is the unit vector of the easy axis direction and K_u the uniaxial anisotropy constant. When the uniaxial anisotropy unit vector is perpendicular to the film plane this is referred to as perpendicular magnetic anisotropy (PMA).

Interfacial anisotropy

In multilayer structures consisting of a non-magnetic material and ferromagnetic material, a perpendicular magnetic anisotropy can arise at the interface due to stress, spin-orbit coupling, and hybridization of orbitals between the ferromagnetic elements and oxides or heavy metals. In materials with high spin-orbit coupling (such as heavy metals like Pt,Ta,W or Pd) the hybridization of the $5d$ orbitals of the heavy metal and $3d$ of the ferromagnetic metal at the interface leads to an enhancement of the out-of-plane orbital moment of the ferromagnetic material and induces as well a parallel magnetic moment in the heavy metal [26] [27]. This results in a strong PMA when stacking multilayers based on heavy metal/ferromagnetic metal repeats and is highly influenced by the lattice arrangement in the material (crystal quality and roughness). A similar phenomenon is also observed in the case of transition metal/oxide interfaces such as Fe/MgO, however, in this case, the hybridization between the out-of-plane Fe $3dz2$ and O $2pz$ orbitals causes the strong PMA due to a significant transfer of charges from Fe to O orbitals [28]. In this last case the degree of oxidation at the interface is critical as it determines the number of Fe-O bonds [29]. For ferromagnetic thin films, PMA competes with the shape anisotropy. The multiple sources of anisotropy can then be described by into a single effective anisotropy factor as:

$$K_{eff} = K_v + \frac{K_s}{t} - \frac{\mu_0 M_s^2}{2} \tag{1.10}$$

Where K_v are the bulk sources of anisotropy (i.e magnetocrystalline anisotropy) K_s is the surface anisotropy constant and t the thickness of the ferromagnetic film. Looking to K_{eff}, it is clear that PMA is highly dependent on the ferromagnetic material thickness, and for a critical thickness value, the shape anisotropy overcomes the PMA causing the uniaxial anisotropy constant to fall in the plane of the sample. By definition, positive K_{eff} corresponds to a perpendicular magnetic anisotropy. Typical values of critical thickness are for example 1.4 nm for FeCo/MgO interfaces or 1 nm for Co/Pt bilayers. Shape anisotropy was the main source of anisotropy utilized for in-plane MRAM cells, in this case, the storage layer geometry was crucial to control the data retention of the memory cells. Today's most common MRAM realizations are based on the use of interfacial anisotropy arising from the Storage layer/MgO interface and it constitutes one of the main phenomena utilized in this thesis for the optimization of the magnetic properties of the multilayers comprised in our stack

1.1.4 Interlayer exchange coupling: Synthetic Antiferromagnetic structure

In the previous sections we focus on the free energy associated with the magnetization of single nanomagnets and thin films. The ferromagnetic or antiferromagnetic order of the magnetic moments within a magnetic material was introduced depending on the sign of the exchange interaction energy. In multilayer structures, when a thin non-magnetic metal (1 nm) is introduced between two ferromagnetic metal layers, an interlayer exchange coupling is normally produced. The energy associated to this type of coupling is expressed as E_{IEC}=-$J_{IEC}\cos(\Theta)$, where here, the sign of J_{IEC} determines the antiferromagnetic or ferromagnetic coupling and Θ is the relative angle between the layer magnetizations. This interaction is know as Ruderman-Kittel-Kasuya-Yosida (RKKY) and originates from the formation of spin-polarized quantum well states sharing the magnetic information between the two ferromagnetic layers [30] [31]. At the time of its discovery, the amplitude and sign of the J_{IEC} was found to oscillate with the non-magnetic metal thickness [32]. Therefore, the thickness of the non-magnetic spacer can be tuned to attain the maximum ferromagnetic or antiferromagnetic coupling between the layers. These structures are know as synthetic Antiferromagnetic structure (SAF) and is one of the key components in MTJs for MRAM applications. In fact, as mentioned at the beginning of this section, the reference layer in an MTJ must remain unchanged or pinned in order to be able to read the resistance state of the memory cell. In particular for perpendicular magnetic tunnel junctions (p-MTJ), this is achieved by coupling the reference layer electrode though an extremely thin metallic spacer (about 0.2 nm) to a high PMA multilayer structure consisting in various Co/Pt repeats. In this case, the spacer thickness must ensure a strong ferromagnetic coupling, thus fixing the reference layer magnetization. On the other hand, once the p-MTJ is patterned into pillars, the reference layer generates a stray field acting on the storage layer magnetization. This magnetostatic interaction between the electrodes leads to a tendency of the MTJ to remain in the parallel configuration depending on the strengh of the RL stray field, affecting the writability of the memory. The solution is found by coupling the reference layer/Co/Pt multilayers via RKKY coupling to another Co/Pt multilayer structure. In this case, the spacer thickness is such that the coupling between the full structure is antiferromagnetic normally based in using a thin 0.9 nm Ru layer. The full structure is then considered a SAF type reference layer forming a flux closure, compensating the stray field generated by each magnetic moment. In general, the SAF is a key element in spintronic devices as it allows to fix the magnetization of a layer while minimizing the stray field. A detailed description of this materials stacks are given in the materials and optimization chapter for the samples utilized in this thesis.

1.2 Magnetization dynamics

1.2.1 Thermally activated switching: The thermal stability factor

In magnetic tunnel junctions for memory applications, the time required to keep the information stored is one of the most important characteristics in a memory chip. The information is intrinsically stored by the magnetic orientation of the storage layer magnetization with its two minimum energy states with respect to the reference layer magnetization. This implies that the uniaxial magnetic anisotropy and the volume of this magnetic layer are most often defining the energy barrier separating the bistable states of the memory cell ΔE= $K_u V$. As introduced in previous section 1.8 in this chapter, various origins of uniaxial anisotropy were described, explaining the possible magnetic orientation depending on the sign of the final effective anisotropy of the layer. First-generation MRAM was based on in-plane shape anisotropy produced by the demagnetizing field, presenting low values of maximum anisotropy. As the amplitude of this source of anisotropy was based on the geometry of the storage layer element, these devices presented limitations in scalability and reduced values of retention/energy barrier. Then, the development of storage layers with perpendicular magnetic anisotropy allowed reaching smaller dimensions as a result of a higher reachable intrinsic anisotropy. This was one of the main motivations for adopting perpendicular magnetic tunnel junctions (p-MTJ) as the main spintronic devices to be used in MRAM applications [33]. For a nanometer disk with a cell diameter "D" under the single-domain approximation, the energy barrier can be estimated by accounting for all the possible sources of anisotropy as :

$$\Delta E = K_{eff} V = (K_v + K_s - \frac{\mu_0 M_s^2 (3N_z - 1)t}{4})\frac{\pi D^2}{4} \tag{1.11}$$

This equation is derived from the difference in energy between the minimums at 0 and 180 of the storage layer magnetization angle with the easy axis direction taking into account the anisotropy energy $\text{E}_{anisotropy}$=$K_{eff}\sin^2(\theta)$ as shown in figure.1.3. In bits of information stored in an MTJ, the state of the storage layer magnetization can be reversed by thermal fluctuations causing the loss of information for a given time and temperature. The characteristic thermally activated switching time of the Storage layer is described by an Arrhenius law as follows :

$$\tau = \tau_0 exp(\frac{\Delta E}{k_B T}) \tag{1.12}$$

Where τ_0 is reversal attempt time of approximately 1 ns, T is the temperature and k_B the Boltzmann constant. When the energy barrier is comparable to the thermal energy ($k_B T$), the magnetization of the free layer will reverse randomly between the two possible stable configurations. If the measurement time of the magnetization τ_m is higher than the characteristic thermally activated switching time defined in Eq.1.17, the nanomagnet magnetization will reverse several times during the measurement. These conditions results in and average zero magnetization or apparent superparamagnetic state. On the contrary, if τ_m is lower than the characteristic time, the magnetization is not reversed, thus being blocked in the initial state. The temperature in which the measurement time an the characteristic thermal activated switching time equals is refereed as Blocking temperature (T_B). Finally, the thermal stability factor of an MRAM cell is thus expressed as the ratio between the energy barrier to overcome and the thermal energy:

$$\Delta = \frac{\Delta E}{k_B T} \tag{1.13}$$

The value of the thermal stability factor depends on specific applications, however, typical values of $\Delta = 40$ result in a data retention time of 10 years at room temperature (298 K). On the other hand, another source of increase or decrease of the thermal stability factor is the presence of an external field acting on the storage layer magnetization. As discussed the previously, the uncompensated stray field generated by the reference layer in a full MTJ structure can cause the stabilization, or on the contrary, the destabilization of the storage layer magnetization. This flaw is normally reduced or completely suppressed by the use of SAF structures. In this thesis, we will observe that this could also be employed to further increase the storage layer thermal stability factor with the use of our proposed stack design (see the following chapter 2 "The ASL-DMTJ a Double magnetic tunnel junction with a switchable assistance layer"). The enhancements in thermal stability factor can be expressed as :

$$\Delta_{coupling} = \Delta_{anisotropy} \left[1 + \frac{H_{coupling}}{H_{anisotropy}} \right]^2 \tag{1.14}$$

Where $H_{anisotropy} = 2(K_{eff}/\mu_0 M_s)$ is the effective anisotropy field and $H_{coupling}$ is the field produced by a stray field or interlayer exchange coupling promoting a ferromagnetic coupling.

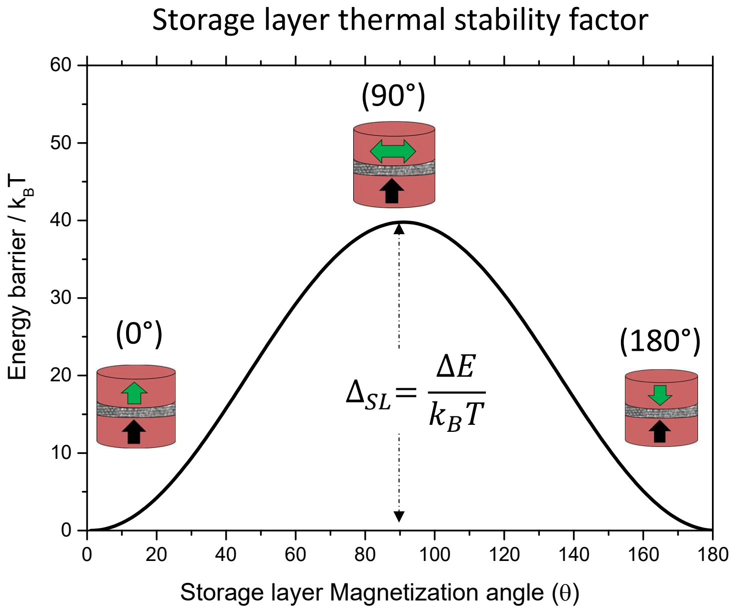

Figure. 1.3: Energy barrier between 0 and 180 for a storage layer with perpendicular uniaxial anisotropy and its associated thermal stability factor.

Equations 1.11 and 1.14 based on an uniform reversal of the nanomagnet magnetization presents experimental limitations at the time of describing the energy barrier defining the thermal stability factor and its variations against an external field [34] [35]. Reported experimental data for perpendicular magnetic tunnel junctions shows that the validity of the single domain approximation highly depends on the cells diameter, deviating the extracted thermal stability factor from those predicted by just accounting for the volume and the uniaxial anisotropy energy of the layer. In addition, the quadratic dependence of Δ with the diameter is neither fulfilled for cells larger than 50 nm. This deviation results on the overestimation of the thermal stability factor predicted for greater storage layer diameters related to the non-coherent rotation of the magnetization by domain nucleation and motion. This reversal mechanism has indeed a lower energy barrier to overcome by the thermal energy in the system and is defined by the energy of the domain wall [36], resulting on a thermal stability factor defined by :

$$\Delta = \frac{4\sqrt{A_{ex} K_u} D t}{k_B T} \tag{1.15}$$

Where A_{ex} is the exchange energy of the nanomagnet (Storage layer in our case). Contrary to the single domain approximation, this definition of thermal stability factor scales linearly with the cell diameter and a cross-over is found for which the magnetization reversal is no longer defined by a coherent rotation of the magnetization but rather by the nucleation of a domain and subsequent domain-wall movement reversal of the storage layer magnetization.

The limits of the macrospin model in terms of cell diameter are determined by the sub-volume size defining whether the energy barrier to reverse is lower for the definition given by Eq.1.11 or 1.15, typical experiments reported the cross-over diameter limit for the coherent reversal model at 20 to 50 nm [37] [38].

1.2.2 Field induced switching : The Stoner-Wohlfarth model

The simplest analytical model to describe the effect of an applied magnetic field on the magnetization of a single-magnetic particle, is the so-called Stoner-Wohlfarth model [39]. This model is based on the evaluation of the magnetic orientation at equilibrium by minimizing the total free energy of the nanomagnet's magnetization. The applied field influence is accounted for by adding the Zeeman energy to the uniaxial anisotropy energy. Again, for the case of a nano-disk shaped magnetic body, the total energy of the system is:

$$E_{total} = [K_v + K_s - \frac{\mu_0 M_s^2 (3N_z - 1]t}{4}) sin^2(\theta) V - \mu_0 M_s H_{ex} cos(\theta - \phi) V \tag{1.16}$$

Where H_{ex} is the amplitude of the external field and ϕ its angle with respect to the unitary vector of anisotropy (i.e easy axis). Figure.1.4 illustrates the typical geometrical representation of the Stoner-Wolfarth model for the different combinations of external field z and x components. For a complete reversal of the magnetization, the total components H_x and H_z must fall outside the region defined by the astroid. Then, the respective hysteresis curves $m_z(H_{ex})$ for a given ϕ are found as numerical solutions at equilibrium $dE/d\theta$=0 as a function of the external field amplitude. The most interesting solutions to this m(H) curves are at ϕ=90 and ϕ=0 . The first (ϕ=90) corresponds to a hard axis hysteretic response where the magnetization gradually rotates following the field until reaching saturation (H_{ex}=H_k). The second (ϕ=0), corresponds to an easy-axis hysteresis curve with a sharp reversal of the magnetization at H_{ex}=H_k. This value of the field is referred to as the coercive field (H_c) and defines the minimum field amplitude to reverse the magnetization between its two stable states (at θ= 0 and 180 0) [40]. In reality, this is a crude simplification of the hysteresis behavior of a ferromagnet. Normally H_c is found to be lower than H_k due to nonuniform reversal by nucleation and propagation of a domain wall through the nanostructure.

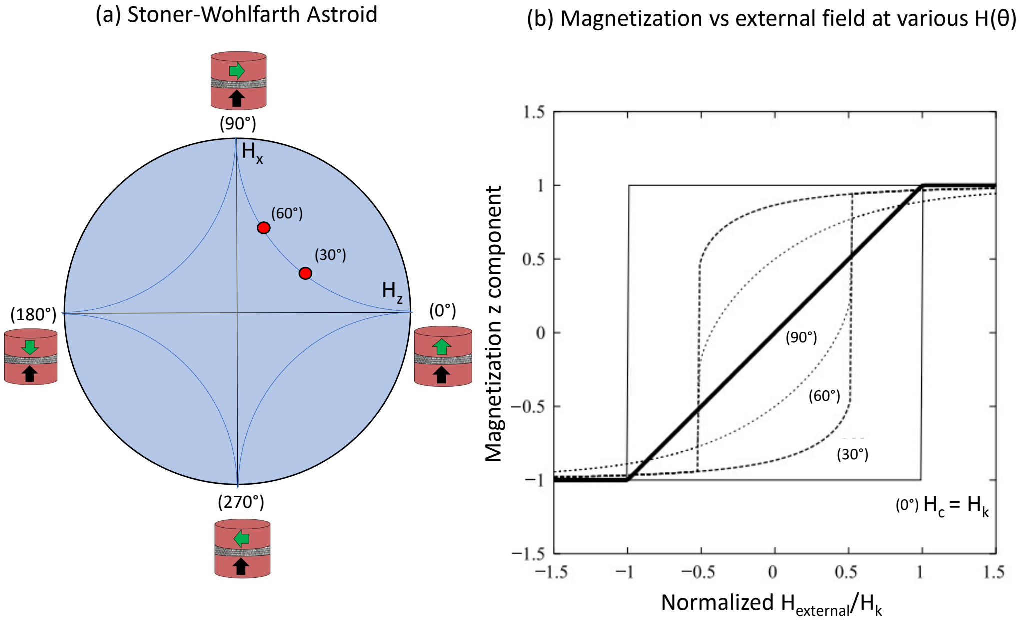

Figure. 1.4: (a) Stoner-Wolhfarth astroid. (b) Hysteresis loops as a function of the external field applied in the H_x and H_z plane. Image adapted from [40].

1.2.3 Current induced switching : The spin transfer torque phenomena

The effect of spin transfer torque (STT) by an incoming polarized current was predicted by Slonczewski and Berger in 1996 [41] [42]. It is nowadays the main writing mechanism utilized in MRAM giving rise to the Spin transfer torque MRAM technology (STT-MRAM). Considering the same FM/NM/FM structures as the ones described previously for GMR and TMR (the non-magnetic spacer can be either a metal or an insulator), the spin-transfer torque effect can be seen as a reciprocal phenomenon to the spin polarization of the conduction electrons [43]. When a spin-polarized current enters a ferromagnetic layer with a transverse local magnetization, the conservation of the total angular momentum causes a reciprocal torque on both, the local magnetization and the spin of the incoming electrons. This is better understood with the illustrations in figure.1.5.(a) and (b). In the case of a current flowing from FM_1 to FM_2 (figure.1.5.(a)), the local magnetization $\vec{M}_1$ of the first layer polarizes the conduction electrons in the same direction as its local magnetization $\vec{m}_1$. These polarized electrons then tunnel or are diffused through the non-magnetic spacer conserving its spin polarization. When the spin-polarized current ($\vec{m}_1$) reaches the second FM_2, it once again gets polarized but along the local magnetization of the second layer $\vec{m}_2$. At this moment, the spin angular momentum is conserved therefore the transverse component of $\vec{m}_1$ is absorbed by the local magnetization $\vec{M}_2$. The result of this process is the transfer of a torque that tends to align $\vec{M}_2$ with $\vec{M}_1$, thus stabilizing the parallel configuration in the structure.

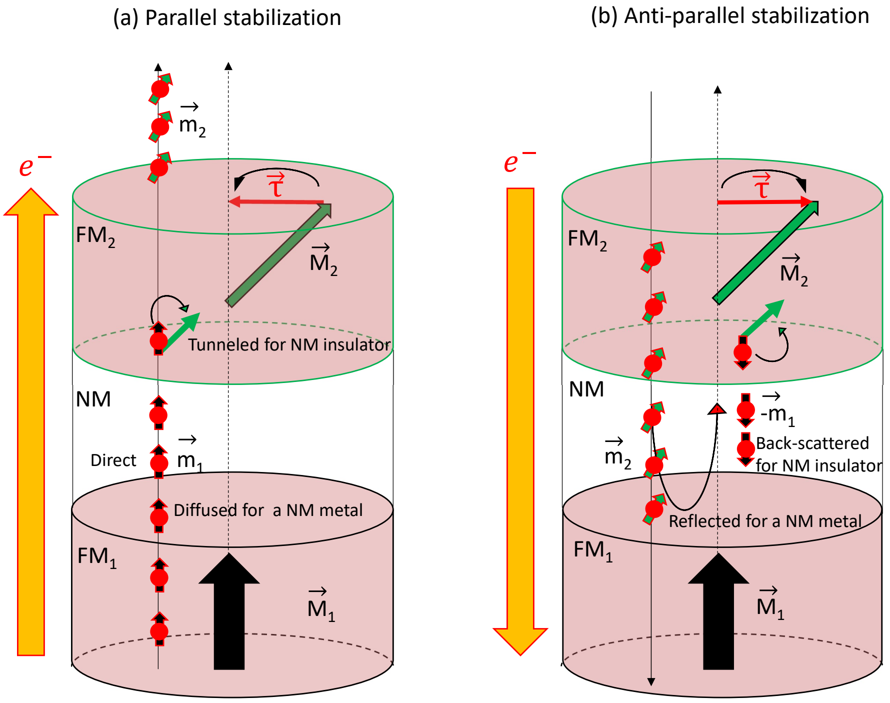

Figure. 1.5: Illustration of the parallel (a) and anti-parallel (b) stabilization between $\vec{M}_2$ and $\vec{M}_1$ imposed by the spin transfer torque depending on the current flow direction.

On the contrary, when the current flow is inverted, (current from FM_2 to FM_1 in figure.1.5.(b)), the electrons with spin opposite to $\vec{M}_1$ are back-scattered and exert a spin transfer torque by the same mechanism on $\vec{M}_2$. In this case, as the reflected electrons are with a spin along the $-\vec{m}_1$, an anti-parallel alignment between $\vec{M}_2$ with $\vec{M}_1$ is stabilized. The current direction controls then the stabilization of the parallel or anti-parallel configuration between the electrodes magnetization. The torque acting on $\vec{M}_2$ can be expressed as the contribution of two terms and is dependent on the voltage amplitude V :

$$\vec{\tau} = \vec{\tau_{\parallel}} + \vec{\tau_{\perp}} = \gamma a_{\parallel} V \vec{m}_2 \times (\vec{m}_2 \times \vec{m}_1) + \gamma a_{\perp} V^2 (\vec{m}_2 \times \vec{m}_1) \tag{1.17}$$

Where $\tau_{\|}$ in Eq.1.17 is called a damping-like torque,$\tau_{\perp}$ is a field-like torque and γ is the free electron gyromagnetic ratio. In general, the field-like torque is considered to be negligible with respect to the damping-like and is not considered in our calculations [44]. A more detailed description of the material parameters controlling these torques is given in the following chapter 2 section "Transport model for DMTJ structures with a switchable polarizer" 2.2.2 with the numerical simulations of our device concerning the damping-like prefactor $a_{\|}$ [45]. For the case of a spin-valve structure, the spin polarized current will conduct through the non-magnetic spacer, this corresponds to the diffusive transport of the current which spin polarization will depend on the characteristic scattering length of the spacer metal, thus determining the population of spin polarized electrons arriving at the FM_2 that effectively transfers is angular moment. On the contrary, for the case of magnetic tunnel junctions, the spin polarized electrons tunnel from the FM_1 to FM_2 through the insulating spacer. This implies that the spin polarized electrons are rather transmitted ballistically and its tunneling probability (Depending on the parallel or anti-parallel state of the MTJ) will determine if the STT acting on the FM_2 is exerted by direct tunneling electrons (AP MTJ state majority electrons from FM_1 tunneling towards FM_2 favoring the MTJ parallel state) or are accumulated at the FM_2/NM interface (P MTJ state in which the minority electrons in FM_2 are accumulated thus favoring the MTJ anti-parallel state). In essence, the STT effect reversing the magnetization of FM_2 is basically similar independently of having a metal or an insulator as a non-magnetic spacer.

1.2.4 Landau-Lifshitz-Gibert-Slonczewski equation : critical switching current by STT

Following the discussion of spin-transfer torque phenomena and considering the previous $\mathrm{FM}_1/\mathrm{NM}/\mathrm{FM}_2$ system described in the previous section, the magnetization dynamics of M_2 under applied field and voltage can be easily described by integrating the Landau-Lifshitz-Gibert-Slonczewski [46] [47] (LLGS) equation (see also figure.1.6:

$$\frac{d\vec{m_2}}{dt} = -\gamma(\vec{m_2} \times \mu_0 H_{eff}) + \alpha(\vec{m_2} \times \frac{d\vec{m_2}}{dt}) + \gamma a_{\|} V \vec{m_2} \times (\vec{m_2} \times \vec{m_1}) \tag{1.18}$$

Let us consider that the magnetization $\vec{M_2}$ is in a non-collinear orientation with respect to an effective field $(\vec{H_{eff}})$, where $\vec{H_{eff}}$ involves any magnetic field acting on $\vec{M_2}$, this are, external applied fields, uniaxial anisotropy field of the layer, and stray fields or interlayer exchange coupling from $\vec{M_1}$.

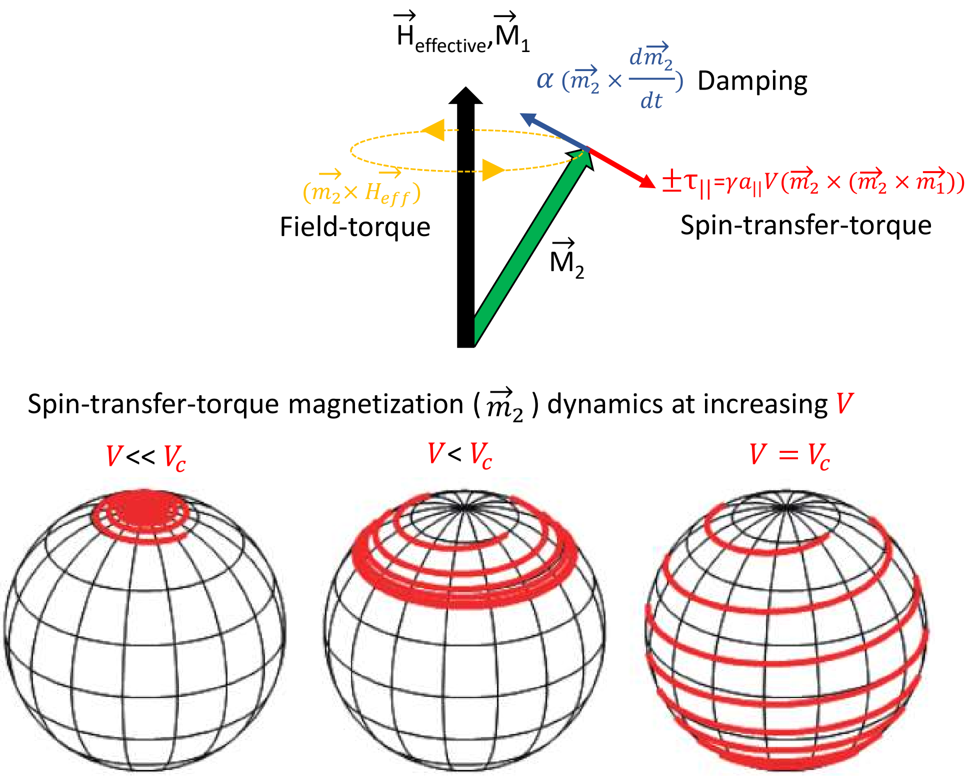

Figure. 1.6: Schematic showing the effect of the different terms from the LLGS equation with examples of the integration of the LLG equation giving the $\vec{M_2}$ magnetization dynamics for $V << V_c$,$V < V_c$,$V = V_c$ causing small precession, higher amplitude precession and full reversal of the magnetization respectively.

The effect of this field is divided into two terms; First, the Larmor conservative precession term or field-torque. This term causes the a continuous precession of the magnetization $\vec{M_2}$ with a constant angle around the direction of $\vec{H_{eff}}$. Second, the Gilbert relaxation term, which describes the dissipation of the energy of $\vec{M_2}$ out of equilibrium with a viscous force (Damped magnetization dynamics) [48]. Where α is the phenomenological Gilbert damping constant and depends on the material but also on the experimental conditions [49]. This term in the equation makes the magnetization reach the minimum energy state parallel to the direction of $\vec{H_{eff}}$. Then, if a constant voltage is applied across the structure and only considering the STT-damping-like torque, the spin-polarized current injected from FM$_1$ will exert a torque perpendicular to the magnetization $\vec{M_2}$. This torque behaves as a damping or anti-damping depending on the current direction and the magnetic orientation of the polarizer ($\vec{M_1}$). Under the conditions of having an STT acting in the opposite direction of the damping, the precession and frequency depend on the voltage amplitude. For lower values of Voltage, steady-state excitation of $\vec{M_2}$ can be sustained [50]. If the voltage reaches a critical value (V_c), the magnetization of FM$_2$ can be reversed to another stable minimum of energy. This mechanism is the principal writing procedure to write STT-MRAM memory cells and in the devices in this thesis. For the case of conventional perpendicular STT-MRAM, the critical voltage threshold corresponds to the LLGS solution when the STT overcomes the Gilbert damping. In the case of modeling this structure for a perpendicular anisotropy MTJ (p-MTJ) with $\vec{M_1}$ fixed and FM$_2$ with an out-of-plane uniaxial anisotropy, this condition allows to calculate the characteristic critical switching current between the two possible perpendicular orientations as [51] :

$$I_c = \frac{V_c}{R} = \frac{2e}{\hbar}\frac{\alpha\mu_0 M_s Vol H_k}{\eta_1} \tag{1.19}$$

Where R is the resistance state of the magnetic tunnel junction before the reversal (either R$_P$ or R$_{AP}$), M_s the saturation magnetization of FM$_2$ and η_1 the spin polarization efficiency of FM$_1$. Note that the critical switching current is proportional to the product between the anisotropy field and the volume of the layer, thus the higher the thermal stability factor of the memory, the higher the critical current to write.

1.3 Towards high performance p-STT-MRAM

1.3.1 Applications and challenges of p-STT-MRAM

Achieving energy efficient STT-MRAM memory cells is one of the major goals towards universal use of MRAM technology [52]. Traditional computer architectures consist of a pyramid-like memory hierarchy with a variety of data storage technologies depending on the application level. These levels are mainly defined by the access time to read the stored information or speed specifications, which in the end, controls the power consumption, cost, and memory density of the technology [53] [4]. Starting from the fastest and closest to the central processing unit, at the top of the hierarchy in figure.1.7, stands the three on-chip levels of cache memory (L1, L2, and L3). These levels are dominated by the use of Static random access memory (SRAM), characterized by its ultra-fast speed (1 to 10 ns), low density, and high power dissipation in standby. Following the CPU caches and starting with off-chip technologies is the main memory, with high density, fast speed (30 ns), based on 1-transistor 1-capacitor DRAM. Finally, at the base of the pyramid and sustaining all the weight of the non-volatile permanent memory are the hard drives, solid states drives, and Flash memory, for which specifications are centered on ultra-high density and low cost at the expense of speed (10 µs).

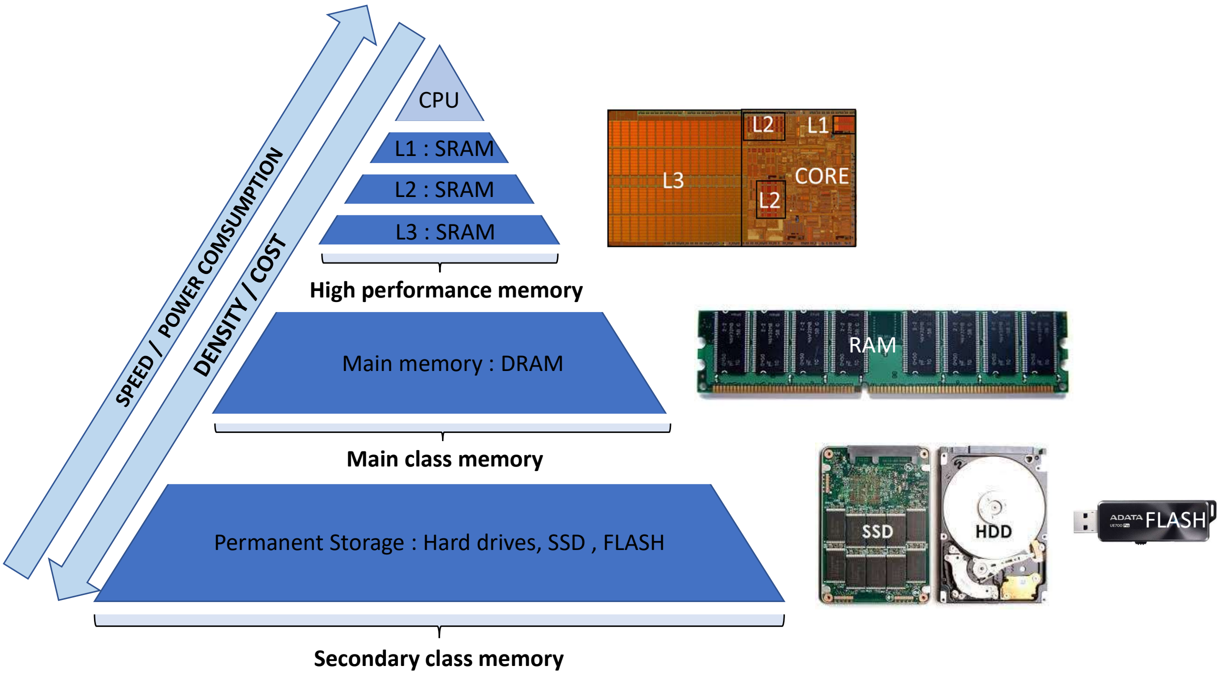

Figure. 1.7: The simplified memory hierarchy of nowadays computer architectures. Speed and power consumption of the memory technologies increase with the higher the level in the hierarchy, while density and cost are reduced for decreasing levels.

Since its onset during the 90s, MRAM technologies were presented with the ability to be potentially used at each of these three levels due to their endurance, high speed, scalability, and non-volatility [54]. This possibility triggered almost 30 years of MRAM development, generating important advances involving materials, magnetic tunnel junction stack designs, and a variety of research in spintronic phenomena to write more efficiently the magnetic memory cells. Spin transfer torque, spin-orbit torque [23] [55] [56], voltage control anisotropy [57] are clear examples of the last. Perpendicular STT-MRAM (p-STT-MRAM) technologies are the most adapted for a high variety of applications. However, nowadays industrial use of p-STT-MRAM is limited to specific levels and applications in the memory hierarchy. Applications in which the beneficial characteristics of p-STT-MRAM represent an important reduction on the power consumption of the integrated circuits. An example of this is the use of p-STT-MRAM as embedded flash memory in IoT applications (Internet of the things) for ICs in need of low power integrated non-volatile storage memory or as a substitution to traditional DRAM. For DRAM applications, the non-volatility of STT-MRAM removes the need for the refreshing process of the information stored, decreasing dramatically the power consumption. However, for DRAM application as main memory, the capacity of STT-MRAM chips still needs to be increased to 1Gbit presently up to tens of Gbit. Another foreseen application of STT-MRAM is that of the last cache memory levels on the processors. This type of memory is considered high performance due to a combination of high speed and information retention, that is now dominated by the use of SRAM technologies. This last type of memory presents several disadvantages, two of those being the low density and the static power leakage due to the constant power supply needed to maintain the information stored. The possible use of p-STT-MRAM based technology at this level is attracting more and more industrial players to the development of high performance p-STT-MRAM memory cells.

A well-known overview of what is considered a high performance p-STT-MRAM memory cell can be described by considering the three main basic functionalities that must be fulfilled simultaneously [54] : 1) High tunnel magnetoresistance ratio (TMR) between the magnetic tunnel junction high and low resistance states, thus ensuring enough resistance difference, and avoiding reading errors (Readability). 2) Low STT switching current of the free layer magnetization, for low power consumption, fast switching speeds, and MTJ enhanced endurance (Writability). 3) Enough retention or the free layer thermal stability factor (Δ), proportional to the energy barrier between its two possible magnetic configurations, and must be at least 40 times the thermal activation energy for a data retention time of 10 years ($\Delta = \Delta E/(k_B T) = 40$). This last requirement is also paramount in order to scale down the memory cells and achieve high density memory arrays [58] while the critical current density determines the size of the transistor providing the current for switching. One of the main important challenges while developing high performance p-STT-MRAM memory cells is to overcome the dilemma of increasing the thermal stability factor while reducing the critical switching current. As seen in the previous sections, for p-STT-MRAM memory cells, the free layer energy barrier is commonly defined by the perpendicular magnetic anisotropy arising from the magnetic metal/oxide interface with the tunnel barrier (FeCo/MgO) and the volume of the layer. In addition, the energy barrier is known to be proportional to its critical switching current by spin-transfer torque (figure.1.9). Increasing the thermal stability of the storage layer (SL) has a direct impact on the critical switching current of the device, presenting a compromise in the optimization of the device performance. The trade-off between thermal stability and critical switching current is defined in terms of figure of merit (Δ/Ic) used as a quantitative measurement of a memory cell efficiency [59].

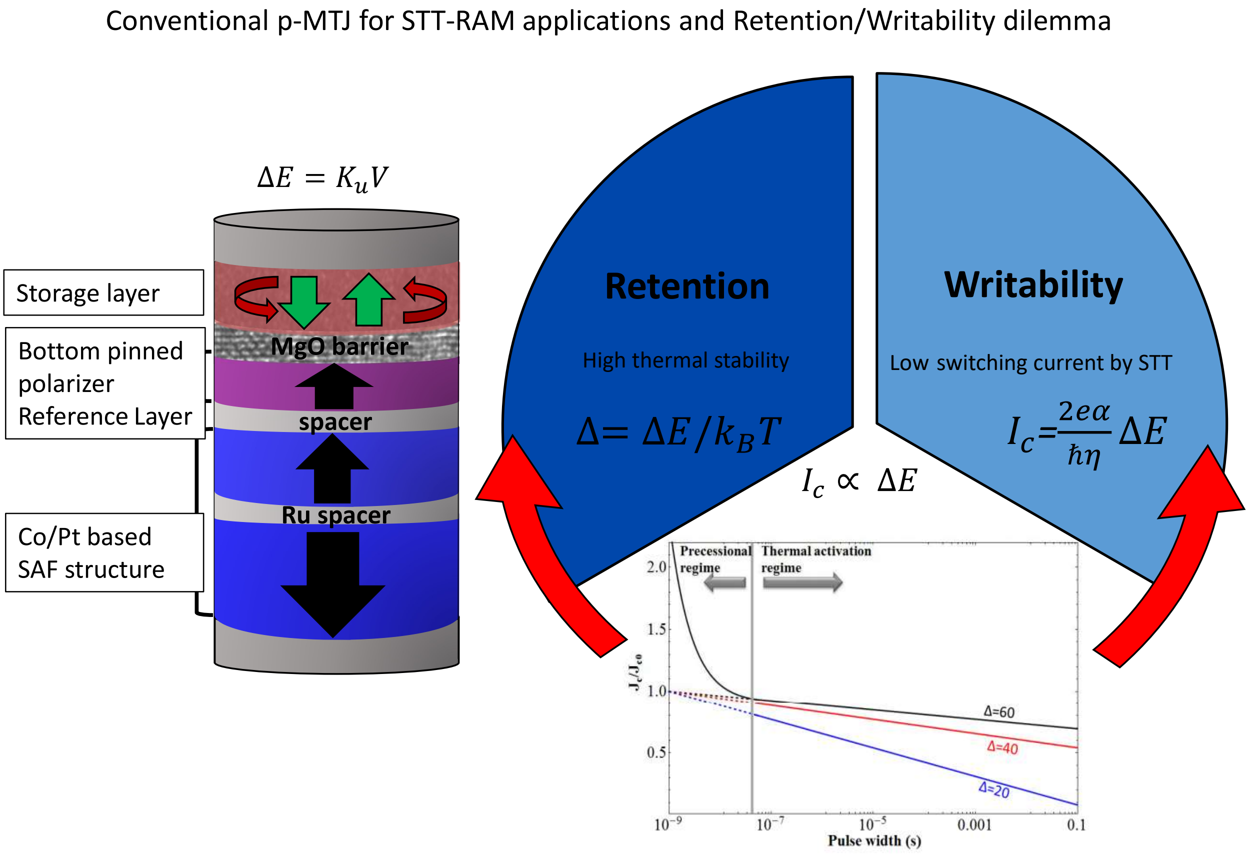

Figure. 1.8: Conventional p-STT-MRAM stack with the Writability and Retention dilemma, showing the relation between critical switching current, thermal stability factor and switching time. Image taken and adapted from [54].

1.3.2 Breaking the p-STT-MRAM dilemma

Finding strategies to enhance performance by increasing the figure of merit has been a common focus of p-STT-MRAM research for the last few years. The strategies involved are summarized in two main branches. Through materials engineering of the storage layer itself and MTJ structure in general or stack design strategies centered on the engineering of new p-MTJ variants. The first strategy relies on decreasing the Gilbert damping of the storage layer or increasing the spin polarization efficiency of the magnetic electrodes/barrier quality[60] [61] [62] (increasing TMR while reducing the resistance-area product (RxA)). The second strategy consists of stack designs with multiple polarizing layers, which are based on reducing the critical switching threshold of conventional p-MTJ stacks by employing an additional source of STT from a secondary polarizer [63] [4]. The magnetic configuration and properties of these secondary polarizers define the spin-transfer torque exerted on the storage layer magnetization and the specific switching dynamics of the device. Figure 3 (a-e) shows a selection of the different MTJ structures found in the literature; (a) canted in-plane polarizer [64],(b) spin precessional current in-plane polarizer [65] [66] and (c) out-of-plane synthetic antiferromagnetic polarizer [67] [68]. These p-MTJ stack designs make use of an orthogonal STT to reduce the incubation time of the storage layer or assist during the reversal thus reducing the critical switching current. However, the thermal stability of the storage layer is maintained so that, at the end, all structures present an overall enhancement in the figure of merit.

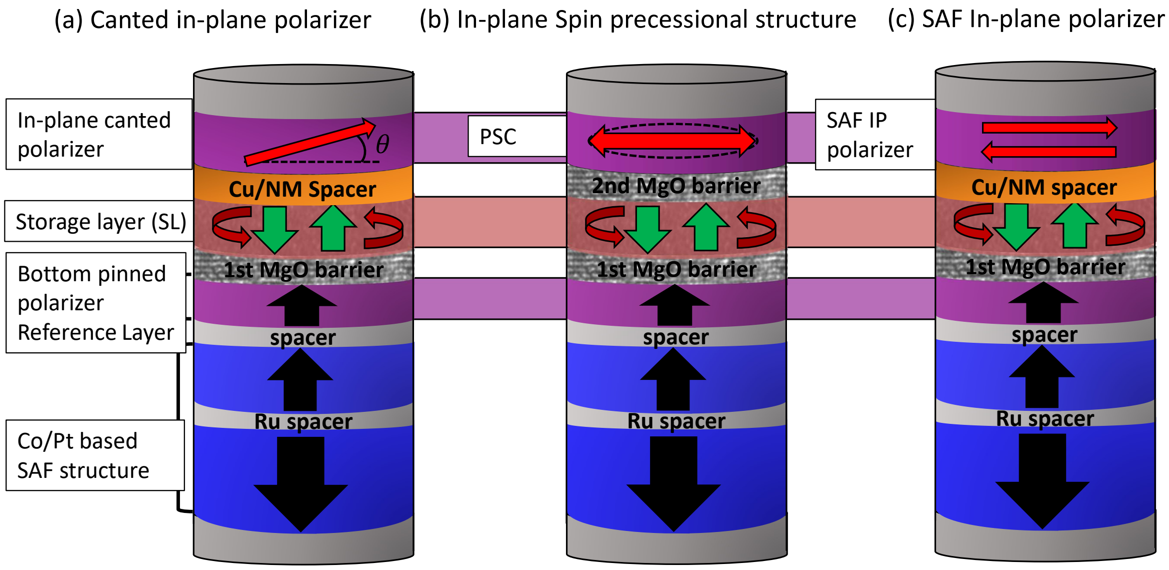

Figure. 1.9: Examples of state of the art p-MTJ variants, (a) Canted in-plane polarizer [64]. (c) Spin precessional current in-plane polarizer [65] [66]. (d) In-plane synthetic antiferromagnetic polarizer [67] [68].

One of the most promising p-MTJ variants proposed in order to overcome the p-STT-MRAM writing/retention dilemma is the use of double magnetic tunnel junction structures (p-DMTJ). In these structures, the storage layer is sandwiched between two tunnel barriers. This trilayer is itself inserted between two polarizing layers, usually of fixed magnetization and perpendicular to the plane (collinear with the storage layer magnetization). The thermal stability of the storage magnetization is then increased thanks to the presence of not only one but two interfacial anisotropy contributions arising from the two magnetic metal-oxide interfaces between the FeCoB storage layer and the MgO barriers ($\Delta E \simeq 2K_uV$). In the most common realization of a p-DMTJ, the two fixed polarizers are set in anti-parallel configuration. In this situation, the net STT efficiency is strongly increased due to additive STT contributions from the top and bottom spin polarizing layers. The first experimental realizations of p-DMTJ structures were reported by IBM with the work of Gu et al. [69] (2015) and supported by the detailed theoretical descriptions by Daniel Worledge [70] (2017). Their results support an achievable factor of 2 reduction in critical switching current. These results were encouraging providing that one of the tunnel barriers is maintained with a much lower RxA than the other. In fact, despite the figure of merit enhancement, the two tunnel barrier absolute tunnel magnetoresistance amplitudes subtract from each other, reducing the maximum device TMR. The losses in TMR can be minimized by reducing the serial resistance introduced by the second tunnel barrier. In addition, following these first studies, a modification on the top polarizing layer was proposed by Chavent et al. [71] (2021) at SPINTEC, and developed by Paulo Coelho during his thesis [72] (2019). Their p-DMTJ stack consists of optimizing the top polarizer to be able to reverse its magnetization between two possible configurations. Figure.1.10 and 1.11. (a) and (b) depicts these two configurations and the torque exerted on the SL magnetization between operation modes, introducing as well the typical p-DMTJ stack based on a storage layer sandwiched between the two tunnel barriers and pinned top/bottom perpendicular polarizers.

(a) STT in Write mode

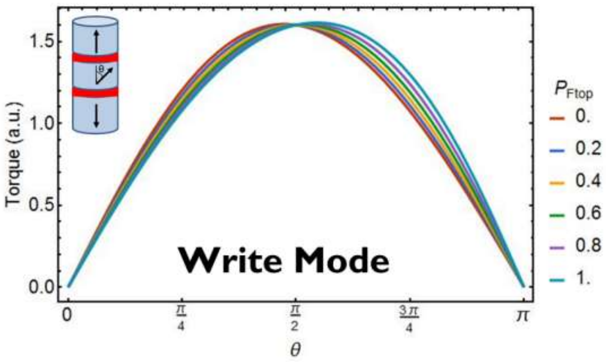

(b) STT in Read mode

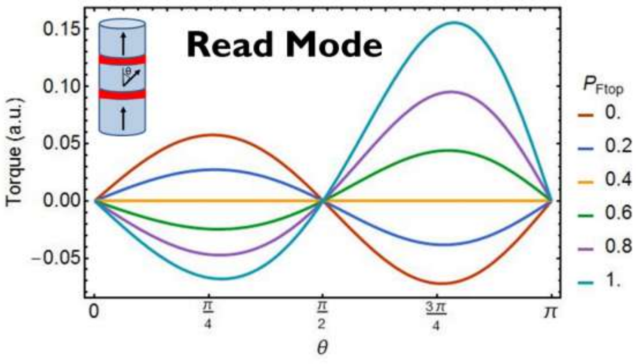

Figure. 1.10: STT exerted on the SL magnetization in (a) write and (b) read modes of operation. Image taken from [71] [72].

In this case, the top polarizer is denoted as read/write mode control layer, thus allowing to modulate the net STT from both tunnel barriers and the TMR amplitude. In write mode, both polarizers are anti-parallel, so their STT contributions to the storage layer add up. When having the two polarizers in parallel alignment, the net STT substracts, and the TMR amplitude is the highest. Thanks to the successful engineering of the top polarizer, they showed the possibility of maximizing the TMR to ensure faster readouts without the risk of read disturb events, while the critical current was reduced in the case of setting properly the top and bottom polarizer (i.e anti-parallel alignment).

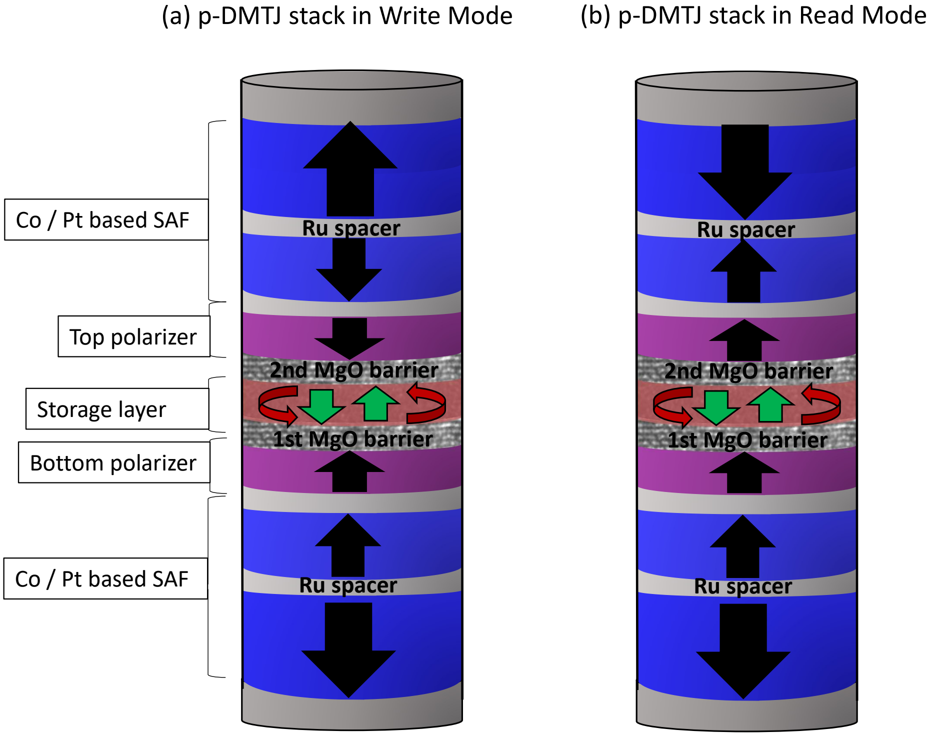

Figure. 1.11: (a) Write and (b) Read modes of operation depending on the magnetic configuration between the top and bottom pinned polarizers, introduction as well of the general stack composition for conventional p-DMTJ structures.

Another example of today's state of the art p-DMTJ structures is the recent publication from IBM (G.Hu et al. [73], 2021) with a p-DMTJ structure with a novel spacer separating the storage layer from the top polarizer. Their results are based on a spacer that provides spin-torque in the second interface without any associated serial resistance. Also recently, IMEC reported BEOL-compatible p-DMTJ having 100-120% TMR based on the optimization of the storage layer materials, opening the possibility for the integration of these kinds of structures as embedded-MRAM for low power applications (Rao et al. 2020 [74]). In general, all these new developments highlight the interest from both industry and research centers to come up with solutions enhancing the performance of p-DMTJ stacks due to its potential to bring p-STT-MRAM technologies to the higher efficiency level. As it is discussed at the beginning of the next chapter, with the introduction of the stack design developed during this thesis, these structures are not easy to realize experimentally and present some drawbacks related to the top polarizer and the SAF structure. Our proposed device aims to provide solutions to the main challenges of p-DMTJ devices but with a simpler and thinner structure.

Chapter 2

The ASL-DMTJ: a double magnetic tunnel junction with a switchable assistance layer

2.1 The ASL-DMTJ stack design

The perpendicular DMTJ structure can be considered as the main source of inspiration for the stack design developed during this thesis [75][76] [69] [77]. Several similarities in their fundamental principles of operation are adapted, namely, the way of reducing the critical current to switch the FL magnetization [70] [78] [79], some considerations regarding the tunnel barriers serial resistances [80] [73], and the materials composition of the free layer and of the reference layer [72]. Therefore, it is imperative to compare what our proposed stack design brings new to the same problem for which the standard p-DMTJ structures were conceived, which is the increase of the figure of merit of p-STT-MRAM by extending the retention time of the storage layer while decreasing its critical current to write. As was mentioned in section 1.3.2 in the introductory chapter, apart from other types of realizations based on the use of secondary polarizers, the double magnetic tunnel junction was the first stack design presenting a real improvement in STT writing efficiency [69]. Despite the advantages provided by this structure, some difficulties can arise at the time of developing, fabricating and achieving a symmetrical critical current to switch the free layer magnetization. Fortunately for the engineer, these difficulties are centered on the same part of the stack, the top polarizer. The first difficulty is related to the fine control of its perpendicular anisotropy [81] [74]. The stability of this magnetic layer must be high enough so that its magnetization remains fixed during the operation of the device with voltage, while being able to be brought into anti-parallel alignment with respect to the bottom polarizer [75]. Under these conditions, an additive STT will be exerted on the SL magnetization no matter the current direction flowing through the junctions (i.e voltage polarity). This usually implies that the top polarizer is designed to have a lower coercivity than that of the bottom polarizer, so that it can be initialized with an external magnetic field without affecting the magnetic orientation of the bottom polarizer. As mentioned in the introduction chapter (Section 1.1.4 concerning the SAF structure), for standard p-STT-MRAM stacks, to achieve high perpendicular anisotropy in a hard reference electrode, the FeCoB layer in contact with the MgO barrier is commonly exchange coupled through a thin metallic insertion to a Co/Pt multilayer synthetic antiferromagnetic structure (SAF) [82] [83]. It turns out that the perpendicular anisotropy of each SAF structure depends strongly on the crystallographic texture of the Co/Pt multilayers (i.e fcc 111) [84] [85] [86]. While high anisotropy can be easily obtained in bottom polarizers, by using a seed layer that promotes the required texture [87] [88] [89], a top polarizer must be grown seedless on top of the tunnel barrier. Therefore, without the required strong texture, the coercivity often results insufficient, yielding detrimental magnetic stability to the hard top polarizer.

Another shortcoming of conventional p-DMTJs lies in the requirement to compensate the stray fields generated by the top and bottom polarizers. In general, the number of Co/Pt repetitions in the SAFs are optimized such that, at the time of patterning the pillar, the dipolar fields between the two RKKY-induced anti-ferromagnetic coupled portions of the SAF are cancelled. Therefore, no stray fields affect the FL magnetization. For the case of having two SAF structures in the same embodiment, as for p-DMTJs, a precise balance of four magnetic moments is now required. Then, any remaining uncompensated field acting on the FL magnetization will favor a specific parallel or anti-parallel alignment when switching by spin-transfer torque, resulting in a significant asymmetries in the critical switching currents between the AP to P and P to AP transitions [73]. The final challenge concerns the fabrication of these devices. Considering that each SAF/polarizer represents at least 80% of the device thickness in a single MTJ, adding a secondary pinned top polarizer multiplies the total thickness by almost a factor of 2. The additional thickness results in extended ion beam etching times during the device nano-patterning introducing defects at the MTJs sidewalls due to ion irradiation damage and metallic redepositions [90] [91] [92]. These defects can then lead to a decrease in the spin polarization efficiency of the MTJs. In contrast to conventional p-DMTJs, the device developed during this thesis is simpler and thinner. This device, so-called assistance layer double magnetic tunnel junction (ASL-DMTJ), relies on the use of a switchable top polarizer that acts as an assisting layer (ASL) [93]. Figure.2.1.(a)-(b) illustrates the comparison between a conventional p-DMTJ structure and the ASL-DMTJ stack. The structure essentially comprises three magnetic layers; first, the reference layer (RL) or main spin polarizer, with the highest stability of the stack. Secondly, the storage layer (SL), whose magnetic orientation with respect to the RL stores the high and low resistance state of the memory. Third, the Assistance layer (ASL), acting as a secondary spin polarizer, and depending on whether its magnetic orientation is parallel or anti-parallel with respect to the RL, controls the STT efficiency of the SL switching. Figure.2.1. (a) represents a simple schematic of the ASL-DMTJ stack design.

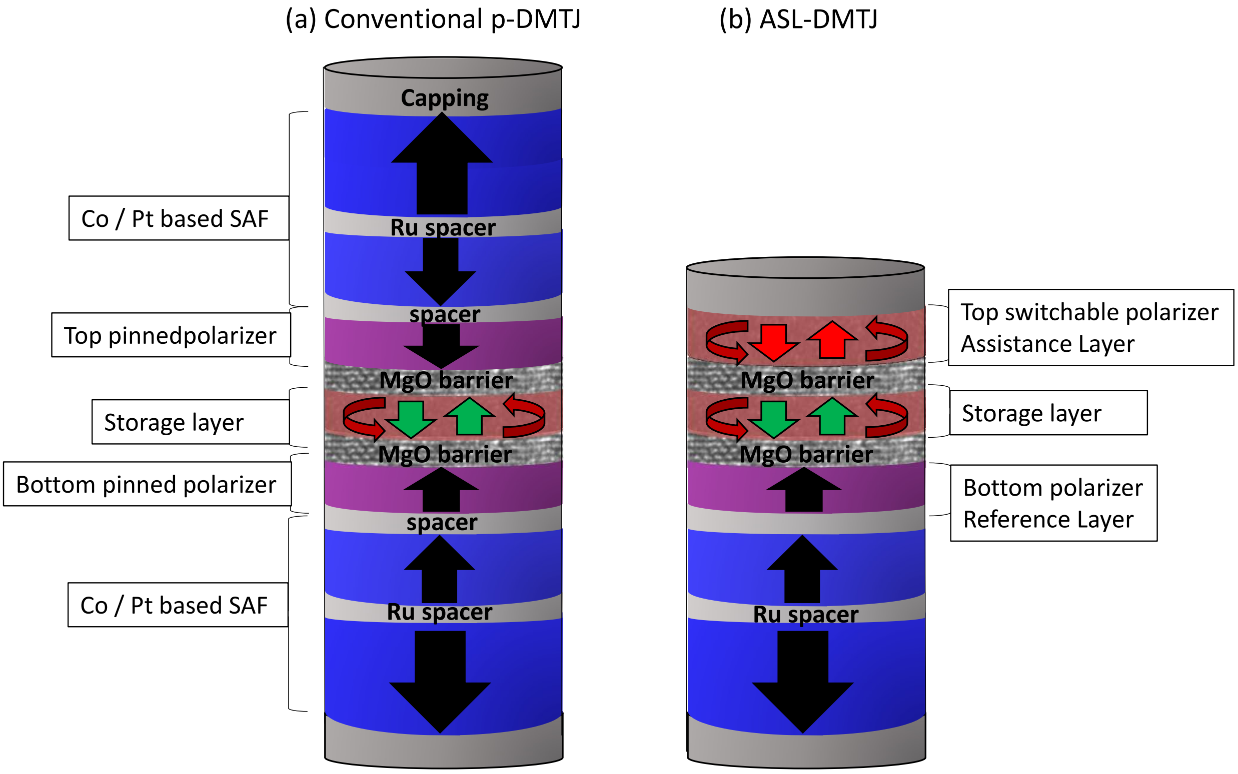

Figure. 2.1: Stack comparison between (a) a conventional p-DMTJ with static top polarizer and bottom reference layer and (b) an ASL-DMTJ with a switchable top polarizer.

The ASL must be designed to change its magnetic orientation during or before the write operation in such a way that it maximizes the STT efficiency [76] [94] [72] [69], while always ending parallel to the SL magnetization. When the two layers (ASL-SL) are left in parallel configuration, the retention of the SL is enhanced due to their ferromagnetic coupling. As is discussed numerically in this chapter, to achieve these properties, the layers coupling and relative thermal stability factors must be fine-tuned.

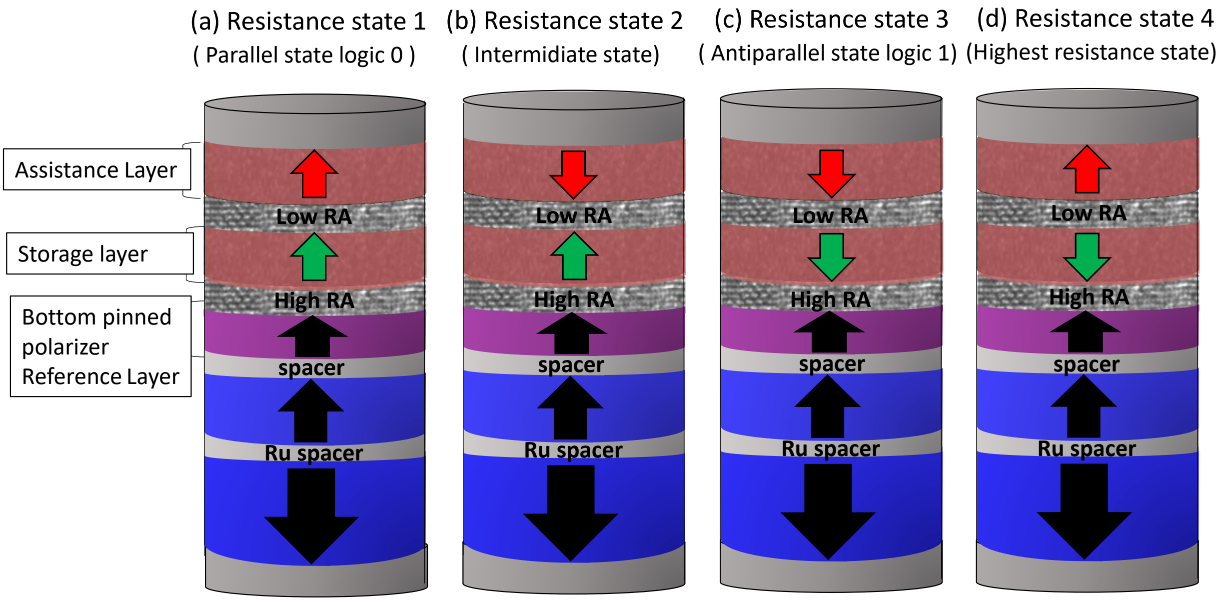

Figure. 2.2: Simple schematics of the ASL-DMTJ possible magnetic configurations i.e Resistance states (Provided that the RA of the second MTJ is lower than that of the first MTJ). (a) State of least resistance with all MTJs in parallel configuration. (b) Intermediate resistance state with the ASL/SL MTJ anti-parallel while the SL/RL MTJ in parallel alingment. (c) Second intermediate resistance state with the ASL/SL MTJ parallel, while the SL/RL in anti-parallel alignments. (d) highest possible resistance state with all the MTJs within the structure are in anti-parallel alignment

In order to obtain a sufficiently large read-out signal, the RA and TMR of the various tunnel barriers in the ASL-DMTJ structure are chosen to be different. The maximum RA and TMR are provided by the MTJ between the SL and the RL, while lower RA and TMR are used for the MTJ between the ASL and SL to reduce the serial resistance. More details on how these barrier properties are modulated are given in chapter 3 ”Materials and experimental methods” section 3.1 ”MTJ and magnetic stack deposition”. Besides, these differences in barrier electrical properties enable the electrical characterization of the ASL-SL reversal orders, allowing the determination of which layer is switching at a given value of field or voltage. As illustrated in Figure.2.2.(a),(b),(c) and (d), depending on the magnetic orientations of the ASL and SL, and considering the distinct barrier's electrical properties, the two MTJs comprising the ASL-DMTJ can be stabilized in four resistance states [69] [95]; Resistance state one (R1), with the lowest resistance, for which the two MTJs are in parallel configuration. Resistance state two (R2), with the second MTJ in anti-parallel configuration, while the MTJ between the SL and RL remains in parallel configuration. Resistance state three (R3), inverse of R2, with the SL and RL magnetized in anti-parallel while the ASL and the SL are magnetized parallel. And last, Resistance state four (R4), or highest resistance state, for which both MTJs are in anti-parallel configuration. The magnetic orientation of the ASL not only controls the STT amplitude. The ferromagnetic coupling with the SL favors the parallel state between them. This increases the stability of the storage layer magnetization and therefore the memory cell retention. It is important to mention that this coupling can not only originate from dipolar interaction, but also, to some extent, from an interlayer coupling through the thin oxide barrier between the ASL and SL. Details on this idea will be discussed in chapter 4, section 4.1.3, concerning the "Materials optimization of the Assistance layer and Storage layer coupled system" subsection 4.1.3 "ASL/SL coupling through low oxidation MgO tunnel barriers". The operating principles of our proposed device are then based on increasing the thermal stability of the SL in resistance states 1 and 2, where the magneto-static energy of the two layers is minimal, these states being the ones used to store the low resistance (logic 0) and high resistance (logic 1) of the memory. Contrary to conventional p-DMTJ structures comprising bottom and top pinned polarizers, the ASL-DMTJ switching dynamics relies on the interplay between the ASL and the SL coupled system in the various possible magnetic configurations, submitted to their mutual spin transfer torques and ferromagnetic coupling.

2.2 Numerical investigations of the ASL-DMTJ working principles

2.2.1 Magneto-static energy calculations of the ASL-SL magnetizations dipolar interaction

To evaluate the influence of the ferromagnetic coupling between the two layers magnetization (i.e. ASL and SL), we will start with double-macrospin numerical calculations of their magneto-static energy. This first qualitative study aims to provide the reader with a clear explanation of the mechanism underlying the increase of the SL thermal stability, as well as the impact of the layers relative thermal stabilities on the minimum energy paths to change its magnetic orientation. It is then a matter of extracting the energy barriers separating the various magnetic configurations of the ASL-DMTJ introduced in the previous section (figure.2.2.(b) to (e)). In the following calculations we will only focus on the magnetic interaction between the ASL and SL magnetic bodies, assuming there is no stray field produced by the RL on these layers. As described in the introduction section (Chapter 1, "Gibbs free energy of a nanomagnet" in section 1.8), in a simple macrospin approximation, the free energy of a nanomagnet essentially depends on its effective anisotropy field, on the Zeeman energy when there is an external magnetic field, and on the demagnetizing field determined by the geometry of the nanomagnet. Then, each of the layers in our modelled system has its respective perpendicular effective anisotropy constant (K_{eff}), whose value is provided by the sum of the positive surface anisotropy arising from the MgO interfaces (K_s/t_{layer}) and its negative internal demagnetizing field ($-\frac{1}{2}\mu_0 M_s^2(N_x - N_z)$) [96]. Equation 2.1 shows the expression of the anisotropy energy applicable to any of the nanomagnets comprised in the system, with t and M_s being the thickness and magnetic saturation of the layer, d the cell diameter, and ϕ the angle of the magnetization unit vector with respect to the normal vector to the plane.

$$\mathrm{E}_{anisotropy}(\phi) = \left(\left(\frac{K_s}{t} - \frac{1}{2}\mu_0 M_s^2(N_y - N_z)\right)\left(1 - cos^2(\phi)\right)\right) \tag{2.1}$$

The magnetic coupling energy of the system is expressed as the Zeeman energy originated from the ASL dipolar field acting on the SL magnetization. To facilitate these calculations, the magnetization vectors are rotated only in the $y - z$ plane. Therefore, the y and z components of the ASL dipolar field are extracted from the product between its M_s and its dipolar tensor. This dipolar tensor is determined by the surface magnetic charges generating the field from the ASL body, and the distance between the layers (center-to-center distance of the layers adding the MgO spacer); $|H_y| = M_{s_{ASL}} N_{dip_y}$, $|H_z| = M_{s_{ASL}} N_{dip_z}$. Then, the dipolar energy between the ASL and SL magnetization vectors, is determined by Eq2.2:

$$\mathrm{E}_{dipolar}(\phi_{SL}, \phi_{ASL}) = \mu_0 M_{s_{SL}} \left(|H_y|\, sin(\phi_{SL}) sin(\phi_{ASL}) + |H_z|\, cos(\phi_{SL}) cos(\phi_{ASL})\right) \tag{2.2}$$

Finally, the total magnetic energy of the system as a function of the magnetization direction of the layers can be calculated with Eq. 2.1, by adding the anisotropy energy of each layer and its dipolar coupling interaction energy. Similar energy calculations were performed by Nishioka et al [97] for the thermal stability evaluation on double interface composite free layers of the form MgO/(FeCoB1)/insertion/(FeCoB2)/MgO. In their model, they performed calculation of Δ with the magnetic coupling between these layers through a thin metallic insertion. In our case, the two layers are separated by a tunnel barrier and only the magneto-static coupling energy is considered.

$$\mathrm{E}_{total}(\phi_{SL},\phi_{ASL}) = E_{anisotropy}(\phi_{SL}) + E_{anisotropy}(\phi_{ASL}) + E_{dipolar}(\phi_{SL},\phi_{ASL}) \tag{2.3}$$

To obtain the energy surfaces for each of the possible magnetic configurations, the angles ϕ_{SL} and ϕ_{ASL} in Eq.2.3 are rotated from 0° to 180°. A basic example of the resulting energy surface for the case of suppressing the dipolar coupling between the layers is presented in figure.2.3(a). In this case, and for the following discussions in this chapter, the layer thicknesses used are t_{SL}=1.4 nm, t_{ASL}=1.6 nm, and t_{MgO}= 1.2 nm for the MgO tunnel barrier, with a diameter size of 40 nm. The K_u for each of the layers are chosen such that the SL presents a much higher thermal stability factor than that of the ASL at room temperature (Δ_{SL}=40 to Δ_{ASL}=13). This imposed difference in thermal stability factors is controlled through the uniaxial anisotropy constant ($K_u = K_s/t_{layer}$), considering the double MgO interface of the SL, the single MgO interface of the ASL, and the difference in the thicknesses of the layers ($K_{u_{ASL}}$=2 MJ/m^3 and $K_{u_{ASL}}$= 1 MJ/m^3). In terms of magnetic saturation, the value is set equal for both at 8.5 10^5 A/m due to the similarities in magnetic volume and composition. From this energy surface, one can determine the minimum energy path between the combination of angles corresponding to the ground states (Nodes 1 to 3 in figure.2.3.(b)). Then, with the extracted paths, it is clear to observed that the magnetic reversal route starts from the layer with the lowest stability, i.e the ASL. Note that in this example, since there are no dipolar interactions, there is no energy difference between the parallel and anti-parallel alignments (Nodes 1-3 and 2). The respective thermal stability for each layer then corresponds to the maximum energy values along the minimum energy path, or values at which each of the magnetization angles crosses 90°.

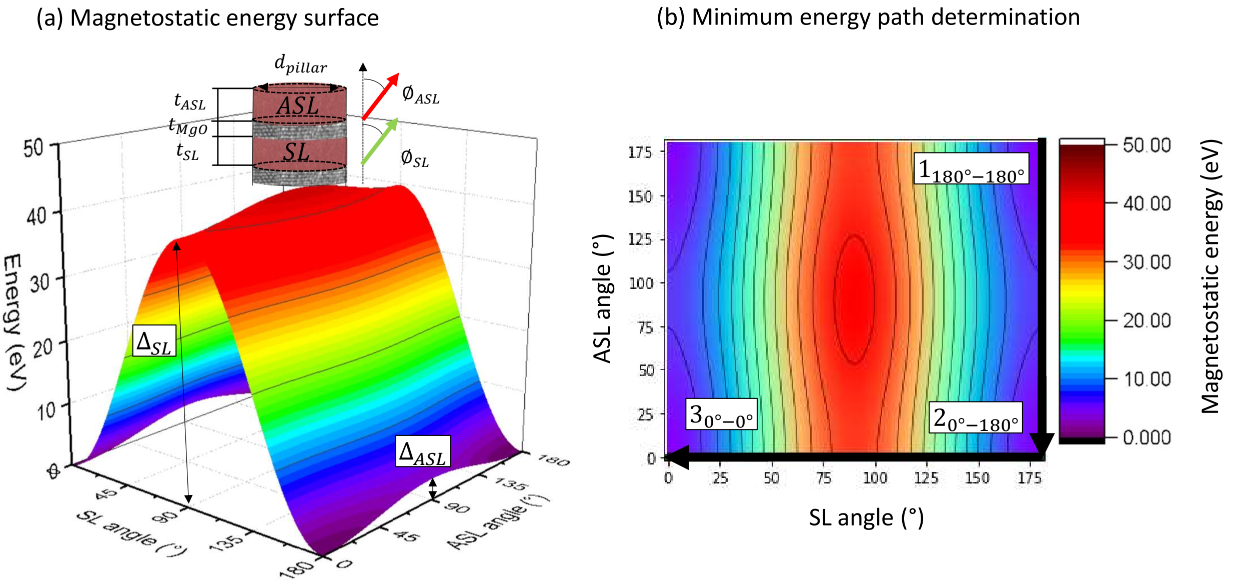
(a) Magnetostatic energy surface

(b) Minimum energy path determination

Figure. 2.3: (a) Calculated energy surface without dipolar coupling between the layers. (b) Resulting minimum energy path determination between the two parallel alignments (Nodes 1 to 3) of the ASL-SL system.

According to the same procedure, figure.2.4.(a) shows the resulting energy surface when introducing the magnetic coupling energy between the layers. In this case, the minimum energy path remains identical between nodes 1 and 3, following the same magnetic route as in the previous example, which is given by the layers thermal stability factors. However, due to the dipolar interaction, a local energy minimum appears at node 2 (Δ_{0-180}=9.22), increasing the magnetostatic energy of the ASL-SL coupled system in the anti-parallel alignments (0°-180° equal to 180°-0°). Although at this local minimum the thermal stability factor of the storage layer is decreased $\Delta_{180} = \Delta_{SL} - \Delta_{0-180}$=35.8, it serves as a theoretical confirmation of the possibility of independently reversing the layers.

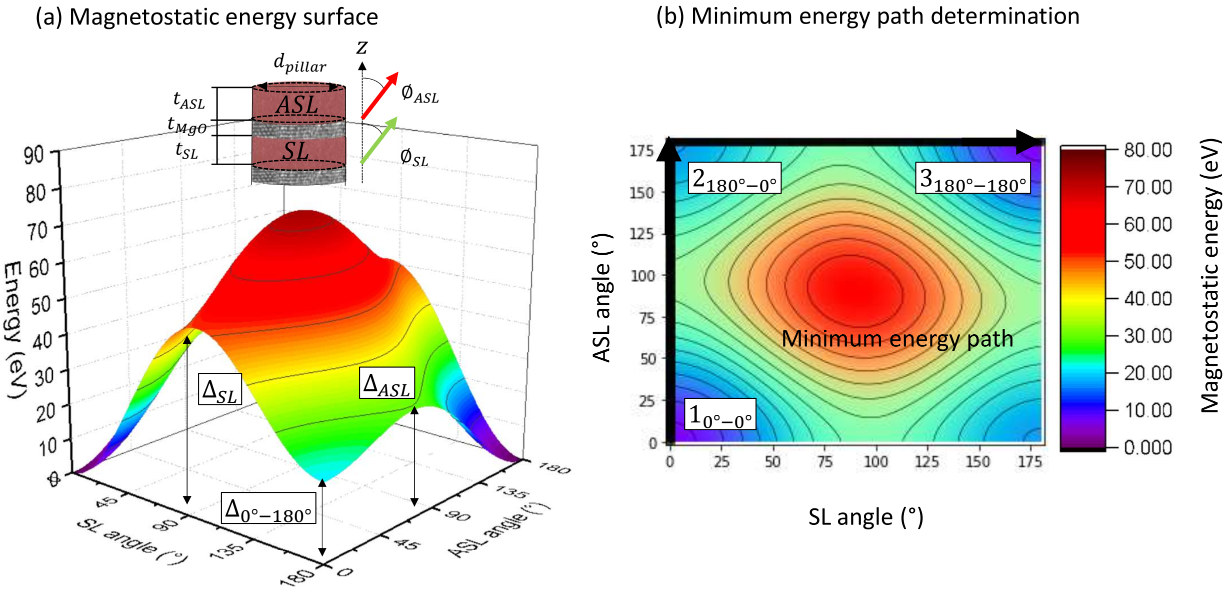
(a) Magnetostatic energy surface

(b) Minimum energy path determination

Figure. 2.4: a) Calculated energy surface with dipolar coupling between the layers. (b) Resulting Minimum energy path determination between the two parallel alignments (Nodes 1 to 3) of the ASL-SL system.

Finally, the evaluation of the magneto-static influence on the SL thermal stability factor is performed by comparing the energy barriers extracted with the same method but at various dipolar coupling amplitudes. Figure.2.5 depicts the minimum energy paths as a function of the relative angles between the layers magnetization vector, where 0°-360° corresponds to any parallel alignment (up-up down-down) and 180° to any anti-parallel alignment (up-down down-up) of the ASL-SL magnetization vectors. These energy paths are extracted from the surfaces in Fig.2.3, Figure.2.4 and the case of doubling the dipolar coupling interaction. The increase in dipolar energy between the magnetizations has two effects; first the already introduced rise of the local energy minimum in the anti-parallel states at 180°, second the reciprocal increase in energy barriers for each magnetic layer in the system at 90° and 270°. In this study, the effect of the stray field produced by the ASL on the SL is the main source for the data retention enhancement. The parallel configurations at 0° and 360° corresponds to the resistance states R1 and R3 of the ASL-DMTJ, in which the thermal stability of the device is maximized due to the ASL-SL ferromagnetic coupling. Table 2.0 summarizes the thermal stability values for each layer and the 180° configurations for the three assumptions of dipolar energy interactions. In this quantitative study, we see that only a dipolar coupling might not be sufficient to improve the SL thermal stability. However, the rise in the magneto-static coupling required to rise the SL thermal stability factor could also be accounted for other sources of exchange like coupling through the thin oxide barrier, thus being possible to increase the SL thermal stability factor by up to 10 points.

Table. 2.0: Layers Thermal stability factors at difference dipolar coupling energies : Δ_{SL} taken between the $\phi_{SL} = 0°$ to $\phi_{SL} = 90°$ configuration with $\phi_{ASL} = 0°$. $\Delta_{180}°$ for the SL taken from the configuration $\phi_{SL} = 180°$ to $\phi_{SL} = 90°$. Δ_{ASL} taken between $\phi_{ASL} = 0°$ to $\phi_{ASL} = 90°$ with $\phi_{SL} = 180°$.

	Δ_{SL} (k_BT)	Δ_{180} (k_BT)	Δ_{ASL} (k_BT)
No dipolar coupling	40	0	13
Dipolar coupling	45	35.8	18.12
Dipolar coupling x2	50	31.55	24

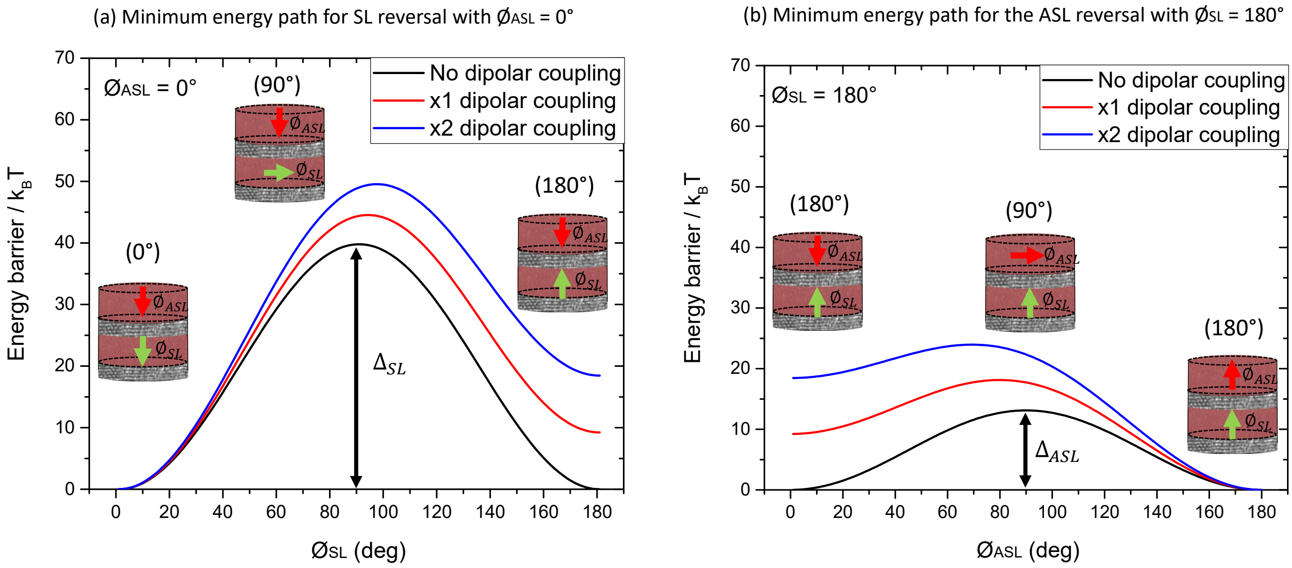
(a) Minimum energy path for SL reversal with ØASL = 0°

(b) Minimum energy path for the ASL reversal with ØSL = 180°

Figure. 2.5: Comparison of the minimum energy paths at various dipolar coupling amplitudes fir (a) the individual reversal of the SL magnetization and (b) the individual reversal of the ASL magnetization. Indicative magnetic configurations at the minimum and maximum values for the determination of the SL thermal stability factor.

2.2.2 Transport model for DMTJ structures with a switchable polarizer

The conductance of a single MTJ is well-known to be dependent on the electrodes magnetic orientation (relative angles of magnetization). John Slonczewski set the basis for the definition of this dependence by deriving its expression in [98]. It can be expressed in a simpler way as in equation 2.4:

$$G_{MTJ} = G_{90} + \frac{1}{2}\Delta G(m_i \cdot m_j) \tag{2.4}$$

Where m_i and m_j are the ferromagnetic electrodes magnetization unit vectors. Its amplitude is set by the value at the perpendicular state :

$$G_{90} = \frac{(G_{180} + G_0)}{2} \tag{2.5}$$

And the total conductance variation from the two parallel and anti-parallel states at 0° and 180° with Eq2.6, related with the junction tunnel magneto resistance amplitude as a function of the conductance (Eq2.7):

$$\Delta G = G_0 - G_{180} \tag{2.6}$$

$$TMR = \frac{(G_0 - G_{180})}{G_{180}} \tag{2.7}$$

For a p-DMTJ, both magnetic tunnel junctions are connected in series. Thus the total resistance of the equivalent electrical network will be the sum of each MTJ resistance state comprised in the structure (figure.2.6). Defining the total resistance in terms of conductance leads to:

$$R_{total} = \frac{1}{G_1} + \frac{1}{G_2} \tag{2.8}$$

Where G_1 and G_2 are defined by the TMR and RA of each respective barrier and the relative magnetic orientation of the ASL and SL between 0° and 180° while the RL remains fixed at 0°.

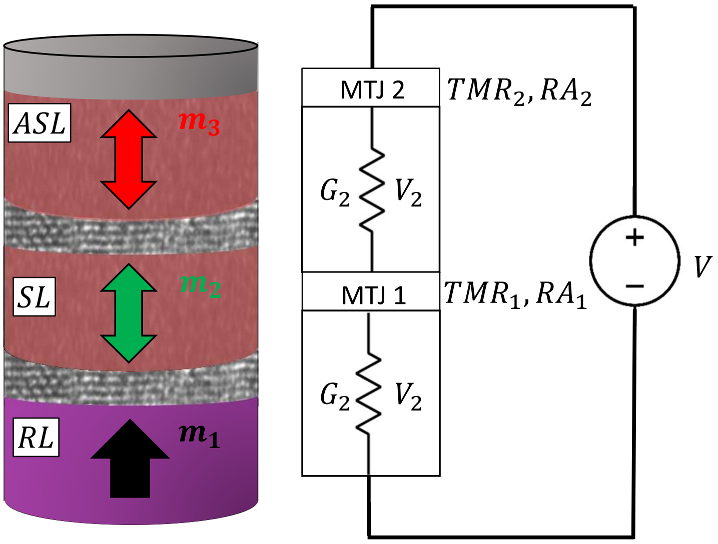

Figure. 2.6: Schematics of the ASL-DMTJ equivalent network for the calculation of the serial resistances and voltage drops across the tunnel barriers.

The Voltage drops V_1 and V_2 across the barriers can then be computed considering the two junctions serial resistances and maintaining a constant current (I) through the device (Eq2.9 and Eq2.11).

$$V_1 = I \cdot R_1 = I \cdot \frac{1}{G_1 = G_{1,90} + \frac{1}{2}\Delta G(m_1 \cdot m_2)} \tag{2.9}$$

$$V_2 = I \cdot R_2 = I \cdot \frac{1}{G_2 = G_{2,90} + \frac{1}{2}\Delta G(m_2 \cdot m_3)} \tag{2.10}$$

And the total voltage applied in the full DMTJ:

$$V_{total} = V_1 + V_2 \tag{2.11}$$

From these last expressions it is obvious that the total potential applied across the full DMTJ are linked to the magnetic configuration of the two magnetic tunnel junctions thus determining the total resistance state. For the case of fully perpendicular electrodes and providing that $RA_1 > RA_2$, the result is the already introduced possible magnetic combinations, leading to the resistance states [69] [76] [72] $R_1(P-P) < R_2(AP-P) < R_3(P-AP) < R_4(AP-AP)$ for ASLSL-SLRL MTJ states. These resistance states will control in essence the net STT acting on the SL magnetization under applied voltage and the device thermal stability when the ASL and SL are set in parallel alignment [93]. As we will see on the dynamic macrospin simulations under applied voltage and field, changes of this efficiency can be ascribed to changes on the ASL magnetic state.

Finally, we have to consider the main approximations taken for the damping like prefactor ($a_{//}$) produced by the incoming spin polarizer current from each magnetic electrode, hence also related with the transport model. The damping like prefactor term is a well-known phenomenological transport parameter that depends on the polarization efficiency of the electrodes (η), related with the MTJ tunnel magnetoresistance amplitude by Julliere's model [99] (introduction chapter 1, section 1.1.2). Considering that both electrodes are based on identical materials with the same interfacial quality with the oxide barrier, we assumed that the polarization from the various electrodes in each MTJ are equal [100] and only defined in our model by the chosen barriers tunnel magnetoresistance (TMR_1 or TMR_2) with Eq.2.12 [59]:

$$\eta = \sqrt{\frac{TMR(TMR+2)}{2(TMR+1)}} \tag{2.12}$$

$$a_{//_{i-j}} = \frac{\hbar}{2e}\frac{\eta G_0}{\mu_0 M_{s,j} t_j A} = \frac{\hbar}{2e}\frac{\eta_i}{\mu_0 M_s t R_0 A} \tag{2.13}$$

Where M_s and t are the saturation magnetization and thickness of the layer "j" on whose magnetization the spin transfer torque is exerted and $\mathrm{R}_0 A$ is the parallel-RxA of the barrier under consideration. As it will be explained in the following section (2.2.3 "Electromagnetically coupled ASL-SL LLGS equations"), the final damping like factors utilize during the temporal discretization of each layers magnetization dynamics under STT, will be the product between the $a_{//_{i-j}}$, the voltage drop on each barrier (V_1 and V_2) and the free electrons gyromagnetic ratio (γ) [101].

2.2.3 Electromagnetically coupled ASL-SL LLGS equations

Coherent rotation based (macrospin) simulations were performed in order to understand the magnetization dynamics of the ASL/SL coupled system, as well as to recognize and reproduce the main features observed experimentally. For this purpose, two coupled Landau-Lifshiftz-Gilbert-Slonczewski (LLGS) equations (one by layer) including mutual damping-like spin-transfer torque and dipolar fields between the layers were integrated upon the application of out-of-plane magnetic field and/or voltage pulses. These simulations are then utilized throughout this chapter to understand the working principles of the ASL-DMTJ switching sequences, their specific conditions of materials properties, and influence of their ferromagnetic coupling and mutual STT. In this way, the fundamental basis for a correct operation of the device at 0 K is laid. In addition, the confrontation of these simulations with experimental results on modeled devices is also used for the efficient target of the main properties to optimize the magnetic stack materials in chapter 4 "Materials optimization of the Assistance layer and Storage layer coupled system" section 4.2.2].

One of the main characteristics of our model, is the two different spin transfer damping-like torques to which the ASL and SL are subjected. These torques are dependent on the relative magnetic orientation or resistance state stabilized on the ASL-DMTJ, which changes dynamically during the write operation. The ASL magnetization dynamics is relatively straightforward to calculate, as only a single torque is exerted on its magnetization vector by the spin polarized current from the SL [102] [101]:

$$T_{//_{ASL}} = -\gamma a_{//_{SL-ASL}} V_2 m_{ASL} \times (m_{ASL} \times m_{SL}) \tag{2.14}$$

On the other hand, for the SL, there are two contributions with opposite signs; one contribution coming from the RL and a second from the ASL. This gives a better insight to the already mentioned feature of DMTJ structures, where for the same voltage polarity, the amplitude of the total torque exerted on the SL depends on the polarizers relative magnetic orientation (STT addition when ASL-RL are in AP state, STT-Subtraction when ASL-RL are in P state). An extensive theoretical study was proposed in 2017 by Daniel Worledge, for the numerical modeling of spin-torque dynamics involving DMTJ structures [70].

$$T_{//_{SL}} = -\gamma a_{//_{RL-SL}} V_1 m_{SL} \times (m_{SL} \times m_{RL}) + \gamma a_{//_{ASL-SL}} V_2 m_{SL} \times (m_{Sl} \times m_{ASL}) \tag{2.15}$$

In both equations, γ is the free electron gyromagnetic ratio, while $a_{//_{SL-ASL}}$, $a_{//_{ASL-SL}}$, and $a_{//_{RL-SL}}$ together with the voltage drops on each of the barriers are computed following the transport model detailed in the previous section. No field-like torques are taken into account for either layers, as it was shown by Timopheev et al[101] to have negligible influence on the STT switching process in p-MTJs.

Then, considering the torques defined with equations 2.14 and 2.17, the time evolution of the m_{ASL} and m_{SL} unitary vectors obey the LLG+STT equations:

$$\frac{dm_{ASL}}{dt} = -\gamma(m_{ASL} \times \mu_0 H_{eff,ASL}) + \alpha_{ASL}(m_{ASL} \times \frac{dm_{ASL}}{dt}) + T_{//_{ASL}} \tag{2.16}$$

$$\frac{dm_{SL}}{dt} = -\gamma(m_{SL} \times \mu_0 H_{eff,SL}) + \alpha_{SL}(m_{SL} \times \frac{dm_{SL}}{dt}) + T_{//_{SL}} \tag{2.17}$$

The RL remains fixed during all the integrations. Acting only as a polarizer for the first junction, it is only included in $T_{//_{SL}}$. The factors α_{ASL} and α_{SL} are the respective damping parameters for the free layers. Various energy contributions are taken into account in the effective field calculation: self-demagnetizing, PMA field, external applied field, and mutual dipolar field interaction between the SL and ASL. The effective field acting on each layer is then given by: $H_{eff,i} = H_{demagnitizing,i} + H_{anisotropy,i} + H_{dipolar,j-i}$, where subscripts $j-i$ indicate the dipolar field of layer $\jmath$ acting on layer $\imath$. The same convention stands for the STT damping-like factor coefficients, which first subscript indicates the layer acting as polarizer and second, the layer receiving the spin polarized electrons.

Note that the magnetic orientation of each of the two switchable layers in the system mutually influences the two LLGS equations through their dipolar fields and their reciprocal spin transfer torques.

2.2.4 Heat diffusion equation and self-heating dependent effects

Until this point in the document, the introduced magneto-static calculations along with the coupled LLG+STT model for the integration of the ASL-DMTJ magnetization dynamics, were centered on a qualitative evaluation at absolute zero temperature. In reality, the ambient temperature as well as self-heating effects produced by the current flowing through the devices have a strong impact on the magnetic properties of the multi-layers and stochastic fluctuations of the magnetization vectors [103]. For this reason, it is important to evaluate the impact of the joule heating in our proposed stack design. Moreover, in double barrier MTJs, this heating is further enhanced considering that the SL is sandwiched between two insulating thermal barriers [104]. The main assumptions taken into account in our model to introduce the heating effects in the ASL-SL coupled system, are based on a model already developed by N.Strelkov et al [105]. In their study, a good agreement was obtained between their macrospin-based model including self-heating effects and experimental results on single-MTJs with different FL material compositions and pillar sizes. Furthermore, they showed how the joule heating during the application of a voltage pulse, may lead to important asymmetries on the critical voltages to switch the storage layer magnetization (i.e voltage polarity). They identified two possible mechanism behind these heating asymmetries with the voltage polarity. A first one is due to the fact that when electrons tunnel through a tunnel barrier, they are injected as hot electrons in the receiving electrode. They loose their excess energy by inelastic scattering in this electrode so that heat is mostly produced in the receiving electrode within a length scale which is the inelastic scattering length (in the nanometer range [106]). On the other hand, what influences the magnetization switching is the heating dynamics before the reversal, which is determined by the initial resistance state of the junction. The heating power will therefore be different according to the initial configuration of the junction. In this section, this model is described and implemented to each of the layers comprised in our simulated system, the ASL and the SL.

For the temperature dependent numerical simulations, the initial temperature is initially set at 300 K before applying the writing pulse. The thermal effects include two main contributions. First, thermal activation is described by a temperature dependent random field ($\vec{H_{TR,i}}(T)$) in equation 2.22) included in the effective field acting on each magnetic layer ($\vec{H_{eff,i}}$) in each layer LLG+STT equations). Secondly, the Joule heating during the application of the writing voltage pulse is taken into account by computing the temperature rise, solving the heat diffusion differential equation 2.18.

$$\frac{V^2}{R_{state}} = C\frac{dT}{dt} + Q(T - T_0) \tag{2.18}$$

The heat capacity C and heat transfer coefficient Q are effective parameter set in our simulations to be $10^{-14}\ V^2/K\Omega$ and $10^{-6}\ V^2 s/K\Omega$ respectively representing the overall specific heat of the pillar and heat conductance between the pillar center and the surrounding electrode [105]. The ratio C/Q is then the characteristic time needed to reach an asymptotic temperature during the writing pulse, being 10 ns for the coefficients given above. Figure.2.7.(a) and (b) shows a comparison between the maximum temperature reached at increasing applied voltage pulses amplitudes with 100 ns pulse. In this example the heating-cooling characteristic time was set at longer times to highlight the heat transfer process from Eq.2.18 (40 ns). As expected from what was suggested before, depending on the initial resistance state of the junctions, the maximum value of temperature is reached for the less resistive state of the ASL-DMTJ (R1 state where all the junctions are in parallel configuration). In this example the heating-cooling characteristic time was set at a higher times to highlight the heat transfer process from Eq.2.18.

Then, at each integration step (dt) of the LLG+STT equations, the value of resistance and voltage pulse amplitude are evaluated and the total rise in temperature is obtained. The temperature dependent effects on the main magnetic properties of uniaxial anisotropy, M_s and STT damping like prefactor on the storage layer due to the temperature rise during the writing pulse can then be taken into account. In our studies, not only the SL but also the ASL magnetic properties are influenced by this heating and the same value of temperature is assumed for both layers in this simple heat diffusion model.

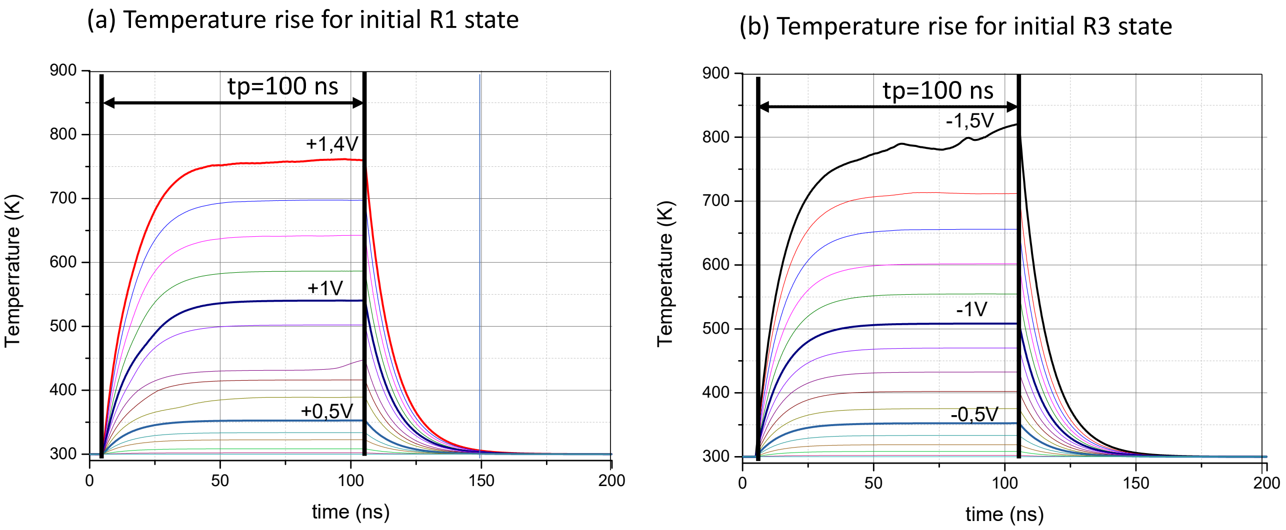

Figure. 2.7: Temperature rise as a function of time during the application of 100 ns voltage pulses at increasing amplitudes for; (a) positive voltages from R1 state and (b) negative voltages from R3 state. Changes in the temperature during the aplication of the the voltage pylse can be attributed to reversal of the magnetic orientation varying the Total resistance state of the ASL-DMTJ.

Finally, the associated variations of M_s, K_u and $a_{//}$ for the SL and ASL are calculated following the same approach as in [105] and verified experimentally [107]. The spin transfer prefactor $a_{//}$ follows a similar Bloch law as the saturation magnetization, accounting for the fact that the magnetic electrode spin polarization decreases with increasing temperature [108]. This is also responsible for the decrease of the TMR amplitude with temperature. These temperature dependent variations are described by equations:

$$M_{s_i} = M_{s_{0,i}} \left(1 - \left(\frac{T}{T_c}\right)^a\right)^b \tag{2.19}$$

$$K_{u_i} = K_{u_{0,i}} \left(\frac{M_{s,i}(T)}{M_{s,0}}\right)^c \tag{2.20}$$

$$a_{//_{i-j}} = a_{//_{0,i-j}} \left(1 - \left(\frac{T}{T_c}\right)^a\right)^b \tag{2.21}$$

And the amplitude of the white-noise field introduced as thermal fluctuation is:

$$H_{TR,i}(T) = \sqrt{\frac{2\alpha k_B T}{\gamma_0 \mu_0 M_{s,i}} dt} \tag{2.22}$$

Where $M_{s_{0,i}}$, $K_{u_{0,i}}$ are the parameter values at 0 K for the saturation magnetization and uniaxial anisotropy, $a_{//_{0,i-j}}$ is given by expression 2.13 and ”a” ”b” and ”c” are taken to be 1.73, 1 and 2.2 respectively from fitted to experimental data in [105].

These three equations can be applied to both the SL and ASL. Figure.2.8.(a) and (b) show the representation of equations 2.19 and 2.20 for varying values of $M_{s,0}$ and critical temperature T_c. We note that in this modeling, we do not make a distinction between the notions of Curie temperature and blocking temperature (noted T_B later in chapter 4) of the SL and ASL layers because we are using the relations (2.19) to (2.21) in a phenomenological approach. For this reason, we rather use the name "critical temperature" for T_c. For low values of the layers critical temperature such as 400 K, obviously, the superparamagnetic state is reached much faster upon heating than for higher values such as 800 K. $a_{//0,i-j}$(T) follows the same trend as M_{s_i}(T). The K_{eff}(T) variation for low T_c (figure.2.8.(b)) plays a quite important role in the layers dynamics since calculated change of sign upon heating means a reorientation of the anisotropy from perpendicular to in-plane anisotropy. This study on the influence of the layers critical temperature emphasizes the importance of properly tuning the thickness and composition to adjust this temperature or alternatively, minimize the heating by reducing the junction RA. More details on the materials optimization at thin film and at patterned device level will be discussed in chapter 4 in connection with this matter.

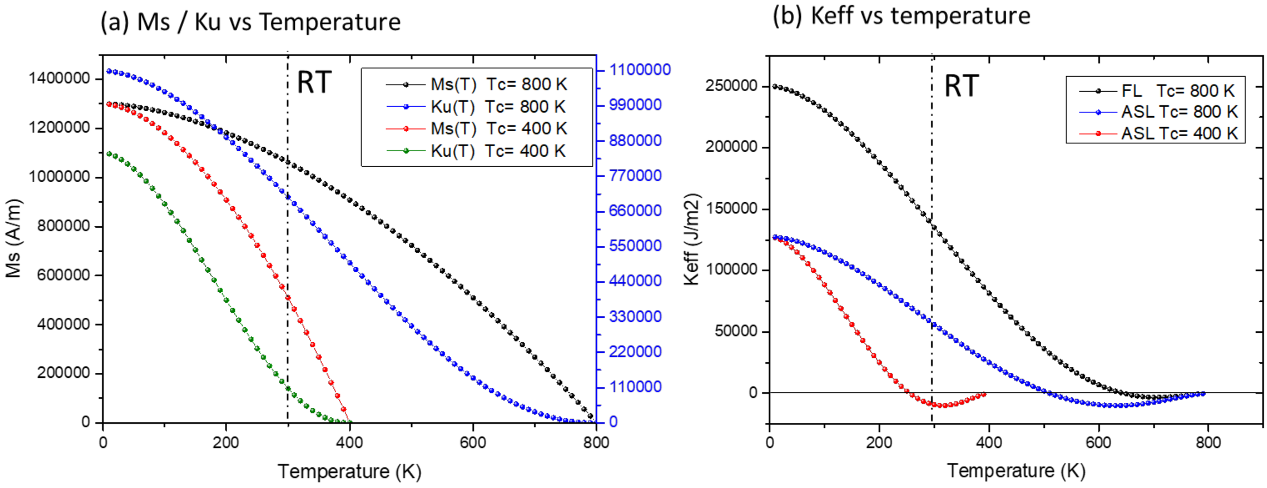

Figure. 2.8: (a) Temperature dependent Magnetic saturation and uniaxial anisotropy constant at 800 K and 400 K critical temperatures. (b) Resulting effective anisotropy constant from (a) for the SL an ASL for different assumptions on the layer critical temperature.

2.2.5 STT and field induced dynamics

The switching dynamics along with the stable configurations under applied field and/or voltage of the ASL-DMTJ depends on several factors, so to speak; the relative thermal stability of the ASL and SL, determining the minimum energy path of the coupled system (Chapter 2 section 2.2 subsection 2.2.1 "Magneto-static energy calculations of the ASL-SL magnetizations dipolar interaction"), the STT that each layer is subjected to, with a single torque acting on the ASL (Eq.2.14) while an additive or subtractive torque acts on the SL magnetization (Eq.2.17) and the strength of the ferromagnetic coupling between the layers, that fundamentally controls the final energy barriers (i.e thermal stability) at parallel alignment (Resistance states R1 and R3) and at anti-parallel alignment (Resistance states R2 and R4) between the layers magnetization. In this context, two types of devices can be realized depending whether the ASL is set anti-parallel to the RL before or during the writing operation of the memory.

Field induced dynamics for $\Delta_{ASL} > \Delta_{SL}$

Due to its similarity to conventional p-DMTJ structures, we will start by studying the first type of device. In this case, the stability of the ASL magnetization must be engineered to be higher than that of the SL. As a result, the energy barrier hierarchy of the three magnetic layers in the structure will be $\Delta_{RL} > \Delta_{ASL} > \Delta_{SL}$. Figure 2.9.(a) shows the minimum energy path for the ASL/SL magneto-static energy indicating the reversal route between the possible magnetic configurations. The energy barriers difference is imposed by just inverting the layers position in the simulated ASL-DMTJ and using the same layer's materials parameters and volume as the ones introduced in section2.2.1 in this chapter (Δ_{SL}= 24 Δ_{ASL}= 50 with double dipolar coupling interaction). For the LLGS numerical integration under field or voltage, the damping parameter of the layers is set to be equal to 0.01 due to its comparable thickness and material composition.

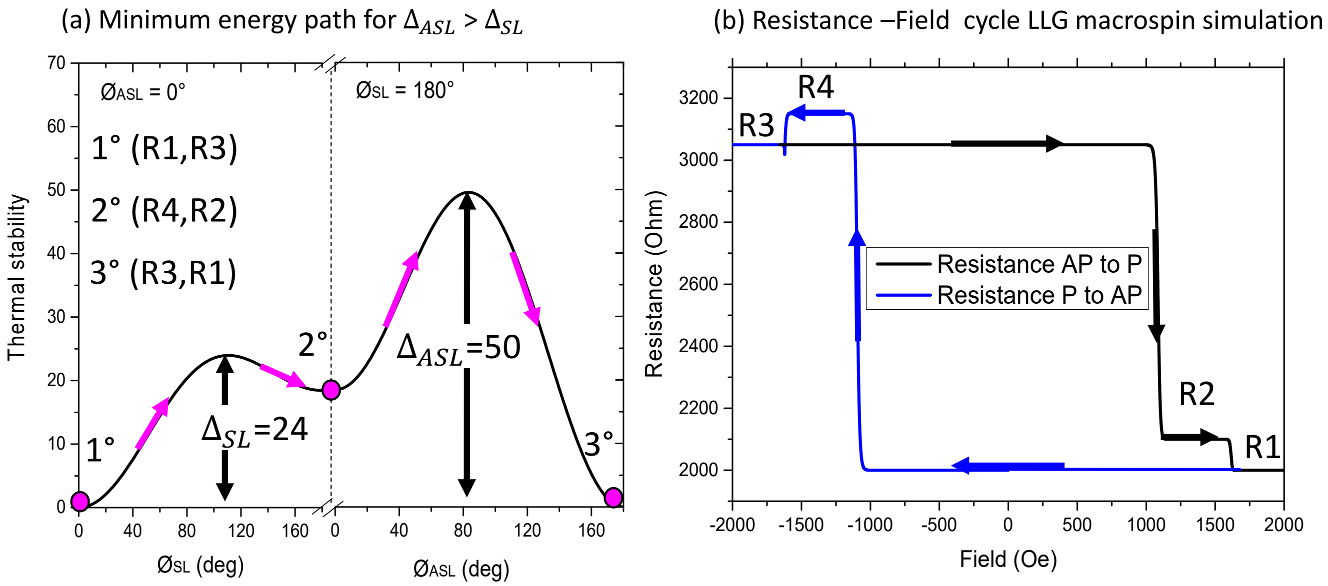

Figure. 2.9: (a) Minimum energy path between the possible stable ASL-SL magnetic configurations for $\Delta_{ASL} > \Delta_{SL}$, indicating the most probable magnetic reversal route. (b) Numerical macrospin simulation of the resulting resistance-field cycle at 0K.

Under these conditions (i.e $\Delta_{ASL} > \Delta_{SL}$), the ASL-DMTJ magnetic reversal sequence corresponds to the one shown in figure.2.9.(b), where a simulation at 0 K of the device resistance response under an applied perpendicular field is presented. Note that when switching by an external magnetic field, the two layers are subjected to identical field amplitudes.

The difference in energy barriers yields the switch of the SL with less stability first (±1100 Oe), followed by the ASL (±1600 Oe) with higher stability. The four resistance states and MTJs switching sequences are then visible thanks to the difference in barriers tunnel magnetoresistance, being 70 % for the barrier between the RL and the SL and 30 % for the barrier between the SL and the ASL. Henceforth, these values of TMR remains the same for all the simulations discussed in this chapter. Schematics on the magnetic configurations for the full ASL-DMTJ stack are presented bellow figure.2.10.(a) and (b) to ease the interpretation of the switching orders (negative field sweep, transition from P(R1) to AP(R3) and positive field sweep, transition from AP(R3) to P(R1)).

(a) Negative field sweep direction

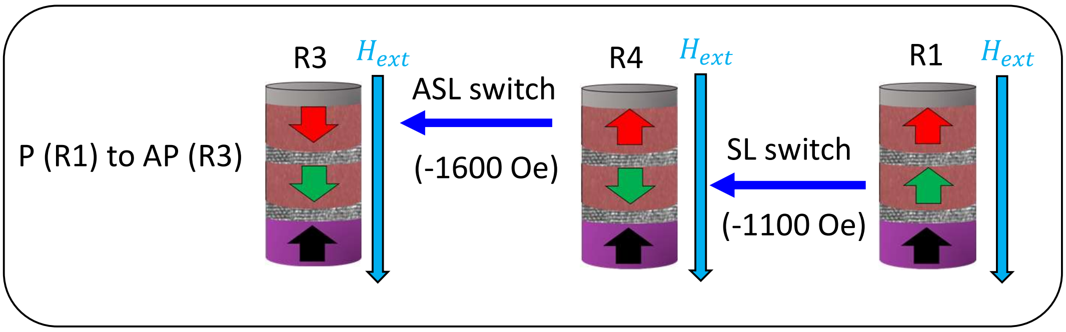

(b) Positive field sweep direction

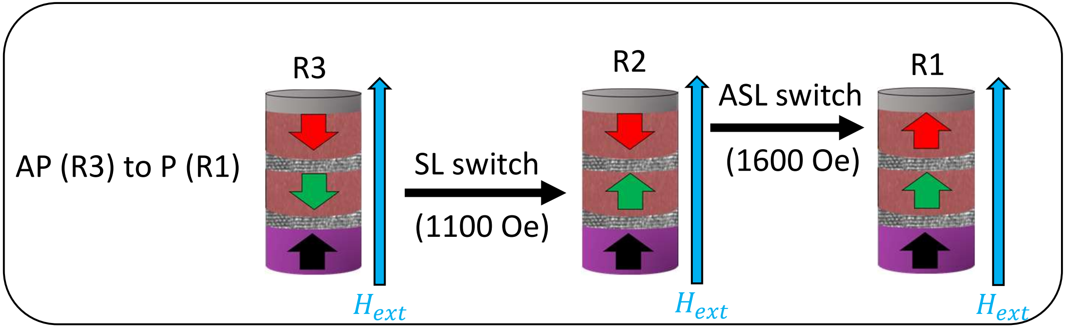

Figure. 2.10: Switching sequence schematics between the ASL-DMTJ magnetic configuration/resistance states having $\Delta_{ASL} > \Delta_{SL}$ for: (a) Negative field sweep direction and (b) positive field sweep direction.

Voltage induced dynamics for $\Delta_{ASL} > \Delta_{SL}$

In contrast to the reversal with field, at the time of applying a voltage pulse, each of the layers will be submitted to distinct STT contributions. Depending on the initial resistance state, the SL will experience the additive or subtractive STT contributions from the ASL and the RL injected spin polarized currents. In addition, the STT acting on the ASL will be influenced by the SL magnetic orientation. Figures.2.11.(a) and (b) shows the simulated resistance vs voltage pulse amplitude (R-V) hysteretic response for high and low maximum voltage ranges. For the following explanations, supportive schematics are given in figure.2.12.(a)-(b) for the STT contributions acting on the SL and ASL provided by the magnetic configurations and reversal sequences. Figure.2.11.(a) depicts the R-V cycle under applied voltage between ±1.2 V. A clear asymmetry is observed on both, the resistance states sequences and critical voltages to switch depending on the ASL-DMTJ initial magnetic configuration. For positive voltage polarities, when starting from the R3, a critical voltage of $V_{R_3\ to\ R_2}$= 0.1 V is required to reverse the SL magnetization (R3 to R2 transition).

This critical voltage to switch results from the additive STT contributions from the ASL and RL. Then, by increasing the voltage pulse amplitude to $V_{R_2\ to\ R_1}$= 0.5 V, the ASL switches due to the STT exerted from the SL polarized current, ending in the R1 state (R2 to R1 transition). The ASL-DMTJ is therefore finally written in parallel configuration (R1) where the ferromagnetic coupling enhances the SL thermal stability.

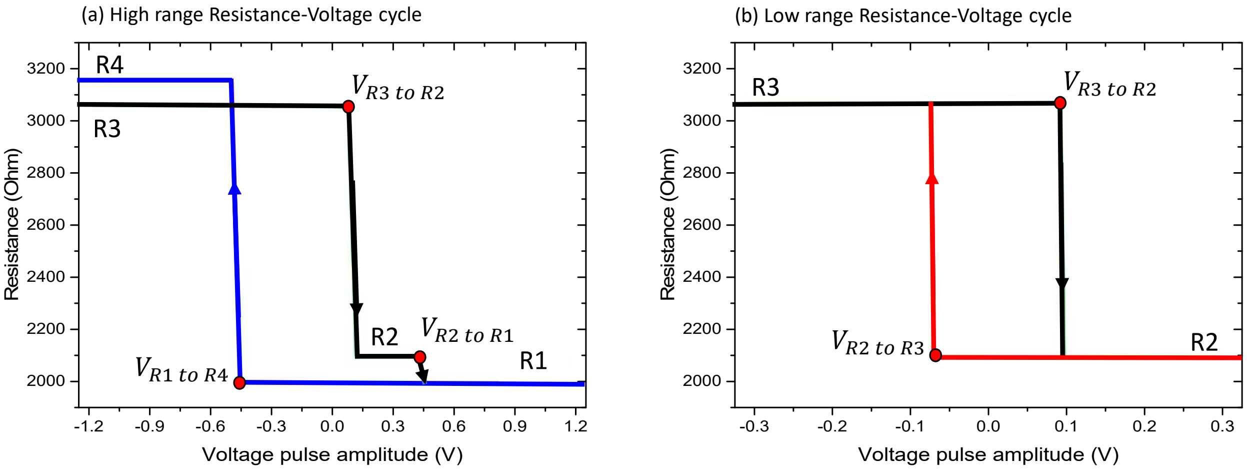

Figure. 2.11: (a) Numerical macrospin simulation of the resistance response with voltage pulse amplitude for; (a) High maximum voltage range (±1.2 V) and (b) low maximum voltage range (±0.3 V).

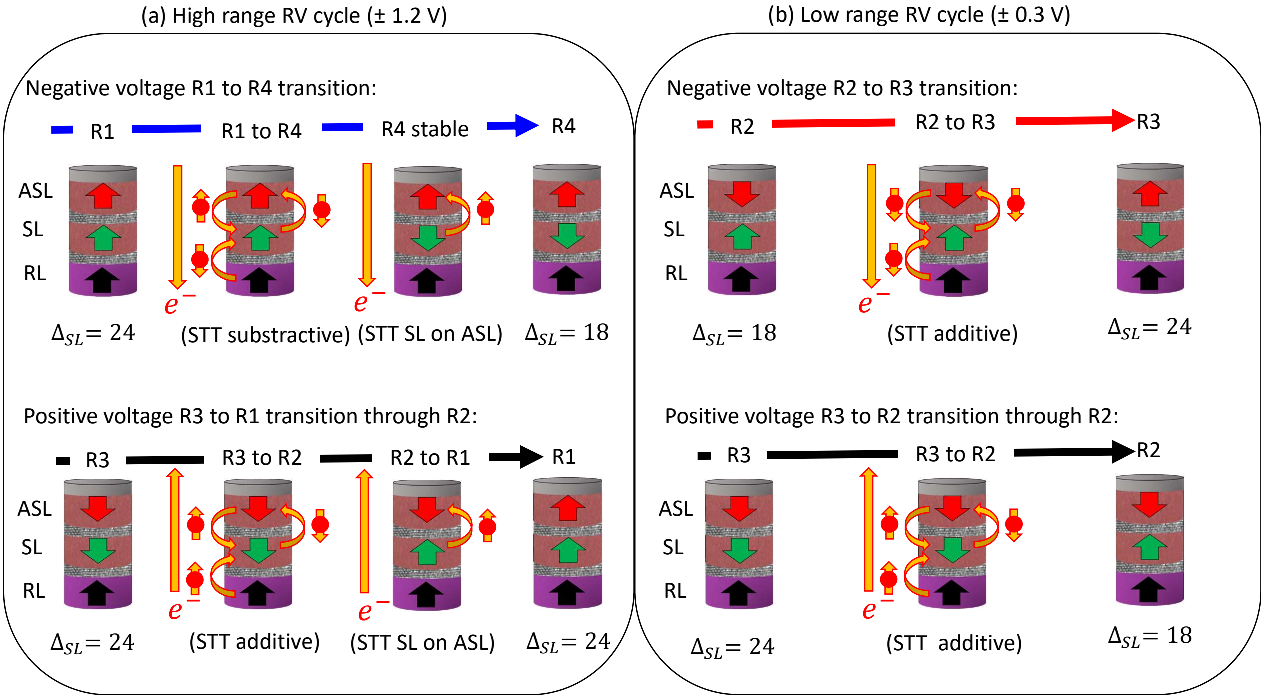

Figure. 2.12: Schematics of the STT contributions vs magnetic configuration of the ASL-DMTJ for the various reversal sequences and voltage polarities (i.e current polarities) in Fig.2.11.(a) high range R-V cycle and Fig.2.11.(b) low range R-V cycle

The opposite situation takes place with negative voltage polarities. When starting from R1 state, due to the parallel configuration between the ASL and the RL, a subtractive STT acts on the SL. The SL magnetization is then subjected to a reduced net STT. As a result, the reversal takes place at $V_{R_1\ to\ R_4}$= -0.5 V, ending in R4 state. Moreover, once the R4 state is reached, the STT exerted from the SL stabilizes the ASL magnetic orientation, thus preventing the reversal to R3 with negative voltages. Besides, ending in the R4 magnetic configuration reduces the SL thermal stability due to a higher coupling energy between the layers in anti-parallel alignment. This kind of response can be avoided to some extend by reducing the maximum applied voltage. Figure 2.11.(b) represents the R-V cycle at lower voltage ranges (±0.3 V). Under the conditions that the junctions are initialized in R3 state and by preventing the ASL switching at pulse amplitudes above $V_{R_2\ to\ R_1}$=0.5 V, the double STT can be achieved for both switching directions. In fact, R2 and R3 states correspond to the magnetic configurations in which the magnetization of the two polarizing layers (RL and ASL) are anti-parallel, maximizing the net STT acting on the storage layer independently of the writing direction. However, prior to the write operation (SL reversal), the ASL must be set in anti-parallel alignment with the RL magnetization, as in the case of standard p-DMTJ structures. Although it is feasible to exploit the double STT for both transitions, as for the previous study at higher voltage ranges, the final magnetic configurations between the ASL and SL for both transitions leads to different SL thermal stabilities in R3 and R2. In this case, the impact of the magneto-static coupling energy between the final configurations (R2-R3) can be seen directly on the critical voltages to switch for each transition. The Lower $V_{R_2\ to\ R_3}$= -0.075 V for the transition in which the second MTJ (between the ASL and SL) is in anti-parallel configuration (R2) while the higher $V_{R_2\ to\ R_3}$= 0.1 V when it is in parallel configuration (R3) before the writing operation. Details on the Δ_{SL} at the various magnetic configurations resulting from this dynamics under voltage are also indicated in figure.2.12 which are taken respectively from the minimum energy path calculations in figure.2.9.(a) in static conditions. Considering that the device must be first initialized into R3 to exert an additive STT in both voltage polarities, added to the resulting uneven thermal stabilities in the final magnetic configurations, the conclusion of this theoretical study is that the case of having $\Delta_{ASL} > \Delta_{SL}$ is not compatible with an overall increase in STT switching efficiency. However, it works as a perfect example to introduce the influence of the initial magnetic orientation, the role in the dynamics of the layer's relative stabilities, and the conditions for which the SL is reversed with the highest attainable STT amplitude.

Field induced dynamics for $\Delta_{SL} > \Delta_{ASL}$

As for the previous study, in this subsection we will discuss the case of an ASL-DMTJ device in which the ASL is designed to have lower stability than the SL, thus switching its magnetic orientation during the write operation. As was concluded in the previous case. To achieve efficient STT switching, the RL and ASL magnetization must be always anti-parallel prior to the switching of the SL magnetization. Furthermore, it must be ensured that both layers end up parallel in resistance states R1 and R3 where the magneto-static energy is minimum, thus increasing the SL thermal stability in static conditions. Then, as we will see in the following macrospin simulations, for this device to work, the energy barrier hierarchy of the magnetic layers in the stack need to be $\Delta_{RL} > \Delta_{ASL} > \Delta_{SL}$. Following the same procedure as for the previous concept, figure.2.13.(a) shows the inverted minimum energy path for the ASL/SL magneto-static energy between the possible magnetic configurations. Due to the inversion on the relative stability between the layers, the simulated resistance response as a function of applied external field shows an inversion as well on the reversal orders (figure.2.13.(b)). In this case, the ASL with less stability (±1100 Oe) switches first, followed by the SL switching (±1600 Oe). Details also on the MTJs magnetic configurations for each field sweep direction involved in the ASL-DMTJ are shown in figure.2.14.(a) and (b).

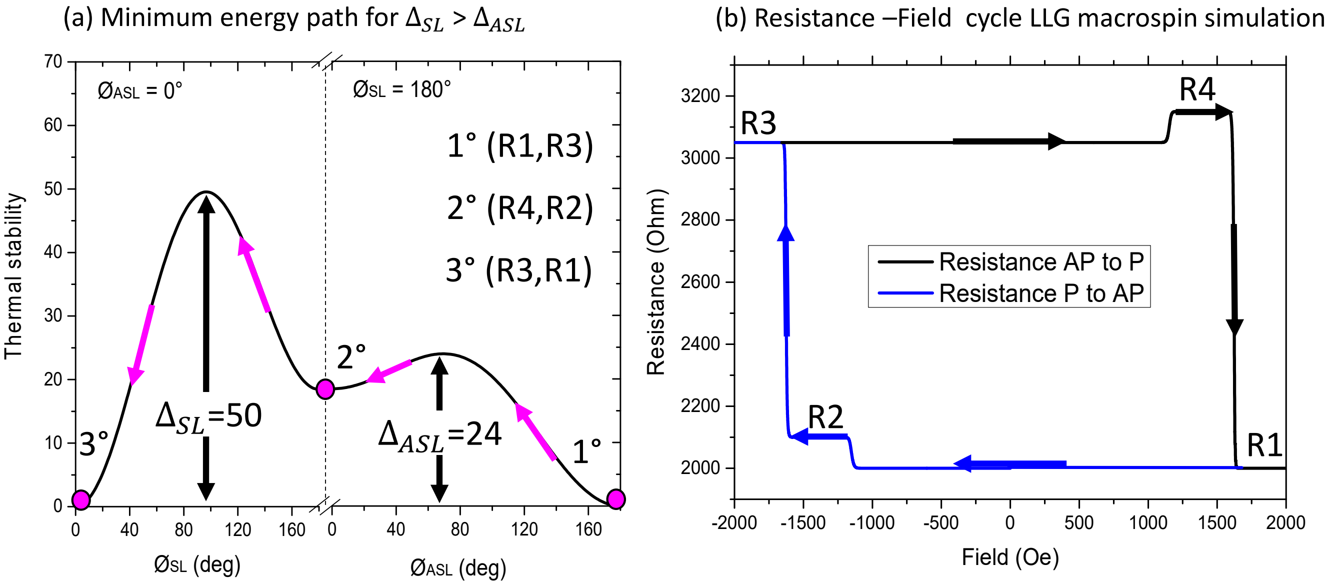

Figure. 2.13: Minimum energy path between the possible stable ASL-SL magnetic configurations for $\Delta_{SL} > \Delta_{ASL}$, indicating the most probable magnetic reversal route. (b) Numerical macrospin simulation of the resulting resistance-field cycle at 0K.

(a) Negative field sweep direction

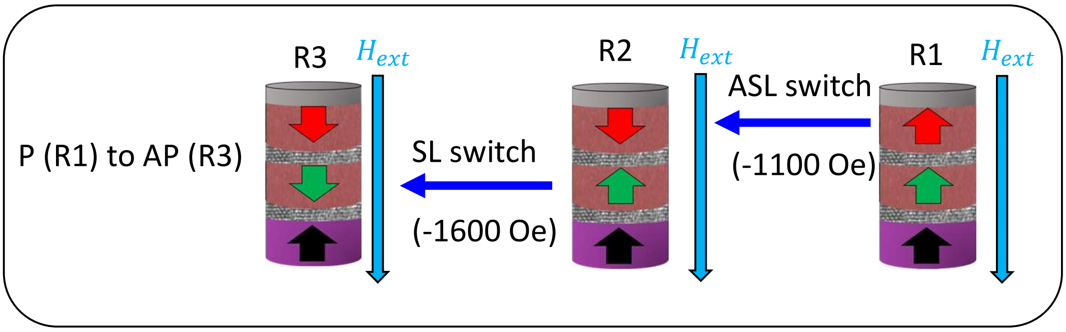

(b) Positive field sweep direction

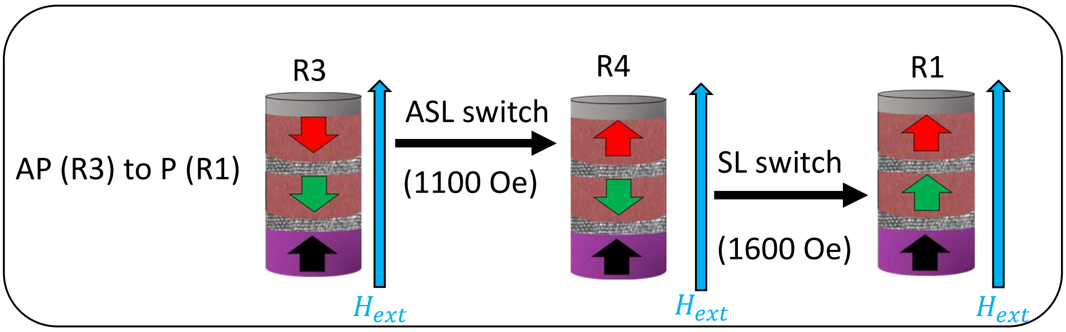

Figure. 2.14: Switching sequence schematics between the ASL-DMTJ magnetic configuration/resistance states having $\Delta_{ASL} > \Delta_{SL}$ in Fig.2.13 for: (a) Negative field sweep direction and (b) positive field sweep direction.

Voltage induced dynamics for $\Delta_{SL} > \Delta_{ASL}$

In the conditions $\Delta_{SL} > \Delta_{ASL}$, there is also a significant difference between the resistance response obtained with the field sweep and that associated with voltage sweep. Figure.2.15.(a) shows a modeled resistance-voltage loop for this case of ASL-DMTJ device. Only R1 and R3 resistance states are visible, being the final stable parallel and anti-parallel state of the memory. In addition, no apparent asymmetries are observed on the critical voltage to switch, regardless of the initial magnetic configuration. A comparison with a single-MTJ R-V cycle is also presented in figure2.15.(b) for a later evaluation of the critical switching current with respect to the ASL-DMTJ. For the single-MTJ, the storage layer thermal stability arises only from the interfacial anisotropy existing at the two interfaces with the MgO barriers, and just one STT contribution from the RL reverses the SL magnetization. In our model, this is achieved by maintaining the same parameters for the SL while suppressing all influences from the ASL in its LLGS equation i.e; the ASL dipolar interaction (ASL dipolar tensor components set at zero), and the secondary torque exerted by the ASL spin polarized electrons through the 2nd barrier (2nd barrier TMR_2=0 so its spin polarization efficiency is neglected). In addition, the serial resistance introduced by the second insulating layer is suppressed, thus explaining lower resistance values in AP and P states for the single-MTJ . Figure.2.16 depicts the different SL/ASL switching sequences during the writing operation to get additive STT contributions on the SL magnetization, in other words, during the application of the negative or positive voltage pulses to switch.

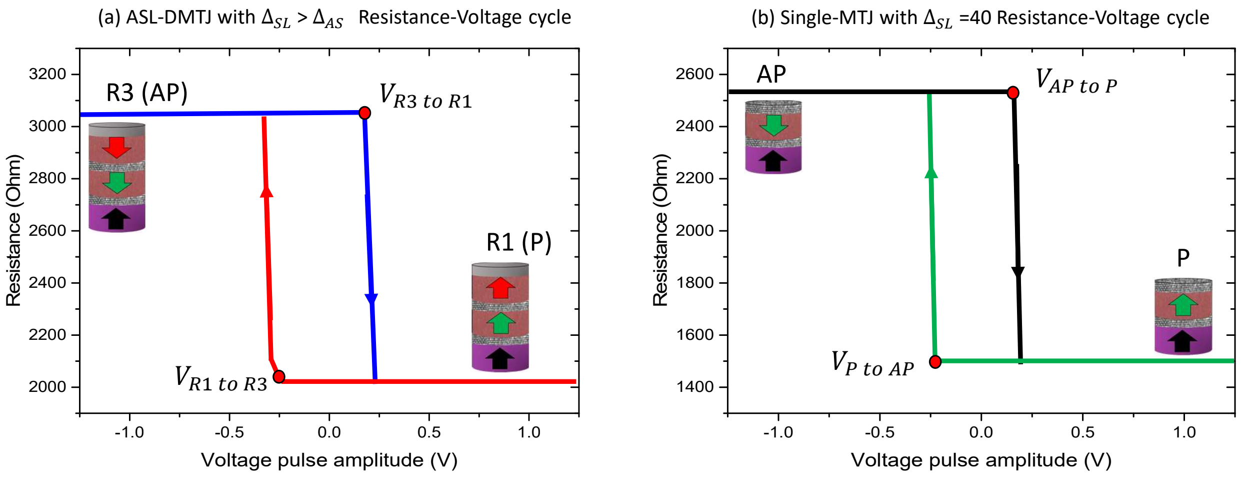

Figure. 2.15: Numerical macrospin simulation of the R-V cycles for; (a) ASL-DMTJ having $\Delta_{SL} > \Delta_{ASL}$ and (b) the corresponding Single-MTJ without influence from the ASL.

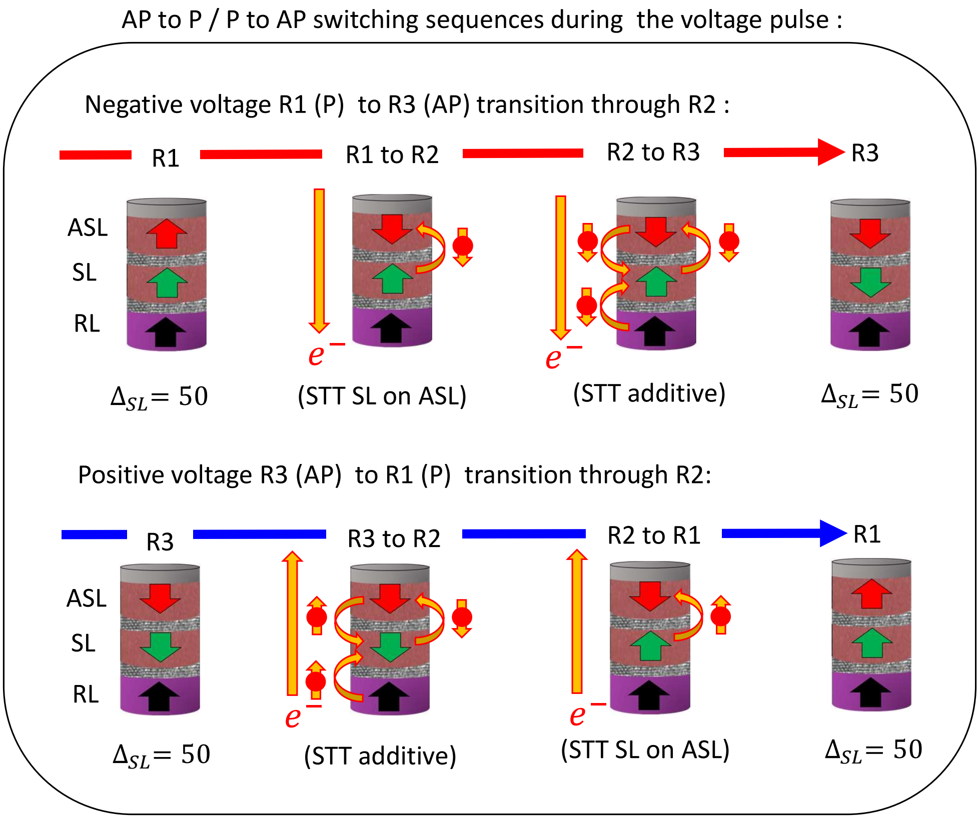

Figure. 2.16: STT contributions vs resistance states for P (R1) to AP (R3) and AP (R3) to P (R1) switching sequences during the voltage pulse, both transitioning through R2.

Since the SL and ASL magnetizations are always initially parallel (R1 and R3), this implies that in the P (R1) to AP (R3) transition, the junctions must proceed through the intermediate resistance state R2. Thanks to its lower stability, the ASL is first reversed and set in the correct magnetic orientation by the STT from the SL back-scattered polarized electrons. Once the device is in R2 state, the SL magnetization is able to switch by the additive STT from both, the ASL and RL. On the other hand, for the AP to P transition, the SL switches first to state R2 under STT influences from both RL and ASL, followed by the ASL switching to state R1, thus ending parallel to the SL magnetization. Real-time macrospin simulations at 0 K confirm these switching dynamics as illustrated in figure.2.17.(a) and (b) respectively for P(R1) to AP(R3) and AP(R3) to P(R1) transitions. These specific reversal processes are confirmed later experimentally with time-resolved observations while the writing pulse is applied. (see chapter 5, 5.2 ”Field and voltage induced dynamics”)

(a) Real time P (R1) to AP (R3) transition :

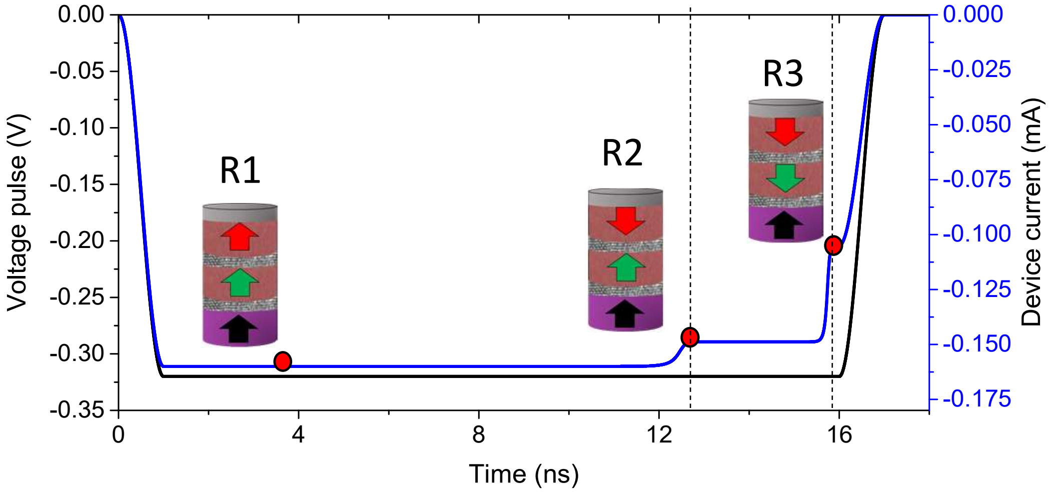

(b) Real time AP (R3) to P (R1) transition :

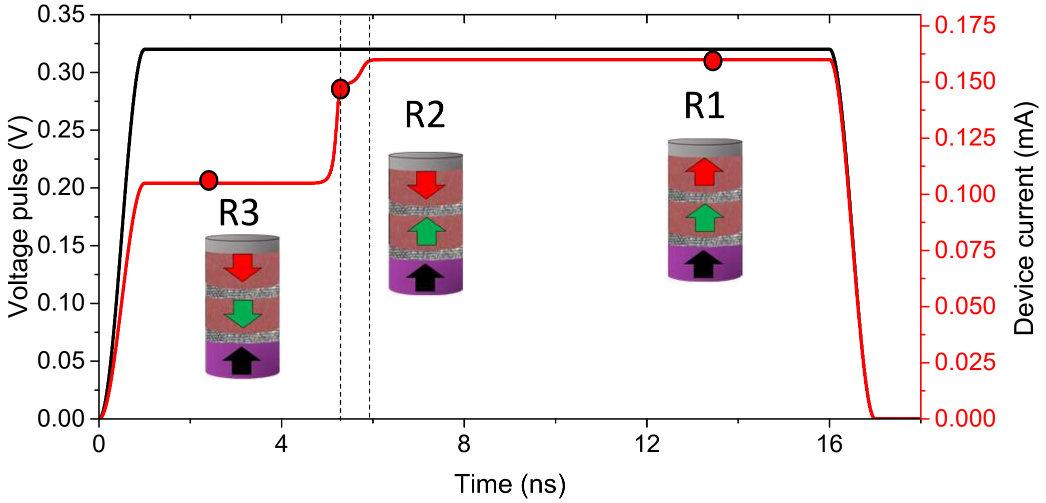

Figure. 2.17: (a) Real time macrospin simulations during the write operation of (a) the P(R1) to AP(R3) transition and (b) the AP(R3) to P(R1) transition.

Decreasing the ASL stability allows to reduce proportionally its critical switching current, aligning its magnetic orientation in the desire configuration from P to AP, and thus allowing to employ the double STT effect. Moreover, independently of the writing direction, the layers are always ending in the highest stability states. From these time dependent numerical simulations, an intrinsic asymmetry in terms of switching time is expected between the two writing directions. This is ascribed to the fact that the P to AP transition requires a first switch of the ASL magnetization so that its STT influence on the SL adds to that from the RL (t_{P-AP}= 15 ns). On the contrary, for the AP to P transition, the double STT acts on the SL magnetization as soon as the voltage pulse is applied, thus yielding a reduced SL magnetization reversal time (t_{AP-P}= 5 ns). The switching times for each transition are taken at the moment at which the SL-RL MTJ reverses (stabilization of R2 for P to AP and stabilization of R3 for AP to P). Similar switching dynamics were already theoretically reported by [109] in double magnetic tunnel junctions, comprising a dynamic reference layer acting as a switchable top polarizer. Their work concluded that the structure presents the same performance as a standard DMTJ with bottom and pinned polarizers but with a thinner and simplified stack design. Different to our proposed ASL-DMTJ, this dynamic reference layer could be set in stand-by conditions (at V = 0) in any magnetic configuration with respect to the SL magnetization. In our ASL-DMTJ, we optimized the structure to always follow the switching sequences presented in this section. The working principle of our device relies on benefiting from the magnetic configurations R3 and R2 to exert a double STT on the SL magnetization during the application of the voltage pulse, while always ending in static conditions in magnetic configurations R1 (P) and R3 (AP) in which the two switchable layers are parallel to maximize the thermal stability factor of the SL.

2.2.6 Conclusions : Overall increase in figure of merit (Δ/I_c)

In this chapter we introduced the ASL-DMTJ stack design and a first assessment of its theoretical working principles of operation at absolute zero temperature. The single domain models utilized for the numerical investigations are explained and discussed, showing the origins and conditions in which the SL thermal stability is enhanced while a secondary STT contribution allows for an efficient STT magnetization reversal. At first, magneto-static calculations of the ASL-SL coupled system describes their mutual rise in energy barriers when independently switching the layers magnetization, enhancing thermal stability factor of both the ASL and the SL. The magnetic interaction between the layers allows the quantitative extraction of the individual thermal stability factors in the various possible magnetic orientations within the ASL-DMTJ device. These configurations leads to four possible resistance states, that can be identified providing an asymmetry in the barrier's electrical properties. Due to the ferromagnetic nature of the dipolar interaction, the thermal stability of the storage layer magnetization is increased for the cases in which the two layers are set in a parallel alignment. The estimated dipolar interaction between the ASL and SL magnetization may not be sufficient for a drastic increase in the device thermal stability. However, the SL-ASL coupling may not be simply of magneto-static origin but also exchange-like through the barrier separating these two layers. As a result Δ_{SL} can be increased up to 10 points with respect to the case where only the PMA provided by the double MgO interface contribute to the SL stability. Following the magneto-static calculations, the ASL-DMTJ transport model and the coupled LLGS equations for each layer were presented, giving a general picture of the mutual influences that each layer magnetization has on both the voltage drops between the barriers and their dynamics under field and/or spin-transfer torque. The studied ASL-SL reversal sequences are found to be highly dependent on the balance between the layers relative thermal stability factors, given by their volume, effective PMA and magnetic coupling interaction. On this basis, two types of devices were discussed; one having the $\Delta_{ASL} > \Delta_{SL}$ and a second having $\Delta_{SL} > \Delta_{ASL}$. In both cases, the resistance response under applied field differs substantially with the one obtained under voltage. These differences are ascribed to the distinct torques exerted on each layer when a voltage is applied on the device (single STT on the ASL while an additive or substractive STT on the SL). In the first case (i.e $\Delta_{ASL} > \Delta_{SL}$), important asymmetries are found on the critical voltages to switch for each writing direction as well as the final magnetic configuration between the ASL and SL (Negative voltages R1 to R4 transition while positive voltage R3 to R1 transition through R2). The initial magnetic configuration between the polarizing layers (ASL and RL) are responsible for the control of the net STT acting on the SL, thus causing the asymmetry on the critical voltages to switch. This situation can be solved by properly initializing the ASL in anti-parallel alignment with respect to the RL (recovering R3 state from the R4) and reducing the maximum positive voltage applied (preventing the ASL to reverse to the total parallel R1 configuration for the R3 to R2 transition). However, independently of the writing direction, one of the transitions always results in an anti-parallel alignment between the ASL and SL, hence two unequal energy barriers of the SL magnetization. Then, due to the complexity of operation and the failure to increase the device thermal stability factor in static conditions, it was concluded that this case is not suitable for the improvement in STT writing efficiency. The solution to this limitations is found by reducing the ASL thermal stability to be lower than that of the SL ($\Delta_{SL} > \Delta_{ASL}$). In this second study, it was confirmed that the storage layer is subjected to additive STT contributions from the reference layer and the ASL throughout its P(R1)-to-(R3) and AP(R3)-to-P(R1) transitions. Moreover, as the device always ends up in a parallel configuration between the ASL and SL, the SL thermal stability factor is reinforced independently of the writing direction. Thus, when necessary, the ASL magnetization is reversed by the spin-polarized current from the SL. This implies that the ASL is set in the correct anti-parallel alignment with the RL at the beginning of the negative writing pulse (P(R1) to AP(R3), transiting through R2 for negative voltage polarities), while being brought in parallel alignment with the SL at the end of the positive writing pulse (AP(R3) to P(R1), transiting through R2 for positive voltage polarities). The evidences of this initial study indicate an overall enhancement in the device figure of merit (FOM=Δ_{SL}/I$_c$) with our concept. As introduced in the first chapter, the figure of merit is used as a measure of a memory cell STT writing efficiency in STT-MRAM applications. Let's now compare the FOM of our ASL-DMTJ concept to the case of a single-MTJ stack comprising the same storage layer but without any influence from the assistance layer (Comparison introduced in figure 2.15 section **??** in this chapter). At First, the increase is evident in terms of thermal stability, being $\Delta_{ASL-DMTJ}$=50 for the ASL-DMTJ and $\Delta_{single-MTJ}$=40 for the single-MTJ, corresponding to the values given in table.2.0. The critical current to switch both devices can be extracted by simply applying Ohms law to the voltage thresholds obtained from their respective R-V numerical simulations and the initial resistance states (I$_c$=V$_c$/R$_{inital}$. For the single-MTJ this leads to I$_{c_{P\rightarrow AP}}$= 159 μA and I$_{c_{AP\rightarrow P}}$= 94 μA, whereas I$_{c_{R1\rightarrow R3}}$= 120 μA and I$_{c_{R3\rightarrow R1}}$= 60 μA for the ASL-DMTJ. In both switching directions, the ASL-DMTJ critical switching currents decreased by 30 μA. Although not presenting a dramatic decrease, similar values where recently obtained experimentally by G.Hu et al [73] on conventional p-DMTJs. Considering then the enhancement in thermal stability that the ASL-DMTJ also brings, our concept based on a switchable top polarizer results in a nearly twofold increase in figure of merit (FOM) (FOM$_{Single-MTJ_{AP\rightarrow P}}$= 0.42 against FOM$_{ASL-DMTJ_{R3\rightarrow R1}}$= 0.83 and FOM$_{Single-MTJ_{AP\rightarrow P}}$= 0.25 against FOM$_{ASL-DMTJ_{R3\rightarrow R1}}$= 0.41). These enhancements in performance are in line with the results reported in the first demonstrated experimental p-DMTJ [69] and theoretically with a similar structure in [109].

Chapter 3

Materials and experimental methods

3.1 MTJ and magnetic stack deposition :

Throughout this work, all materials comprised in the magnetic tunnel junctions and various samples for materials optimization were deposited employing a Magnetron sputtering technique on 100 mm thermally oxidized silicon wafers. Magnetron sputtering is a physical vapor deposition (PVD) technique widely adopted both in industry and research due to a combination of high deposition rates, high throughput, and relatively good materials quality [110]. It is based on ion bombardment of the target material to be deposited. Figure 3.1 (a) and (b) show a simple schematic of the sputtering process at two different geometries. To start the process, an Argon gas is injected inside the chamber at 2x10-3 mbar. The Argon atoms are then ionized and accelerated towards the target by a direct current discharge between the Cathode (behind the target) and Anode (facing the cathode), thus generating a localized plasma near the target. Then, the accelerated Ar+ ions collide with the target surface atoms, causing the removal and vaporization of the target material. This vapor then precipitates and condensates as a thin film on the substrate. The deposition rate of the target material depends mainly on the plasma density (number of ions in a given volume) and the Ar+ velocity (energy of the ions). The ion bombardment of the target is also responsible for the generation of secondary electrons. The key characteristic of this technique is the use of a magnetic field parallel to the target surface, which confines the generated secondary electrons and increases the probability of Ar ionization. As a consequence, a highly dense plasma is created near the target surface, increasing the target sputtering efficiency and deposition rate. Following these principles, it is clear that a low chamber pressure (10^9 mbar) is needed before initializing the sputtering process, ensuring the stabilization of the Ar plasma, maximizing the target sputtering process, and preventing the introduction of impurities during the materials growth. As shown as well on the schematics, two geometries can be used for depositing a certain material. One is the on-axis deposition (Fig.3.1.(a)), where the substrate is rotated at 600°/s and directly placed facing the target center. This geometry allows the deposition of uniform material thicknesses, however, the coated thin films will present an inherent inhomogeneity between the center and edges. This is a common issue of this kind of technique caused by a gradual reduction of the deposition rate with the distance to the target center. This inhomogeneity is particular to each specific target material and must be considered when analyzing devices properties or thin film materials optimization as a function of wafer position, equation 3.1 expresses the fitted expression in order to estimate the deposited thickness as a function of distance to the target center :

$$\mathrm{t}_{dep} = (P1 + P2(d)) \cdot t_0 \tag{3.1}$$

Where P1 and P2 are fitted parameters linked to the specific target material defining the deposition rate, d is the distance between the target center and the wafer position, and t_0 the on axis deposited material thickness (material thickness deposited at the exact center of the target).

As an example, The interpolated distribution of deposited thickness is shown for the case of depositing 1 nm of FeCoB. The second possible geometry (Fig.3.1.(b)) is the off-axis deposition, which is used to induce a gradient of thickness throughout the wafer at a given axis direction. This is achieved by simply depositing without rotation and locating the substrate center with an offset of 100 mm from the target center. As shown on the interpolated distribution of deposited thickness (Eq.3.1), at this range of distances, we can benefit from the change in deposition rates to induce a gradual factor of 2 variations between the wafer edges. All the set of the samples in this work where deposited by Stephane Auffret at Spintec.

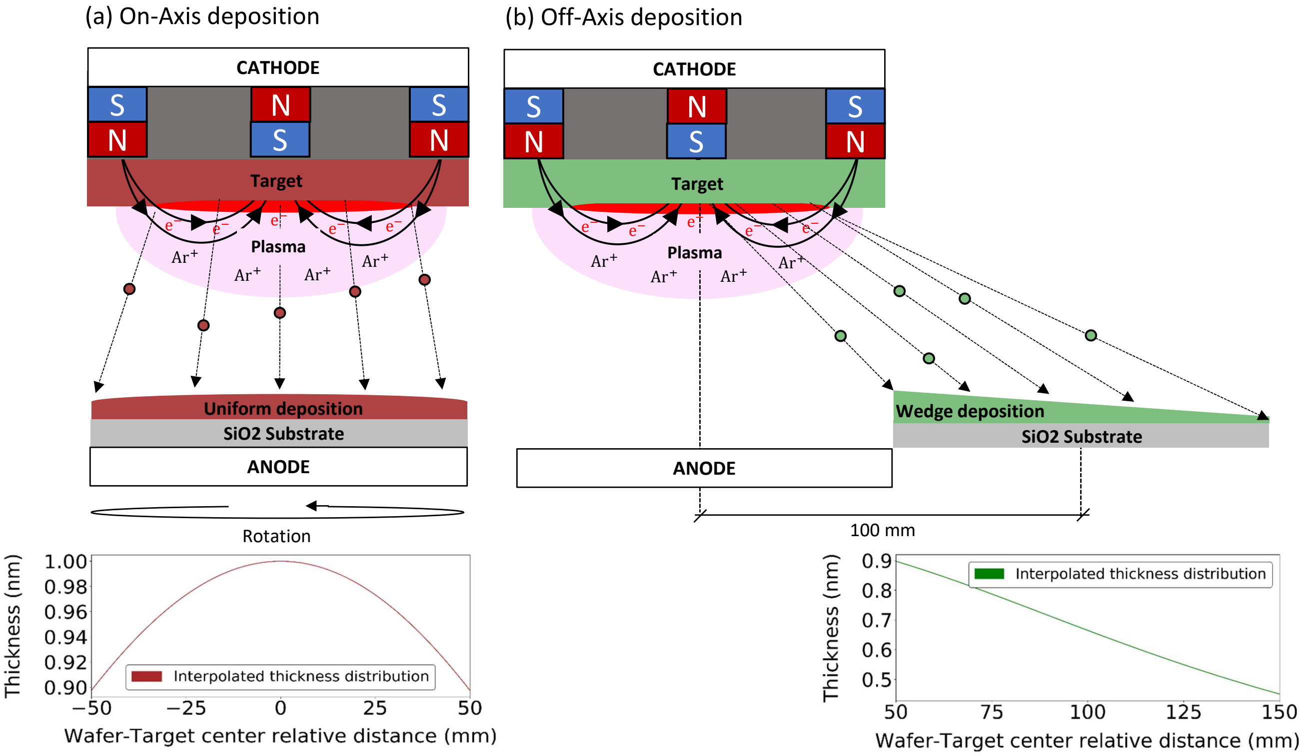

Figure. 3.1: (a) On-Axis uniform thickness deposition.(b) Off-Axis thickness wedge deposition

Our magnetron sputtering system consists of a load lock, the main deposition chamber with 12 possible target materials, and a chamber to perform natural oxidation treatments and surface etchings [111] [112] [113] [114]. In this context, all insulating materials in this thesis were based on natural oxidized MgO barriers. The procedure to deposit the oxide barriers is divided into three steps, a first deposition with a metallic Mg target, followed by oxidation, and a second Mg deposition. The base pressure in this chamber is also critical (10^9 mbar), and intended to minimize the water molecules during oxidation. Indeed MgO films are known to be highly hydrophilic [115], so any moisture in the chamber will introduce impurities at the oxide interface by the formation of a $Mg(OH)_2$ thin layer, thus affecting the TMR and magnetic electrodes surface anisotropy [116] [115]. Another possibility would be to deposit RF sputtered MgO barriers, which results in a better material quality by the use of a MgO target and an RF discharge sputtering of the insulating material [117]. In our case, the oxidation step of the metallic Mg adds another control parameter, not only to modulate the electrical properties but also when used as a source of perpendicular interfacial anisotropy. As we will discuss in the materials optimization chapter, the possibility to vary the relative amount of Mg thickness and oxidation conditions can be used to control the interfacial anisotropy of the magnetic layers after annealing. On the other hand, the deposited Mg thickness can be maintained (1.2 nm in our case 0.7Mg/Oxidation/0.5Mg) and vary the oxidation conditions, resulting in different RA, TMR, and indirect exchange coupling amplitude through the oxide tunnel barriers between the electrodes.

Five oxidation conditions are used in our samples, which differ in the chosen combination of pressure and oxidation time. Table 3.0 shows the RA and TMR values for the different oxidation conditions for the MgO barriers deposited in this work. The electrical properties reported in table 3.0 are taken from current in-plane tunneling measurements (CIPT) at full sheet film before this work [118]. Experimental verification of the quality of the barrier and electrical properties was only possible from statistical analysis of these properties on patterned magnetic tunnel junctions.

Table. 3.0: TMR and RA at different oxidation conditions

Pressure (mbar)	Time (s)	RA (Ωµm2)	TMR (%)
3x10-3	1	1.2	27
3x10-3	5	2.3	31
3x10-2	5	4.8	60
3x10-2	10	5.4	35
3x10-2	30	10	80

3.2 Annealing and MTJ crystallization :

During the development of magnetic tunnel junctions, the post-deposition annealing treatment is one of the most important steps. As already introduced in chapter I, the MTJ spin polarization efficiency essentially determines the final TMR and spin-torque efficiency, maximizing the readability of the memory cell and minimizing the critical current to switch the storage layer magnetization. In order to maximize these MTJ properties, it is crucial to achieve an epitaxial texture of the magnetic electrodes matching the MgO barrier crystalline bcc (001) structure [119]. Considering that CoFe-based magnetic electrodes and that all the SAF multilayers naturally grow with fcc (111) structures, one of the major breakthroughs on sputtered MTJs was the introduction of Boron in the composition of the MTJ electrodes. When sputtering a CoFeB target, the deposited electrodes are initially amorphous on both sides of the tunnel barrier. The MgO barrier can then grow with a rough (001) bcc texture on top of the amorphous CoFeB magnetic electrode. The electrode/MgO/electrode stack must be subjected to an annealing process (in the range 250°C-400°C) in order to crystallize the electrodes and improve the crystallinity of the MgO barrier. Fig.3.2.(a) and (b) depicts an over-exaggeration of the structural changes produced in the MTJ after the annealing process. In our case, all magnetic electrodes comprised in the MTJ stacks are based on an iron-rich $Fe_{72}Co_8B_{20}$ alloy. Although presenting higher damping, the choice of Fe rich rather than Co rich is based on the fact that Fe wets better on the MgO surface, thus allowing to grow smooth layers. For the case of Co rich alloys, the high surface tension results in islands growth and therefore rough layers. Moreover, from ab-initio calculations, Fe rich electrodes are known to be able to develop higher values of TMR and PMA [120] [121]. During the annealing, the boron atoms diffuse out of the FeCoB alloy and get absorbed by forming borides compounds with the non-magnetic layers in contact with the FeCoB amorphous electrodes [122] [123] (Normally based on metals such as Ta, Mo or W [124] [125] [126] [127]). Then, the already textured MgO further crystallizes and acts as a seed layer for the FeCo crystalline growth. The annealing procedure consists of 10 minutes at 300°C, 10^{-6} mbar of pressure, and without the application of an external magnetic field. The annealing temperature was varied to optimize the material properties in terms of perpendicular magnetic anisotropy of the Storage layer-Assistance layer and the TMR amplitude of the double magnetic tunnel junction structure. However, once patterned the full stack, instabilities induced on the SAF stability caused by interdiffusion in the Pt/Co multilayers at higher annealing temperatures (above 300°C) lead to the conclusion that higher temperatures were detrimental to the reliability of the devices.

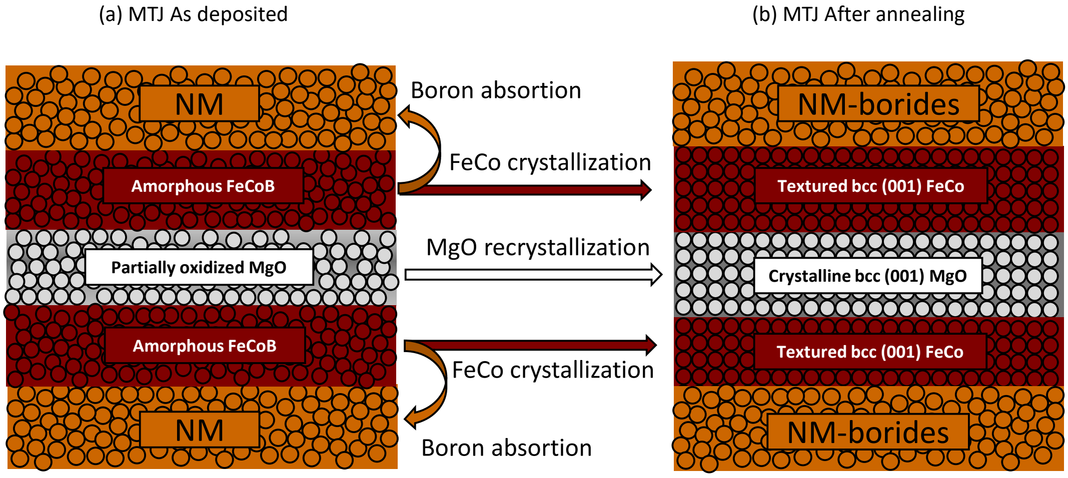

Figure. 3.2: (a) MTJ amorphous FeCoB electrodes structure and partially oxidized MgO barrier as deposited.(b) MTJ Texturized FeCo electrodes structure and Crystalline MgO barrier after annealing.

3.3 Magnetic properties characterization at thin film:

The deposition and annealing of the magnetic stacks were followed by the systematic characterization of the magnetic properties at sheet film level. These characterizations were performed both for the samples dedicated to materials optimization and for nano-fabrication. The main technique used was a magneto-optical Kerr effect (MOKE) magnetometer. This kind of technique not only permits the fast mapping of the magnetic properties before the fabrication but also the study of the evolution of the full sheet films magnetic properties in the same growth conditions. Figure.3.3 depicts a real image of the NanoMOKE3® measurement system, while Fig.3.4.(a) illustrates the schematics. The fundamental principles of the MOKE rely on how a polarized light beam is reflected on the surface of a magnetized material [128]. Providing a light beam linearly polarized with respect to the propagation direction (p-polarization or s-polarization Fig.3.4.(b)), the polarization will experience two main changes when reflected on a material with a certain magnetization.

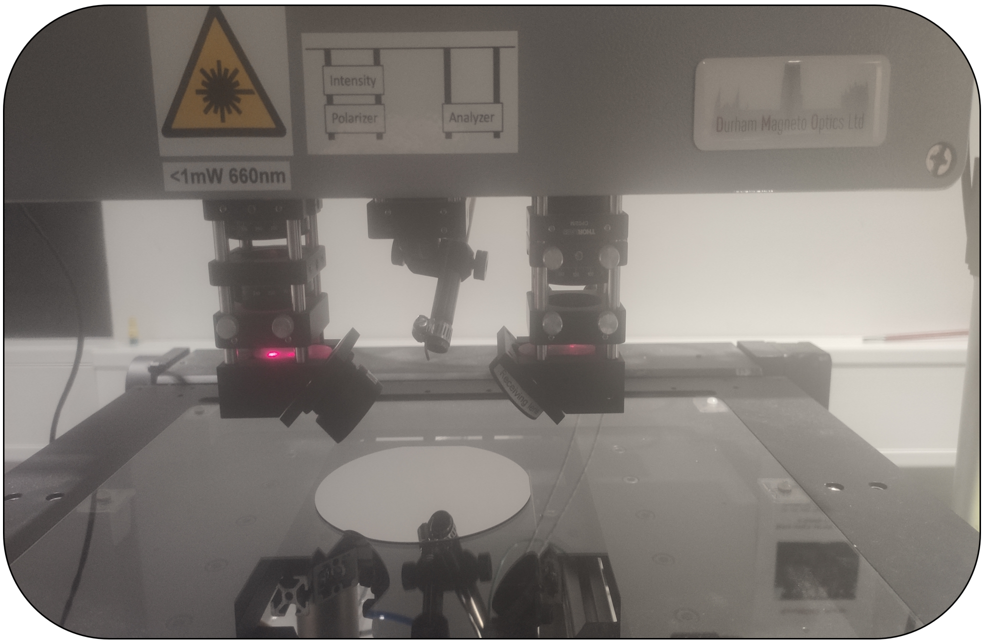

Figure. 3.3: NanoMOKE3® (Durham Magneto Optics) automated measurement system.

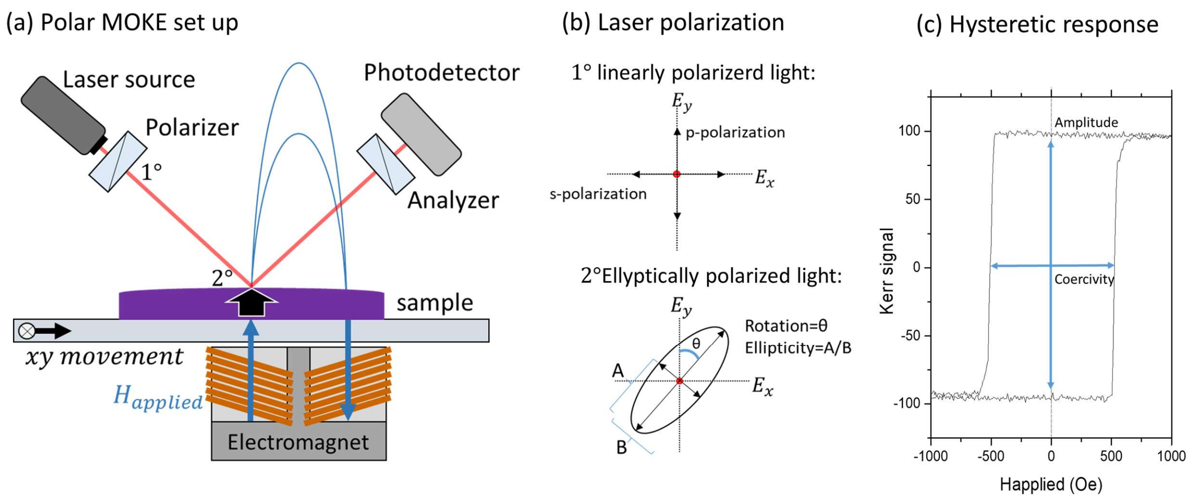

Figure. 3.4: (a) Polar MOKE set up schematics between showing the polarized laser beam and the perpendicularly magnetized sample. (b) Comparison between linearly polarized light and elliptically polarized light. (c) example of the hysteretic response extracted from the Kerr signal as a function of applied perpendicular magnetic field.

For the case of having a p-polarized beam, the Lorentz force will generate an out of phase perpendicular s-component, and a rotation from the original p-polarized direction. The result will be an elliptically polarized beam with its major axis “A” rotated and “B” the generated s-component. These two main changes are denoted as Kerr rotation (angle ϑ) and Kerr ellipticity (A/B ratio), being the first one directly proportional to the sample’s magnetization. Due to its symmetry, the same can be applied for the case of having an initially s-polarized beam. Depending on the geometry between the incident plane of the light and the magnetization of the sample, three main Kerr effects can be employed. The longitudinal and transverse, where the magnetization is in the sample’s plane, and parallel or perpendicular to the incidence plane, or the Polar Kerr effect, where the magnetization is out of the sample’s plane and parallel to the incidence plane. The last is the main Kerr effect used in this thesis and the one explained in this section. The MOKE magnetometer setup consists of a Laser source with 660 nm in wavelength followed by a polarizer, that induces a p-polarization in the light beam. When generated and polarized, the focused beam shines an area of around 400 nm on the magnetized sample, reflecting on the surface and changing its polarization. Finally, the elliptically polarized light beam passes through an analyzer and the light intensity is measured by a photodetector, extracting the Kerr ellipticity and the rotation respectively. This process is repeated while ramping the field up and down between the maximum amplitude up to ±3900 Oe, thus obtaining the sample magnetic hysteresis loop. The value of the magnetization amplitude is proportional to the Kerr intensity and the direction depends on the sign of the ellipticity (direction of the generated s-component). Fig.3.4.(c) shows an example of the hysteresis curve vs field extracted with this method. This type of measurement is quite appropriate to get the shape of hysteresis loops but does not allow to get quantitative values of the material spontaneous magnetization or effective perpendicular anisotropy [129]. However, it is possible to extract the total signal amplitude and coercivity which are dependent on these material’s properties [130]. This last and the possibility of measuring the evolution of the magnetic properties at different positions of the wafer makes this technique a powerful tool for fast and efficient materials optimization.

3.4 Devices nanofabrication :

The device nano-fabrication constitutes a key step in the research work involved in this thesis. Crucial parameters like the TMR, final resistance, and magnetic properties such as effective anisotropy and magnetic saturation are affected by the final patterned diameter (volume of the magnetic layers) and defects induced during the fabrication process. In addition, the magnetoresistance response under applied voltage by either spin-transfer torque effect or self-heating effects can only be characterized once the memory cell is properly contacted and patterned. In the following section, the main steps of fabrication are detailed for the patterning of a single MTJ nano-pillar and its electrical contacts. The same process can be applied to double magnetic tunnel junctions stacks. Fig.3.5 presents the simple schematics as well as a combination of optical microscopy (OM) and scanning electron microscopy (SEM) images of the nano-micro-fabrication process flow. In general, the fabrication is divided into four critical levels, involving five lithography steps: i) Magnetic stack deposition, ii) MTJ patterning, iii) bottom electrode etching, iv) pillar encapsulation, and v) top electrode deposition. All the levels of fabrication were already optimized and developed by the MRAM group at Spintec and performed at the Plateforme Technologique Amont (PTA). Before starting the fabrication process, the magnetic stack-MTJ deposition and annealing are followed by an Ar+ surface etch, the deposition of 3 nm of Ru, and 150 nm of Ta hard mask. The first critical level, the magnetic stack-MTJ patterning, starts with an e-beam lithography (Fig.3.5.(1)). At this step, the device's nominal diameters are patterned on a polymethyl methacrylate (PMMA) resist, ranging from 50 to 100 nm. Once exposed and developed, the patterns are filled with the evaporation of 20 nm of Cr and a lift-off (Fig.3.5.(2)). At these two steps, it is only possible to verify the processes by OM, observing the alignment marks also patterned and filled with Cr. The Cr nano-disks then work as a mask for the reactive ion etching (RIE) of the Ta hard mask (Fig.3.5.(3)),)), ending at the Ru layer that acts as a stop layer for the RIE process. SEM imaging at this step shows the resulting conical shape for a 100 nm nominal Cr, having 130 nm of Ta hard mask base. Then, The magnetic stack-MTJ is patterned by means of ion beam etching (IBE) (Fig.3.5.(4)). The etching angles are one of the most critical parameters during the IBE. In our case, we perform a two-angle etching combination. First, the etching angle is set at 35° with respect to the normal of the wafer. This angle reduces the resulting conical shape of the pillars after the etching and minimizes the metallic re-depositions of the multilayers being etched. These re-depositions can lead to pillar enlargements and serial resistances shorting the tunnel barriers and thereby reducing the measured TMR. Then the shutter is closed when starting to etch the bottom electrode Pt, ensuring that the SAF multilayer is properly patterned for a correct stray field compensation. The entire process is monitored by secondary ion mass spectroscopy (SIMS). The IBE step finishes by trimming the pillar at an angle of 80° with respect to the normal of the wafer. The trimming time is adjusted to reduce the diameter of the pillars until the nominal size is recovered (SEM image Fig.3.5(4)). This ensures as well the complete elimination of any metallic re-deposition on the MTJ sidewalls. Once patterned, the subsequent steps are dedicated to patterning the bottom contact. This is done by a combination of UV-lithography and a RIE of the bottom electrode Pt (Fig.3.5(5) and (6)). To avoid any possible shorting, it is imperative to remove all the Pt surrounding the resist pattern.

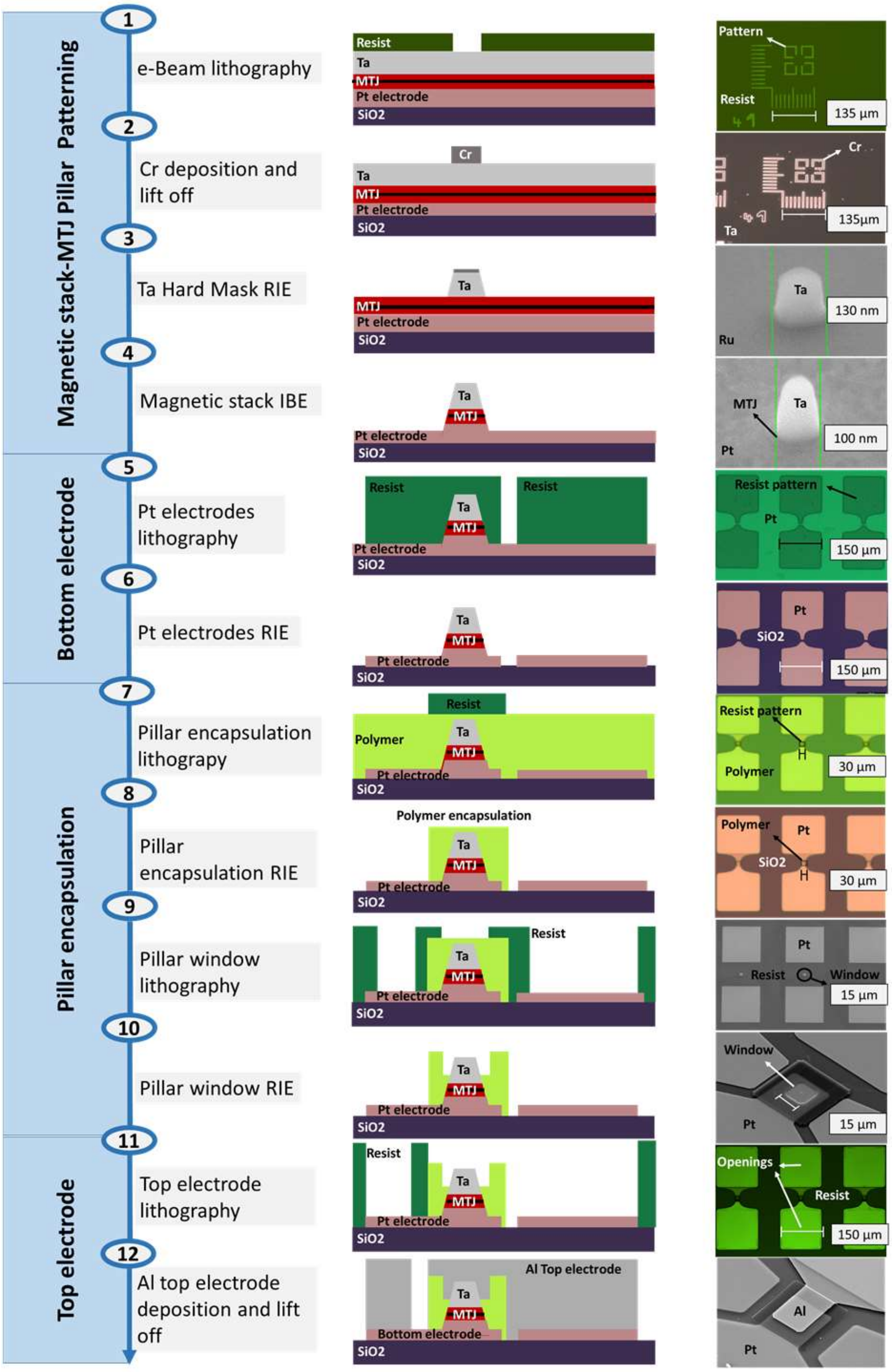

Figure. 3.5: Standard Nano-Micro-fabrication process flow used by the MRAM group at Spintec; (1) e-beam lithography, and nominal MTJ pillar patterning. (2) 20 nm Cr deposition and Lift-off. (3) Ta hard mask patterning by RIE. (4) Magnetic stack and MTJ patterning by IBE. (5) Pt electrodes UV-lithography. (6) Pt electrodes patterning by RIE. (7) Pillar polymer encapsulation UV-lithography. (8) Pillar encapsulation patterning by RIE. (9) Pillar encapsulation contact window UV-lithography. (10) Pillar encapsulation contact window etching by RIE. (11) Top electrode UV-lithography. (12) Aluminum top electrode deposition and lift-off

The next critical step of the process is the encapsulation of the pillar with a polymer. This encapsulation passivates the MTJ and enables the contact with the top electrode. The process is divided into two steps of UV-lithography and RIE of the polymer. The first step creates an encapsulation of 30x30 μm protecting the pillar (Fig.3.5.(7)-(8)), the second opens a window and reduces the polymer thickness so that its top surface reaches approximately half of the Ta hard mask height (Fig.3.5.(9)-(10)). This second step is one of the most critical as an over-etching of the polymer will shorten the MTJ when depositing the top electrode. The last steps in the process flow consist of the last UV-lithography with a negative resist and the deposition of 10 nm of Cr and 300 nm of Al top electrode (Fig.3.5.(11)-(12)). It is important to mention that an IBE pre-etching is performed before depositing the top electrodes, the fabrication is then completed with a lift-off. For sake of simplicity, the nano-fabrication steps just mentioned are only focused on the case of one device. However, as introduced in section 3.1, all samples in this thesis were fabricated in 100 mm SiO2 wafers, Fig.3.6.(a) and (b) show a comparison between the wafer before and after the fabrication. The four main levels of the fabrication produce a total of 173 dies, with 168 devices per die, resulting in a total of 29064 devices per sample.

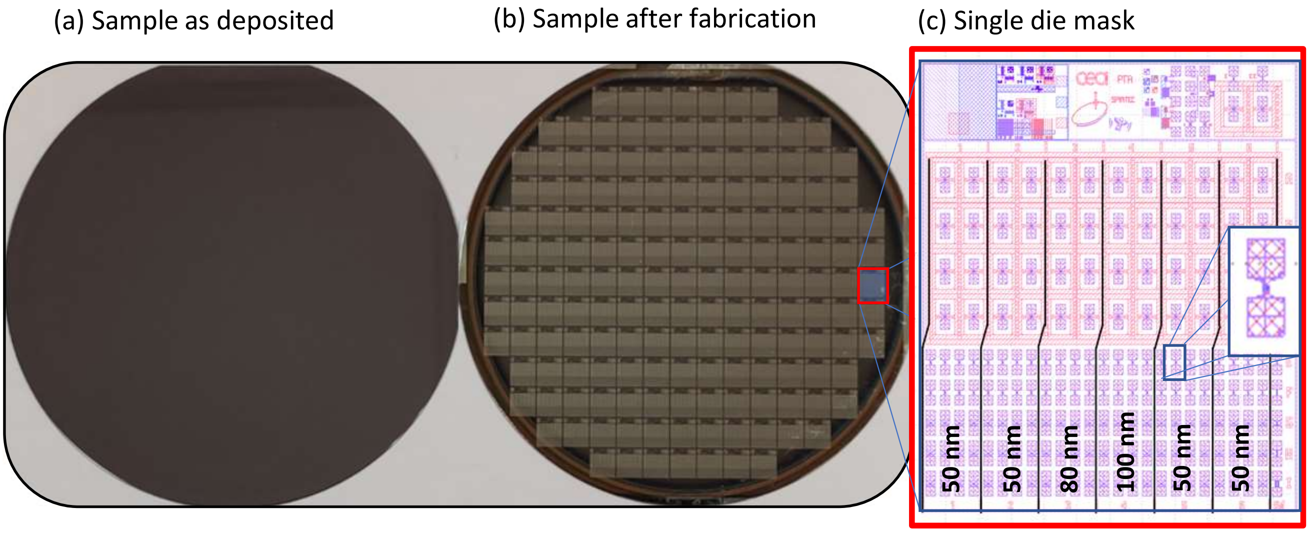
(a) Sample as deposited

(b) Sample after fabrication

(c) Single die mask

Figure. 3.6: Comparison between post-fabrication wafer (a) and (b) after-fabrication wafer.(c) Lay-out of each single die mask indicating as well the different nominal pillar sizes per column.

3.5 Devices electrical characterization:

3.5.1 Characterization under applied field

Wafer yield and determination of device TMR

Once the nanofabrication process is completed, the wafer yield is evaluated with an automated prober station (Figure.3.12.(a)-(b)). This equipment allows a fast mapping of the individual device's electrical and magnetic properties by extracting their magnetoresistance response as a function of a perpendicular magnetic field (Resistance-field loop RH). The perpendicular magnetic field is produced by an electromagnet directly placed above the microprobes contacting the device's top and bottom electrodes. A Kepco DC generator supplies the electromagnet, reaching a maximum field of 3000 Oe. Then the field is swept linearly between the maximum and the minimum applied field by triggering the power supply with a wave generator. A low bias current is applied with a source meter, obtaining the device resistance from the voltage drop with a digital multimeter. The wafer yield is evaluated by filtering out the short or open circuit devices due to possible fabrication flaws. This is a key point for identifying problems related to specific critical steps during the fabrication process. Short circuit devices can exhibit an over-etch of the polymer window before the deposition of the top electrode. Open circuit devices can result from possible losses of pillars during the patterning or from an under etch of the polymer window before contacting

(a) Automated prober station

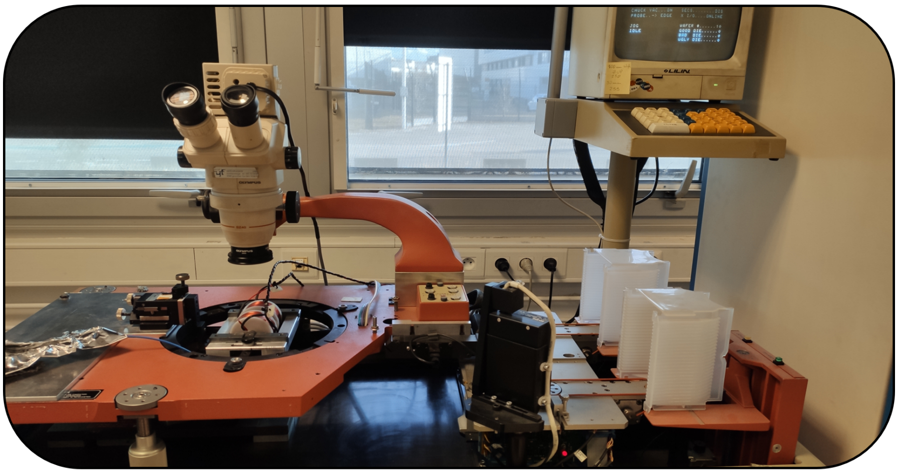

(b) Example of a wafer under characterization

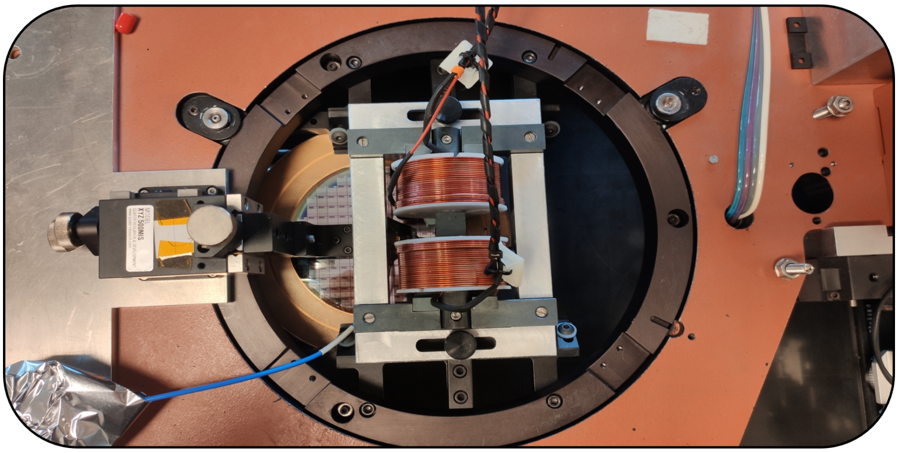

Figure. 3.7: (a) Image of the automated prober station utilized for the electrical characterization vs wafer position. (b) Example of a wafer under characterization with the electromagnet placed directly above the probes contacting the device.

Fig.3.8.(a) presents an example of a processed wafer with a 50 percent yield, showing a clear difference between the center and the edges. Correlation between the regions presenting short/open devices with the fabrication steps causing the loss of devices is crucial for correct process optimization and its adaptation to new stack designs. On the working devices, 20 RH cycles are repeated at a sweeping field frequency of 5 Hz, averaging and fitting the magnetoresistance response. Finally, the TMR, along with the magnetic properties such as the coercive field and the coupling field, can be extracted for different wafer positions and device sizes. This allows one to correlate different devices characteristics like material thicknesses or nominal diameter with their electrical and magnetic properties. Fig.3.8.(b) shows the impact of introducing a thickness wedge on the device's coercivity, showing a clear example of the use of these mappings for materials optimization. From the association between the device TMR and the minimum resistance at different pillar sizes (Fig.3.8.(c)), it is possible to estimate the effects induced on the MTJ during the fabrication. Possible metallic re-depositions will produce parallel resistances, decreasing the barriers TMR and device resistance, while oxides in the hard mask will produce serial resistances, increasing the device resistance and reducing the TMR as well. For a series resistance, the experimental values obtained from the devices measured TMR as a function of minimum resistance can be fitted to the following expression:

$$\mathrm{T}MR = \frac{TMR_{nominal} \cdot RA_{nominal}}{RA} \tag{3.2}$$

Where $TMR_{nominal}$ and $RA_{nominal}$ are taken from table.3.0 from previous measurements via CIPT, and the value of RA is estimated taking into account the nominal diameters of the pillars defined with the e-beam mask during the fabrication and the measured minimum resistance. On the other hand, for the case of parallel resistances the fitted expression is defined by:

$$\mathrm{T}MR = \frac{TMR_{nominal}}{(\frac{RA_{nominal}}{RA} \cdot (TMR_{nominal} + 1) - TMR_{nominal})} \tag{3.3}$$

Apart from evaluating the origins behind the reduction in the devices measured TMR with this expressions, and correction to the nominal diameters can be applied in order to estimate the value of the device electrical diameter, this correction includes the variations in size from the nominal values for each device size while considering the RA value of the junctions to be constant and equal to the one obtained by CIPT. In addition, the correct patterning of the SAF structure can be evaluated by checking the coupling field as a function of pillar size (Fig.3.8.(d)), giving an idea of the dependency between the stray field amplitude produced at different SAF diameters. This first characterization produces enough statistical data to target devices with specific electrical and magnetic properties, perform materials optimization at the device level or identify the main defects introduced during the fabrication process.

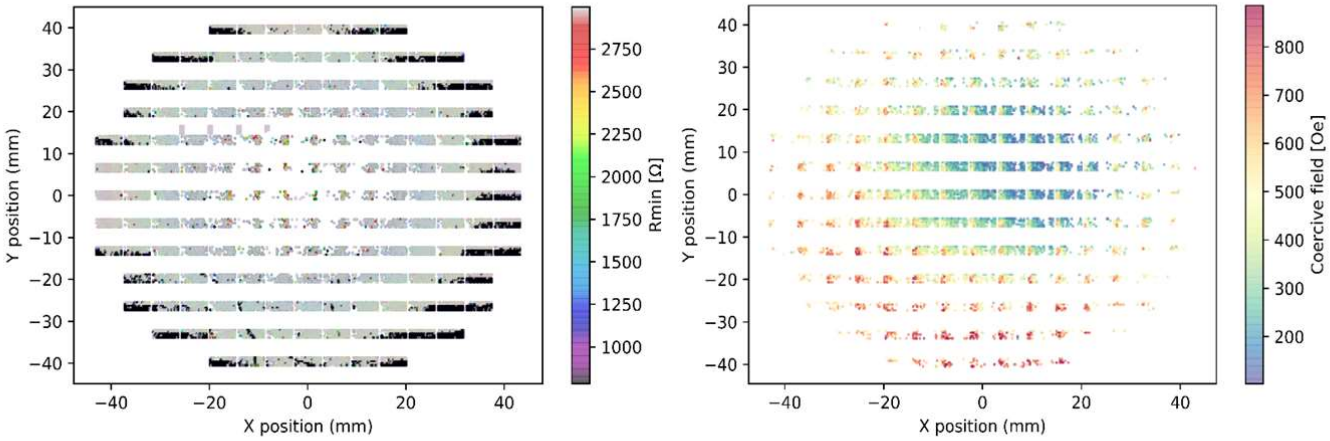
(a) Yield mapping : 11% shorts 37% open

(b) Device coercivity mapping

(c) TMR vs device minimum resistance

(d) Coupling field vs device electrical diameter

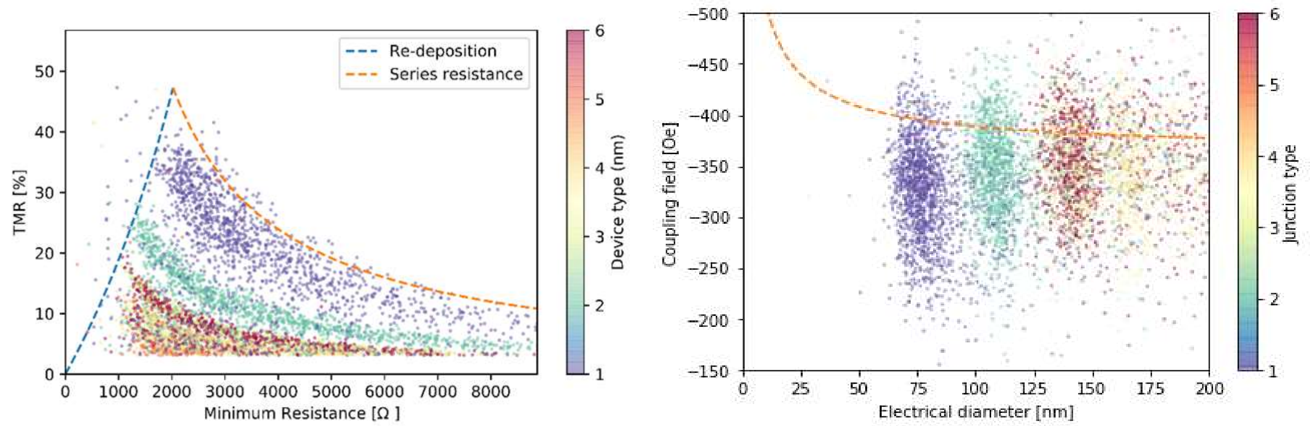

Figure. 3.8: (a) Minimum resistance at parallel state and Short - Open devices vs wafer position. (b) Variation of device coercivity vs wafer position by introducing a materials wedge. (b) TMR vs device type (Nominal diameter ascending from 1 to 6, 50 to 100 nm. (d) Coupling field produce by the SAF stray field vs device electrical diameter.

Thermal stability extraction with field

As introduced in the first chapter, the thermal stability factor for standard p-STT-MRAM is defined as the ratio between the storage layer energy barrier between its two states in equilibrium and the thermal energy. This energy barrier will directly depend on the effective perpendicular magnetic anisotropy and the volume of the layer under the single domain approximation describing a coherent reversal of the storage layer magnetization. In this section, we will introduce the main method employed for the thermal stability extraction with a perpendicular magnetic field. The method, so-called switching field density (SFD), is based on Sharrock's theory [131] (Eq.3.4) for the probability of switching a magnetic nano-particle under an applied magnetic field [132]:

$$\mathrm{P}\left(t\right) = 1 - exp\left(\frac{H_k}{2t_0 R_h}\sqrt{\frac{\pi}{H_k}} erfc\left(\sqrt{\Delta_0}\left(1 - \frac{H\left(t\right)}{H_k}\right)\right)\right) \tag{3.4}$$

where erfc(x) is the error function:

$$erfc(x) = \frac{2}{\sqrt{\pi}}\int_x^{\infty} e^{(-x'^2)}dx' \tag{3.5}$$

The SFD method can be easily implemented to the statistical distribution of coercive fields obtained from a cycled R-H loop. This coercive fields are extracted fitting the R-H loops obtained to a Stoner-Wolfarth model. Although in our work the cell diameters are ranging from 50 to 100 nm (over the size limits for the macrospin approximation), this method is widely utilized in similar cell diameters [38], and applied in this thesis for a qualitative estimation of the devices thermal stability factor and the evaluation of the effect of the coupling between the Storage layer and Assistance layer between samples with the ASL-DMTJ stack with respect to control samples without the Assistance layer influence. The method routine was developed by Luc Tillie in our RH data analysis algorithm as part of his thesis [113]. Equation.3.6 shows the SFD expression obtained by deriving the probability of switching as a function of the applied field H. The derivation dP/dH leads to:

$$SFD(H) = \frac{1}{t_0 R_h} exp\left(-\frac{H_k}{2t_0 R_h}\sqrt{\frac{\pi}{H_k}} erfc\left(\sqrt{\Delta_0}\left(1-\frac{H}{H_k}\right)\right)\right) exp\left(-\Delta_0(1-\frac{H}{H_k})^2)\right) \tag{3.6}$$

Where t_0 is the switching attempt time set at 1 ns and R_h is the sweeping rate of the field. This rate depends on the sweeping frequency used during the measurement (1 to 5 Hz). As explained in the previous section, the field is swept linearly, so it can be considered as $H(t) = R_h t$, being $H(t_0) = H_c$. The anisotropy field H_k and the thermal stability factor Δ_0 are therefore extracted from the fitting of this expression to the device's experimental coercive field distribution [133]. Fig.3.9.(a) shows an example of this kind of measurement with 50 cycles for a device with $\Delta = 43$, indicating as well the distribution of coercive fields for each switching transition.

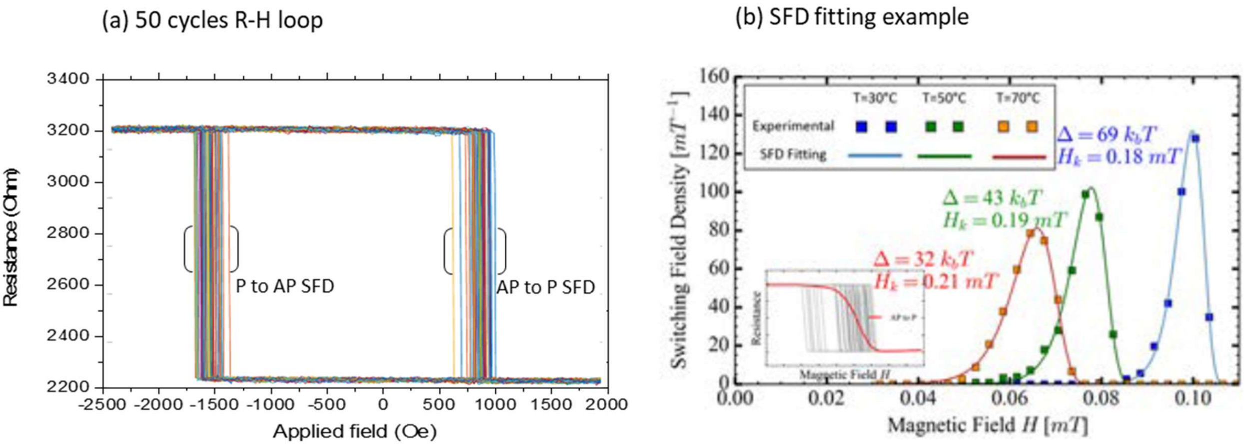
(a) 50 cycles R-H loop

(b) SFD fitting example

Figure. 3.9: (a) Example of a resistance vs perpendicular field loop cycled 50 times, indicating each of the H_c distribution for each transition. (b) Example of fitting of Eq.3.9 into the H_c distribution at increasing measurement temperatures (image taken from [132]).

With this kind of method, the width and height of the distributions determine the estimated thermal stability factor. This is depicted in Fig.3.9.(b), taken from [132], where a comparison is made between the evolution of the obtained thermal stability factor and the device temperature. At higher temperatures, the width of the coercive field distribution spreads, due to increased stochasticity of the storage layer switching. Correlatively, the maximum SFD value is reduced resulting in lower extracted thermal stability factors. This accelerated retention extraction method is a widely used technique for its speed and simplicity. In our case, as it will be presented in the last chapter, the ASL-DMTJ devices present particular switching dynamics with the magnetic field. The SFD remained the method of choice to evaluate the assistance layer effect on the storage layer's stability.

3.5.2 Characterization under applied voltage

Thermal stability and critical switching current extraction with voltage

Analogously to the SFD method, a similar procedure can be applied to the case where the switching of the devices is induced by a train of voltage pulses of increasing amplitude. Contrary to the case of switching by field, with the method explained in this subsection, is possible to estimate the critical switching current by spin-transfer torque from the cumulative distribution of switching voltages. In this case, the current dependent Sharrock's expression for the switching probability is [113] [132]:

$$\mathrm{P}\left(I\right) = 1 - exp\left(\frac{t_p}{t_0} exp\left(\Delta_0 \left(1 - \frac{I}{I_c}\right)\right)\right) \tag{3.7}$$

where t_p is the pulse length, and I is the voltage amplitude of the pulses divided by the resistance state of the device (parallel state or anti-parallel state). Fig.3.10 depicts the three main steps of the measurement routine. First, 50 R-H cycles are performed to extract any possible offset field produced by the reference layer magnetization (Fig3.10.(a)). Determining this field is critical as it will cause an asymmetry on the switching probability of the transitions with voltage, impacting as well the extracted values of critical switching voltages (V_c). In addition, the device thermal stability factor is estimated with the SFD method. Following this first characterization with the magnetic field, a resistance vs voltage pulse amplitude (R-V) loop is conducted to observe the device electrical switching by STT. For each voltage pulse amplitude, a single succession of writing and reading pulses pattern is applied. The acquisition time of the reading pulse is set much longer (1 μs) than the writing (100 ns), thus allowing for a precise evaluation of the memory resistance state. The writing pulse voltage amplitude is then increased linearly and the R-V loop cycled 50 times. If needed, a constant field compensating the offset field is applied during the full measurement (Fig3.10.(b). From the obtained statistical distribution of switching voltages, the switching probability at each voltage pulse amplitude is acquired (Fig3.10.(c)). Finally, from the fitting of equation3.7, the values of V_c for each transition are estimated as well as another assessment of the thermal stability factor. The critical current densities are then calculated considering the pillar area and the initial parallel or anti-parallel resistance state.

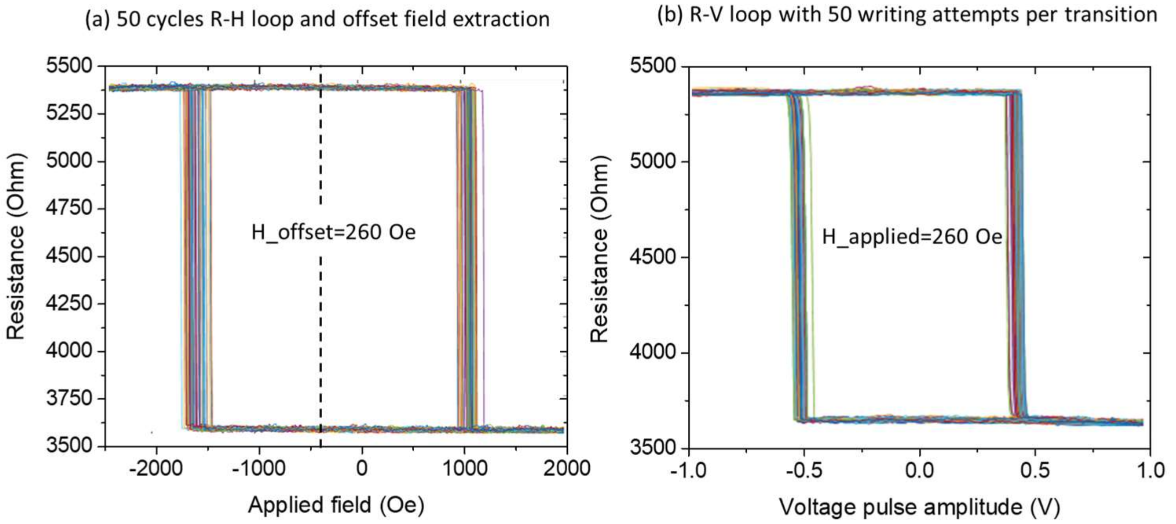

(c) Switching probability fitting

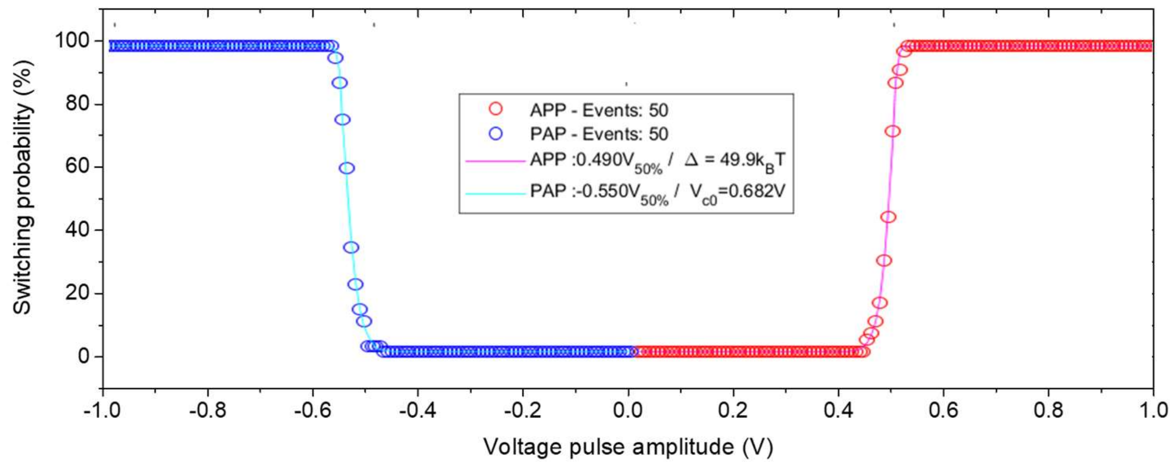

Figure. 3.10: (a) SFD method prior to the voltage-resistance loop extraction and determination of the offset field.(b) Resistance vs voltage pulse amplitude for 50 writing attempts per transition.(c) Switching probability and Eq.3.7 fitting for thermal stability and critical switching voltage extraction.

Time resolved writing dynamics

At the time of developing new concepts for p-STT-MRAM, the experimental evaluation of the time resolved magnetization dynamics by STT is one of the most important aspects. Parameters such as incubation and switching time can be acquired by characterizing in real-time the resistance transitions during the application of the writing pulse. Moreover, the ASL and SL specific switching sequences introduced in chapter 2, can only be verified by observing the ASL-DMTJ transient resistance state throughout the writing operations. In this section an entire description of the real-time setup and measurement procedure are explained. Fig3.11 depicts the schematics of the transmission line assembly between the instrumentation and the device under characterization. The experimental procedure is as follows; First, a pulse generator outputs two voltage pulses with opposite signs and 100 ns in length. Then, a power combiner unites these two pulses conforming a square pattern of negative and positive pulses. The first pulse is set with a voltage amplitude providing 100% probability of switching (P_{sw}), initializing the resistance state. The second pulse is set with a voltage amplitude with 50% P_{sw} to observe the switching dynamics of the write operation under investigation. A succession of 10^8 pulses with this pattern are applied to the junctions. Finally, the transmitted voltage is amplified before acquiring the signal with an oscilloscope ($V_{ocilloscope}$).

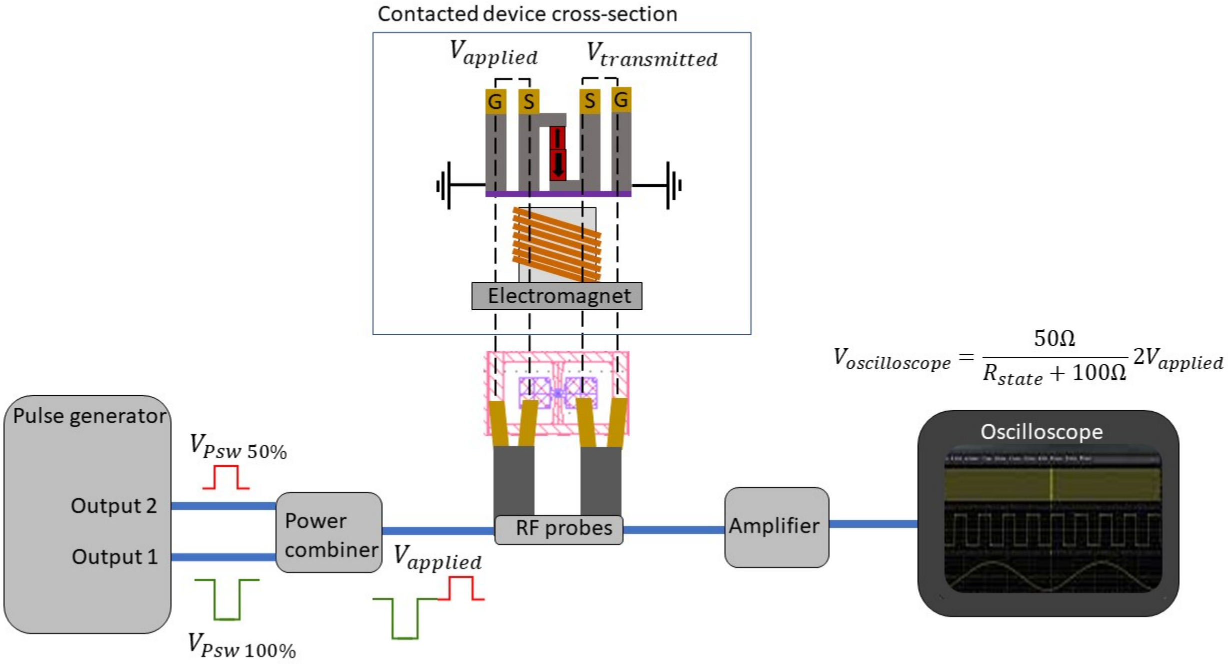

Figure. 3.11: Set up schematics of the transmission line assembly between the instrumentation and the device for the real-time characterization of the ASL-DMTJ switching dynamics.

Real time instrumentation set up

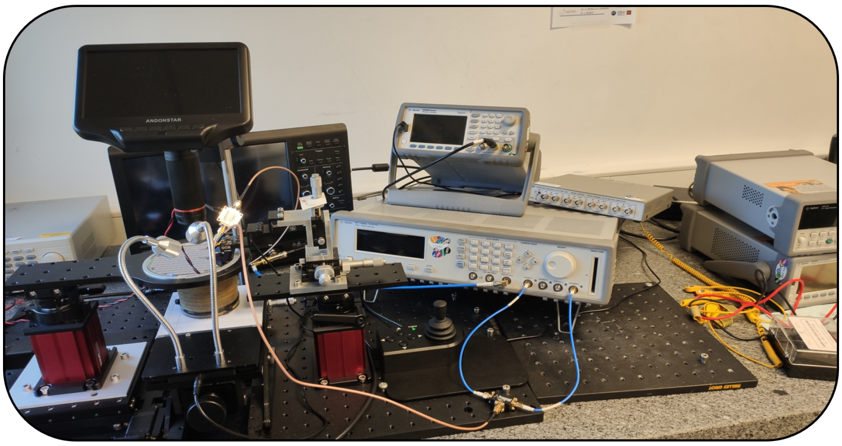

Figure. 3.12: Real time instrumentation setup ilustrated in figure.3.11.

It is important to highlight that the voltage acquired on the oscilloscope will be inversely proportional to the resistance state of the junctions, thus allowing us to observe the magnetization dynamics for each MTJ from the change in the transmitted voltages in real-time. An electromagnet is placed below the sample in case of requiring a compensation field or modulating the switching probability between states. The data obtained from the oscilloscope is then analyzed in order to filter only the pulses resulting in a successful writing event. Fig3.13.(a) shows an example of the measured transmitted voltage pattern from an ASL-DMTJ for the case of evaluating the AP to P transition, indicating in the red window the real-time reversal region. As already introduced in this section, a negative voltage pulse is applied to stabilize the AP state, then a second positive voltage pulse is applied to evaluate the transmitted voltage changes during the AP to P write operation. A detailed overlap of 10^4 switching events are evaluated as in Fig3.13.(b), giving a clear picture of the switching path during the application of the voltage pulse originated by the respective change in the magnetic orientation of each MTJ comprised in the device

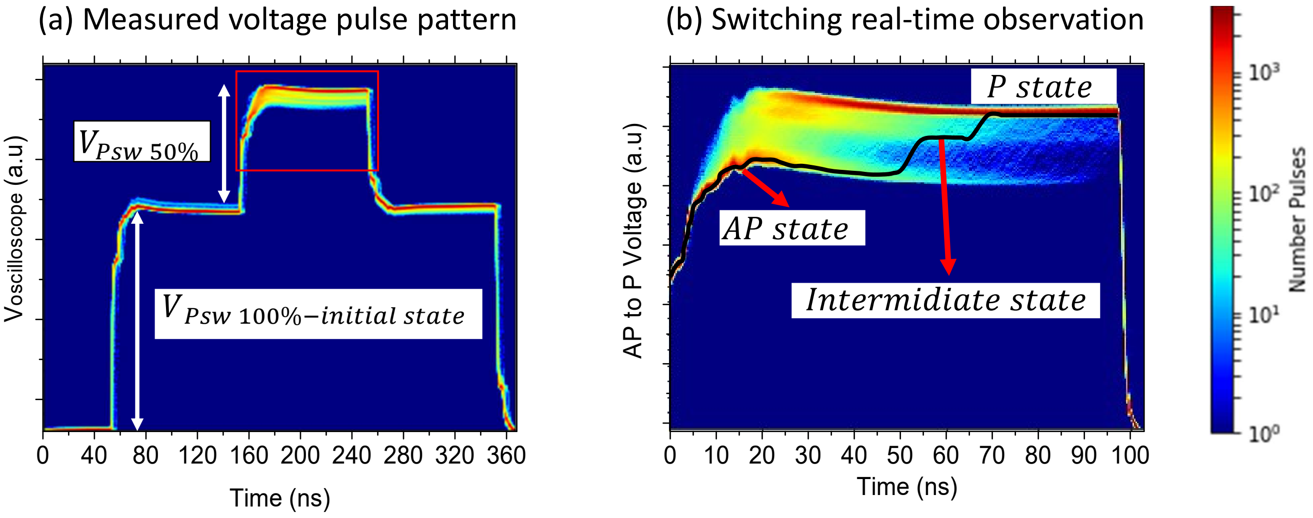

Figure. 3.13: (a) Example of negative and positive voltage pulse pattern, applied for real time observation of the switching dynamics for the AP to P transition. The red window region shows the real time reversal region detailed in (b). (b) Example of the switching dynamics evaluation for the AP to P transition, indicating the transient resistance state between the two stable configurations of the memory.

3.6 Characterization under applied voltage and field

3.6.1 Stability voltage-field diagrams

Important device characteristics can be extracted from voltage-field stability phase diagrams. These measurements allow us to characterize the STT influence and self-heating temperature effects on the device switching field (H_{sw}) [134]. The measurement is based on performing a succession of resistance-field loops after the application of a train of voltage pulses. The voltage pulse amplitude directly influences the switching field of the device. The measurement proceeds in three phases for each applied field and pulse voltage: 1) Slowly sweeping the magnetic field (at 5Hz); 2) applying a 100 ns voltage pulse of amplitude (V_p) at each field point; 3) measurement of the resistance after each pulse at a small dc bias of 50 mV. The resistance measurement integration time is 100 μs, such that the magnetic system relaxes to a stable magnetic configuration and is thermalized at room temperature. The switching field is averaged from 15 R-H cycles. The stability phase diagram is finally constructed repeating this procedure in the whole pulse voltage amplitude range. Figure3.14.(a) depicts the voltage-field phase diagram extracted for a standard p-STT-MRAM single MTJ, where regions plotted in red and blue stand respectively for maximum and minimum resistance states (logic 1 or 0), corresponding to the stabilization of the anti-parallel (AP) and parallel (P) alignment of RL and SL magnetization [93]. The green region represents a bi-stable region, where both magnetic configurations can be stabilized, with clear boundaries separating P and AP stability regions. For voltage pulses greater than ±0.25V, there is a linear dependence of the H_{sw} with the voltage pulse amplitude, corresponding to the STT contribution of the spin-polarized current from the reference layer. This contribution to the H_{sw} reduction by the STT effect can be better seen in Figure3.14.(b). At low voltage amplitudes (0.02V), the resistance-field loop shows the device's coercive field without any effect induced by the voltage pulses. Then, depending on the voltage polarity, one of the switching fields will start to decrease asymmetrically. Negative voltage polarities will decrease the AP to P (-0.43 V) while maintaining the P to AP switching fields and positive voltage polarities will have the inverse response, the reduction of the P to AP (+0.35V) while maintaining the AP to P switching fields.

This kind of response with voltage is the main characteristic defining the STT effect in the stability diagrams, and continues linearly till the total value of coercivity reaches zero (see Fig.3.14(c)). From the fitting of this linear response, the H_{sw}/V_p ratios for each transition can be obtained, leading to a quantitative estimation of the STT efficiency of the device under investigation. Other means to observe the STT effect on the measured R-H cycles of the devices, is an apparent increase on the coupling field (see figure.3.14.(d) positive and negative voltage ranges where the STT is the main phenomenon reducing the coercivity). This is understood from the fact that at a certain voltage polarity the STT only reduces one of the H_{sw} for each transition, the R-H cycles are then shifted from the real value of the stray field from the RL at -388 Oe, causing an apparent variation of the coupling field vs voltage.

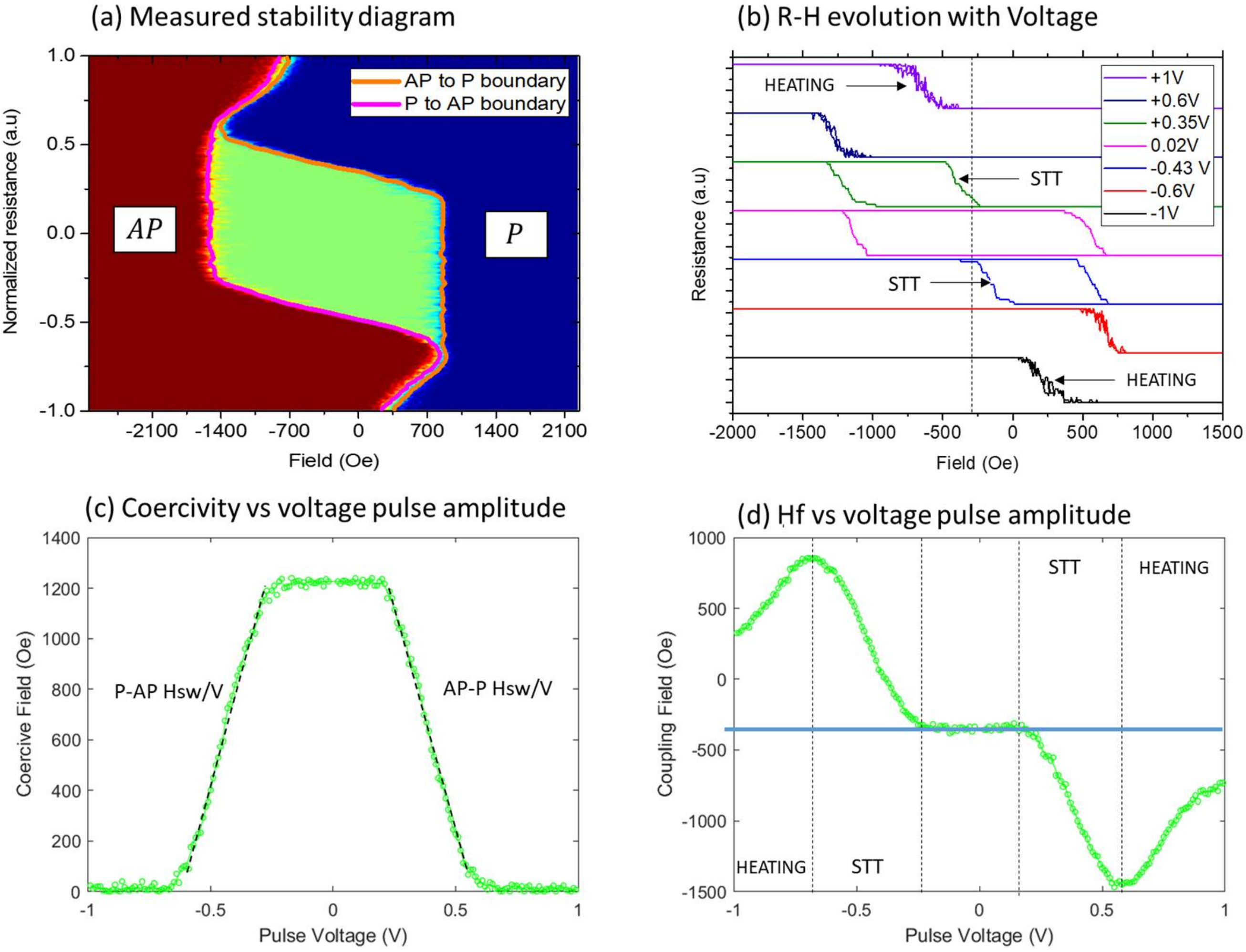
(a) Measured stability diagram

(b) R-H evolution with Voltage

(c) Coercivity vs voltage pulse amplitude

(d) Hf vs voltage pulse amplitude

Figure. 3.14: (a) Single MTJ standard stability phase diagram, indicating the switching field boundaries for AP to P and P to AP stability regions. (b) Resistance-Field loops at different voltage pulse amplitudes.(c) Evolutionf of the device coercivity as a function of the V_p.(d) Apparent coupling field as a function of V_p.

Another practical application for the stability diagrams is the characterization of the joule heating on the magnetic properties of the devices. Indeed, the switching fields of the storage layer magnetization are not only reduced by the STT, but also by the rise in temperature induced by Joule heating during the application of the voltage pulses. Details on the theory behind the impact of this temperature rise can be found in chapter 2 subsection 2.23, showing the relation between the maximum temperature reached during the application of the voltage pulse, and the reduction of the MTJ electrode's magnetic saturation, effective perpendicular anisotropy, and spin polarization efficiency.

The storage layer magnetization is then submitted to both the STT and the Joule heating, and the balance between both phenomena will determine the main mechanism for reducing the device's switching fields. In our example, this can be observed in the diagram at higher absolute V_p values ($> |\pm 0.65V|$) and on the R-H loops at ±1V in Fig.3.14(b). Independently of the voltage polarity, both switching fields are reduced symmetrically and the R-H is shifted towards the stray field produced by the reference layer, reducing in this case, the apparent coupling field as the storage layer magnetization becomes softer against external magnetic fields (Fig.3.14(d)). This simple example for a single MTJ device shows the amount of information available with this kind of technique, being one of the most useful methods to characterize the heating and the STT effects on patterned devices. In our work, the fact that the ASL-DMTJ stack design includes several insulating barriers amplifies the Joule heating influence produced on both the ASL and SL comprising a coupled system. As seen in the ASL-DMTJ working principles, this can affect the SL switching and retention properties but also the ASL ability to act as a second polarizing layer. In this work, the stability voltage-field diagrams and their confrontation with simulations are utilized as a useful resource for the optimization of the device's magnetic properties at the patterned device level.

Chapter 4

Materials optimization of the Assistance layer and Storage layer coupled system

4.1 Materials optimization at thin film level

4.1.1 Single interface MgO/FeCoB based Assistance layer

Since its first observation in 2002 in Pt/CoFe/AlOx based half MTJ stacks [135], the interfacial perpendicular anisotropy between transition metals and the oxide tunnel barrier has been widely adopted as a way of obtaining out-of-plane easy axis on the in magnetic layers for spintronic devices. In 2010, the first reported p-MTJs devices of the form Ta/CoFe/MgO/CoFe/Ta showed a great combination of high tunnel magnetoresistance (120%), high thermal stability at 40 nm diameters and low switching currents (49 μA) of the free layer magnetization [33] [22]. In addition, all these advancements were achieved with materials compositions already used for in-plane MTJs, by finding the precise electrode thickness for the PMA to overcome the demagnetizing energy of the layer. For this reason, it rapidly became the standard structure to be used as a perpendicular free-layer electrode, thus paving the way for STT-MRAM technologies to achieve high density and performance. Within approximately ten years, important advances were made in order to further improve these properties. In general, both TMR and PMA are quite sensitive to the degree of oxidation of the metal/oxide interface and the crystal quality of the materials comprised in the MTJ. Therefore, the MTJ annealing procedure, the MgO oxidation conditions and the composition of the boron absorbing layers are critical for the modulation of these properties. These advances were mainly based on these last points; by varying the material composition of the electrode itself (E.g changing the relative percentage of Fe and Co in the alloy composition [120]), the nature of the metallic capping/insertion layers that absorbs the Boron from the FeCoB layer during annealing (E.g the use of Mo or W instead of Ta minimizing the atomic diffusion of the metal towards the MgO barrier [19]) or multiplying the electrode/oxide interfaces to increase its total surface anisotropy (E.g p-DMTJs sandwiching the free layer between two MgO barriers [75] [61] [136], or even Quad [137], Hexa and Octa interfaces [58]). Previous research has already established the main procedures to modulate and optimize the magnetic and spintronic properties of free layers for p-STT-MRAM. In the context of this thesis, the ASL and SL are fundamentally two free layers that are magnetically coupled across the tunneling barrier between them, and these strategies can be applied for the optimization of their individual PMA amplitude, magnetic coupling and spin-polarization efficiency. In this subsection we will focus on the initial optimization of the ASL perpendicular anisotropy based on a single-interface metal/FeCoB/MgO structure. As introduced in chapter 2 with the numerical investigations of the ASL-DMTJ working principles, for a correct operation of the device with voltage, an ASL with lower stability than the SL is required. In principle, since in our structure the SL is sandwiched between two tunnel barriers (MgO/FeCoB/metal/FeCoB/MgO), this condition can be easily obtained as two metal/oxide interface contributes to its effective PMA [61] while only one MgO/FeCoB interface contributes to the ASL PMA. Therefore, with a suitable combination of ASL and SL thickness, a higher PMA will be always induced on the SL magnetization than on the ASL [138]. In the following study, we will investigate the effect of varying the thickness of the magnetic electrode (i.e single-interface ASL) and its interfacial oxidation conditions on the resulting PMA after annealing. The composition of the sample consists of a half p-MTJ stack with the SL and RL as dead magnetic layers, the idea is to optimize the ASL PMA with out any other magnetic signal from the rest of magnetic layers comprised in the full stack. The composition of the sample is as follows: [Substrate/Ta 3/FeCoB 0.4/Mg 0.5(30s Oxidation 3x10^{-2} mbar)Mg0.7/FeCoB 0.2/Ta 0.2/FeCoB 0.2/Mg 0.5 (1s Oxidation 3x10^{-3} mbar)Mg ”y” wedge/FeCoB ”x” wedge/Ta 3], with the materials thickness in nm. Figure.4.1.(a) and (b) shows the coercivity and remanence data obtained by MOKE as a function of position on wafer with an external perpendicular field. The thicknesses of both RL and SL layers at 0.4 nm of FeCoB are chosen low enough to be magnetically dead after annealing. Two thickness gradients are introduced in the structure; One along the wafer ”x” axis direction with a gradient on the top FeCoB thickness (1.3 to 1.7 nm), and a second along the wafer ”y” axis direction with a thickness gradient on the Mg in direct contact with the FeCoB (Total MgO from 1 to 1.6 nm). The first gradient is intended to monitor the perpendicular anisotropy of the free layer as a function of its thickness. The second modifies the electrode/MgO oxidation conditions at the interface. This is achieved by varying the deposited Mg thickness while maintaining the same natural oxidation parameters (see chapter 3 section 3.1 ”MTJ and magnetic stack deposition”). The parameters of oxidation conditions were set at the minimum oxygen pressure and time (3x10^{-3} mbar for 1 s), corresponding to the minimum RxA obtained by CIPT in table.3.0 for a barrier thickness of 1.2 nm.

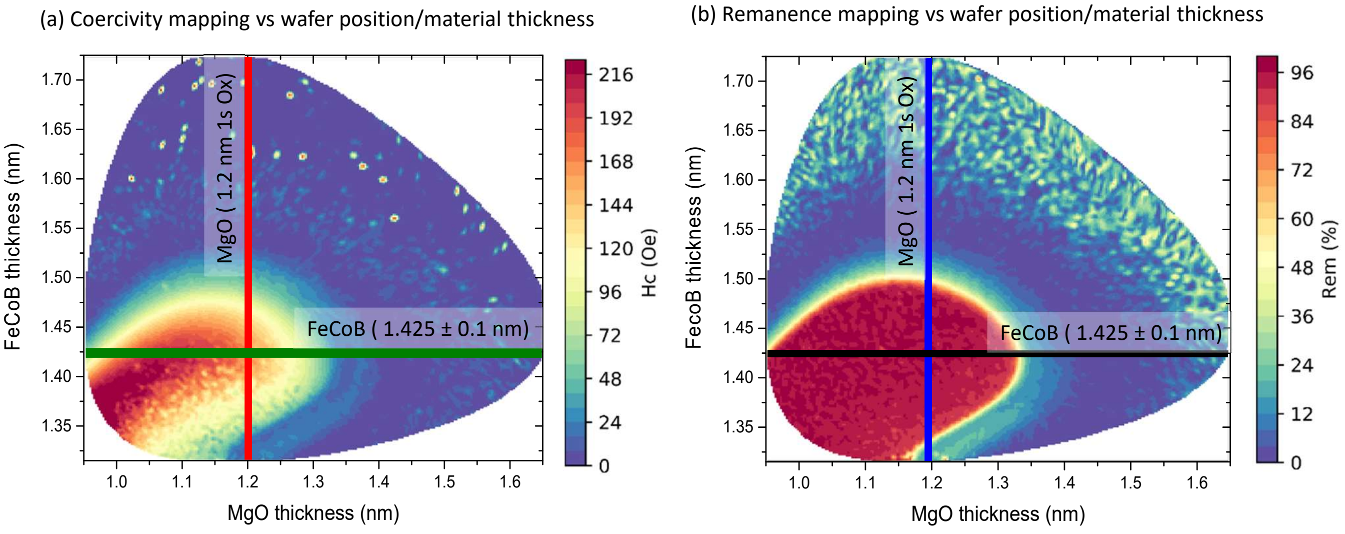

Figure. 4.1: (a) MOKE mapping of the coercivity vs FeCoB/MgO thickness with an external perpendicular field.(b) MOKE mapping of the remanence vs FeCoB/MgO thickness.

The tunnel barrier oxidation parameters were chosen considering that the top barrier RxA must be minimized for a reduction of the serial resistance in the full ASL-DMTJ structure. Samples were annealed under 10^{-6} mbar at 300°C without an external magnetic field for 10 minutes. From the mappings in figure.4.1, a clear region is observed at low thicknesses of both FeCoB and MgO wherein PMA arises after the annealing treatment with the coercivity of the FeCo layer reaching a maximum and the remanent magnetization being 100% of its value at saturation. Details on the MOKE technique as well as the measurement procedure can be found in chapter 3 section 3.3 "Magnetic properties characterization at thin film", and the same procedure is utilized to extract all the MOKE data discussed in this chapter. Important care must be taken when varying both the electrode and the barrier thickness. Indeed there is a direct correlation between the MgO thickness, the final PMA of the electrode and TMR of the junction. Nistor et al. reported the first study of these properties on natural oxidized MgO barriers [139]. They concluded that a good correlation exists between the thickness of MgO providing the highest TMR ratio and the electrode's interfacial anisotropy. In our studies, the impossibility at that moment to perform CIPT measurements did not allow the same correlation to be made. However, for the the oxidation conditions used, the maximum TMR value was known from our previous studies to be obtained for a thickness of 1.2 nm of MgO. For this value of barrier thickness, the variation of coercive field and remanence with the deposited FeCoB thickness of the electrode follows the trends shown in Figure.4.2 (corresponding to the Blue and red vertical lines in figure.4.1.(a) and (b)). Schematics of the material stack are also illustrated for a clear understanding of the layer under investigation and its interface with the oxide barrier.

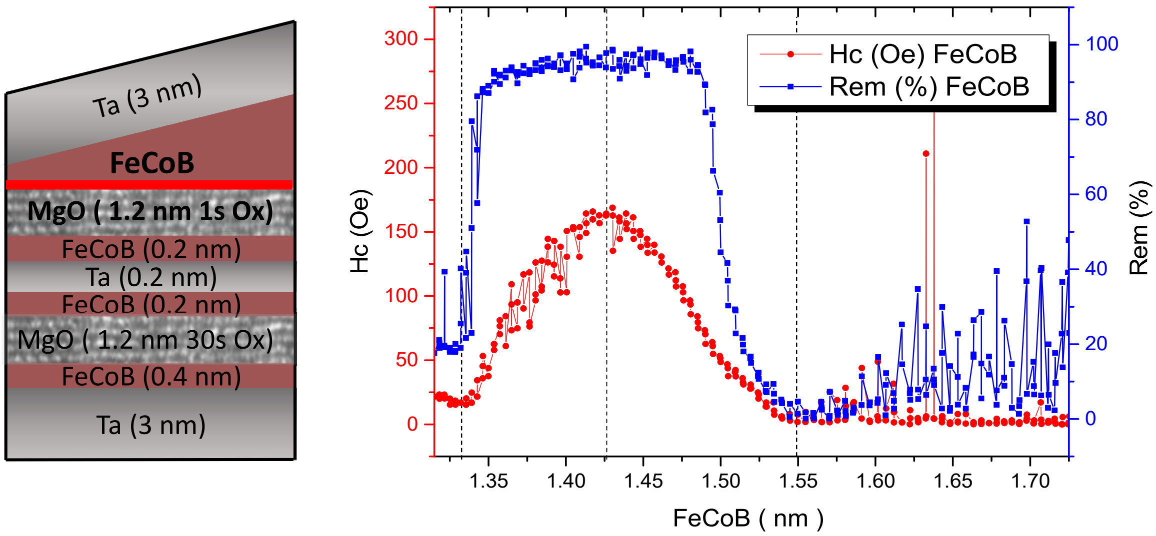
FeCoB wedge in ASL/SL half MTJ stack and Remanence/Coercivity vs FeCoB thickness

Figure. 4.2: (a) Stack schematics with respective materials thicknesses including a wedge on the the top FeCoB electrode and a constant MgO thickness of 1.2 nm.(b) Coercivity and remanence extracted of the FeCo layer as a function of its thickness after annealing at 300°C.

From the evolution of remanence and coercivity, one can determine the range of FeCoB thicknesses for which PMA arises after annealing. Therefore, for all deposited thicknesses presenting a 100% remanence (1.34 nm > t_{FeCoB} > 1.55 nm), the layer is perpendicularly magnetized. The maximum PMA is obtained at 1.425 nm where the maximum coercivity is reached. At thicknesses below this value, the PMA of the layer is gradually reduced due to the migration of Ta from the capping towards the FeCo/oxide interface [140].

The diffusion of Ta is also responsible for the creation of a magnetic dead layer, which at 1.34 nm of FeCoB, shows up as a drastic decrease of the ASL remanent magnetization and coercivity [141]. For thickness higher than 1.425 nm, the PMA of the layer decreases as the balance between the surface anisotropy (contribution to the effective bulk anisotropy varying inversely proportional to the layer thickness) and the shape anisotropy (which tends to align its magnetization in-plane) is modified. Over this range of thicknesses, the FeCo magnetization reorients and a crossover between perpendicular to easy-plane anisotropy is observed at a critical thickness of 1.55 nm. Above this value, the extracted remanence and coercivity are those from typical hard-axis hysteresis cycles, corresponding to an easy-plane magnetized M-H cycle with zero remanence and coercivity (Note that the noise in the remanence is an experimental artefact due to the lack of saturation with the external perpendicular field applied). As already introduced, the magnetic electrode PMA can also be modulated by modifying the FeCo/MgO oxidation conditions. Figure.4.3 shows the case of varying the MgO thickness for a constant deposited FeCoB thickness of 1.425 nm (Green and black horizontal lines in figure.4.1.(a) and (b)). In this case, the maximum coercivity values are obtained at a slightly lower thickness of MgO (1.1 nm), which can be ascribed to optimal oxidation of the deposited Mg. On the contrary, the FeCoB coercivity presents a parabolic decrease with increasing MgO thicknesses. This variation in PMA is caused by a remaining metallic Mg layer at the FeCo interface affecting the formation of Fe-O electronic bonds at the origin of the interfacial anisotropy [142] [139]. At MgO thicknesses above 1.35 nm, the PMA vanishes as no oxygen is able to reach the interface, thus causing the magnetization of the FeCo layer to fall in the samples plane.

MgO wedge in half ASL/SL MTJ stack and Remanence/Coercivity vs MgO thickness

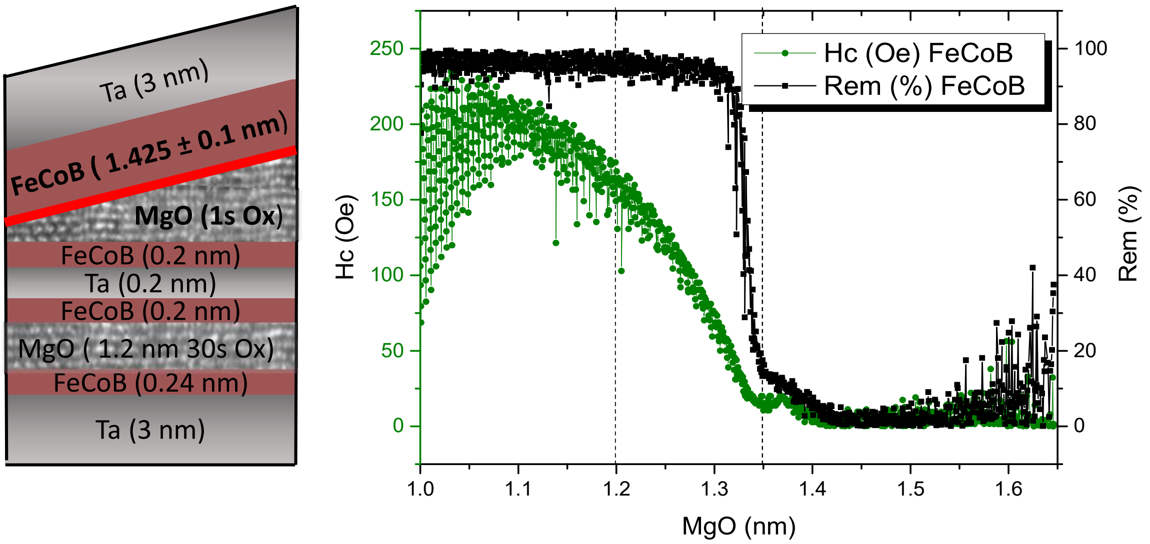

Figure. 4.3: Stack schematics with respective materials thicknesses varying the top barrier MgO thickness for a constant FeCoB thickness of 1.425 nm.(b) FeCoB layer coercivity and remanence as a function of MgO thickness after annealing at 300°C.

As already discussed, the TMR amplitude will also be influenced by these changes in oxidation conditions and barrier quality. However, it can provide other means for adjusting the thermal stability of the ASL magnetization. In fact, the structure investigated in this initial study is meant to optimize the ASL in our ASL-DMTJ structure so that it can be switched by STT from the SL and exhibit a weaker thermal stability than the SL one. This means that a suitable combination of barrier thickness providing the maximum spin polarization transmission (at 1.2 nm) and a relatively thick FeCoB layer (at 1.5 nm) will ensure enough PMA and switchable capability of the ASL magnetization (still perpendicular but with low thermal stability factor)[141]. In addition, minimizing the PMA of the ASL will also decrease its switching current by the spin polarized current from the SL. The results obtained in this initial study are later applied on full stacks in patterned devices for the first proof of concept of our device [93].

4.1.2 Double interface MgO/FeCoB/MgO based storage layer

In the previous section, the optimization of the ASL properties were discussed based on the use single-interface /MgO/FeCo. Concerning the SL, a larger anisotropy is required than for the ASL. One way to increase SL thermal stability factor is based on the use of two metal/oxide interfaces in free layers of the form MgO/FeCoB/metal/FeCoB/MgO. These kind of structures lead to an important improvement in the effective perpendicular anisotropy of the magnetic layers (Considering that $K_{eff}=2K_s/t -\frac{1}{2}\mu_0 M_s^2(N_x - N_z)$) [143] [144]. The first applications of these structures were found in p-MTJs for STT-MRAM cells as a way of increasing the thickness of the free layer without reducing their net PMA. This allowed to enhance the TMR amplitude and improve the downsize scalability of STT-MRAM cells [61] [138]. This concept can also be used in double MTJ [76], considering that the free layer magnetization is de-facto sandwiched between two tunnel barriers. This allows realizations of p-DMTJ structures [141] [78]. As already mentioned, the same principle can be applied in our ASL-DMTJ in order to provide the SL with a higher thermal stability factor than the ASL one. In this kind of double-interface free layers, as for the ones with a single-interface, three main critical parameters control the final PMA of the electrode at full sheet film; the relative thicknesses of the two FeCoB layers, the composition and thickness of the metal insertion in the middle, and the annealing temperature. Figure.4.4 illustrates the double-interface free layer stacks compositions investigated in this section, also refer as composite free layers. The detailed description of the deposited stacks is: [Substrate/Ta 3/FeCoB 0.4/Mg 0.5(30s Oxidation 3×10^{-2} mbar)Mg 0.7/FeCoB "x" wedge/Ta or W 0.2/FeCoB "y" wedge/Mg 0.5 (1s Oxidation 3×10^{-3} mbar)Mg 0.7/FeCoB 0.4/Ta 3] and (thickness in nm). The only variation between the samples compositions concerns the nature of the nonmagnetic insertion layers (Either Ta or W).

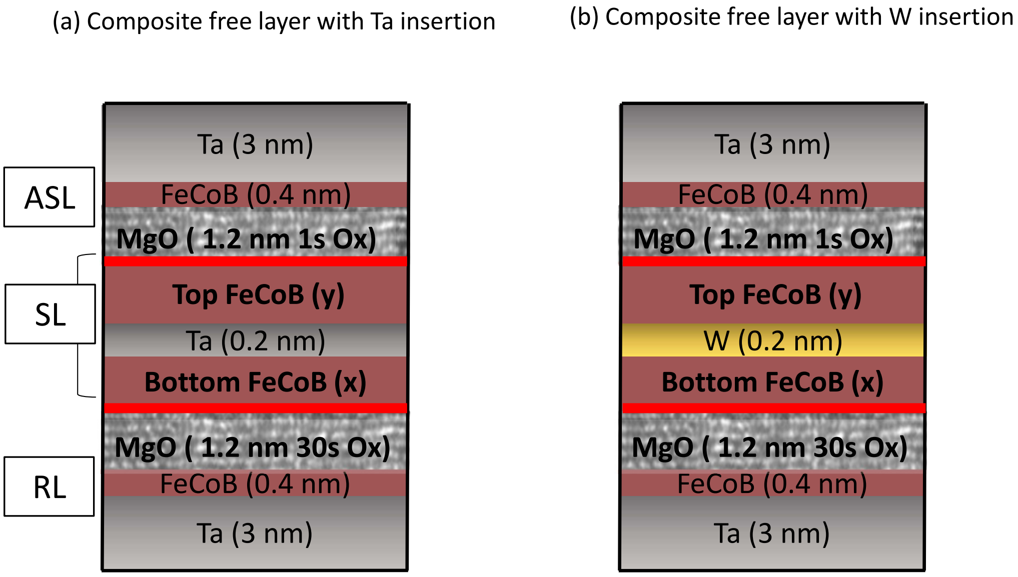

Figure. 4.4: Composite free layer stack schematics varying the deposited thickness of top and bottom FeCoB ferromagnetic layers; (a) with Ta insertion layer and (b) with W insertion layer.

The purpose of this metallic insertion is twofold: to attract the Boron during the post-deposition annealing treatment and maintain a strong ferromagnetic coupling between the two FeCoB layers. Hence, its composition and thickness control respectively the final achievable annealing temperature [111] [145], and the strength and nature of the coupling [141] [146] (ferromagnetic or anti-ferromagnetic).

In both samples, the top and bottom FeCoB layers are deposited with a cross-wedge with the same thickness gradient (0.55 nm to 1.05 nm), along the "x" direction of the wafer for the bottom FeCoB, whereas along the "y" direction for the top one. The Ta and W insertion layers are kept at a thickness of 0.2 nm, which corresponds to the minimum thickness that ensures a good combination of ferromagnetic exchange coupling, Boron absorption capabilities [111] and low damping for the highest STT switching efficiency [147]. The ASL and RL with 0.4 nm thickness are rendered non-magnetic after annealing since in this section we focus on the SL properties. The first tunnel barrier in the half-MTJ stack RL/Bottom-FeCoB is prepared under high pressure (3x10^{-2} mbar for 30 s) resulting in higher TMR (80 %) and RA (10 Ωμm2) for 1.2 nm of MgO. On the contrary, the top barrier in the half MTJ stack top-FeCoB/ASL is prepared with low pressure and shorter oxidation time (3x10^{-3} mbar for 1 s) minimizing its RA (1.2 Ωμm2) at expenses of TMR (20 %). As shown by Cuchet et al [141], the different natural oxidation conditions of the barriers should not have a noticeable impact on the PMA for each FeCoB/MgO interface, but only on the final electrical properties when utilizing these structures in full p-MTJs stacks. This is due to the fact that in underoxidized junctions, the oxygen tends to migrate to the FeCoB/MgO interface upon annealing so that the interfaces become stoichiometric while the bulk of the barrier tends to get depleted in oxygen. The values of coercivity and remanence for the two sample stacks presented in Fig.4.4, are shown in the MOKE mappings in Fig.4.5.(a) to (d) for 300°C annealing and all the combinations of top and bottom FeCoB thickness.

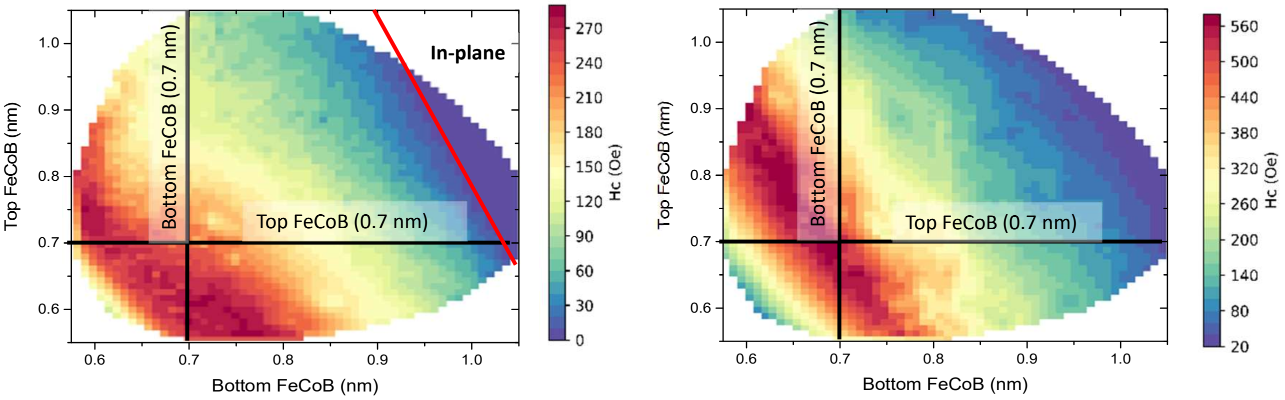
(a) Coercivity mapping annealed at 300 °C with Ta insertion

(b) Coercivity mapping annealed at 300 °C with W insertion

(c) Remanence mapping annealed at 300 °C with Ta insertion

(d) Remanence mapping annealed at 300 °C with W insertion

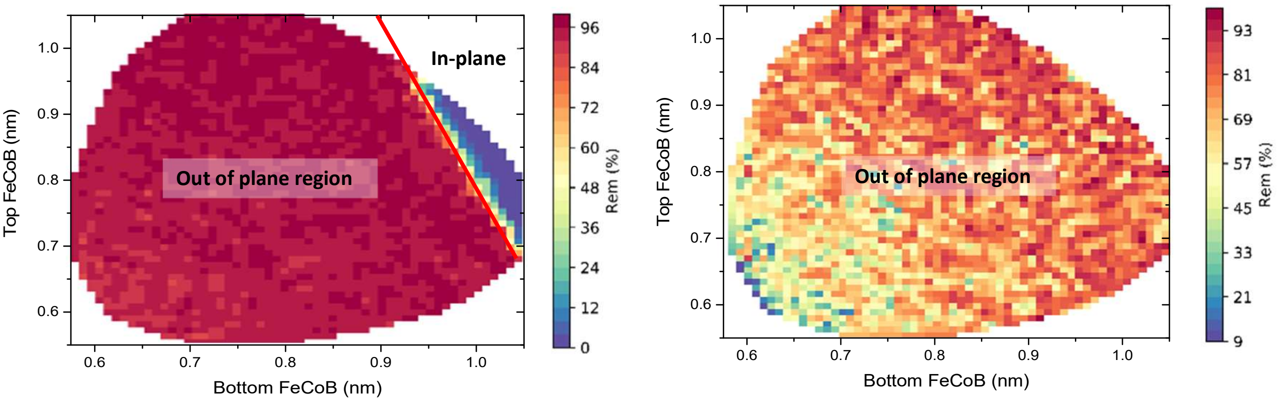

Figure. 4.5: Coercivity mapping extracted from samples in figure.4.4.(a) with Ta insertion and (b) W insertion after 300 °C annealing. (c) and (d) remanent magnetization mapping extracted for the same samples as in (a) and (b).

We will start by comparing the coercivity values obtained from the composite free layer with Ta insertion against the single interface at the same annealing temperature (300 °C). At a total thickness of 1.4 nm (with top and bottom FeCoB at 0.7 nm as indicated in Fig.4.5.(a)) the coercivity has practically doubled from 125 Oe for the single interface (Fig.4.2) to 240 Oe for the double interface. These enhancements in coercivity can be ascribed to a direct increase in the effective perpendicular anisotropy of the free layer [146] [111]. Then, if the top FeCoB layer is kept at 0.7 nm, the bottom must be increased up to 1.1 nm to enter the in-plane region (total critical thickness of 1.8 nm). With the use of composite free layers, the final PMA of the free layer is enhanced, almost doubling the coercivity for equal thicknesses and rising the critical thickness by 0.25 nm for the transition to in-plane anisotropy. Further enhancements in PMA can be achieved by using a refractory metal such as tungsten as an insertion layer [111] [125] [148]. In this case, for the combination of FeCoB thicknesses discussed above (1.4 nm), the coercivity obtained after 300 °C annealing reaches 500 Oe. This represents a 100% increase with respect to the composite free layer with Ta insertion. The improvement in interfacial anisotropy that W brings is due to the high mechanical stiffness of this metal considered as being refractory. This stiffness prevents the diffusion of the W atoms towards the MgO interfaces during the annealing treatment thus yielding a higher PMA on both FeCoB layers. Moreover, for all the combinations of thickness explored, no in-plane region appears for the sample with W insertion (Remanent magnetization at 100 % all over the wafer in Fig.4.5.(d)). On the other hand, Figure.4.6.(a)-(d) shows the stacks PMA regions vs FeCoB thickness, from the MOKE mappings extracted after 400°C annealing.

(a) Coercivity mapping annealed at 400 °C with Ta insertion

(b) Coercivity mapping annealed at 400 °C with W insertion

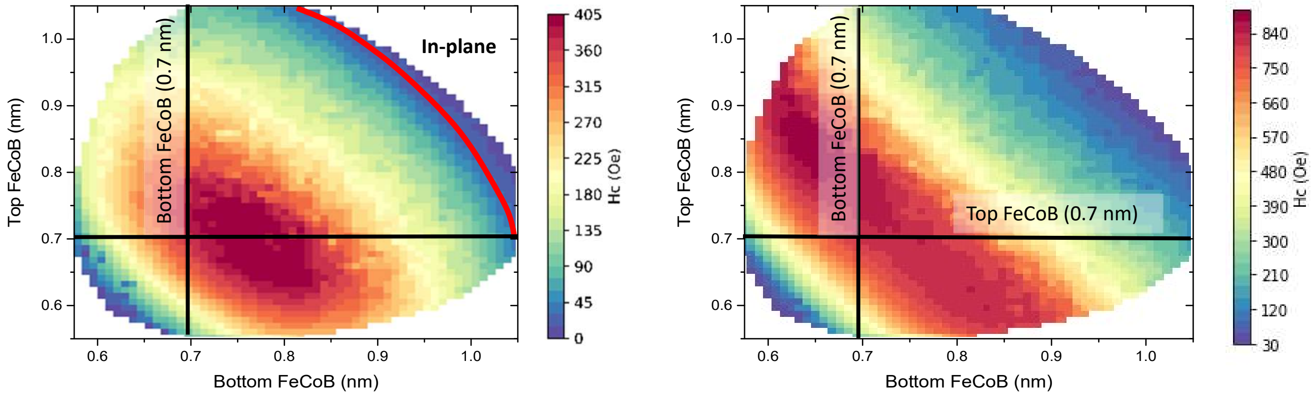

(c) Remanence mapping annealed at 400 °C with Ta insertion

(d) Remanence mapping annealed at 400 °C with W insertion

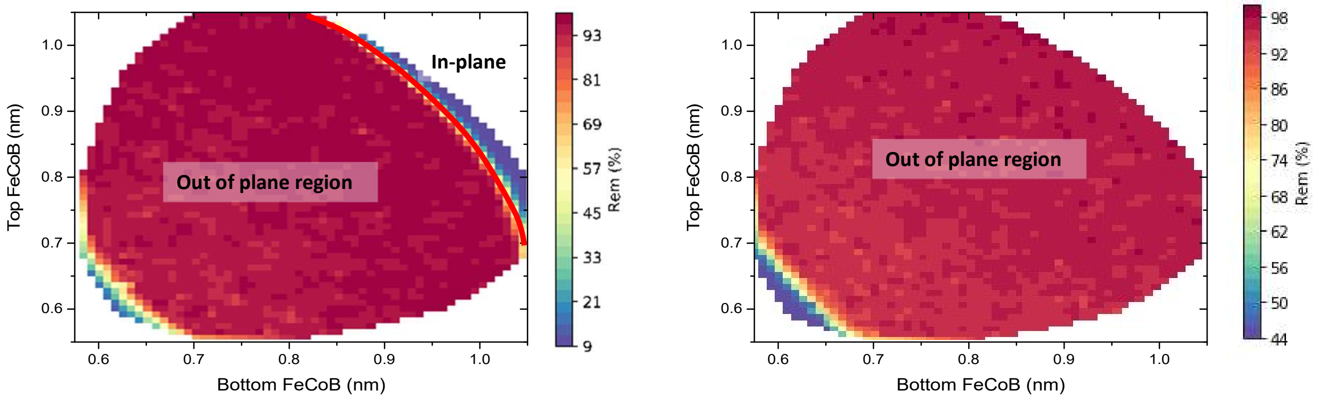

Figure. 4.6: (a)-(b) Coercivity and (c)-(d) remanent magnetization mappings extracted for samples with composite free layer as in figure.4.5 after 400 °C annealing.

Comparing to the previous magnetic properties mappings, both composite layers present increased values of coercivity upon annealing at 400°C, with a shift of the maximum PMA regions towards higher thickness of FeCoB. The remanent magnetization mappings clearly show that the stacks have a perpendicular magnetization practically for all FeCoB thicknesses in the wafers. Upon annealing at higher temperatures, the stack with W insertion layer, once again outperforms the one with Ta, reaching a coercivity of the FeCoB layers of up to 900 Oe, compared to 405 Oe for the one with Ta. These results are in agreement with a variety of works related to this kind of double MgO interface free layers [148] [145], and acknowledge the main strategies utilized in this thesis to tune the storage layer effective anisotropy in our device concept. The thermal robustness that W provides to the stack at 400°C annealing is not only important to achieve high PMA values of the free layer magnetization. The higher ranges of FeCoB thickness and amplitude of the PMA regions discussed at different annealing temperatures are in direct correlation with a better quality of the interfaces. Furthermore, the possibility to reach 400°C anneal will result in better crystal quality of the tunnel barriers and electrodes and therefore higher TMR amplitude [148] [111]. In addition, both stack compositions are Back End Of the Line compatible with the CMOS process (BEOL). However, despite the benefits provided by W insertion in the SL in terms of TMR and PMA, composite free layers incorporating W are also known to yield higher Gilbert damping of the free layer magnetization, which will affect its critical current to switch by STT [149]. The two subsections discussed above, based on measurements at wafer levels, presented the main materials parameters in terms of composition and variable thickness of the ASL and SL ferromagnetic layers that could be introduced in our stack to modulate the relative thermal stability between the ASL and the SL. The final thickness and composition of both layers will be based on the results obtained with these mappings in patterned devices which will be discussed in section 4.2.

4.1.3 ASL/SL coupling through low oxidation MgO tunnel barriers

During the development of the first magnetic tunnel junctions based on AlOx tunnel barriers, apart from studies based on the understanding and control of its transport properties [150] [151], researchers also addressed the existence of an indirect exchange coupling between the two ferromagnetic electrodes [152]. With the next generation of MgO-based junctions, extensive studies on this phenomenon followed, showing the dependency of the coupling amplitude with the barrier thickness [153] [154] [155]. These studies were based on experimental results obtained on epitaxial in-plane MTJs. Their findings were in good agreement with previous theoretical models developed by Slonczewski [156] and Bruno [157] [158], which rely on the quantum mechanical tunneling of electrons between the magnetic electrodes through the tunnel barrier, and assumed to be perfectly homogeneous with ideally flat interfaces. In experiments, and in particular sputtered MTJs, the crystal quality is not ideal, the deposited layers grow with a certain roughness. In this case, a Néel coupling can arise from the dipolar interactions between magnetostatic charges which appear on both barrier interfaces due to their correlated roughness [152]. This Néel coupling always favors parallel magnetic alignment in the two adjacent magnetic electrodes in the case of in-plane magnetized MTJs. The Néel coupling model was later adapted to perpendicular MTJs with the work of Moritz et al [159], reporting a change from ferromagnetic to anti-ferromagnetic coupling depending on the effective anisotropy of the electrodes. As was just presented, different results in the literature point to multiple origins for the indirect exchange coupling observed in MTJs. Nistor et al tried to clarify this issue in fully perpendicular and sputtered MTJs, giving the main experimental evidences to differentiate between them [160]. Their results suggest that one can determine the source of the coupling by looking into its sign and dependence with the electrodes/barrier thickness. In this section, we will discuss the theoretical models, and applied them to identify the nature of the coupling observed as a function of the barriers oxidation conditions and thicknesses of the free layer electrode and barrier. The following discussion will only focus on experimental data obtained at full sheet film, so no magnetostatic coupling between uncompensated stray fields generated by the electrodes is possible. We will start first with a brief overlook of the main theoretical models explaining each of the origins of the interlayer coupling through an insulator barrier. Then, based on the predictions given by these models, and supporting our results with previous works reported in similar p-MTJ structures, we will try to give an general picture of the main mechanism behind the interlayer coupling through the low oxidation barrier utilized in our ASL/SL coupled system.

Bruno's theory on interlayer coupling through quantum interference:

For simplicity, we will center on the model proposed by Bruno. In his model, the coupling between the electrodes sandwiching the tunnel barrier is ascribed to quantum interference of their tunneling electron waves [157]. These reflections are mediated by the spin polarization of the electrons (either spin up or down) in the electrodes interfaces with the barrier. The resulting indirect coupling through the tunnel barrier depends on both the spacer thickness and the ferromagnetic layer. Figure.4.7 shows the variation of the amplitude and sign of this coupling with the spacer and the ferromagnetic layer thickness respectively. For spacer thickness between 2 and 1 nm, the coupling is anti-ferromagnetic and increases exponentially with decreasing spacer thickness. The ferromagnetic regime is only reached for extremely low spacer thickness, which experimentally, would not be possible to distinguish from one caused by the direct exchange of the ferromagnetic electrodes through pinholes. One of the most important aspects of this model is the prediction of an oscillatory variation of the coupling amplitude with the magnetic electrode thickness [158]. These dependencies were later investigated by Lavinia Nistor in her thesis [161] as a function of barrier thickness on SAF/CoFeB/MgO/CoFeB structures and on Co/MgO/Co electrodes with tunnel barriers prepared by natural oxidation (see Figure.4.8(a) and (b)). On one hand, she reported an anti-ferromagnetic coupling in both structures. In the SAF/CoFeB/MgO/CoFeB pMTJ, the coupling was ascribed to roughness induced Néel coupling, which will be covered in the following subsection.

This was supported by the fact that the coupling was decreasing with the annealing temperature, as the crystal quality and interfaces where improved. On the other hand, for the case of the Co/Mg/Co system, they evidenced the oscillatory behaviour predicted in Bruno's model, in which the coupling is anti-ferromagnetic for spacer thickness higher than 1 nm and oscillates with the thickness of the electrodes.

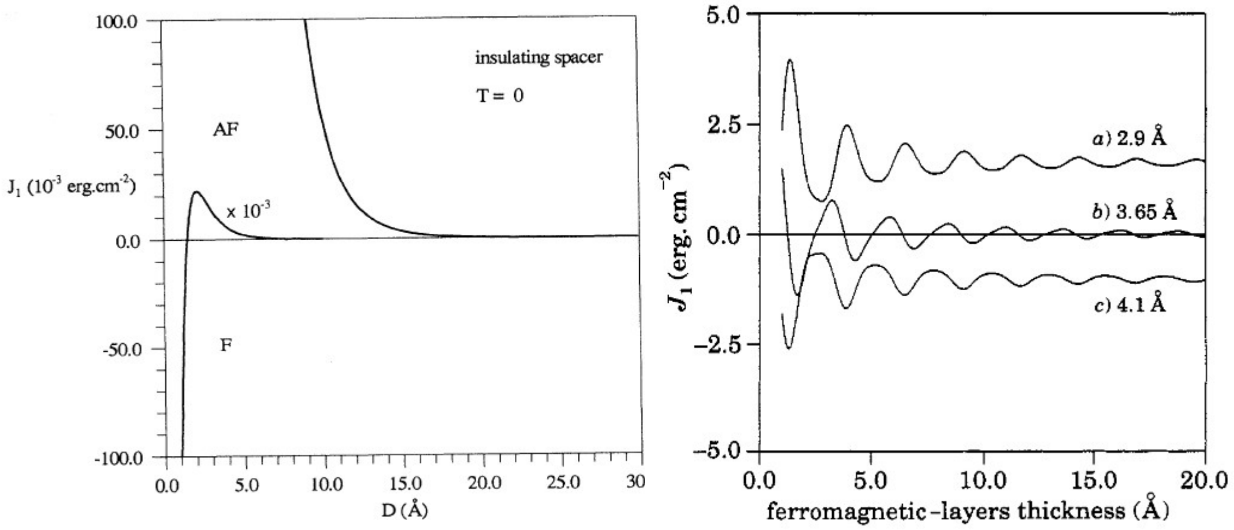
Bruno's quantum interference coupling model

Figure. 4.7: Bruno's model predictions for the indirect exchange coupling through an insulator as a function of the spacer thickness and the ferromagnetic electrode. Images were taken from [157].

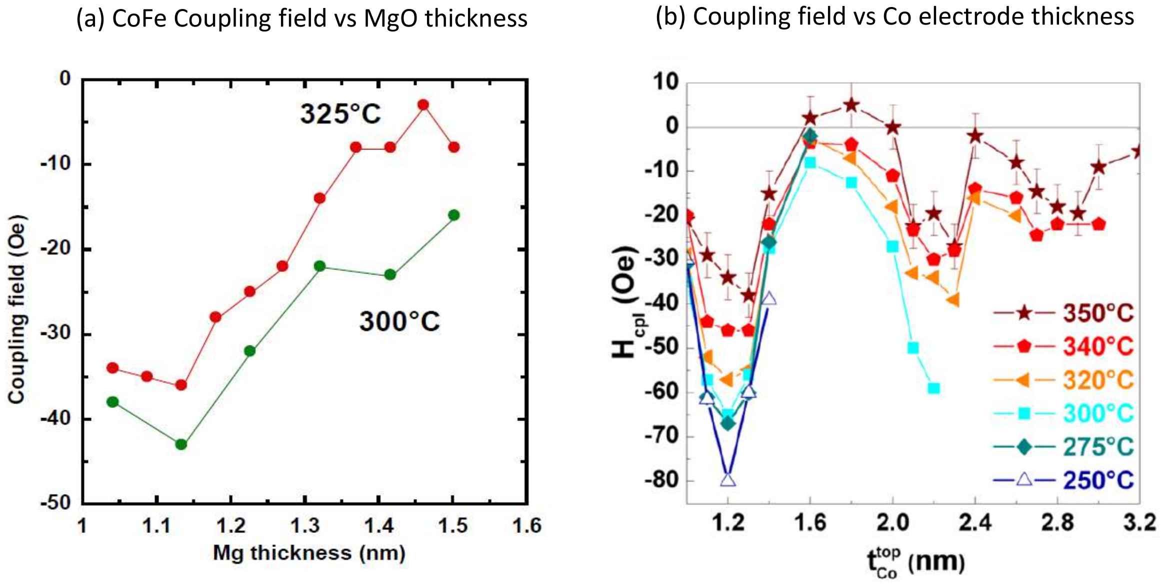
(a) CoFe Coupling field vs MgO thickness

(b) Coupling field vs Co electrode thickness

Figure. 4.8: (a) Experimental variation of the coupling field vs MgO thickness after annealing at 325°C and 300°C for a SAF/CoFeB/MgO/CoFeB pMTJ structure. (b) Experimental variation of coupling field vs Co electrode thickness for a Co/MgO/Co structure. Images were taken from cite [161] and [160].

Neel's and Moritz's theory on interlayer coupling through dipolar interactions:

As already introduced, other models describe the indirect coupling through a spacer by means of magnetostatic coupling interactions between the two ferromagnetic layers. Louis Néel was the first to propose the idea that layer-to-layer correlated waviness of the magnetic layers can produce a periodic accumulations of magnetic charges at the successive interfaces, causing local dipolar interactions [162]. Also known as orange-peel coupling, this phenomenon was first measured experimentally in in-plane magnetized MTJs layers through an AlOx barrier [152]. This type of coupling, was found to be ferromagnetic. Equation.4.1 expresses the orange-peel coupling model for a sandwich structure of the form fixed magnetic layer-1/non-magnetic spacer/free magnetic layer-2. Here, t_f, M_s are the thickness and saturation magnetization of the layers, h and λ are the amplitude and wavelength of the surface roughness and t_s the spacer thickness. From this definition, the coupling field produced by the fix layer magnetization decreases exponentially with the spacer thickness.

$$H_{coupling} = \frac{\pi^2}{\sqrt{2}}(\frac{h^2}{\lambda t_f})M_s exp(\frac{-2\pi\sqrt{2}t_s}{\lambda}) \tag{4.1}$$

Later, Moritz et al extended the model to multilayers with perpendicular anisotropy and applied it to experimental data on Co/Pt/Co multilayers [159]. Their study concludes that the sign of the coupling strongly depends on the strength of the PMA of the layers. Their findings are summarized in figure.4.9, where the relationship between the sign of the coupling and the uniaxial anisotropy constant of the layers can be seen. For low values of perpendicular anisotropy, the local magnetization is able to relax and follows the localized opposite dipolar charges generated at the interfaces. On the contrary, for high perpendicular anisotropy, the local magnetization remains parallel to the local normal to the surface, generating equal charges on both interfaces and leading to an anti-ferromagnetic coupling.

Moritz et al. Néel coupling in multilayers with perpendicular anisotropy

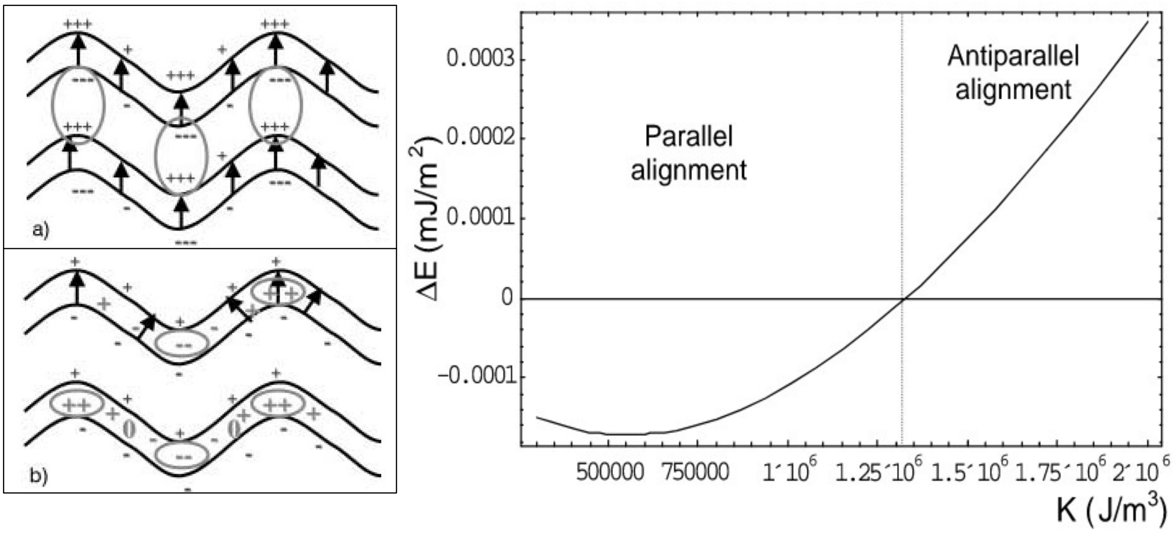

Figure. 4.9: Localized magnetic charges arising on the surface waviness between two perpendicular ferromagnetic electrodes for (a) low perpendicular anisotropy and (b) high perpendicular anisotropy and coupling energy as a function of effective perpendicular anisotropy constant. Images adapted and taken from [159].

Experimental investigations of the interlayer coupling through low oxidation MgO barriers:

In order to investigate quantitatively the strength and dependency of the indirect exchange-like coupling utilized in our ASL/SL coupled system, the clearest way to investigate this phenomenon at full sheet film level is with the stack composition shown in Fig.4.10. The composition is similar to the one deposited to characterize the variations in PMA of the single-interface free layer electrode as a function of tunnel barrier oxidation conditions. In this study, the idea is to grow a full p-MTJ structure with a fixed layer at the bottom and evaluate the coupling field of the top FeCoB free layer from its magnetic response under an applied perpendicular field. An example of the procedure to extract this coupling field is also presented in Fig.4.10, where the shifts on the hysteresis loops of the free layer magnetization at various MgO thicknesses can be observed. Hereafter, all measurements presented in this section were performed with MOKE after annealing the sample at 300°C for ten minutes. The detailed description of the full p-MTJ stack is the following : [Substrate/Ta 3/Pt 25/(Co 0.5/Pt 0.25)x6/Ru 0.9/(/Co 0.5/Pt 0.25)x3/Co 0.5/Ta 0.2/FeCoB 1.2/Mg 0.5(1s Oxidation 3x10^{-3} mbar)Mg "x" wedge /FeCoB 1.5/Ta 3] with thickness in nm. The fixed layer of FeCoB is exchange coupled through a thin metallic insertion of Ta (0.2 nm) to a Co/Pt multilayer SAF structure with strong PMA. The SAF structure is based on 3 and 6 repeats of Co/Pt multilayers that are exchange-coupled via RKKY coupling through a 0.9 nm Ru spacer. This SAF structure is not necessary to study the indirect coupling through the MgO barrier but is used to reproduce to some extend the same growth conditions as for the stacks used in the nano-fabricated devices. The MgO barrier oxidation conditions are set at the minimum pressure and oxidation time with a thickness wedge on the Mg in contact with the free layer FeCoB ranging from 1 to 1.45 nm.

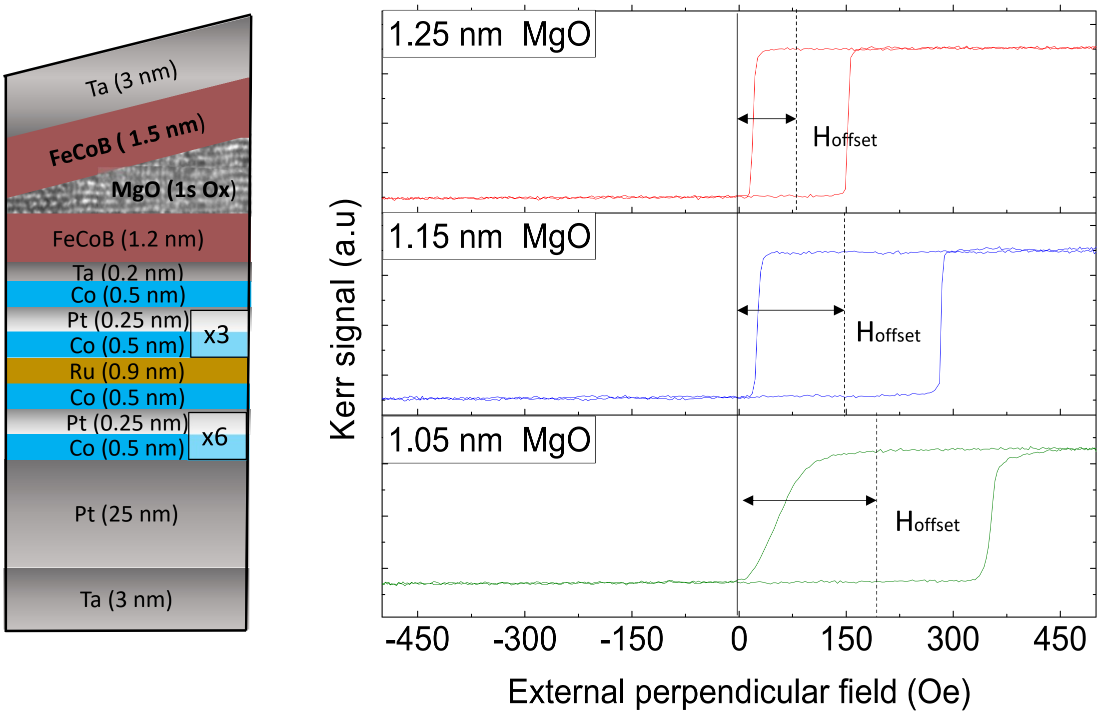

Figure. 4.10: Illustration of the material stack employed for the investigation of the indirect exchange coupling through low oxidation parameters MgO barrier as a function total MgO thickness in the interface. Examples of the coupling field extraction at various final MgO thicknesses after annealing at 300°C.

As concluded in the first section of this chapter, the FeCoB with 1.5 nm is the most suitable for an ASL with low perpendicular anisotropy, providing the best trade-off between reduced thermal stability and TMR for a MgO tunnel barrier of 1.2 nm. Before measuring the sample, the SAF is saturated in such a way that the magnetization of the fixed layer points in the opposite direction to the applied positive fields, meaning that positive coupling fields indicate a ferromagnetic coupling between the electrodes. It was shown in previous sections, that a wedge on Mg thickness leads to the simultaneous variation of the final MgO thickness and of the oxidation conditions at the interface, hence affecting the final achieved PMA amplitude of the free layer's magnetization. Figure.4.11.(a) shows the dependency of measured coercive fields and remanences for the p-MTJ stack introduced above (Fig.4.10). As in the previous case, the perpendicular anisotropy peak is at values slightly below the optimum barrier thickness (1.2 nm at the highest TMR). At low interfacial Mg thicknesses (below 1.12 MgO), an over-oxidation of the FeCo free layer explains the reduced values in coercivity and the remanence drop at 1 nm. In contrast, above the MgO thickness corresponding to the peak of perpendicular anisotropy, the coercivity gradually decreases due to an under-oxidation of the interface.

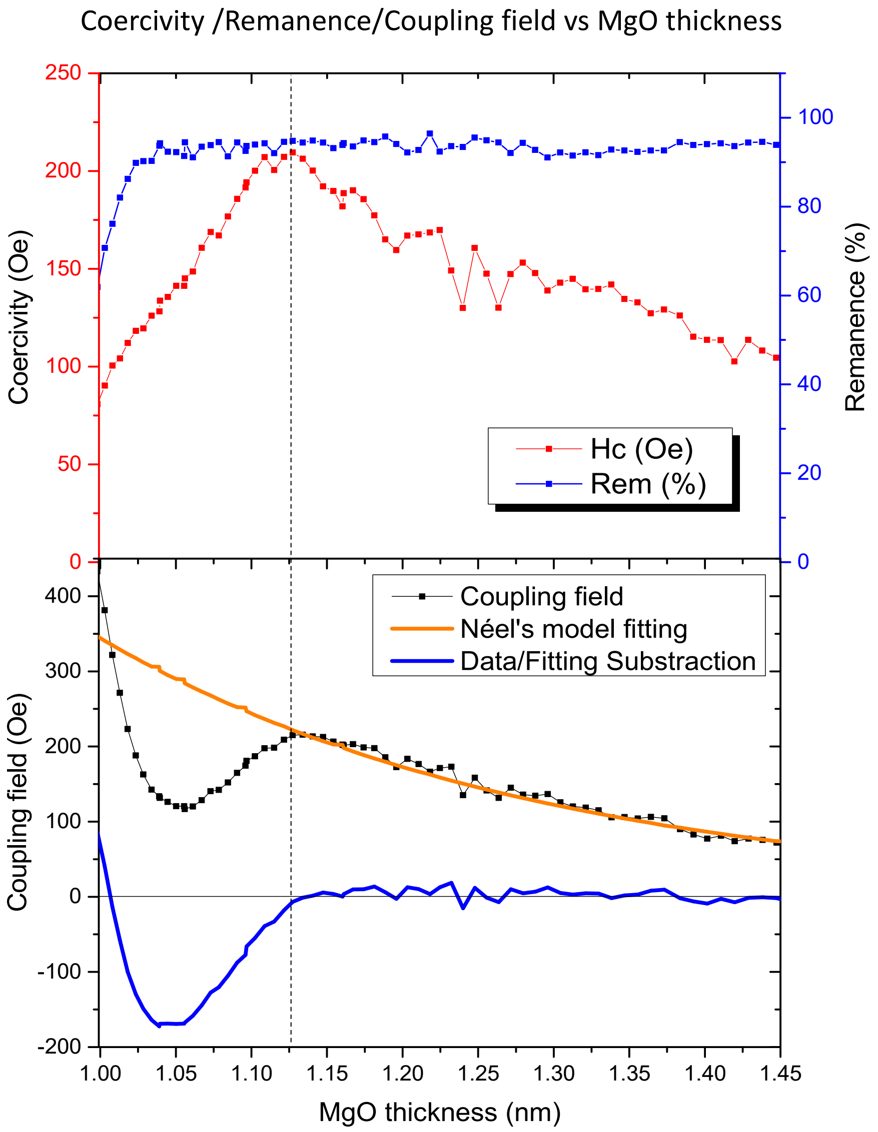

Figure. 4.11: Comparison between coercivity, remanent magnetization, and coupling field vs low oxidation MgO thickness and fitting of the exponential dependence predicted by Neél's model with the barrier thickness.

Figure.4.11.(b) shows that the barrier quality has also an impact on the indirect coupling strength. For all the thickness of MgO investigated, the extracted coupling fields between the electrodes clearly suggest that the coupling is ferromagnetic. This is in direct correlation with the extended orange-peel model proposed by Moritz et al. between perpendicular electrodes (under the condition of weak perpendicular anisotropy). Furthermore, this statement is also supported by the fit of the experimental data with Néel's model (Eq 4.1), in which the coupling amplitude decreases exponentially with spacer thickness, resulting on fitted parameters for the surface roughness of λ = 3 nm of wavelenght and h = 2.7 nm in amplitude. Note that the fitting is only valid for the barrier thickness above 1.12 nm, where the electrode's magnetic saturation is constant. In fact, the over-oxidation of the free layer can lead to the formation of an oxide layer that might be or not magnetic. Results obtained on epitaxial Fe/MgO/γ-Fe_2O_3 structures presented an antiferromagnetic coupling with a ferrimagnetic iron oxide phase [163], which could lead as well to a reduction of the ferromagnetic coupling in our sample. In any case, the total thickness of FeCo and Ms is reduced, which could explain the reduction of the coupling field from 1.12 to 1.05 nm of MgO thickness and the failure of the model to fit the experimental data. On the contrary, from 1.05 nm upwards, the coupling field increases dramatically, reaching 400 Oe at 1 nm spacer thickness. This rapid exponential increase was also predicted by Bruno's model for extremely thin insulating spacer thicknesses. However, in this case, it is likely due to the formation of pinholes through the barrier, leading to a direct ferromagnetic coupling between the electrodes. Similar results were obtained by Lavinia Nistor on low anisotropy structures of the form Ta 5/CoFeB 1/MgO/CoFeB 1.6/TbCo/Pt 2, concluding that the coupling mainly originates from the surface roughness induced with natural oxidized MgO barriers, and in agreement with Moritz's extended orange-peel coupling model. To fully characterize this indirect coupling, the next step was to investigate its dependence with both barrier natural oxidation parameters and free layer thickness. Indeed, if the surface roughness is induced by the natural oxidation parameters of the barrier, and this is responsible for the observed ferromagnetic coupling between the electrodes, it is necessary to determine under which conditions it is maximized or minimized. On one hand, the ferromagnetic coupling in parallel alignment can be employed to increase the amplitude of the coupling for the SL/MgO/ASL system, which in fact is the main source of SL thermal stability enhancement with our ASL-DMTJ concept. On the second hand, this coupling must be avoided in the case of the MTJ between the SL and the RL. If not avoided, the low resistance state (parallel alignment) will be favored in the main barrier storing the information, leading to a higher critical current to switch the SL magnetization for the P to AP transition. Figure.4.12 illustrates the stack composition used for the samples as well as the coercivity and coupling field obtained from the free layer hysteresis loops at different positions of the wafer (i.e deposited FeCoB thickness). The stack composition is similar to the one used in the previous study on the coupling field dependence versus spacer thickness. This time, four samples were deposited with a constant barrier thickness of 1.2 nm and different oxidation conditions (see table3.0): Two samples with longer oxidation time and higher pressure (30 s and 10 s with $3x10^{-2}$ mbar) and two others with shorter oxidation time and lower pressure (5 s and 1 s with $3x10^{-3}$ mbar). To determine the dependence of the coupling amplitude on the thickness of the top electrode, a wedge of FeCoB was deposited covering the entire PMA thickness range for a single interface free layer (From 1.4 to 1.6 nm). As seen from the coercivity values vs FeCoB thickness in Fig.4.12, the four barriers oxidation parameters lead to similar values of maximum coercivity (between 135 to 160 Oe). However, a clear shift in the values of FeCoB thickness at which the PMA arises is observed. These changes in thickness ranges can be explained by either variations in the boron diffusion during the annealing, or an increased over-oxidation of the interface for higher oxidation times (Note the shift towards higher thicknesses to acquire the same PMA in the FeCo layer for the barrier with 30 s of oxidation).

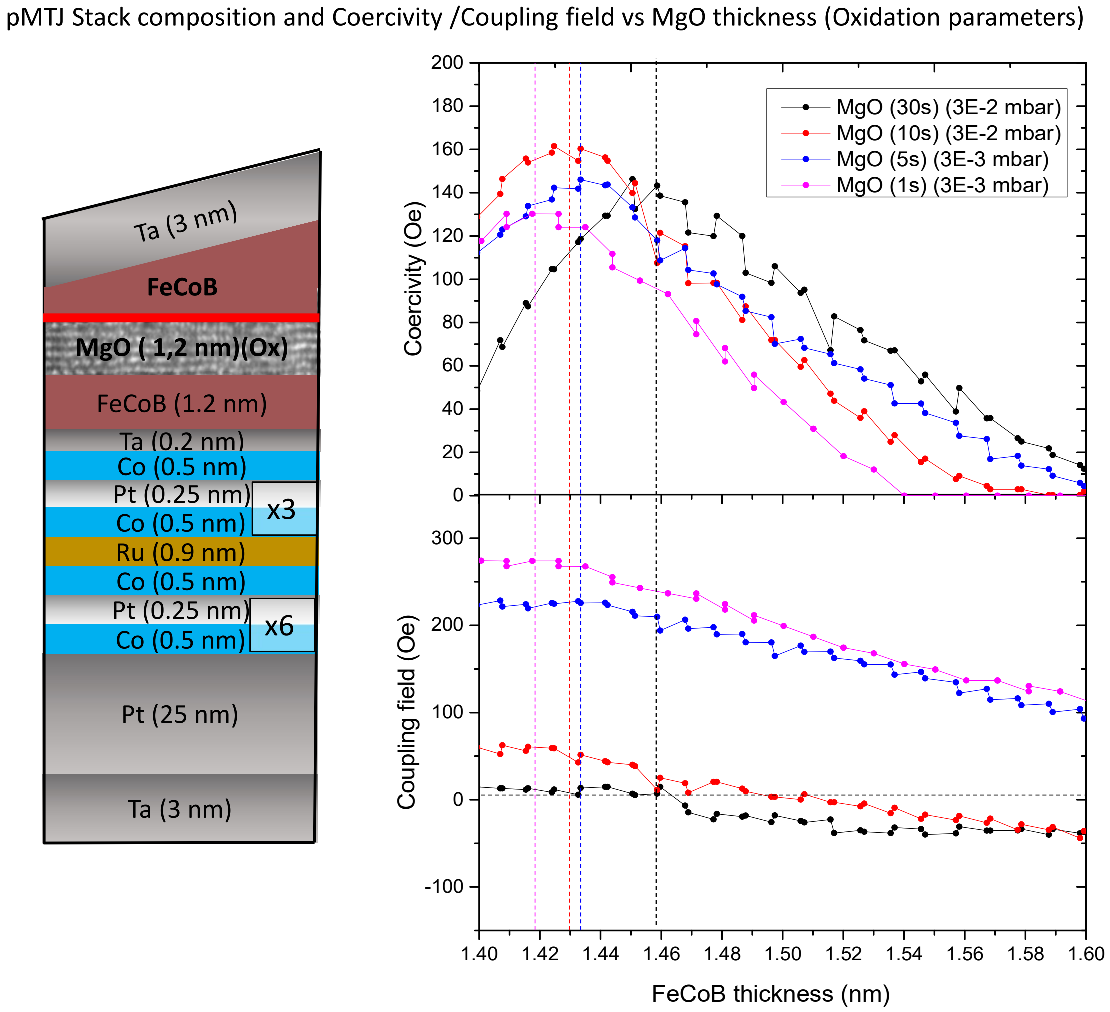

Figure. 4.12: Illustration of the stack composition employed to investigate the indirect coupling dependence at different barrier oxidation parameters. Comparison between coercivity (i.e PMA dependent) and coupling field obtained by MOKE as a function of the FeCoB free layer's thickness at constant MgO barrier thickness and several oxidation conditions.

The results concerning the coupling field show a direct impact of the natural oxidation parameters of the barriers on the interfacial roughness of the electrodes upon annealing. The barriers with the short oxidation times and low pressures present a strong coupling at thin-film level, decreasing linearly with the free layer thickness. In comparison, this coupling practically disappears for barriers with higher oxidation and even changes of sign at increasing FeCoB thickness. The reduced values of coupling fields obtained for the samples with the stronger oxidation indicate a better quality of the barriers, which at the same time will result in smoother interfaces and higher TMR ratios. The exact reasons behind the rising coupling strength in the p-MTJs with weaker natural oxidation parameters are not fully determined. From a simplistic approach, looking to Neel's model, the generated coupling field on the magnetization of the free layer depends on a sinusoidal roughness of the interfaces. The coupling would then be higher for thinner spacers or for a greater amplitude of the surface oscillations. The low oxidation times and pressure might affect the final oxygen content in the barriers, which at the same time leads to the reduced thickness or higher waviness upon annealing. This is in agreement with the much lower values in RxA that this tunnel barriers present by CIPT measurements, having one order of magnitude difference between the barrier with 1 s - 3x10^{-3} mbar and the barrier with 30 s - 3x10^{-2} mbar (1 to 10 Ωµm2 in RxA product).

4.2 ASL-DMTJ materials optimization at patterned device level

4.2.1 Switching voltage asymmetry induced by Joule heating effect in presence of an ASL with reduced blocking temperature

The first assessment on the Assistance layer influence in the SL magnetization by their mutual magnetic coupling and spin-transfer torques was investigated by comparing the statistical properties of patterned devices from a stack consisting of the ASL-DMTJ with a single-interface ASL, with those of devices from a reference stack comprising a magnetic dead layer in-place of the ASL [93]. To highlight the influence of the ASL on the SL magnetization switching, a thickness wedge was introduced on the top FeCoB layer of the composite FeCoB/Ta/FeCoB SL. In this study, the results are reported for devices of 80 nm in diameter. The respective stack compositions are presented in Figure4.13.(a) and (b). Both samples have a wedge on the second FeCoB in the composite Storage layer varying its total thickness from 1.8 to 2.4 nm:

-Sample A with a single-interface ASL of 1.5 nm: [Substrate/Ta 3/Pt 25/(Co 0.5/Pt 0.25)x6/Co 0.5/Ru 0.9/(Co 0.5/Pt 0.25)x3/Co 0.5/Ta 0.2/FeCoB 1.2/ Mg 0.5(30s Oxidation 3x10^{-2} mbar)Mg 0.75/FeCoB 1.3/Ta 0.2 /FeCoB x/ Mg 0.5(1s Oxidation 3x10^{-3} mbar)Mg 0.75 / FeCoB1.5 / Ta 3 nm]

-Sample B with a dead-magnetic ASL: [Substrate/Ta 3/Pt 25/(Co 0.5/Pt 0.25)x6/Co 0.5/Ru 0.9/(Co 0.5/Pt 0.25)x3/Co 0.5/Ta 0.2/FeCoB 1.2/ Mg 0.5(30s Oxidation 3x10^{-2} mbar)Mg 0.75/FeCoB 1.3/Ta 0.2 /FeCoB x/Mg 0.5(1s Oxidation 3x10^{-3} mbar)Mg 0.75/FeCoB 0.4/Ta 3 nm].

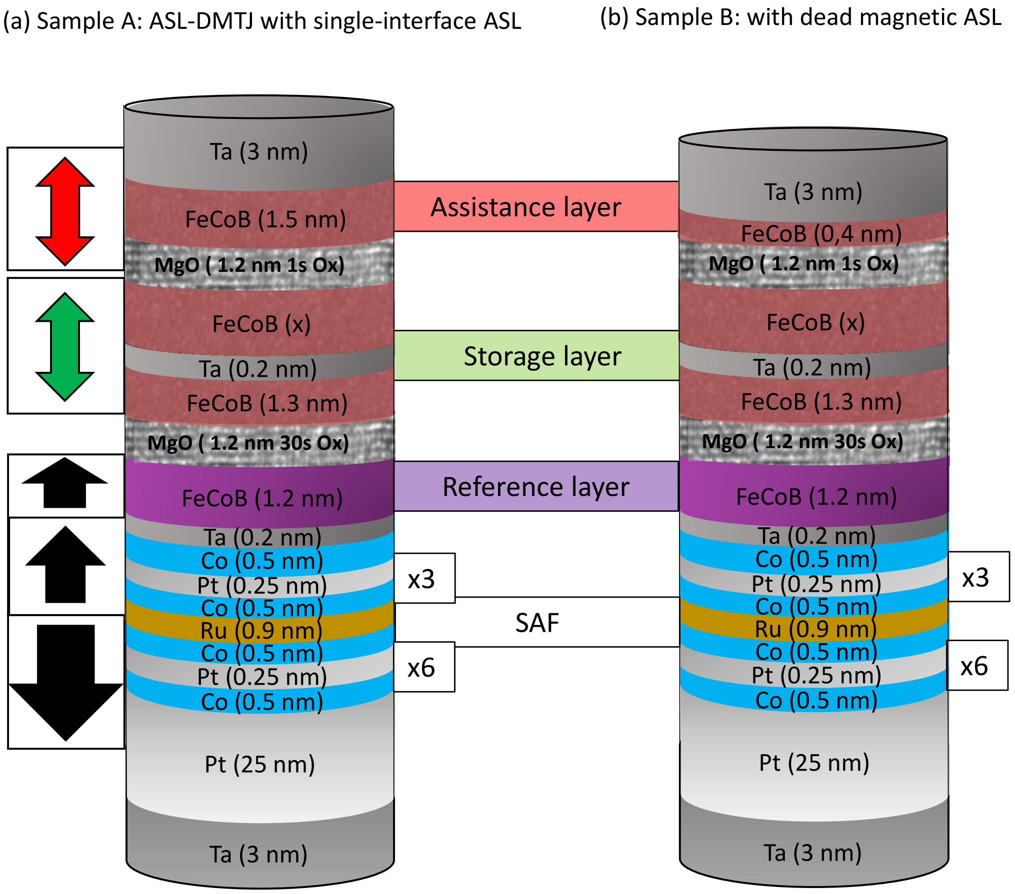

Figure. 4.13: Stack comparison between Sample A with an ASL-DMTJ stack comprising a single-interface based ASL and (b) control sample B with a dead magnetic ASL at 0.4 nm FeCoB.

The purpose of the study was to verify the influence of the SL thickness on the switching dynamics with an external perpendicular field and voltage pulses, considering that its thickness influences its effective perpendicular anisotropy and the magnetic coupling with the ASL, thus allowing for a modulation of the assistance layer influence. In fact, as shown in the introduction chapter, the final free layer thermal stability is not only controlled by its effective perpendicular anisotropy (arising from the interfaces with the MgO), but also by the final volume acquired after patterning the pillar [164]. Like this, varying the SL thickness in patterned devices allows the determination of the volume limits for the devices still exhibiting an out-of-plane magnetization. Then, by depositing a single-interface based ASL on top of the stack, its reduced volume and interfacial anisotropy should suffice to always acquire lower thermal stability than that of the storage layer. For the ASL-DMTJ devices, the chosen thickness for the ASL is set at 1.5 nm, following the results at thin film level shown in section 4.1.1 in this chapter. In reference sample B, the ASL is replaced by a magnetic dead layer 0.4 nm thick, obtained by simply reducing the ASL thickness and taking advantage of Ta diffusion from the Ta capping. When using a switchable ASL, a lower RxA tunnel barrier (1 $\Omega\mu m^2$) is preferably used in the MTJ between the SL and ASL than the one between the SL and RL (10 $\Omega\mu m^2$) to reduce the serial resistance, minimize the TMR drop associated to the presence of this second barrier and maximize the amplitude of the indirect coupling. An example of the resistance vs external perpendicular magnetic field obtained for the two samples A and B is shown in figure.4.14.(a). From this first comparison, it is clear that the ASL-DMTJ (A) device presents much higher coercivity than the case without the ASL (B) at a constant thickness of 2.16 nm of the storage layer. Moreover, along the sweep of the magnetic field, sample's A device do not present any intermediate resistance states from the second MTJ switching between the ASL and the SL. This means that both layers are switching at the same field value independently of the switching direction, finishing at saturation always in parallel alignment (AP(R3) and P(R1)). The fact that the second MTJ switching fields are no observed, is in direct contradiction to the expected resistance responses obtained with the numerical macrospin simulations at 0 K. This could be an indication of several factors: the coupling between the layers is strong enough to prevent the stabilization of the resistance states in anti-parallel alignment (R4 and R2), or the TMR of the second barrier is extremely low, or the layers relative thermal stability are so close that the layers are reversing at the same value of the magnetic field. Nevertheless, the results suggest that the magnetic coupling interaction with the ASL stabilizes the storage layer magnetization out-of-plane, parallel to the SL magnetization, increasing the device coercivity between the two stable configurations in standby conditions. Figure.4.14.(b) supports this idea with a comparison of the device's statistical coercivity data as a function of SL thickness. Reference sample B clearly exhibits a reduction of the storage layer coercivity with increasing thickness from about (250-400 Oe) at lower thickness (1.9 nm) to (0-100 Oe) for the larger thicknesses investigated (2.2 nm). These results are consistent with the expected variation of the effective perpendicular anisotropy with the composite layer thickness. In comparison, the same trend is observed for sample A comprising a 1.5 nm assistance layer. However, over the whole thickness range, the average device coercivity is almost doubled for the ASL-DMTJ as compared to the reference sample. The coupling with the ASL allows the perpendicular magnetic anisotropy to be maintained for SL thickness at least up to 2.1 nm, while the reference sample B shows a magnetic reorientation from out-of-plane to in-plane anisotropy above this thickness.

(a) Device R-H loops extracted from Sample A and B

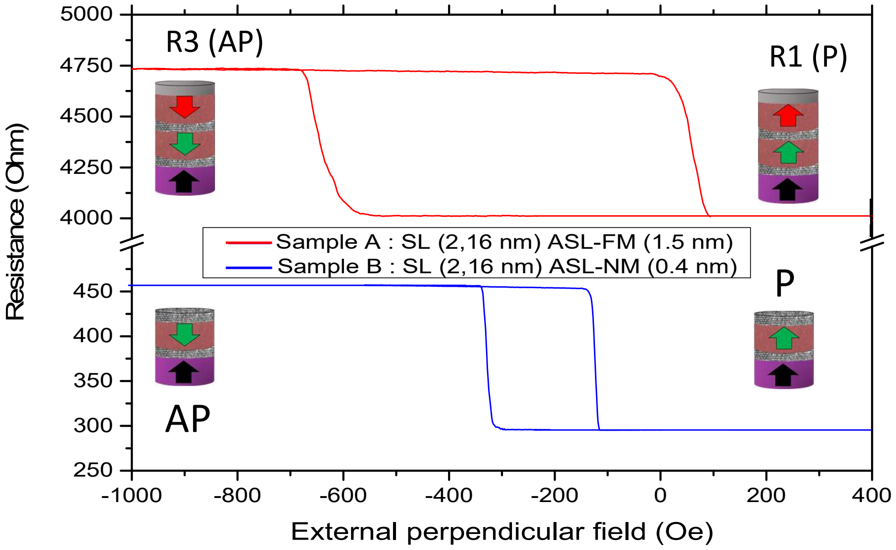

(b) Measured device coercivity vs Storage layer thickness

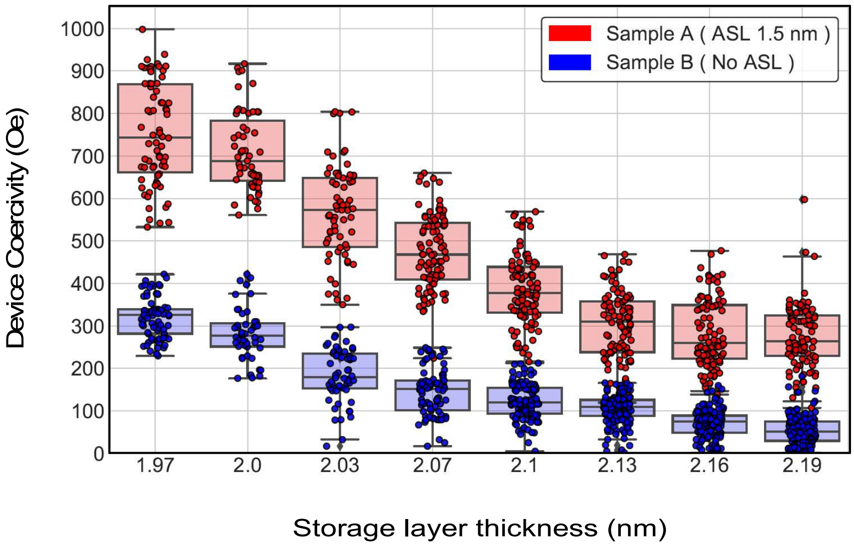

Figure. 4.14: (a) R-H loops comparison between sample A with 1.5 nm ASL and sample B with dead magnetic layer as ASL, both devices with a constant thickness of SL at 2 nm. (b) Comparison of the sample's measured device coercivity as a function of storage layer thickness [93]).

The first problematic encounter with this ASL-DMTJ stack was related to an important asymmetry on the critical voltages to switch the storage layer magnetization between P to AP and AP to P transitions (see figure4.15). One could argue that increasing the thickness of the storage layer could decrease its final thermal stability, thus presenting in these devices similar values of stability than that of single-interface ASL. If this was the case, the desired switching dynamics presented for the case $\Delta_{ASL} < \Delta_{SL}$ in the numerical simulations under applied voltage would not be fulfilled. As a result, this asymmetry could be caused by the different net spin transfer torques exerted on the SL magnetization from the top and bottom polarizers (initial AP(R3) state STT addition or initial P(R3) state STT subtraction as seen when $\Delta_{ASL} > \Delta_{SL}$).

Contrary to expectations, the critical voltage to switch for the AP(R3) to P(R1) transition requires much higher voltage than that of for the P(R1) to AP(R3) transition (0.855 V versus -0.597 V). Besides, these switching voltage, are almost independent on the storage layer thickness (see figure.4.15.(b)). These results could not be explained by only taking into account the STT exerted on the storage layer magnetization. Therefore, other related voltage induced phenomena must be taken into account that also affect the ASL/SL relative thermal stability factors.

(a) Critical voltage extraction for 50 R-V cycles

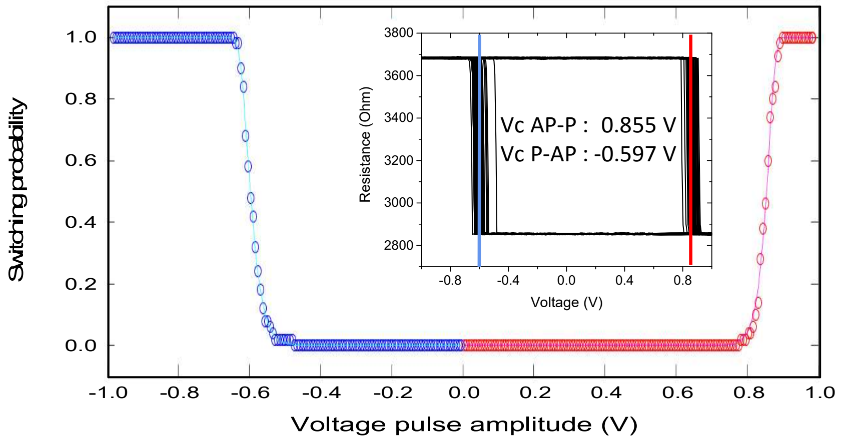

(b) Measured ASL-DMTJ Vc vs Storage layer thickness

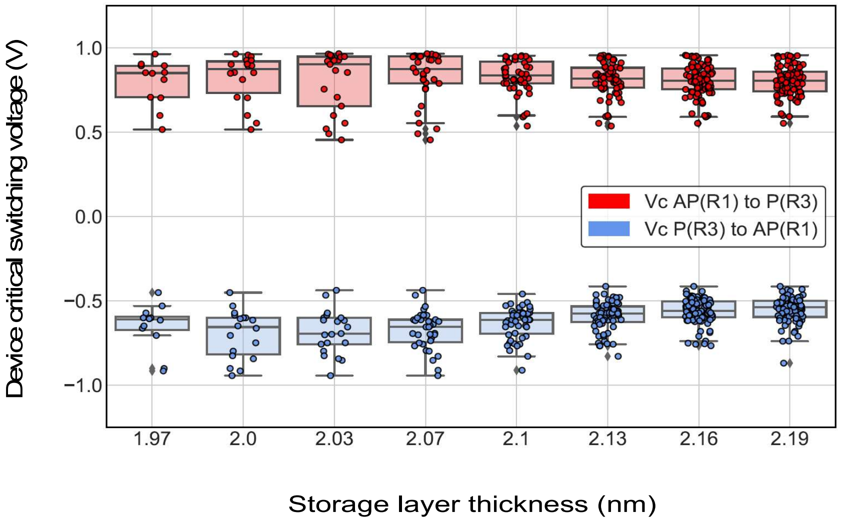

Figure. 4.15: (a) Switching probability vs voltage pulse amplitude for a device from samples A with a SL thickness of 2 nm, insight figure indicating the R-V loop and the extracted critical voltage to switch for each transition. (b) Critical voltage asymmetry between the AP(R3) to P(R1) and P(R1) to P(R3) vs storage layer thickness.

In order to determine the origins behind the asymmetry in the critical switching voltages, stability voltage-field diagrams were performed on both samples as way of investigating the influence of the voltage pulse amplitude on the devices switching fields (H_{sw}). As introduced in the material and methods chapter (chapter 3 section 3.6, this kind of technique not only allows to characterize the STT influence on the devices switching fields, but also the heating caused by the current flowing through the junctions. For this reason, a comparison between the two samples was made to identify the origins of the much higher voltage required to reverse from the AP to P states in the ASL-DMTJ.

The devices from Stack A and B chosen for this comparison have the minimum SL thickness of 2 nm, which ensures that the Stack B devices have enough thermal stability to compare their responses with those of Stack A devices under voltage and field. In the simplest case of a device with a single STT contribution from the RL, as is the case of our reference sample B, the response under applied voltage and field has the typical parallelogram shape characteristic of STT induced switching in p-MTJ (Fig.4.16.(a)). In this diagram, the linear dependence boundaries between the P and AP state and bistable area allows the STT efficiency evaluation defined here as the H_{sw}/V_p ratio (see the blue and red linear fits in Figure.Fig.4.16.(d)). Details on the measurement technique can be found in chapter 3 subsection 3.6.1 with an example of the diagram obtained for a conventional STT-MRAM cell based on a single p-MTJ.

(a) Sample B device stability voltage-field diagram

(b) Sample A device stability voltage-field diagram

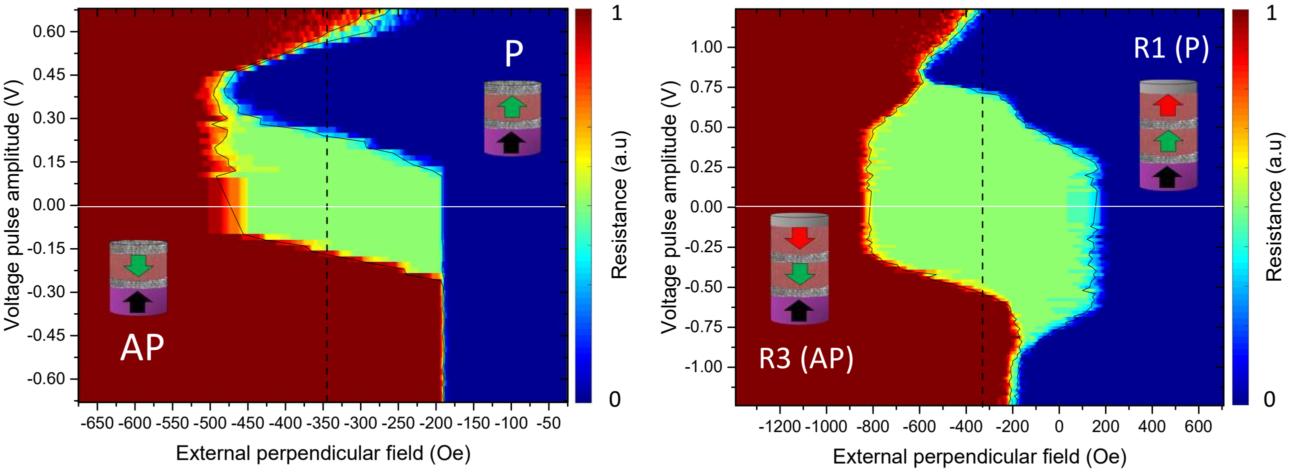

(c) Sample B device switching field / voltage fitting

(d) Sample A device switching field / voltage fitting

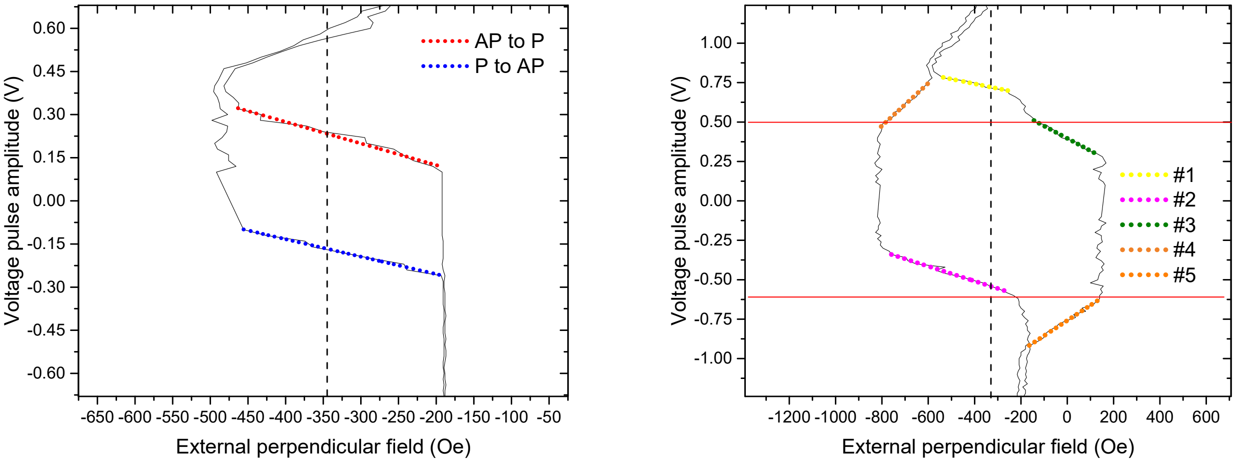

Figure. 4.16: (a) Sample B standard Stability voltage-Field diagram for a conventional STT-MRAM memory cell.(b) Vertical dashed lines corresponds to the offset field for the compensation of the reference layer stray field.(b) Sample A stability voltage-field diagram showing an asymmetry on the extrapolated voltage to switch at the compensation field (0.72 Vc for AP to P) (-0.54 Vc for P to AP).(c) Fitted STT efficiency for the diagram in (a).(d) Doted slopes indicating the dHsw/dVp ascribed to different voltage driven mechanisms from (b. Images taken an adapted from [93]).

The same analysis on sample A with the ASL, shows additional features along its switching field boundaries (see phase diagram in Figure.4.16.(b)). In this diagram, at least 4 different H_{sw}/V_p ratios can be identified, each ascribed to a specific voltage-dependent reduction of the storage layer H_{sw}. Two types of slopes can be considered (see Figure.4.16.(d)): slopes 1 to 3 are mainly related to the STT exerted from both polarizers and slopes 4 and 5 are related to the heating by Joule effect. A detailed explanation and discussion on the mechanisms governing these slopes will be given with numerical simulations in the following discussion. For 4 and 5 the H_{sw}/V_p slopes, the reduction of the devices switching field is mainly caused by the Joule heating during application of the voltage pulses. As a consequence, the SL saturation magnetization and anisotropy start to be reduced at a determined voltage pulse amplitude [104] (around 0.5 V for the left boundary and -0.6 V for the right boundary) resulting in slopes 4 and 5 denoted in orange in Figure.4.16.(d)) [105]. Then, slopes 1, 2, and 3 correspond to different STT efficiency regimes depending on the assistance layer state, involving its magnetic configuration relative to the RL (2 and 3) and superparamagnetic regime (1) [165] [93]. This leads to the second feature characterizing these devices' response, which is the abrupt change in STT efficiency between slopes 1 and 3 at 0.50 V above the horizontal red line for the positive voltages and slope 2 at -0.6 V below the horizontal red line for the negative voltages. Note that at the same voltage pulse amplitudes, self-heating of the junctions starts to degrade the magnetic properties of the storage layer (beginning of the slopes 4 and 5 due to Joule heating independently of the voltage polarity). As we will later see from macrospin simulations, these critical points correspond to a situation where the ASL reaches its blocking temperature. Above these voltage thresholds, due to the rise in temperature induced by the Joule heating in the junctions, the assistance layer reaches a superparamagnetic state during the application of the voltage pulse. In this superparamagnetic state, there is no more spin polarization influence from the ASL. Thus, it no longer acts as an additional spin polarizing layer. The resulting change in STT efficiency translates into an asymmetry in the extrapolated critical voltage to switch from AP to P at 0.72 V and from P to AP at -0.54 V, explaining the fact that a higher voltage is required to switch from AP(R3) to P(R1) that from P(R1) to AP(R3), even if the ASL and RL are already in a configuration in which the total STT on the SL is supposed to add up.

Temperature dependent macrospin simulations of the stability diagrams

?? In order to correlate the magnetization dynamics of the coupled system ASL/SL and understand the main features observed experimentally, temperature-dependent macrospin simulations were performed. The two coupled Landau-Lifshiftz-Gilbert (LLG) equations (one by layer in chapter 2 section 2.2.3) including mutual spin-transfer torques and dipolar coupling were integrated upon the application of out-of-plane magnetic field and voltage pulses. In parallel, the heat diffusion equation was solved to describe the temperature variation in the device associated with Joule heating. As was already shown by Strelkov et al [105], this extension of the model opens the possibility to reproduce qualitatively the shape of the voltage-field diagrams measured experimentally (see chapter 2 subsections 2.2.2 to 2.2.4 describing the adaptation of this model to our ASL-DMTJ structure). Systematic simulations were performed to calculate the voltage-field stability diagrams varying the parameters of the ASL. Thus, for reduced values of the ASL blocking temperature (relative to the blocking temperature set for the SL), we were able to reproduce the main features identified in the experimental diagrams in Figure.4.16.(b) and (d). Table.4.0 summarizes the device characteristics used in the simulations (size, materials properties, layers blocking temperature). The macrospin model takes into account only the dipolar coupling between the ASL and SL. The barriers thickness is set at 1.2 nm as in the experimental devices having both 25% TMR and 2000Ω difference in parallel resistance (RL/SL barrier with RxA= 20 $\Omega\mu m^2$ and SL/ASL barrier with RxA= 6.4 $\Omega\mu m^2$). The electrical properties of the barriers were chosen in an attempt to reproduce the same values of resistance and TMR observed experimentally. Table.4.0 summarizes the device characteristics used in the simulations, where M_{s0} and K_{u0} are respectively the saturation magnetization and uniaxial perpendicular anisotropy at 0 Kelvin, α the Gilbert damping, and T_B the blocking temperature.

Table. 4.0: Layers materials parameters and dimensions:

Parameter	Storage layer	Assistance layer
M_{s0} (kA/m)	1300	1300
K_{u0} (J/m^3)	1.2x10^6	variable
α	0.01	0.01
layer dimensions (nm^3)	80x80x2	80x80x1.5
T_B (K)	800	800/400

Figure.4.17.(a) shows the simulated voltage-field stability diagram averaged from 15 simulated diagrams for a blocking temperature of the ASL slightly above room temperature (T_B=400K) and for an effective perpendicular anisotropy set slightly lower than the SL one (K_{u0} =1.1x10^6 J/m^3). The selection of these specific ASL properties was followed by extensive attempts to reproduce the main features observed on the experimental diagrams. The color code is related to the stack resistance value and the four characteristic resistance states are pointed out on the color scale. Resistance levels R1 and R3 corresponds to the stable parallel and anti-parallel SL/RL configuration, while the ASL magnetization always ends up parallel to the SL one. Depending on the initial configuration of the ASL-DMTJ and on the sweeping field direction, we can extract the two simulated switching voltage-field boundaries depicted in figure.4.17.(b) and (c). Vertical dashed pink lines indicate the switching field of the ASL, while the dashed red horizontal lines indicate the voltage threshold at which the ASL reaches its superparamagnetic state during the writing pulse. Since for a given voltage, the heating power is inversely proportional to the junction resistance ($V^2/R_{initial}$), the two voltage thresholds are asymmetric for P to AP and AP to P switching due to the different initial resistance states. Below these thresholds, the STT exerted on the SL magnetization depends on the relative orientation between the ASL and the RL.In figure.4.17.(b) where the initial magnetic configuration is the P(R1) (dark blue region), negative voltage pulses are applied to switch the device towards the AP(R3). Two STT regimes are identified: for fields higher than the ASL negative switching field (ASL -H_{sw}) and amplitudes of the voltage pulses lower than the superparamagnetic threshold, the ASL magnetization is aligned anti-parallel to that of the RL (light blue region).

There is then an addition of the STT contributions from the ASL and RL acting on the SL magnetization. This correspond to the region denoted as “additive STT” in figure.4.17.(b). On the contrary, for fields lower than the ASL switching field and voltage pulses amplitudes larger than the superparamagnetic threshold, the STT coming from the ASL vanishes. Above this voltage threshold, the STT efficiency drastically changes as the current is only getting spin-polarized by the RL, resulting in only one STT contribution acting on the SL magnetization. For positive voltage polarities, where the STT does not destabilize the initial parallel state, the storage layer switching field is reduced mainly due to Joule heating, as its blocking temperature is higher than that of the ASL (See chapter 2 subsection 2.2.4 for a detailed description of the temperature influence on the layers magnetic properties). Doing the same analysis at increasing fields (figure.4.17.(c)) for positive voltage polarities and the ASL-DMTJ initially in AP(R3) state (yellow region) leads to similar behavior.

(a) Numerical stability diagram with :

ASL K_{u0}= 1.1 E6 J/m3 and T_B = 400K

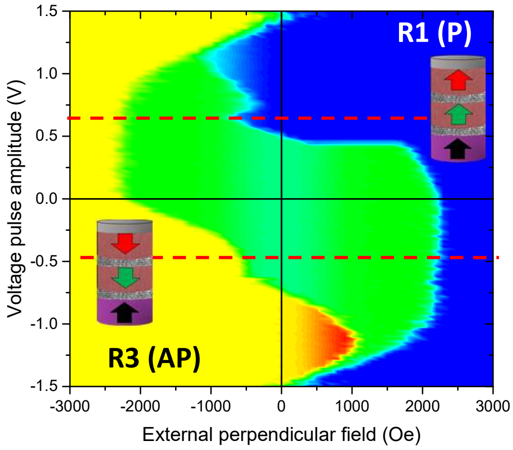

(b) Left switching fields boundary

(c) Right switching fields boundary

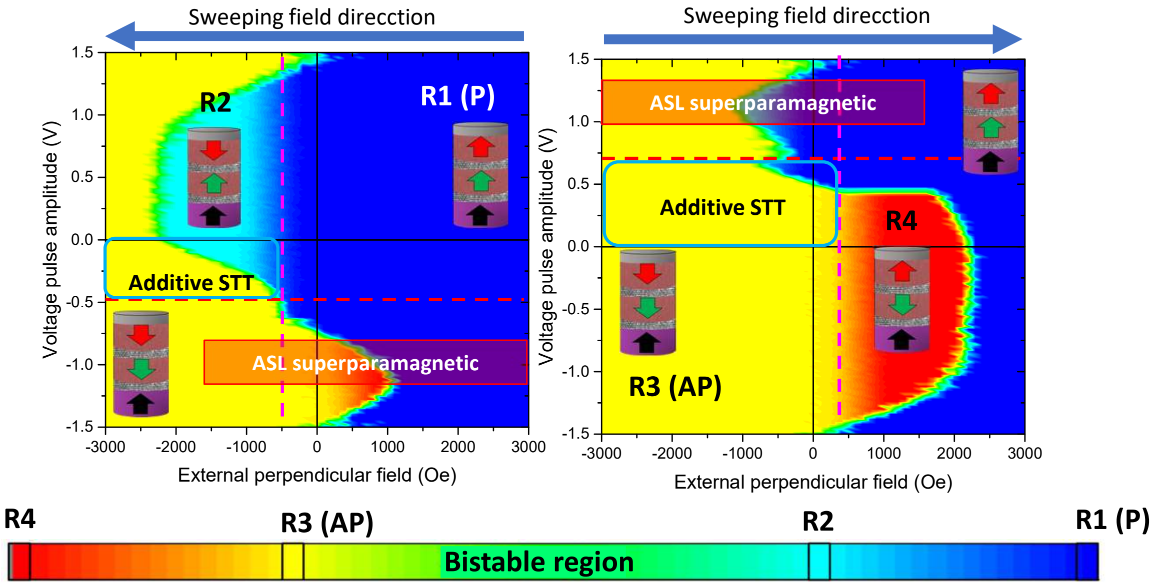

Figure. 4.17: (a) Simulated voltage-field stability diagram taking into account the device temperature variation during write pulse, dashed lines indicating the ASL magnetization switching field. (b) Diagram negative switching fields boundary, stabilization of the ASL/SL coupled system anti-parallel to the RL by negative voltage pulses. (c) Diagram positive switching fields boundary, stabilization of the ASL/SL coupled system parallel to the RL by positive voltage pulses.

In this case, the electrons flowing from the ASL to the RL stabilize the P(R1) configuration. The maximum STT efficiency is found in this case at fields lower than the ASL positive switching field (ASL -H$_{sw}$), as the additive STT contributions from RL and ASL on the SL magnetization already exist in the initial configuration. For fields higher than the ASL positive switching field, the STT contribution from the ASL subtracts to the one from the RL, corresponding to the maximum resistance state (red region). As in the previous case, above the superparamagnetic voltage threshold, the STT coming from the RL alone determines the net STT efficiency. The effect of the joule heating at negative voltage polarities is again similar as in figure.4.17.(b). The STT does not destabilize the AP(R3) initial state, while the SL switching field decreases as its magnetic properties degrade with the temperature rise during the application of the voltage pulse.

Finally, we are able to correlate the above described switching mechanisms with the main features of the experimental diagrams. Slopes 1,2 and 3 or STT related H_{sw}/V_p ratios from Figure.4.16.(b) correspond to different active or superparamagnetic regimes of the ASL and its relative magnetic orientation with respect to the RL magnetization. Slopes 4 and 5 and the abrupt change in STT efficiencies are due to the Joule heating of the device. The increase of temperature during the writing pulse impacts differently the SL and ASL: it reduces the SL switching fields yielding slopes 4 and 5 (Orange linear fits in figure.4.16.(d)) while inducing a superparamagnetic state on the ASL. The fact that the ASL becomes superparamagnetic above these voltage thresholds and not the SL is due to their difference in thickness and interdiffusion with the adjacent Ta capping layer [146], explaining its higher sensitivity to heating. Indeed, the concentration of Ta in amorphous CoFeB alloys is well known to highly influence the curie temperature of single interface-based Ta/CoFeB/MgO electrodes which is supported by Toka et al [166] and [167]. For the ASL to assist the SL magnetization switching in both P to AP and AP to P transitions, the ASL magnetization must be in anti-parallel configuration with respect to the RL, assisting the SL switching thanks to the additive contributions of the torques from RL and ASL, but without reaching the ASL superparamagnetic state. For this reason, further optimization on the ASL blocking temperature must be conducted in order to ensure its functionality as a perpendicular polarizer at higher voltage amplitudes.

Figure.4.18 depicts the main numerical stability diagrams for six different combinations of ASL uniaxial perpendicular anisotropy and blocking temperature. From these simulations, we can already address the possibility of optimizing the ASL anisotropy and blocking temperature and its impact on the diagram shapes. In the cases with low ASL blocking temperature (400K), a clear similarity with the main experimental diagram shapes is observed, independently of the uniaxial anisotropy. The variation in uniaxial anisotropy does not play a significant role as, in all cases, the saturation magnetization and final effective anisotropy of the ASL are reduced by the heating during the application of the pulse.

As a result, even at high values of perpendicular anisotropy ($1.1\text{x}10^6$ J/m^3), with a clear out-of-plane magnetization, the ASL is almost reaching the superparamagnetic state at room temperature (see Heat diffusion equation and temperature-dependent effects in chapter 2 subsection 2.2.4). At the voltage threshold of approximately 0.5 V, the ASL is no longer able to act as an additional perpendicular polarizer, resulting in no additional STT contribution originating from this layer. Below this threshold, independently of the ASL anisotropy, it is still possible to exert a second STT contribution which is added or subtracted from that of the RL depending on the relative orientation of the RL and ASL magnetizations.

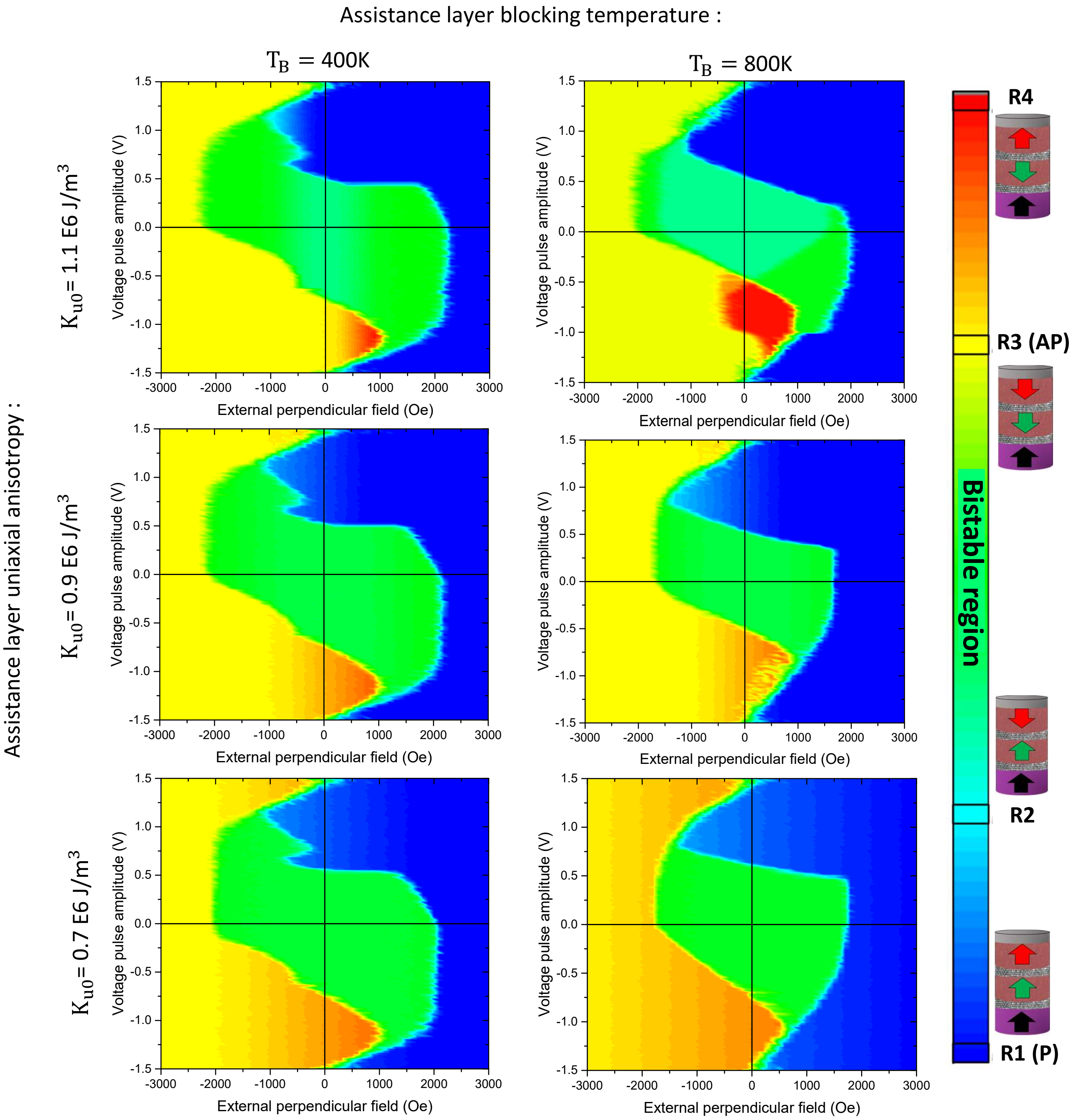

Figure. 4.18: Simulated Stability Voltage-field diagrams for different ASL uniaxial perpendicular anisotropies and blocking temperatures. The color code indicates the resistance states for the modeled simplified ASL-DMTJ. Images were taken and adapted from [93].

This feature does not occur in the ASL-DMTJ with the ASL having a high blocking temperature (800K equal to the one of the Storage layer). For these cases, an impact of the ASL perpendicular uniaxial anisotropy on the diagram shapes is clearly visible (Figure.4.18, right column). The simulations indicate that the ASL magnetization remains always out-of-plane for 1.1x10^6 J/m^3, while it becomes in-plane for reduced values at 0.9x10^6 J/m^3 and 0.7x10^6 J/m^3. When the ASL exhibits in-plane anisotropy, a resistance gradient is observed versus out-of-plane external applied field, since the ASL magnetization gradually rotates to reach the out-of-plane saturation at high fields, parallel to the SL, in resistance states R3 and R1. When comparing with the case for a K_{u0} of 1.1x10^6 J/m^3, the difference appears clearly: instead of a gradual resistance change when the ASL has easy-plane anisotropy, four stabilized voltage-field regions indicated by their corresponding resistance states are observed in the case of the higher anisotropy ASL. The SL coercivity (diagram boundaries at zero voltage) is as well influenced by the ASL preferable orientation, being the highest for the case with 1.1x10^6 J/m^3, in which the ASL magnetization is fully perpendicular. This last case (K_{u0}= 1.1x10^6 J/ and T_B=800K) corresponds to an optimized combination of ASL blocking temperature and anisotropy. By increasing the ASL blocking temperature, it is possible to minimize the influence of the Joule heating on the ASL properties. The additive STT contribution from the ASL is then maintained independently of the voltage pulse amplitude, resulting in symmetric critical voltages switching at zero fields. This can be achieved by increasing the ASL thickness, but still ensuring that the perpendicular anisotropy of this layer remains sufficiently large to orient the ASL magnetization out-of-plane. However, the ASL perpendicular anisotropy must also remain lower than the SL one so that the switching sequences presented in chapter 2 for $\Delta_{ASL} < \Delta_{SL}$ are respected.

4.2.2 ASL blocking temperature and perpendicular anisotropy optimization

To increase the blocking temperature of the ASL layer, we decided to use a composite free layer structure similar to the one used as SL (i.e. sandwiched between two MgO barriers). As introduced in the materials optimization section at full sheet film level, in contrast to single interface MgO/FeCoB electrodes, doubling the oxide interfaces with the magnetic metal allows increasing the thickness limits for perpendicular magnetic anisotropy. Then a resulting higher blocking temperature is expected to confer to the ASL with a larger volume with sufficient robustness against joule heating within the operating voltage ranges. Indeed, it is known that the Curie temperature of ferromagnetic thin films increases with the thickness of the layer (Note that Curie temperature and blocking temperature are close to each other when the measurement time gets very short toward the ns range; in our case, as the acquisition time is 1 μs, it is more accurate to talk about blocking temperature of the layers [138] [168]). Several studies confirm the dependence of blocking temperature on the magnetic layer thickness, Schneider et al. studied this dependence in epitaxial fcc Cu/Co [169] and bcc Fe/Ag [170]. More related to the free layers utilized in this thesis, Sato et al [171] obtained a good correlation between theoretical results based on atomistic simulations and the experimental dependence of the magnetic properties versus thickness of sputtered CoFeB/MgO heterostructures, showing the relationship between the final magnetic saturation and anisotropy dependence with temperature. Besides the higher reachable volumes of the composite free layers, the use of tungsten insertions as boron absorbing layers was also found to have a significant impact on the final PMA.

Figure4.19.(a) shows the stack composition chosen for the optimization of the ASL blocking temperature. The detailed description of the materials stack is:

[Substrate/Ta 3/Pt 25/(Co 0.5/Pt 0.25)x6/Co 0.5/Ru 0.9/(Co 0.5/Pt 0.25)x3/Co 0.5/W 0.2/FeCoB 1.2/ Mg 0.5(30s Oxidation 3x10^{-2} mbar)Mg 0.75/FeCoB 0.8/W 0.2 /FeCoB 0.75/ Mg 0.5(5s Oxidation 3x10^{-3} mbar)Mg 0.75 / FeCoB 1/ W 0.2 /FeCoB 0.75/ Mg 0.5(1s Oxidation 3x10^{-3} mbar)Mg 0.75/FeCoB 0.4/Ta 3 nm] (thickness in nm).

As mentioned above, in this next step of the study, all boron adsorbing layers in the stack were replaced by tungsten, which involves the one in contact with the RL and the two non-magnetic insertions in the ASL and SL composite trilayers. The ASL bottom FeCoB is kept at 1 nm while the top one at 0.7 nm, corresponding to the total composite free layer thickness in this next optimization step. In comparison, the FeCoB layers comprised in the storage layer are both reduced for a maximized perpendicular anisotropy (total SL thickness 1.5 nm with bottom FeCoB at 0.8 nm while top one at 0.7 nm), thus assuring that its thermal stability is higher than that of the composite ASL (see figure.4.5.(b) in this chapter for a comparative in coercivity values obtained at these thicknesses on a composite free layer with tungsten insertion at 300 °C annealing).

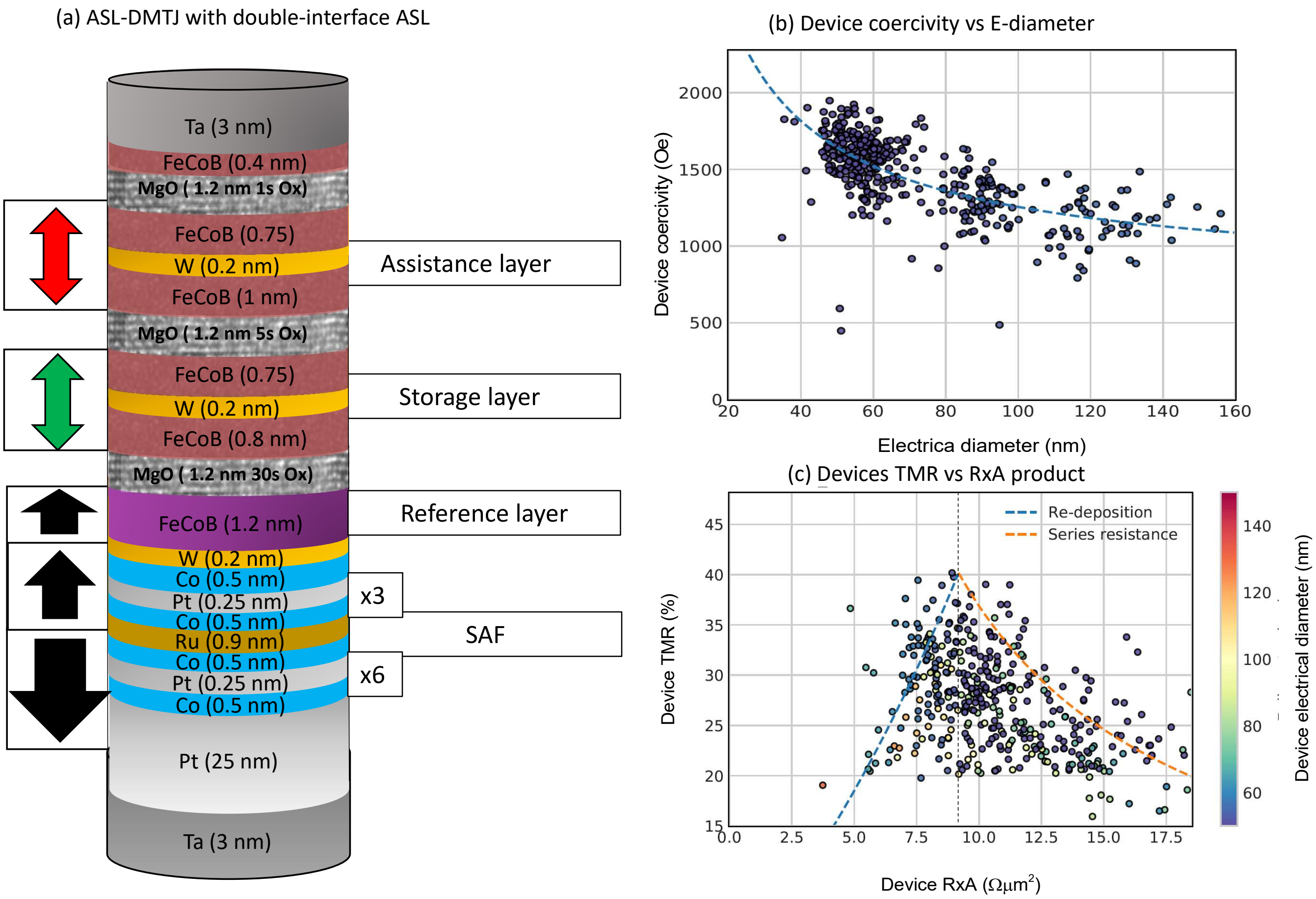

Figure. 4.19: (a) Illustration of the material stack composition for the ASL blocking temperature optimization at patterned device level.(b) Measured device coercivity vs size (electrical diameter). (c) Device's Tunnel magnetoresistance vs RxA product at patterned device level.

For these devices, the barrier in the second MTJ (i.e SL/MgO/ASL) was prepared with stronger oxidation conditions (pressure 3x10^{-3} mbar and longer time 5 s). These oxidation parameters were intended to increase the sensitivity to the ASL switching by conferring a higher TMR to this barrier with the counterpart of a higher serial resistance. Although this improvement in sensitivity is not needed for the final device working principle, being able to observe the resistance states provided by the second MTJ is important to verify the switching schemes of our proposed device and the ASL-SL reversal orders. The third MgO barrier on top of the stack is just acting as capping for the ASL and is only used as a secondary source of interfacial anisotropy for this layer, hence the lowest oxidation parameters were utilized to minimize the total serial resistance (3x10^{-3} and 1 s). Devices were patterned into nano-pillars of nominal diameters of 50, 80, and 100 nm. Reducing the total thickness of the composite SL generally increases the device's coercivity under an external perpendicular field.

Figure.4.19.(b) presents the coercivity data extracted for the three device sizes as a function of the final fabricated electrical diameters. For 80 nm diameter devices, and comparing with the first ASL-DMTJ with a single-interface ASL at 1.5 nm (see figure.4.14.(b)), the coercivity values are increased from 700-750 Oe with a SL of 2 nm and Ta spacer, to 1000-1500 Oe for a SL thickness of 1.5 nm and W spacer. These values of coercivity are consistent with a higher interfacial anisotropy of the SL owing to its reduced thickness and the use of tungsten. Moreover, as observed in the dependence of the indirect coupling with the barriers oxidation parameters (section 4.1.3 in this chapter), the indirect coupling through the barrier should have been reduced for a 5 s oxidation time and pillar diameters generating the same stray field. In fact, the highest values of coercivity are found for devices with a diameter of 50 nm (from 1250 to 2000 Oe) which can be explained by a higher dipolar interaction in parallel alignments between the ASL/SL coupled system. Regarding the final TMR amplitudes, the devices show a variability for each diameter sizes, which is due to the different sources of defects introduced during the fabrication process (Either re-depositions or serial resistances in figure.4.19). In general, the TMR values range between 20 % to 40 %, which are low for real applications but enough for its electrical characterization and the verification of the material properties to be optimized with this stack. Figure.4.20 shows three examples of the resistance response obtained under perpendicular field for 50 cycles on devices diameters of 100 nm (a), 80 nm (b) and 50 nm (c). Regardless of the device size, their respective R-H cycles again exhibit a coherent reversal of both layers between the R1(P) and R3(AP) states at the same coercive field value with no clear signs of any intermediate (R2) or higher (R4) state related with an independent reversal of either the ASL or the SL with external magnetic field.

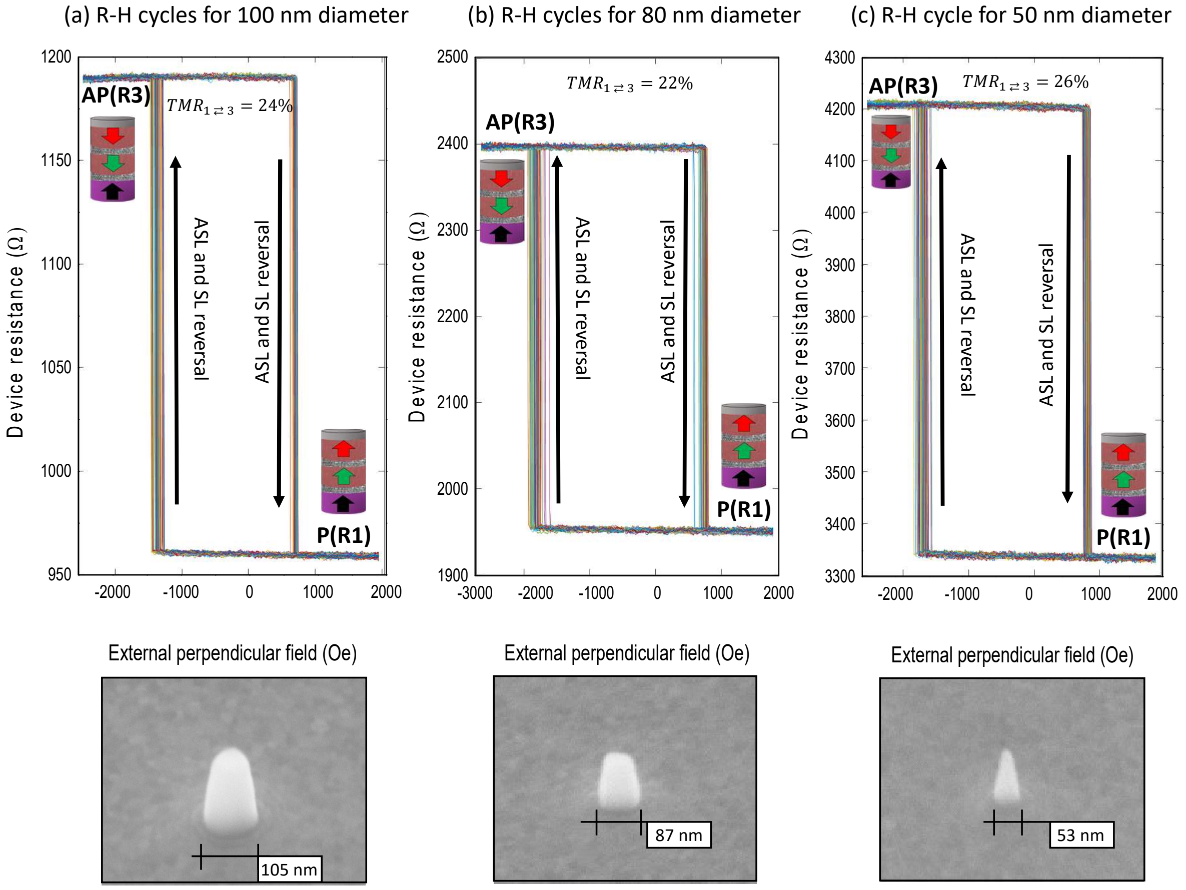
(a) R-H cycles for 100 nm diameter

(b) R-H cycles for 80 nm diameter

(c) R-H cycle for 50 nm diameter

Figure. 4.20: Devices experimental R-H loops obtained for 100, 80 and 50 nominal diameters in nm with a SEM image of each respective device size after the IBE patterning.

Following the same procedure, the study on the impact of the current-induced heating during the application of the voltage pulses was carried out by means of voltage-field stability diagrams. As reminder for the case of the ASL-DMTJ device with a single-interface ASL, and confirmed with the temperature-dependent numerical simulations, any change on STT efficiency observed on the switching field boundaries of the devices will be ascribed to a superparamagnetic regime of the ASL during the application of the voltage pulse. In addition, if the resistance state involving a reversal of the second MTJ are observed at high voltage pulse amplitudes, this would mean that the ASL magnetization remains stable against the Joule heating and is acting as an active electrode in the second MTJ. Figure4.21.(a) and (b) shows the comparison between the numerical simulation with a high ASL blocking temperature and high perpendicular anisotropy with the experimental diagram obtained for a 50 nm diameter device with the composite ASL based stack described in this section (Figure4.19.(a)). The similarities between the simulation and the measured resistance response under-voltage and field clearly evidence that the composite ASL is much more robust against the Joule heating than in the previous section where the ASL was getting superparamagnetic at high voltages. This is supported by the fact that the STT efficiency (i.e STT related H_{sw}/V_p ratios) for both voltage polarities is maintained without any drastic change throughout the voltage ranges of operation.

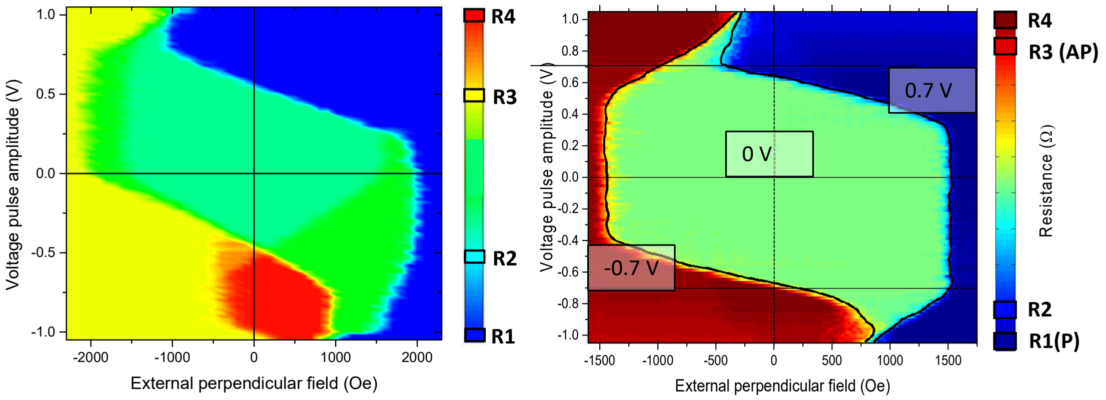

(a) Numerical stability diagram with :

ASL K_{u0}= 1.1 E6 J/m3 and T_B = 800K

(b) Experimental diagram with optimized ASL T_B

ASL MgO/FeCoB/W/FeCoB/MgO at 1.7 nm

(c) R-H cycles from (b) at voltage pulse amplitudes: -0.7 V ,0 V and +0.7 V

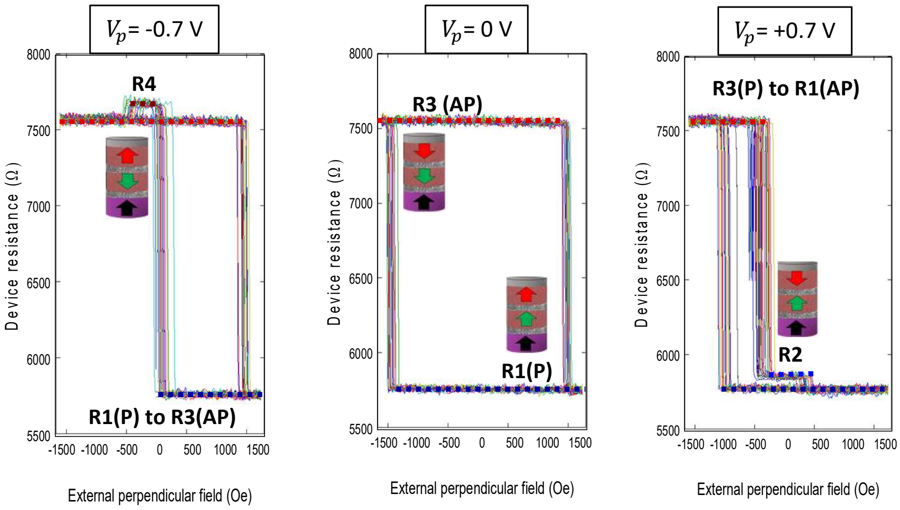

Figure. 4.21: Comparison between a simulated voltage-field diagram (a) with high uniaxial anisotropy and high blocking temperature ASL with (b) experimental diagram obtained for a device of 50 nm with the stack composition in figure.4.20. (c) Comparison between the resistance response under applied perpendicular field at 0 V pulse amplitudes and high voltage pulse amplitudes (-0.7 V and +0.7 V).

The self-heating of the device still has an impact on the storage layer magnetic properties (starting at 0.5 V for positive voltage polarities and -0.7 V for negative voltage polarities), but the STT related H_{sw}/V_p ratios remains constant (especially at zero effective field indicated by the horizontal line). Then, if we look into the R-H loops extracted at high voltage pulse amplitudes (± 0.7 V) and we compare it to the resistance response at 0 voltage (comparison of R-H loops in Figure4.19.(c)), it is possible to discern the resistance states from the reversal of the top MTJ comprising the SL/ASL (R4 at -0.7 V and R2 at +0.7 V). As already discussed, this is clear evidence that the ASL is a magnetically active electrode and is acting as a switchable perpendicular polarizer. However, the reversal orders of the magnetization of the layers are not the desired ones for a correct operation of the memory cell. For negative voltage polarities (-0.7 V), the R1(P) to R3(AP) switching sequence is transiting through the R4 state, indicating that the SL magnetization is reversing first (at 0 Oe) while the ASL magnetization remains parallel with respect to the RL. The storage layer reversal is then followed by the assistance layer by the combined effect of the field and the STT from the SL (at -500 Oe). This implies that the SL is switching under the subtractive STT from both polarizing layers in parallel alignment. On the contrary, for the AP(R3) to P(R1) transition at positive voltage polarities (+0.7 V) the SL is reversing under the additive STT from both polarizers (-500 Oe) followed by the ASL at (+500 Oe). The divergence in net STT acting on the storage layer between the transitions results in different STT efficiencies depending on the voltage polarity (AP(R3) to P(R1) H_{sw}/V_p= -5090 Oe/V while P(R1) to P(R3) H_{sw}/V_p= -3715 Oe/V) due to the initial magnetic configuration between the ASL and the RL. The ASL blocking temperature is hence increased, but its thermal stability relative to the one of the storage layer is higher, thus presenting higher values of the field to reverse its magnetic orientation at the same voltage pulse amplitudes. A more intelligible way to understand the switching sequences of the ASL/SL coupled system is to monitor the magnetoresistance response of the ASL-DMTJ as a function of voltage pulse amplitude. The R-V loops extracted on the three devices sizes in the wafer are shown in figure.4.22.(a), (b), and (c) respectively. Similar resistance responses are retrieved for the devices sizes, presenting an asymmetry on the critical voltage to switch from AP(R3) to P(R1) and P(R1) to AP(R3).

Figure.4.22.(d) shows this asymmetry as a function of the devices nominal diameters, where this time, lower critical switching voltages are required for the AP(R3) to P(R1) transition. Note the similarity with the numerical R-V macrospin simulations at 0K in chapter 2 section **??** "Voltage induced dynamics for $\Delta_{ASL} > \Delta_{SL}$" with a detailed discussion on the origins behind the asymmetry. Recalling these simulations, if the SL thermal stability is lower than that of the ASL, a higher voltage from P(R1) to AP(R3) would be needed to switch its magnetization. This was ascribed to the reduction of the net STT acting on the storage layer if the ASL is not able to be set anti-parallel to the RL before the writing operation. Also, as is seen in the R-V cycles for 50 nm diameters, it is possible to write the memory on the R4 configuration (ending either in R4 or R3), where the ASL would remain aligned anti-parallel to the SL magnetization, thus decreasing the final thermal stability of the device. On the contrary, the AP(R3) to P(R1) transition presents lower values of critical switching voltages and is again sustained by the fact that the additive STT is acting as soon as the voltage pulses are applied. Considering that the resistance states of the memories are read after the application of the voltage pulses (for 1 μs), this implies that the R4 and R2 observed states are stable magnetic configurations with a relatively long lifetime, and that the ASL magnetization remains in the initial magnetic configuration until is reversed at higher voltages by the STT from the SL (After the writing operation of the storage layer magnetization). The resistance response against voltage pulse amplitude we will discussed in the final chapter with the experimental field and voltage induced dynamics (chapter 5 section 5.2) As a conclusion to this section, the use of a composite double interface ASL allows increasing the thickness of the layer while maintaining sufficient perpendicular anisotropy. With a larger ASL volume, the layer exhibits a much higher thermal robustness against the Joule heating produced at high voltage pulse amplitudes (relative to a single-interface based ASL with Ta capping).

(a) R-V loop for 50 nm nominal diameter (b) R-V loop for 80 nm nominal diameter (c) R-V loop for 100 nm nominal diameter

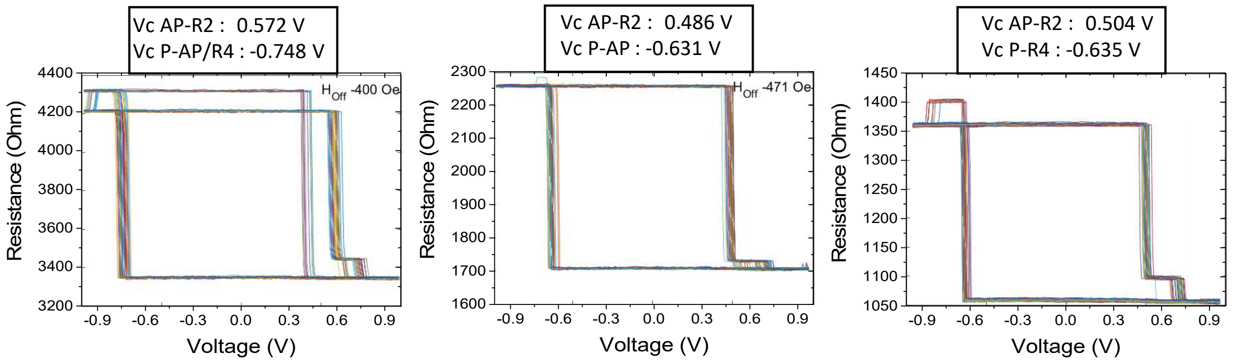

(d) Critical switching voltages for the AP-to-P and P-to-AP as a function of the devices nominal diameters

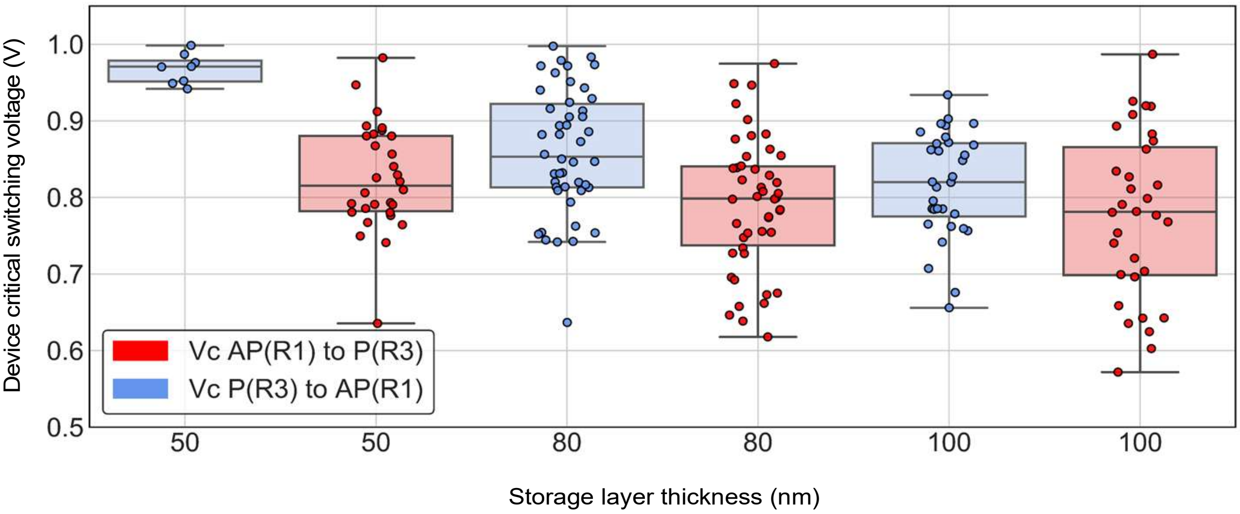

Figure. 4.22: Measured R-V loops for nominal diameters of (a) 50,(b) 80 and (c) 100 nm.(d) Critical switching voltages for the AP-toP and P-to-AP as a function of the devices nominal diameters.

This could be an indication of a successful optimization of the ASL blocking temperature. However, regardless of the device size (ASL and SL volume), the ASL exhibits higher thermal stability than the SL, so the switching sequences required to take advantage of the double spin transfer torques from the RL and ASL on the SL magnetization are not fulfilled independently of the write operation.

4.3 Optimization of the ASL/SL relative thermal stability at thin film level and on patterned devices

At the beginning of this chapter, an example was given on the modulation on the perpendicular magnetic anisotropy of a FeCoB/MgO single interface free layer by varying the Mg content at the interface (i.e. interfacial oxidation conditions). This idea was introduced as an alternative strategy to reduce the electrode's coercivity (related to the PMA amplitude of the ferromagnetic layer) obtained at the full sheet film but at the expense of changing the electrical properties of the tunnel barrier. The same reasoning can be applied for the double-interface based ASL. However, the relative deposited Mg thickness and oxidation parameters of the tunnel barrier between the SL and ASL can be maintained (controlling the electrical properties of the second MTJ in our ASL-DMTJ stack) but the capping utilized as an additional source of interfacial anisotropy can be varied. Thanks to this, the volume of the composite ASL found in the previous section (thickness x area providing the desired thermal robustness against the self-heating under voltage) can be kept while the effective perpendicular anisotropy is lowered by changing the oxidation conditions of the top ASL/MgO interface. This will result in a lowered thermal stability factor of the ASL once the device is patterned, considering that the energy barrier to switch its magnetization will mainly depend on the product of the volume and its uniaxial anisotropy. Figure.4.23 shows the half MTJ ASL/SL stack employed to investigate the effect of varying the oxidation conditions at this interface with the introduction of a Mg wedge in the capping of a double-interface based ASL. A similar stack composition is used as for the single-interface based ASL in section 4.1.1 (see also figure.4.3): [Substrate/Ta 3/FeCoB 0.4/Mg 0.5(30s Oxidation 3x10^{-2} mbar)Mg 0.7/FeCoB 0.2/W 0.2/FeCoB 0.2/Mg 0.5 (5s Oxidation 3x10^{-3} mbar)Mg 0.75 wedge/FeCoB 1/W 0.2/FeCoB 0.75/Mg "x" wedge (1s Oxidation 3x10^{-3} mbar)Mg 0.75 /FeCoB 0.4/Ta 3], with thickness in nm. As in section 4.1.1, the first layers in the stack are deposited in an attempt to reproduce the same growth conditions of the composite ASL on top of the MTJ between the SL and the RL.

Capping MgO wedge in half ASL/SL MTJ stack and Remanence/Coercivity vs MgO capping thickness

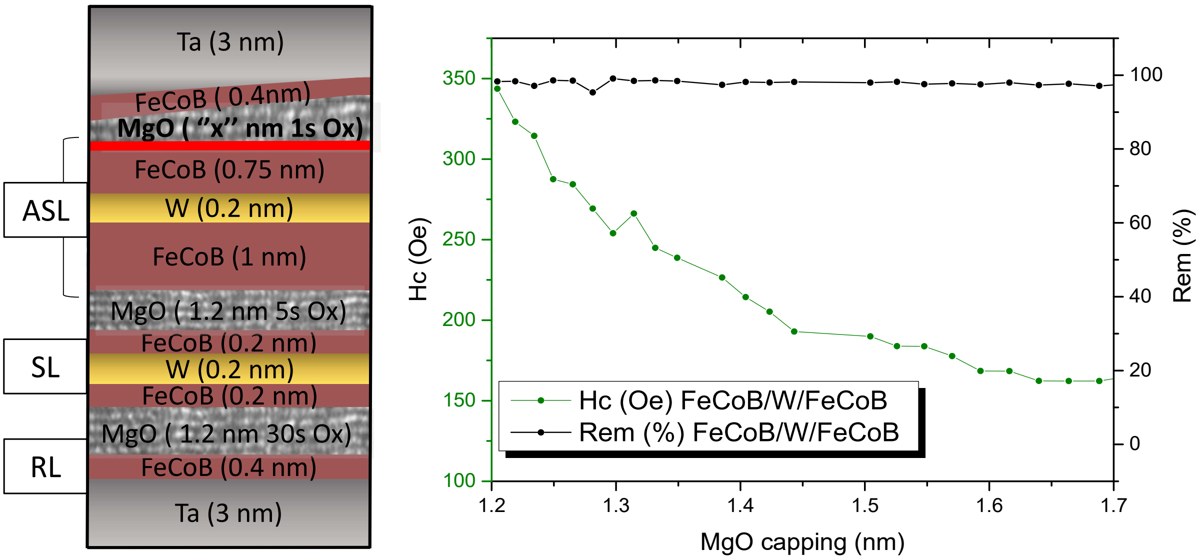

Figure. 4.23: Stack schematics with respective materials thicknesses varying the MgO capping thickness for a total constant FeCoB thickness of 1.75 nm.(b) Coercivity and remanence extracted of the composite layer as a function of capping MgO thickness after annealing at 300°C.

The total thickness of ASL is set at 1.75 nm (FeCoB below 1 nm and above 0.75 nm), this thickness being the one that yields the necessary blocking temperature to provide the layer with sufficient thermal robustness in patterned devices. The oxidation conditions on top of the composite ASL were varied with a Mg wedge ”x” ranging from 1.2 nm (standard thickness for a MgO tunnel barrier used in the previous section as capping for the ASL) to 1.7 nm. In addition to the stack illustration, figure.4.23 shows as well the coercivity values extracted under perpendicular field by MOKE at full sheet film of the composite free layer as a function of MgO capping thickness. Similar to the results obtained before, the PMA of the composite free layer is modulated by changing the oxidation at the top interface, thus resulting in a gradual decrease of the final coercivity with increasing Mg thickness in the capping. Although the degree of oxidation of the top interface is being degraded, contrary to the single interface free layer, the composite free layer remains with an out of plane easy axis thanks to the two surface anisotropy contributions of the oxides layers sandwiching the respective FeCoB layers (As can be seen from the 100% remanent magnetization for the full range of MgO capping thickness investigated). The next step towards the optimization of the ASL thermal stability factor is use the above described method to decrease the ASL effective perpendicular anisotropy at patterned device level. Figure.1.24.(a) illustrates the deposited full ASL-DMTJ material stack, which consists of a modified version of the one utilized for the ASL Blocking temperature optimization in subsection 4.2.2 and introduced in figure.4.19.

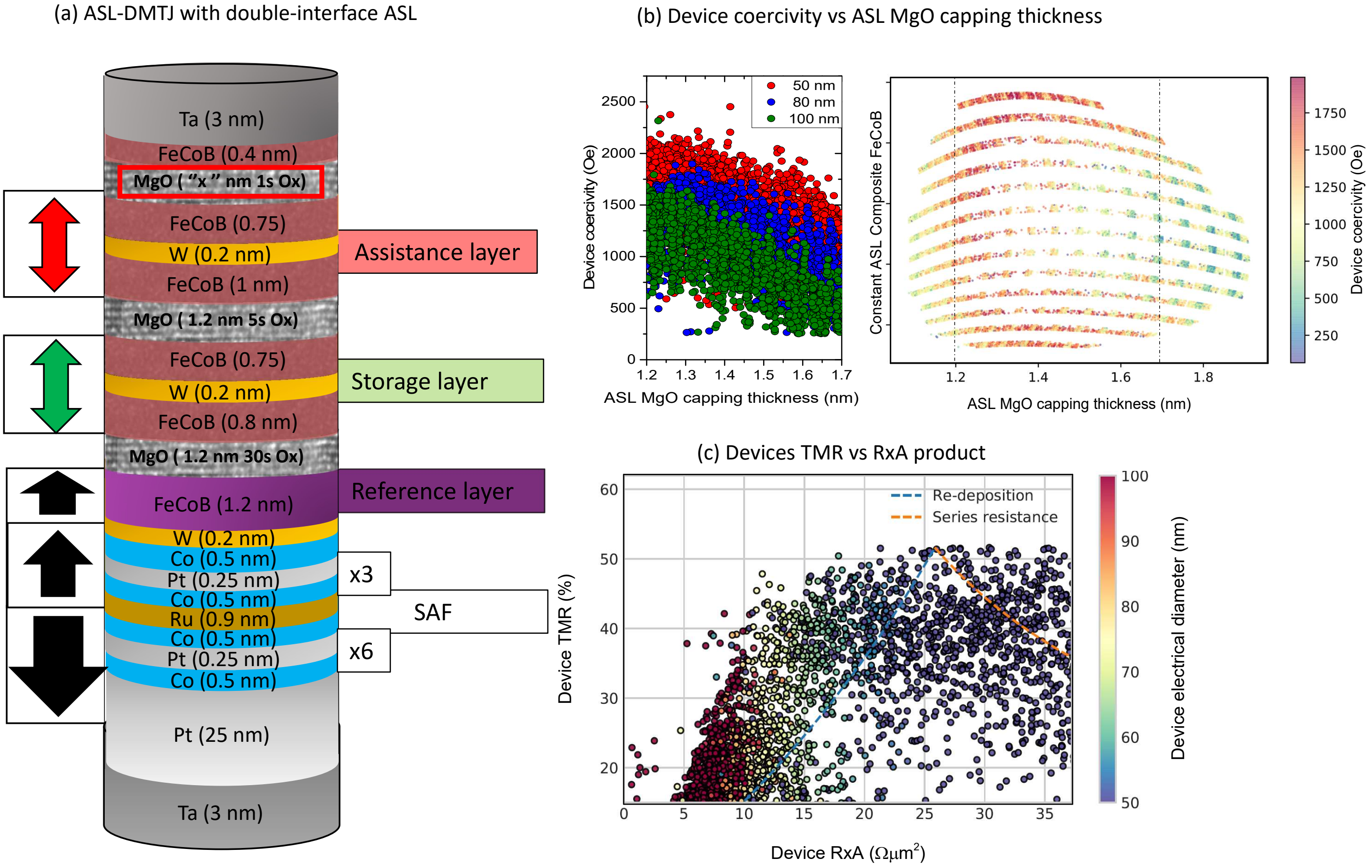
(a) ASL-DMTJ with double-interface ASL

(b) Device coercivity vs ASL MgO capping thickness

(c) Devices TMR vs RxA product

Figure. 4.24: (a) Illustration of the material stack composition for the ASL/SL relative thermal stability optimization at patterned device level.(b) Measured device coercivity as a function of ASL MgO capping thickness. (c) Device’s Tunnel magnetoresistance vs RxA product at patterned device level.

The range of the deposited Mg thickness in the ASL MgO capping are set following the previous study at full sheet film level, accounting for the difference in sputtering rates at the edges of the wafer (total MgO thickness ”x” ranging from 1.1 to 1.9 nm, hence covering at the wafer center the Mg thickness investigated at full sheet film). For the sake of clarity, the detailed material stack composition in nm is:

[Substrate/Ta 3/Pt 25/(Co 0.5/Pt 0.25)x6/Co 0.5/Ru 0.9/(Co 0.5/Pt 0.25)x3/Co 0.5/W 0.2/FeCoB 1.2/ Mg 0.5(30s Oxidation 3x10^{-2} mbar)Mg 0.75/FeCoB 0.8/W 0.2 /FeCoB 0.75/ Mg 0.5(5s Oxidation 3x10^{-3} mbar)Mg 0.75 / FeCoB 1/ W 0.2 /FeCoB 0.75/ Mg ”x” wedge (1s Oxidation 3x10^{-3} mbar)Mg 0.75/FeCoB 0.4/Ta 3].

Pillars were patterned with nominal diameters of 50, 80, and 100 nm and the same FeCoB thicknesses as in the previous section, thus corresponding to equal magnetic volumes for both the ASL (1.7 nm) and the SL (1.5 nm). Interestingly, the measured coercivity of the devices (i.e simultaneous ASL and SL reversal with a perpendicular field) is found to be dependent on the MgO capping of the ASL. Figure.4.24.(b) demonstrates this dependence with the mapping of the devices coercivity extracted at different locations in the wafer (material wedge thickness), showing also the same dependence differentiated by nominal diameters at the central regions of the wafer (homogeneous deposition of the constant material thicknesses). These results were not expected, as the value of the field for the simultaneous reversal of the ASL/SL magnetizations was thought to be dependent on the strength of their coupling, and not on the relative PMA of the layers. However, it is likely that the switching process by field is triggered by the layer with less anisotropy (in this case the ASL), thus explaining to some extent the reduction of the devices coercivity with decreasing ASL perpendicular anisotropy. Nevertheless, this data suggests that the ASL anisotropy is being tailored by reducing the oxidation of its top FeCoB interface and that ASL anisotropy tuning approach works also at the patterned device level. This is also supported by the observation of the same trend in the device’s coercivity with MgO capping thickness independently of the device diameter. The device’s tunnel magneto-resistance ratio is in general raised by almost 10% with respect to the same stack with thinner MgO capping on the ASL in figure.4.19 (more evident for small diameters presenting a maximum 50% in TMR). This could be evidence that the serial resistance introduced by the ASL MgO capping has been reduced as this barrier is more under-oxidized (considering that larger thickness here means more metallic Mg content in the naturally oxidized barrier [139]). Figure.4.25.(a) highlights the devices TMR vs wafer position, showing no clear correlation between the Mg thickness wedge and TMR.

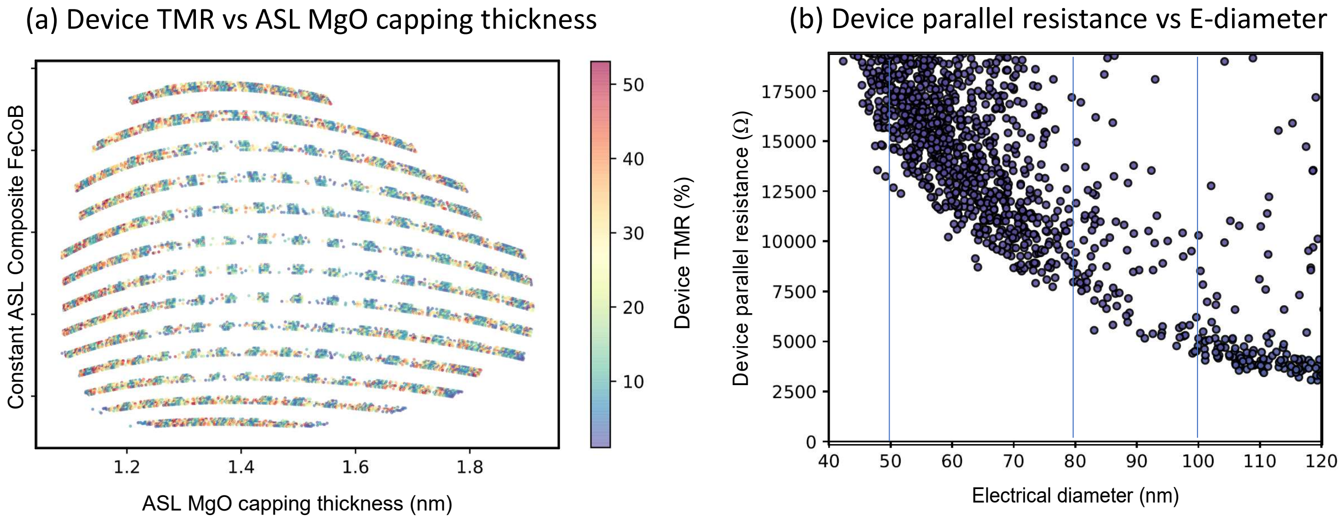

Figure. 4.25: (a) Devices tunnel magneto-resistance vs extrapolated MgO thickness of the ASL capping. (b) Devices parallel resistance vs electrical diameter.

In addition, the extracted RxA at 50 nm diameters is increased by up to 25 $\Omega\mu m^2$. These enhancements in TMR are then more probable from better quality of the barriers after the fabrication process. Moreover, figure.4.25.(b) shows the typical dependency of the device's resistance with the pillar's electrical diameter. For small diameters (between nominal diameters of 50 and 80 nm), the device's parallel resistance rises up to $20K\Omega$ (one order of magnitude higher than the previous sample with a constant thickness of 1.2 nm of MgO capping on the ASL in figure4.19). These large values of resistance are not explained by the serial resistance added by the ASL MgO capping, but rather by possible oxidation of the pillar's Ta hard mask during the fabrication process. Following the optimization of the main materials in this section, an initial assessment can be made to confirm whether the relative thermal stability of the ASL has been indeed reduced by retrieving the resistance response of this optimized ASL-DMTJ stack vs voltage pulse amplitude. The R-V loops extracted for each device's nominal diameter are shown in figure.1.26.(a), (b) and (c) with the confrontation with their respective R-H loops. The devices were measured at the central region of the wafer, meaning that the MgO capping of the composite ASL is roughly around 1.5 nm (ASL MgO capping thickness ranging between 1.4 to 1.6 nm in figure **??**.(b)). As seen from these resistance responses, for all the device sizes, the same values of resistance are acquired under field sweep and voltage sweep at maximum values of either field (± 2000 Oe) or voltage pulse amplitude (± 1 V). These results are a clear confirmation that these ASL-DMTJ devices are being written in the most stable configurations P(R1) and AP(R3) with voltage, hence without stabilizing any intermediate states R4 or R2 after the application of the voltage pulses. The magnetization of both the ASL and the SL thus ends always in parallel alignment independently of the write operation. Comparing to the initial macrospin modeling discussed in chapter 2 section 2.2.5 "Voltage induced dynamics for $\Delta_{SL} > \Delta_{ASL}$", this could be a direct indication that the relative thermal stability factors of the layers are fulfilling the condition of having an ASL with lower thermal stability than the SL. Figure.4.27 depicts a more accurate comparison between the extracted critical voltages for each transition as a function of the nominal diameter size for the devices in the central region of the wafer.

(a) Comparison between R-H and R-V loops for a 100 nm diameter device

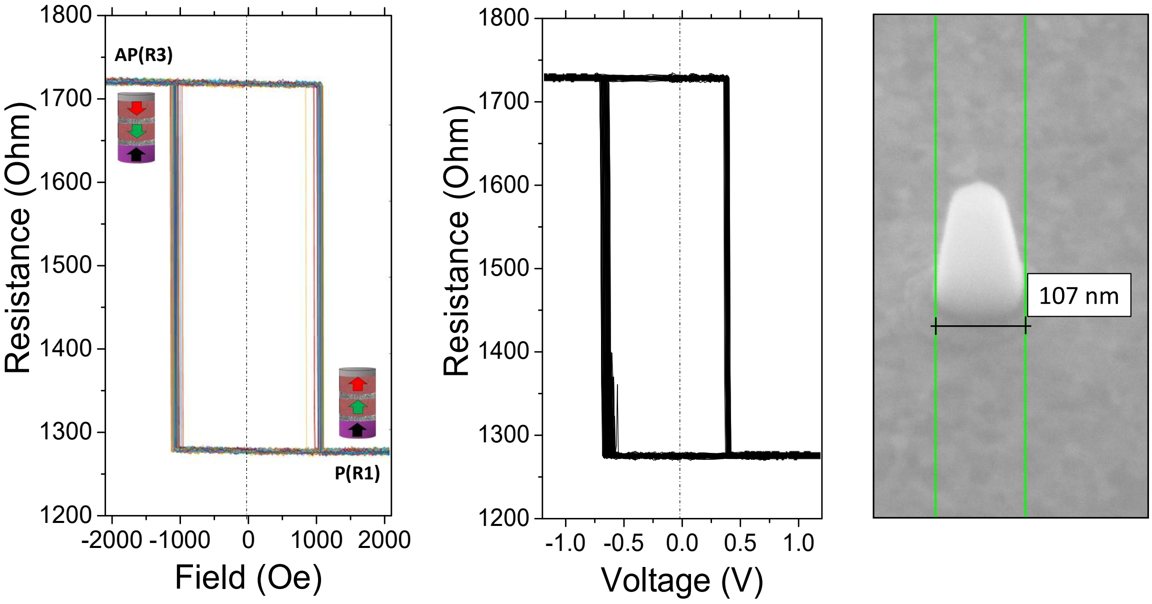

(b) Comparison between R-H and R-V loops for a 80 nm diameter device

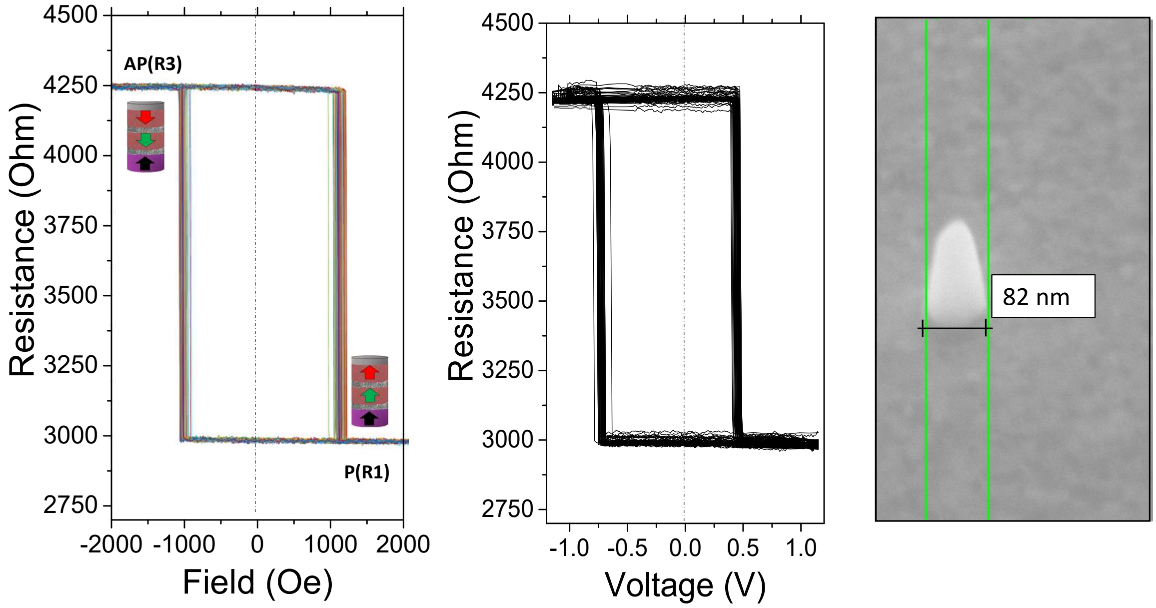

(c) Comparison between R-H and R-V loops for a 50 nm diameter device

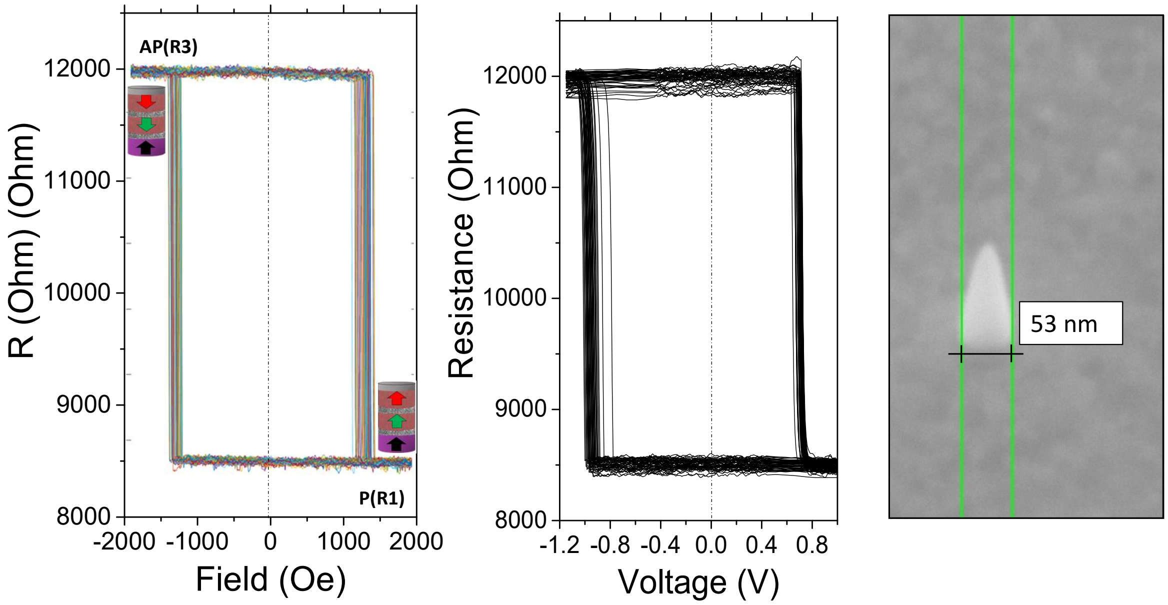

Figure. 4.26: Comparison between the R-H and R-V loops extracted for devices nominal diameters of (a) 100 nm,(b) 80 nm and (c) 50 nm at the central regions of the wafer.

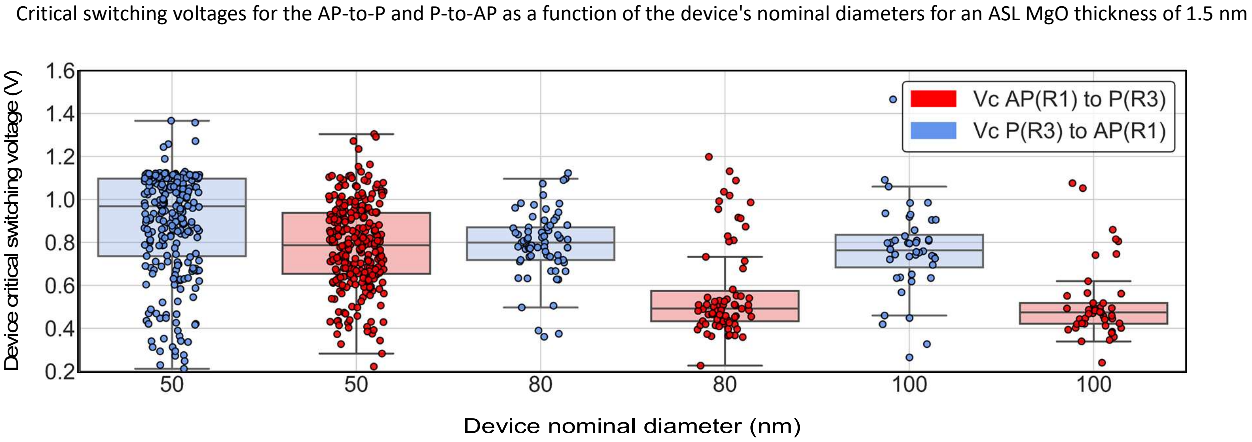

Figure. 4.27: Critical switching voltages for the AP(R3)-to-P(R1) and P(R1)-to-AP(R3) as a function of the devices nominal diameters for devices in the central regions of the wafer (ASL MgO capping thickness between 1.4 and 1.6 nm).

From this comparison, it is observed that for the devices with nominal diameters of 50 nm, the respective voltages for the AP(R3)-to-P(R1) and P(R1)-to-AP(R3) transitions are more symmetric once the PMA of the ASL has been reduced. However, regardless of the nominal diameters of the devices, the P(R1) to AP(R3) transition still involves 0.2 V more of the voltage pulse amplitude than for the transition from AP(R3) to P(R1). Although this study serves as preliminary proof that the ASL PMA has been optimized, the final verification of the required switching sequences to exert an additive STT from both the reference layer and the ASL must be performed by time-resolved measurements of the intermediate resistance state R2 during the application of the writing voltage pulses. These measurements will be addressed in the following chapter 5 which focuses on the experimental evaluation of device STT efficiency and writing dynamics on fully optimized stacks.

Chapter 5

Experimental evaluation of device STT efficiency and writing dynamics

5.1 Optimized device stack description

The spin transfer torque switching efficiency of the optimized ASL-DMTJ was evaluated by comparing it to that of a single-MTJ stack with the same composite storage layer thickness but no Assistance layer (dead magnetic layer in place of the composite ASL) [172]. Figure.5.1.(a) and (b) illustrates the main material stacks of the samples utilized in this chapter for the optimized ASL-DMTJ and the single-MTJ respectively. For the ASL-DMTJ devices, two samples were fabricated with just a variation on the natural oxidation parameters of the barrier in between the ASL and the SL (Tunnel barrier in the second MTJ). As discussed throughout the document, the value of RxA product of this barrier minimizes the dilution of the TMR signal of the main barrier between the RL and the SL, which is in fact the main MTJ that stores the resistance state of the SL with respect to the RL. The main SL-RL tunnel barrier is oxidized at 3x10^{-2} mbar for 30 s, while the ASL-SL tunnel barrier is oxidized at 3x10^{-3} mbar for either 5 s or 1 s (see table.3.0 for a full comparison of TMR and RxA of these barriers). By varying the oxidation parameters of the 2nd barrier in the ASL-DMTJ stack, the reduction in TMR due to the introduction of its series resistance can be minimized. In addition, the comparison of the magnetoresistive properties (i.e TMR and RxA extracted at the patterned device level) between these two samples and the control sample without the ASL can be employed to further evaluate the serial resistance also introduced by the ASL MgO capping. In the end, the proposed optimized stack comprises three insulating barriers, (first SL/RL barrier, second SL/ASL barrier and ASL capping), which can lead to a significant reduction of the device's TMR. Therefore, this issue must be investigated in order to determine the readability of the memory. Along with this study, the ASL-DMTJ stack with higher natural oxidation parameters in the second barrier (thus higher TMR ratio and sensitivity to the SL/ASL reversal orders from the second MTJ) is later investigated in real-time switching experiments for the verification of the specific switching sequences of the ASL/SL coupled system. The detailed optimized stack compositions chosen for these ASL-DMTJ devices are (with material thicknesses in nm):

[Substrate/Ta 3/Pt 25/(Co 0.5/Pt 0.25)x6/Co 0.5/Ru 0.9/(Co 0.5/Pt 0.25)x3/Co 0.5/W 0.2/FeCoB 1.2/ Mg 0.5(30s Oxidation 3x10^{-2} mbar)Mg 0.75/FeCoB 0.8/W 0.2 /FeCoB 0.75/ Mg 0.5(5s or 1s Oxidation 3x10^{-3} mbar)Mg 0.75 / FeCoB 1/ W 0.2 /FeCoB 0.7/ Mg 1.5 nm (1s Oxidation 3x10^{-3} mbar)Mg 0.5/FeCoB 0.4/Ta 3].

While for the control sample with a dead magnetic ASL :

[Substrate/Ta 3/Pt 25/(Co 0.5/Pt 0.25)x6/Co 0.5/Ru 0.9/(Co 0.5/Pt 0.25)x3/Co 0.5/W 0.2/FeCoB 1.2/ Mg 0.5(30s Oxidation 3x10^{-2} mbar)Mg 0.75/FeCoB 0.8/W 0.2 /FeCoB 0.75/ Mg 0.5(5s or 1s Oxidation 3x10^{-3} mbar)Mg 0.75/FeCoB 0.4/Ta 3].

As concluded in the materials optimization at patterned device level (chapter 4 section 4.3), the ASL with double MgO/FeCoB interfaces is kept at 1.75 nm with a constant thickness of 1.5 nm for the top MgO capping (with the lowest oxidation parameters at 1s 3x10^{-3} mbar). Such a combination of FeCoB layer thicknesses and MgO oxide capping led to a high ASL blocking temperature avoiding loss of perpendicular anisotropy due to the joule heating, thus providing the full ASL-DMTJ stack with the required relative thermal stability factors between the SL and ASL (i.e $\Delta_{SL} > \Delta_{ASL}$). For the three samples used in this study, the SL thickness is equal to 1.55 nm. Henceforth, we will refer to the samples as "ASL-DMTJ-LO" (low oxidation time) and "ASL-DMTJ-HO" (high oxidation time) for the two ASL-DMTJ samples with the second tunnel barriers prepared with 1 s and 5 s of oxidation time respectively, and finally "single-MTJ" for the control sample without the influence of the ASL. All magnetic stacks were annealed with no external applied magnetic field at 300°C for 10 minutes and a pressure of 10^{-6} mbar.

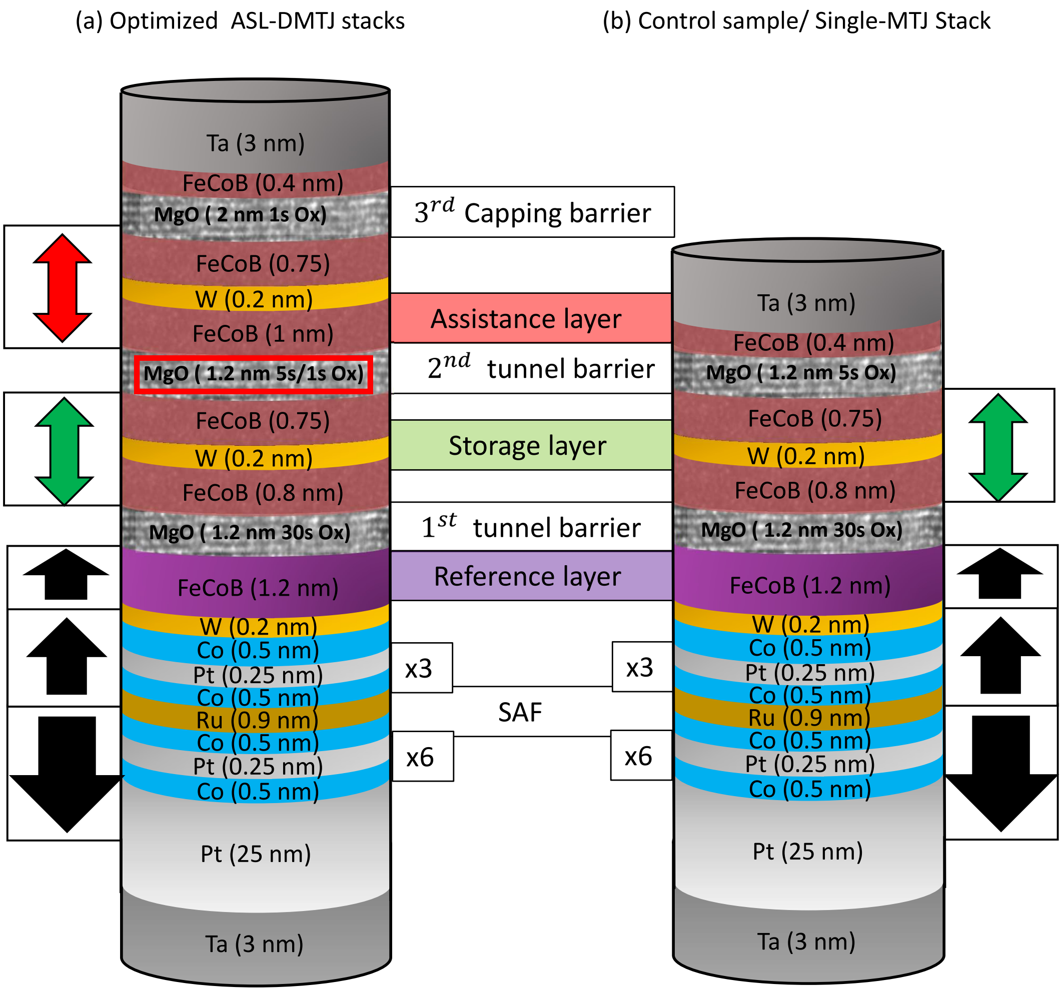
(a) Optimized ASL-DMTJ stacks

(b) Control sample/ Single-MTJ Stack

Figure. 5.1: Stack comparison between the optimized ASL-DMTJ stack comprising a double-interface based ASL and with reduced PMA ($\Delta_{SL} > \Delta_{ASL}$) and (b) control with a dead magnetic ASL at 0.4 nm FeCoB.

In the following study, all statistical distributions of the device's measured properties (TMR, Δ and Ic), are calculated for 700 devices per sample. Figure.5.2 (a) shows the lower TMR signal extracted for the ASL-DMTJ devices regardless of the second barrier oxidation parameters. The reduction that the ASL-DMTJ stacks exhibits is more likely to be explained by the contribution to the serial resistances introduced from both the second barrier and the ASL MgO capping.

In general, for all nominal cell diameters (CD), the single-MTJ reaches a median TMR ratio close to 49%, whereas for the ASL-DMTJ-HO, the median TMR ratio drops by 16%, 21% and 26% for a CD of 50, 80 and 100 nm. The ASL-DMTJ-LO presents less reduction with an average TMR drop of 7%, 15% and 22% at the same values of CD. As was also reported on patterned p-DMTJs with a top pinned polarizer [95] [73], the TMR drop of the main barrier (RL-SL) can be minimized by reducing the serial resistance of the MgO barrier comprised in the second MTJ (Here between the ASL and the SL). The ASL-DMTJ-LO has the second barrier with 1 s of oxidation time thus presenting smaller reduction in TMR with respect to the single MTJ (Note that the single-MTJ stack also has a second barrier for the composite storage layer). The extracted RxA products of the samples are shown in figure.5.2.(b) to (d), where it is clear that the ASL-DMTJ samples have an overall higher value of resistance for all the areas of the junctions. These values of resistance can also be correlated with variations in the area from the nominal diameters or defects and damages introduced during the fabrication (especially for the 50 nm nominal diameters from residual oxides in the Ta hard mask of the pillars, explaining the high values of RxA for the three samples). Nevertheless, these optimized material stacks for the ASL-DMTJ show lower values of TMR mainly from the ASL capping and must taken into account. The TMR signal of the main barrier can be improved by further reducing the serial resistances from the two additional oxide layers introduced in our stack while maintaining a good spin polarization efficiency in the second MTJ (i.e high TMR hence maximizing the mutual STT between the ASL and the SL magnetizations, increasing the secondary STT on the SL and the ASL reversal during the application of the writing pulse).

(a) Comparison of TMR vs device size

(b) Single-MTJ device's TMR vs RxA product

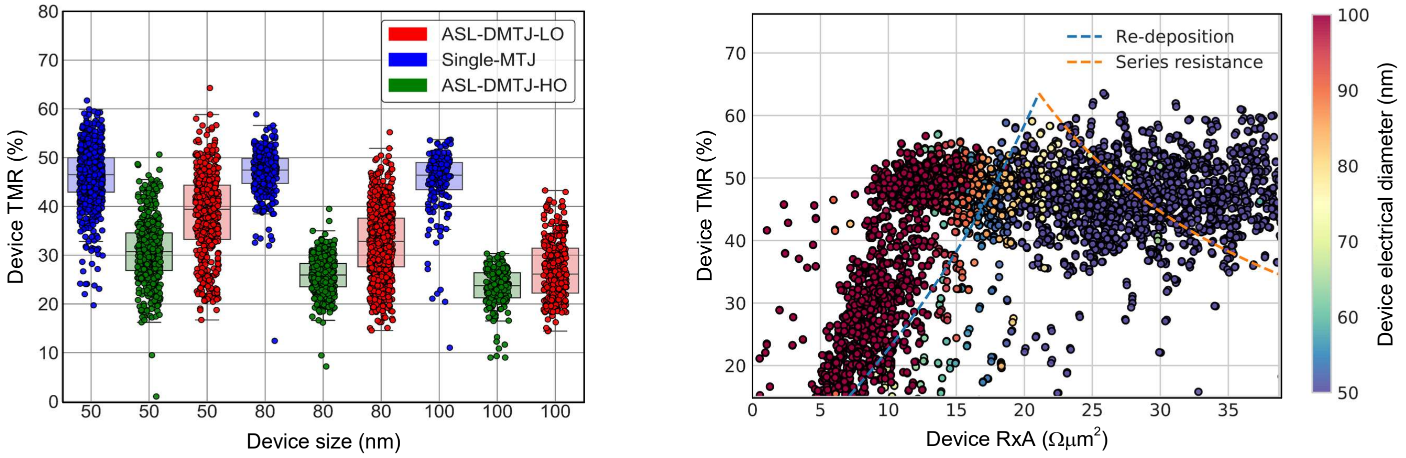

(c) ASL-DMTJ-HO device's TMR vs RxA product

(d) ASL-DMTJ-LO device's TMR vs RxA product

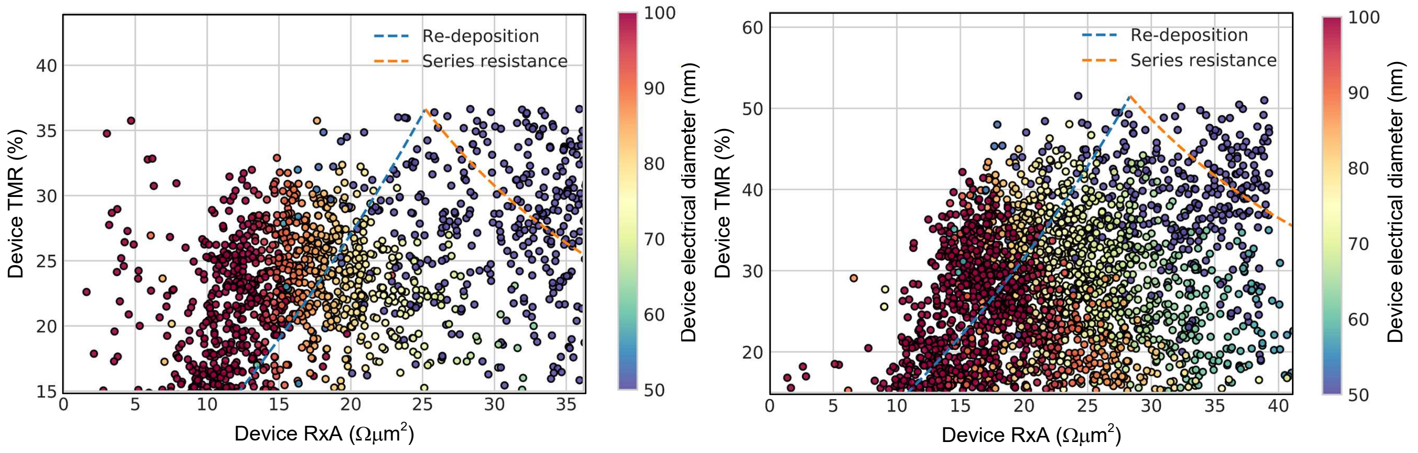

Figure. 5.2: (a) Single-MTJ and ASL-DMTJ device's TMR Tunnel magnetoresistance vs device size. (b) Single-MTJ (c) ASL-DMTJ-HO and ASL-DMTJ-LO (d) devices' TMR as a function of extracted RxA product and estimated electrical diameter.

5.2 Field and voltage induced dynamics

As introduced in the device theoretical working principles, the optimized ASL-DMTJ with $\Delta_{SL} > \Delta_{ASL}$ is required in order to benefit from the magnetic configurations R2 and R3 that produce additive STT contributions from the two polarizers (ASL/RL) and allows the stabilization of the memory cell in resistance states R1 and R3 with the maximum stability in stand by conditions. Independently of the initial state (R3 or R1), both switching sequences first transit through the intermediate resistance state R2 during the application of the writing pulse of voltage. For this reason, two switching sequences must be fulfilled when reversing with voltage from AP to P (R3 to R1) or P to AP (R1 to R3). This was detailed with the numerical simulations in chapter 2 subsection **??**, indicating the magnetic configuration favored by the STT acting on each layer (ASL-SL). An example of the experimental procedure to observe the resistance states and switching dynamics with an external perpendicular field is presented in figure.5.3.(a) to (c), with a comparison between 50 R-H cycles for the single-MTJ and the ASL-DMTJ-HO for devices of various nominal diameters.

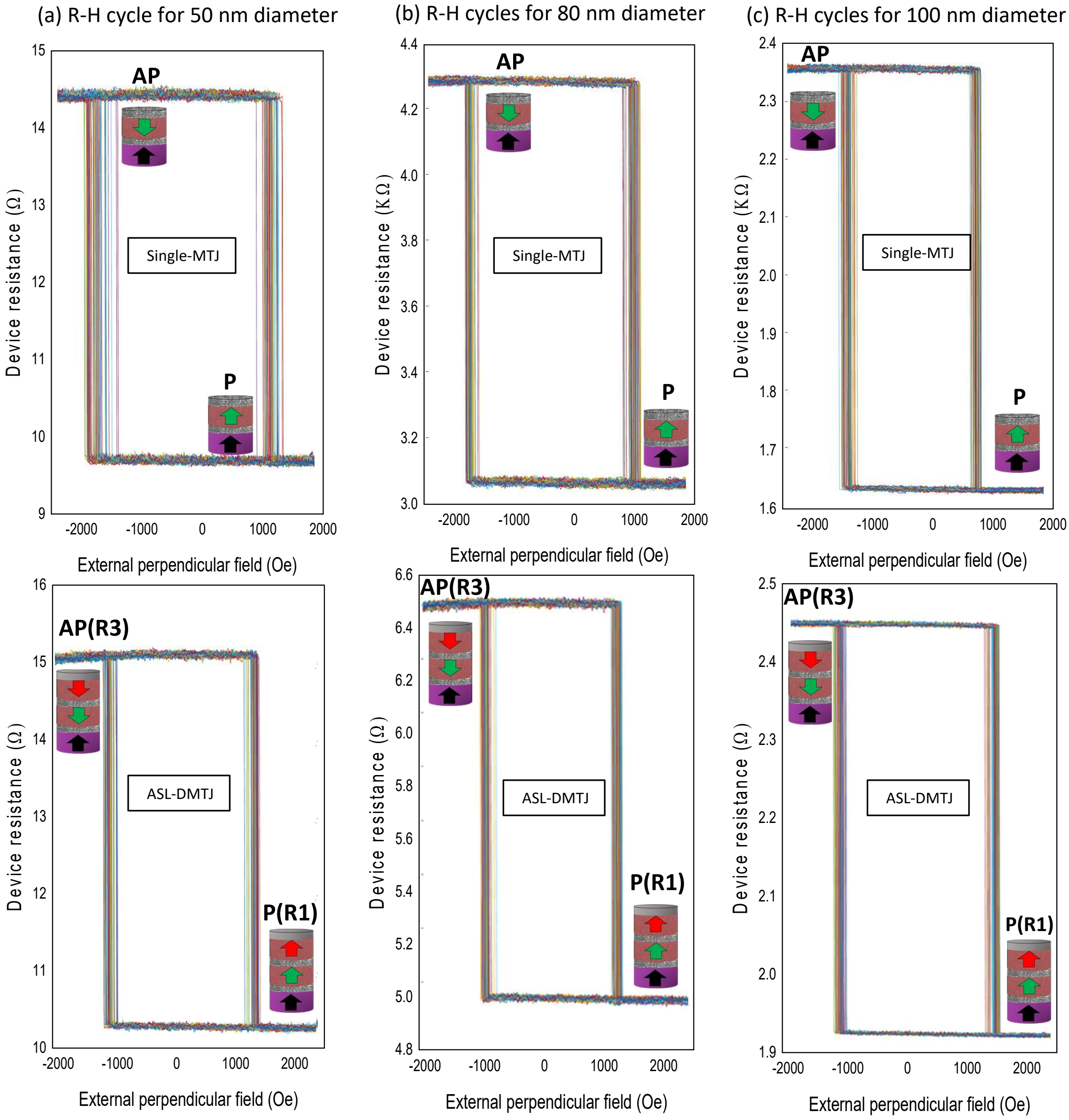

Figure. 5.3: Comparative between the measured device's resistance-Field cycles at nominal diameters of 50 nm (a), (b) 80 nm and (c) 100 nm for the single-MTJ and the ASL-DMTJ-HO.

Once again, for all samples both the SL and ASL magnetization reverse together with the magnetic field, so that the resistance changes from R1 (P state) to R3 (AP state), and thus the top MTJ between the ASL and the SL always ends in a parallel configuration without accessing the intermediate resistance state R2 or the highest resistance state R4 in equilibrium conditions. For a more clear comparison with the voltage induced switching, the devices chosen for this comparison are taken with similar resistances between the control sample and the ones corresponding to the ASL-DMTJ. Note that the single-MTJ R-H cycles show a wider spread in coercive fields (More obvious for smaller volumes of the SL at 50 nominal diameters) which is an indication that the thermal stability of these devices might be lower than that of the ASL-DMTJ devices. In the following subsections, we will make a statistical estimation of the final thermal stability factor of the devices extracted by means of the switching field distribution method (see section 3.5.1 subsection 3.5.1 in chapter 3). On the other hand, figure.5.4 presents the resistance-voltage loops for the devices under investigation (same devices as in figure.5.3). It is important to observe that no stable intermediate state R2 is present independently of the reversal direction after the application of the writing pulses. From this preliminary characterization, the binary nature of the memories is confirmed independently of inducing the reversal of the ASL/SL coupled system by either voltage pulses or field.

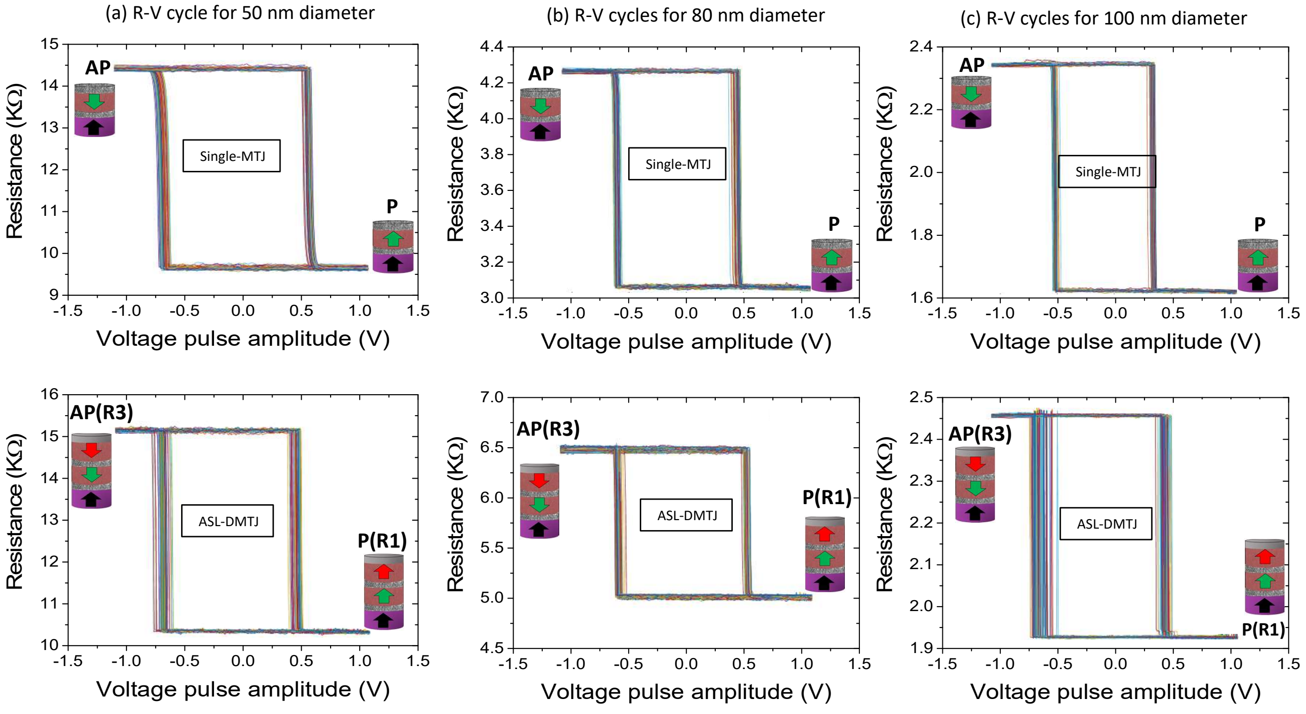
(a) R-V cycle for 50 nm diameter

(b) R-V cycles for 80 nm diameter

(c) R-V cycles for 100 nm diameter

Figure. 5.4: Comparative between the measured device's resistance-Field cycles at nominal diameters of 50 nm (a), (b) 80 nm and (c) 100 nm for the single-MTJ (top row) and the ASL-DMTJ-HO (bottom row).

Validation of the desired switching sequences was possible by performing time-resolved resistance measurements [172] [173]. The experimental procedure to observe the resistance states and switching dynamics is presented in subsection 3.5.2 in chapter 3. A voltage pattern composed of negative and positive square pulses is applied to the cells. The first pulse initializes the resistance state such that the variations in the transmitted voltage through the junctions (Resistance states) can be observed during the second pulse. From the preliminary R-V characterization from figure.5.4, the amplitude of the voltages for the initialization of the memory is determined as well as the writing voltage for the real-time observation of the switching dynamics.

In the time-resolved study, V(AP to P) and V(P to AP) writing voltages were chosen with an amplitude yielding 50% switching probability and a pulse length of 100 ns. In addition, in the R-V cycles presented in figure.5.4 a difference in voltages to switch as well as in switching voltage distributions for AP to P and P to AP are observed (being wider for the P to AP transition), which as will be discussed, is understood from the different switching dynamics for the two transitions. Stable configurations R1 and R3 are identified from the R-H loops in figure.5.3 in the two stable parallel configurations of the ASL/SL coupled system with respect to the RL. Figure.5.5 (a) and (b) summarize the main results for a ASL-DMTJ device of 100 in nominal diameter, depicting the AP to P (R3$\Longrightarrow$R1) and P to AP (R1$\Longrightarrow$3) reversals at zero applied field (I) and with an applied external perpendicular field (II). The magnetic field is applied in order to favor the AP(R3) configuration, therefore, it delays the full reversal of the layers for the AP(R3) to P(R1) transition while it helps the ASL switching and stabilizes the R2 state for the P(R1) to AP(R3) transition. This field is applied to allow a clear observation of the intermediate resistance sate during the full reversal of the layers. It becomes clear that although only states R1 and R3 are stable when the voltage pulses are finalized, the reversal process goes through an intermediate resistance state R2 (IRS). This state lasts through the whole pulse duration and can be stabilized with the negative external field (opposite to the RL magnetization direction). The applied field and voltage level determine the relative probability of the reversal trajectory. During the AP(R3) to P(R1) transition (Figure.5.5.(a)) the SL switches first stabilizing the R2 configuration. This happens with the highest efficiency with the combined STT effects from ASL and RL. Then the ASL finally reverses by the STT from the storage layer spin-polarized current, thus ending in the full parallel configuration (R1).

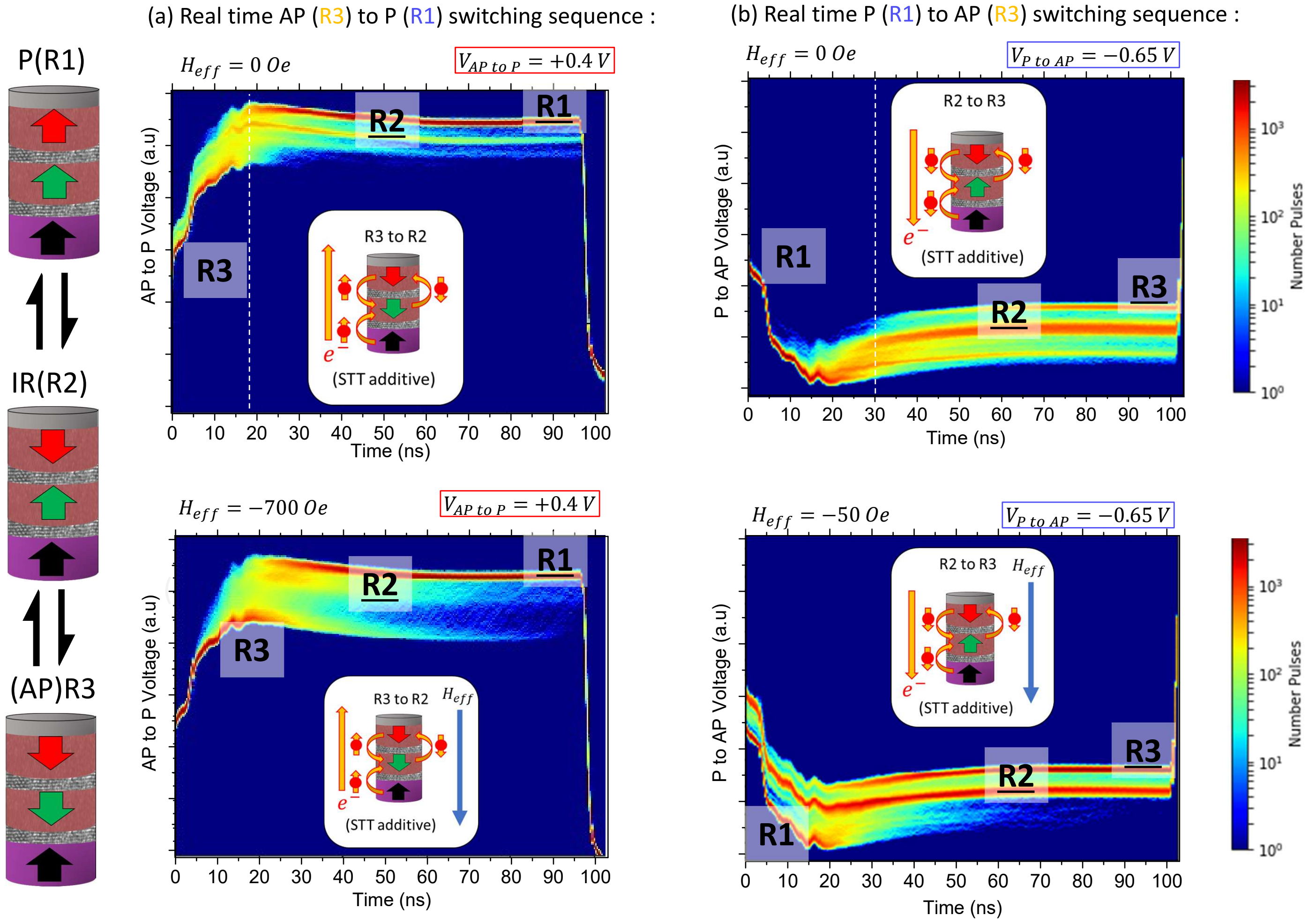

Figure. 5.5: (a) and (b) Real time traces of the switching sequence from AP(R3) to P(R1) and P(R1) to AP(R3) respectively transiting through the R2 state. (c) and (d) same real time traces with a negative applied field favoring the AP(R3) state.

Getting additive STT contributions from both the ASL and RL in the AP(R3) to P(R1) transition is straightforward since in the AP (R3) state, the two polarizing layers are already anti-parallel (i.e RL and ASL). More difficult, is to get the transient anti-parallel configuration between the polarizers corresponding to R2 in the P(R1) to AP(R3) transition, since here, the ASL has to switch first to avoid the R4 state where the net STT on the SL would be reduced. As predicted by the numerical simulations, independently of the writing direction of the memory cell, the switching sequence of the two magnetic tunnel junctions comprised in the ASL-DMTJ always goes through the state R2. This leads to high STT efficiency due to the additive STT contributions from RL and ASL acting on the storage layer independently of the switching direction. Despite the successful confirmation of these specific switching dynamics, the expected asymmetry in switching times for each reversal is also observed experimentally. The full reversal for the AP to P transition (R3 to R2 to R1) requires a minimum of 20 ns versus 30 ns for the P to AP transition (R1 to R2 to R3). This difference in switching times was already expected from the macrospin simulations at 0 K, and attributed to the fact that the ASL magnetization must be switched first during the P to AP transition so the spin-transfer torque exerted by its spin-polarized current adds to the one from the RL.

5.3 Assistance layer influence on Storage layer thermal stability

In this section, we discuss the thermal stability improvements provided by our proposed stack design. The thermal stability factors of single devices were extracted from the statistical distribution of coercive fields (see "Thermal stability extraction with field" in chapter 3 section 3.5.1), by fitting the data from 50 resistance-field loops at a sweeping field frequency of 1 Hz. The switching probability distribution as a function of the magnetic field amplitude is fitted to the SFD model assuming a switching attempt time of 1 ns. Due to the particular switching mechanism with an external perpendicular field, this procedure is the most preferable method used in our samples comparisons to highlight the effect of the parallel coupling between the SL and ASL (Note that independently of the samples composition along the document, all ASL-DMTJ devices are written with field between the P(R1) and AP(R3) where the ASL/SL coupled system is always in parallel alignment). Before continuing with the evaluation of the thermal stability obtained for the optimized stack compositions in this chapter, we will present the first experimental demonstration of the stabilization of the Storage layer magnetization out-of-plane in the limits of the layer perpendicular anisotropy. This study was introduced in the materials optimization at patterned device level (chapter 4 section 4.2.1 with the details on the material stack compositions in figure.4.13). In this section, it was given an initial evaluation of the influence of the magnetic coupling between a single-interface based ASL at 1.5 nm between the parallel ASL-SL configurations (P(R1) to AP(R3)). The devices extracted coercive fields as a function of SL thickness presented a successful stabilization of the SL magnetization when reducing its PMA (see figure.4.14.(b)). The observed rises in coercivity by the influence of the assistance layer can also be translated in enhancement of the SL thermal stability factor. Figure.**??**.(a) shows an increase of the thermal stability factor by 15-20, for the single-interface ASL based ASL-DMTJ (sample A) compared to the reference (sample B) with a dead magnetic ASL.

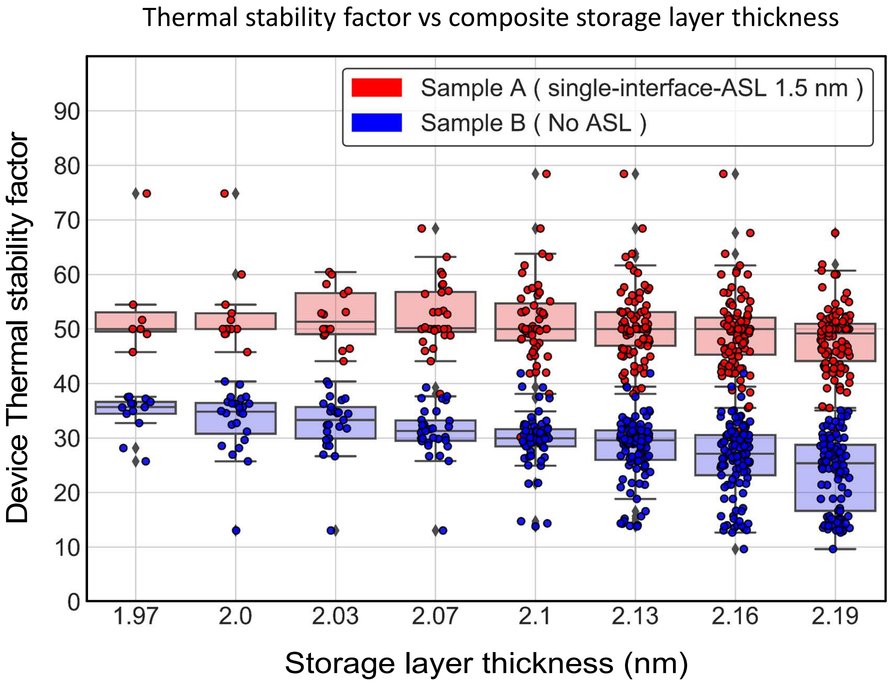

Figure. 5.6: Comparison of Sample A and Sample B thermal stability as a function of storage layer thickness.

The coupling with the ASL allows the perpendicular magnetic anisotropy to be maintained for SL thickness at least up to 2.1 nm while the reference sample B showed a magnetic reorientation from out-of-plane to in-plane anisotropy below this thickness. These results served as initial experimental confirmation of previous predictions based on single-domain simulations on similar stack structures [109] (so-called dynamic reference layer in their publication) and the magneto-static numerical calculations in section 2.2. As in our case, this previous work assumed only magneto-static coupling between the SL and ASL magnetization and reported that the magnetization direction of the top polarizer follows the SL stray field in standby conditions, thereby reinforcing the devices thermal stability in parallel alignments (both P(R1) and AP(R3)). On the other hand, we also evidenced an indirect interlayer coupling through the low oxidation barriers at full sheet film level (Chapter 4 section 4.1.3) which could be employed to further increase the coupling between the ASL and the SL. This coupling between the perpendicular electrodes was found to be ferromagnetic, and its amplitude depends on the oxidation parameters of the MgO tunnel barrier utilized in the magnetic tunnel junction. In this context, the stacks described at the beginning of this chapter concerning the ASL-DMTJ-HO and ASL-DMTJ-LO (figure.5.1.(a)) can be utilized to evaluate the influence of the coupling strength on the device final thermal stability factor at the patterned device level. Figure.5.7 highlights the differences in thermal stability factors between the two ASL-DMTJ stacks and the single-MTJ for the three device sizes under investigation.

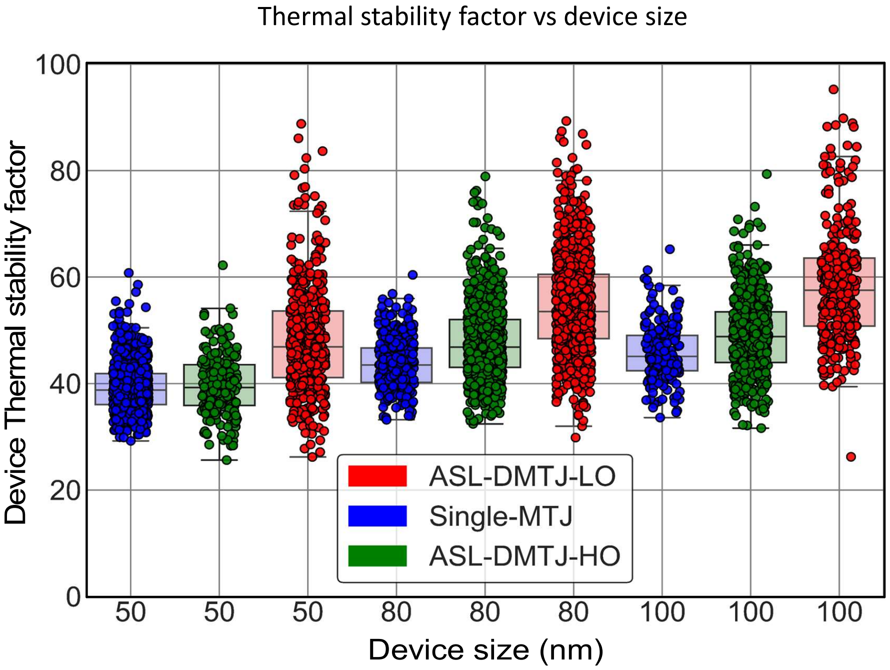

Figure. 5.7: Thermal stability (Δ) as function of device size for the ASL-DMTJ-LO (red), single MTJ (blue) and ASL-DMTJ-HO (green).

The control sample corresponding to the single-MTJ devices already satisfies the 10 year retention requirements with median values of Δ at 40 for the 50 nm diameters, 43 for the 80 nm diameters and 45 for the 100 nm diameters. The ASL-DMTJ-HO, with the second MgO Barrier with a higher oxidation time (reduced indirect coupling between the ASL and the SL), presents comparable median values of thermal stability for the small pillar sizes (CD≤50 nm), increasing only by 4-5 in average for the 80 nm and 100 nominal diameters. On the contrary, the optimized stack with lower oxidation time in the second tunnel barrier (i.e ASL-DMTJ-LO with a higher coupling through the MgO barrier in the second MTJ), reaches an average increase of 10 no matter the pillar diameter, with median Δ of 50, 54 and 58 for the CD of 50, 80 and 100 nm respectively. Then, if we examine the maximum reachable thermal stability factors in this sample, it is possible to obtain even 80 k_BT for all pillar sizes.

It is also important to notice the higher dispersion in Δ extracted for the ASL-DMTJ-LO, which can be explained by the weaker oxidation of the second tunnel barrier, thus leading to variation of the coupling strength of the ASL/SL coupled system from device to device. These results demonstrate the important retention improvements that the ASL-DMTJ stack can bring if the magnetic coupling with the assistance layer is properly adjusted. The next step is to confirm whether the critical current to write the memories by STT is indeed reduced for a final evaluation of the memory cells performance.

5.4 Reduction of Storage layer critical current density

In this section, we focus on the evaluation of the critical current to switch the devices by spin-transfer torque only with the optimized stacks. The devices with the ASL-DMTJ-HO stacks are the ones with verified compliance with the relative thermal stability factors between the ASL and the SL ($\Delta_{SL} > \Delta_{ASL}$) for which the required time-resolved switching sequences was confirmed. The critical current density (J$_c$) comparison was carried out separately for P⟶AP reversal in figure.**??**.(a), and for AP⟶P in (b) due to the specific switching schemes for each writing operation. For the extraction of the devices J$_c$, The values of V_c for each transition were extracted from the fitted statistical distribution of switching voltages to the SCD model for 50 R-V cycles (E.g R-V cycles shown in figure.5.4). Then, the critical current densities were determined considering the pillar nominal area and applying Ohms law with the initial parallel or anti-parallel resistance state of the memories. See the material and method chapter 3, subsection 3.5.2 for a detailed description of the methodology to extract V_c for each transition. Following this study, the additive STT yields a reduction in the extracted median J$_c$ values in both ASL-DMTJ samples for the P⟶AP reversal. The decrease in J$_c$ is only possible if the dual STT contributions from both polarizing layers are acting during the application of the writing pulses. Besides, even if there is only experimental verification of the ASL/SL switching sequences for the devices with a higher sensitivity on the second barrier (i.e devices with the ASL-DMTJ-HO stack), regardless of the oxygen content in the second tunnel junction, these overall reductions in J$_c$ confirm that the double STT is acting in the P⟶AP transition in most devices. The reduction in critical switching currents density is significant for the ASL-DMTJ-LO at higher device CD (larger than 80 nm), with a relative reduction of 0.41 and 0.33 MA/cm^2 for the 80 nm and 100 nm diameters in comparison to the required J$_c$ for writing the single-MTJ devices (with median J$_c$ of 0.98 MA/cm^2 and 1.2 MA/cm^2 for the same nominal diameters). The devices with the ASL-DMTJ-HO stack present slightly higher values of J$_c$ for the P to AP transition at 80 nm diameters, in this case, reducing by 0.21 MA/cm^2 while a similar reduction for the 100 nm devices by 0.30 MA/cm^2. On the other hand, it is observed that the contrary happens at smaller diameters, presenting lower J$_c$ the devices with the ASL-DMTJ-LO stack (decrease of J$_c$ of 0.14 MA/cm^2 against 0.33 MA/cm^2 relative to the single-MTJ devices at 0.9 MA/cm^2 for the ASL-DMTJ-LO and the ASL-DMTJ-HO respectively). The current density of the transition AP⟶P is essentially similar between the ASL-DMTJ-LO and the single-MTJ devices within the interquartile range for 50 and 100 nm diameters, only decreasing for sizes of 80 nm diameters by 0.23 MA/cm^2 (figure.**??**). However, for the ASL-DMTJ-HO there is an important reduction (by a factor of 2) in J$_c$ by 0.33 MA/cm^2 0.41 MA/cm^2 0.54 MA/cm^2 for 50, 80 and 100 nm diameters respectively, taking into account that the values for the single-MTJ are at 0.67 MA/cm^2 0.78 MA/cm^2 0.88 MA/cm^2.

(a) P to AP critical current density

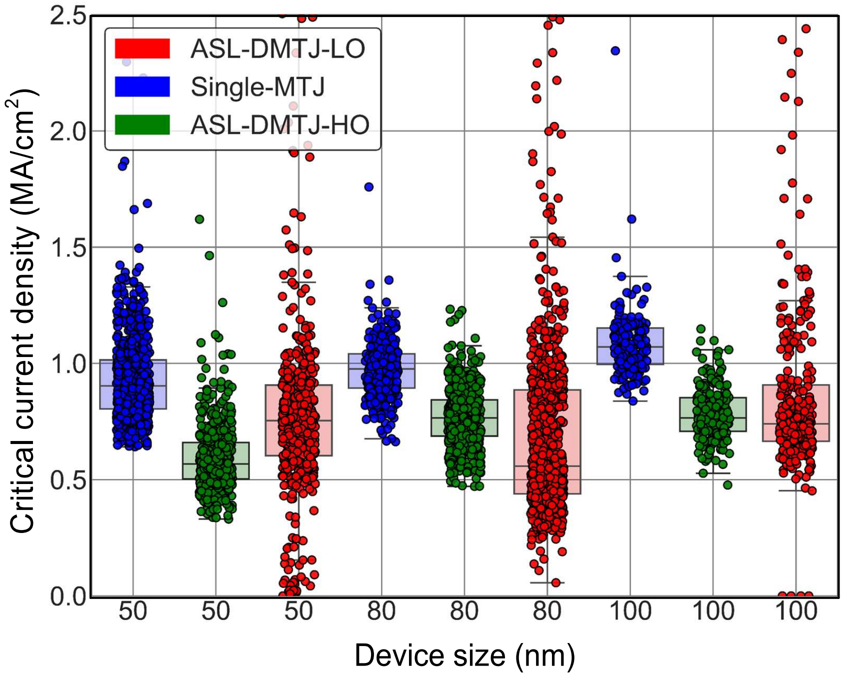

(b) AP to P critical current density

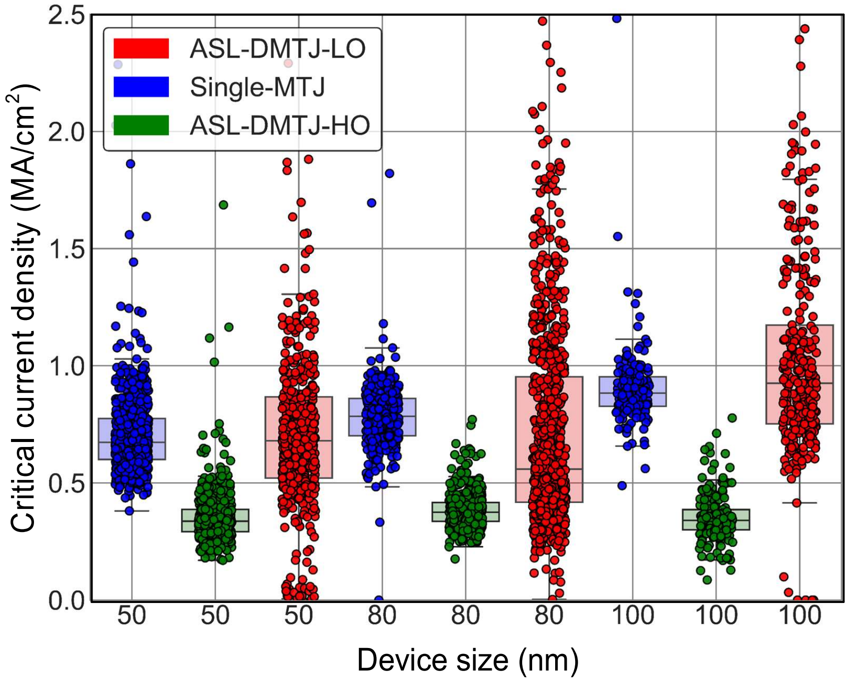

Figure. 5.8: (a) P⟶AP and (b) AP⟶P critical current density comparison as function of device size between the ASL-DMTJ-LO (red), single MTJ (blue) and ASL-DMTJ-HO (green).

The higher reduction in critical current density extracted from the ASL-DMTJ-HO devices for the AP⟶P transition could be explained by the fact that the coupling between the layers is reduced while the TMR of the second junction is increased, thus reducing the energy barrier for switching the SL magnetization (see Δ values in figure.5.7 between the P(R1) and AP(R3) magnetic configurations) and maximizing the secondary STT incoming from the polarized current from the ASL. In general, both ASL-DMTJ samples present an average 30% reduction in J_c to switch for the P⟶AP transition and conservation or 50% reduction for the AP⟶P transition. This happens despite higher stability and lower TMR amplitude reported in the previous sections pointing out an enhanced STT efficiency of the memory cell switching.

5.5 ASL-DMTJ Figure of merit (Δ/I_c) evaluation

Finally, the STT efficiency of the optimized stacks developed during this thesis can be determined. The write efficiency is commonly evaluated by a figure of merit (FOM) defined as the ratio between the barrier height separating the two stable states of the storage layer magnetization (proportional to the logarithm of the memory cell data retention) and its critical STT-induced switching current (Δ/I_c). Note that I_c here is defined by the current required to switch two to carry out the full reversal of both layers with a 100 ns pulse, whereas I_{c0} is commonly defined for 10 ns writing pulse. As discussed in the previous sections of this chapter, the optimized ASL-DMTJ devices mainly showed an increase by 5 to 10 in thermal stability factor with respect to the control sample (i.e single-MTJ) between the most stable configurations corresponding to the ASL/SL coupled system in parallel alignments. These magnetic configurations were found to be the two stable states at equilibrium after being writing the cells by magnetic field or voltage pulses in static conditions. The thermal stability of the storage layer is thus reinforced by the ferromagnetic coupling with the Assistance layer compared to the data retention extracted for the same stack but with a dead magnetic ASL. The increase in thermal stability can be controlled by the oxidation parameters of the barrier between the two layers, modulating the amplitude of the indirect exchange like coupling through the low oxidation MgO barrier. In addition, the critical current densities at the same time are reduced for the P to AP transition by 1/3 and even 1/2 for the AP to P transition when the oxidation conditions of the second barrier are strengthened (yielding a higher TMR in the second MTJ). Figure.5.9.(a) and (b) summarizes the correlation of these results with the calculated figure of merit as a function of device nominal diameters from the data in figure.5.7 and figure.**??**.(a)-(b). For the P$\longrightarrow$AP transition, the median FOM is increased in all cases in the ASL-DMTJ-LO compared to the conventional single-MTJ, with a 100% increase for devices with 80 and 100 nm nominal diameters while a smaller 30% increase is obtained for 50 nm diameter cells. In some best cases, devices at smaller sizes presented high values of thermal stability factor ($\Delta > 80$), together with low switching current. For those devices is possible to achieve up to a 4 fold increase in STT FOM. The devices from the ASL-DMTJ-HO stack show as well a general increase in FOM for the P$\longrightarrow$AP transition at larger diameters. However, in this case, the enhancements are moderate due to the minor improvements in Δ and the higher critical current extracted from these devices than from the ASL-DMTJ-LO stack. On the contrary, for the ASL-DMTJ-HO cells at 50 nominal diameters, the lower rise in Δ is balanced by the reduced I_c, thus presenting similar values in median FOM to the ones from the ASL-DMTJ-LO. The highest enhancement in FOM is actually realized with the ASL-DMTJ-HO devices for the AP to P transition due to the 2x decrease in critical switching current (while the Δ is practically maintained for 50 nm sizes and increases by 5 in average for the larger sizes). Following the FOM trend as a function of pillar size, downscaling the devices is expected to lead to further improvements in efficiency.

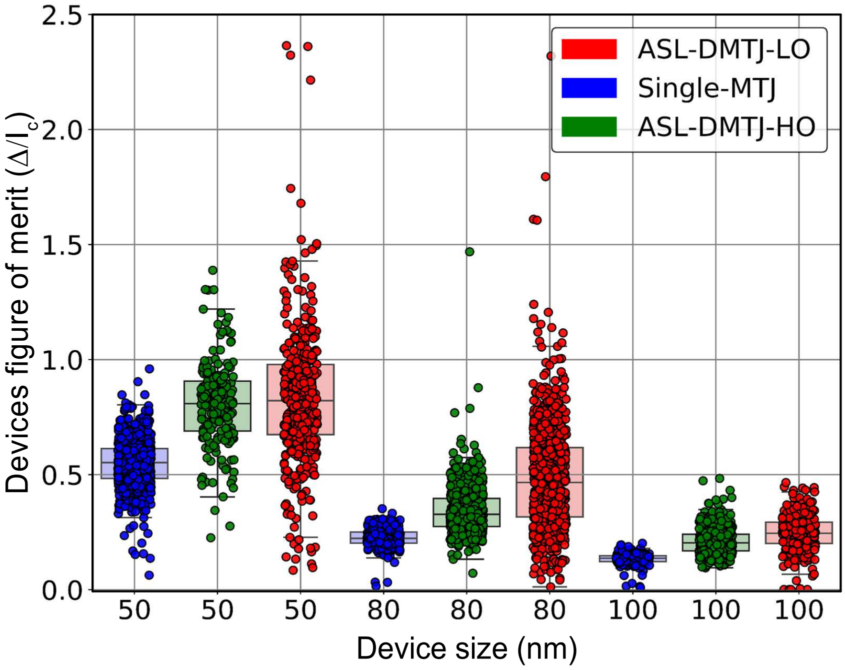

(a) P to AP Figure of merit (Δ/I_c) vs device size

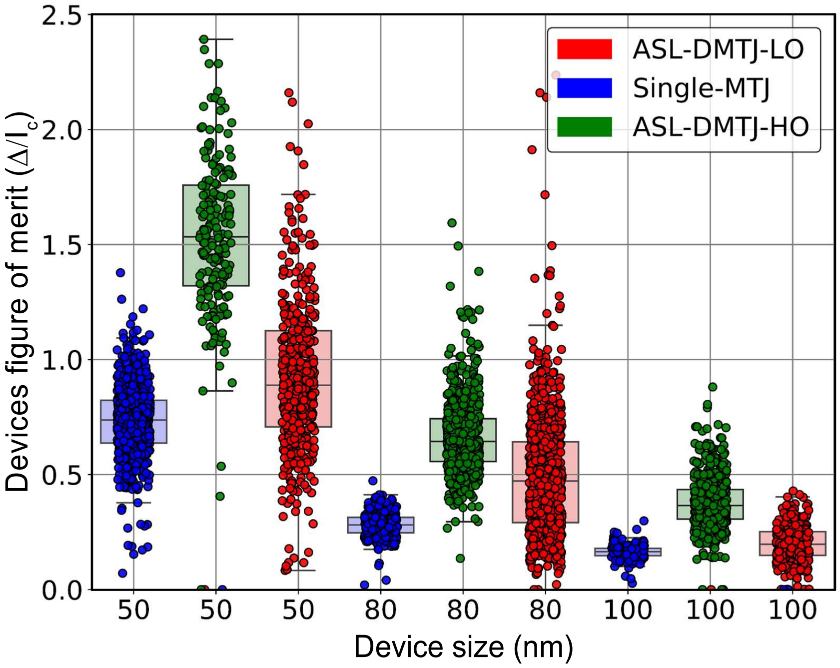

(b) AP to P Figure of merit (Δ/I_c) vs device size

Figure. 5.9: (a) P⟶AP and (b) AP⟶P figure of merit comparison as function of device size between the ASL-DMTJ-LO (red), single MTJ (blue) and ASL-DMTJ-HO (green).

In conclusion, Figure.1.10 summarizes all the devices performances discussed in this chapter for the optimized ASL-DMTJ stacks, benchmarking also our results with previous works on conventional p-DMTJs with two fixed top and bottom polarizers. Both the thermal stability factors and critical switching currents correspond to the median values extracted in section 5.3 and 5.4, with the critical current densities required for the less efficient write operation for each respective cell diameter (CD). Although our devices present low values in TMR, a clear improvement in STT-FOM over state-of-the-art conventional p-DMTJ stack designs is evidenced.

These improvements are achieved with a much simpler magnetic stack which is easier to fabricate (Just adding and optimizing a free layer as a switchable top polarizer and suppressing all the required SAF structure). Future optimization in the tunnel barrier-electrodes quality should easily solve these limitations and further increase the FOM of the ASL-DMTJ devices. All Device's metrics outside of this work were adapted and taken from [69] (IBM 2015) [174] (IBM 2021) [74] (IMEC 2020) [71], [72] (SPINTEC 2021-2019).

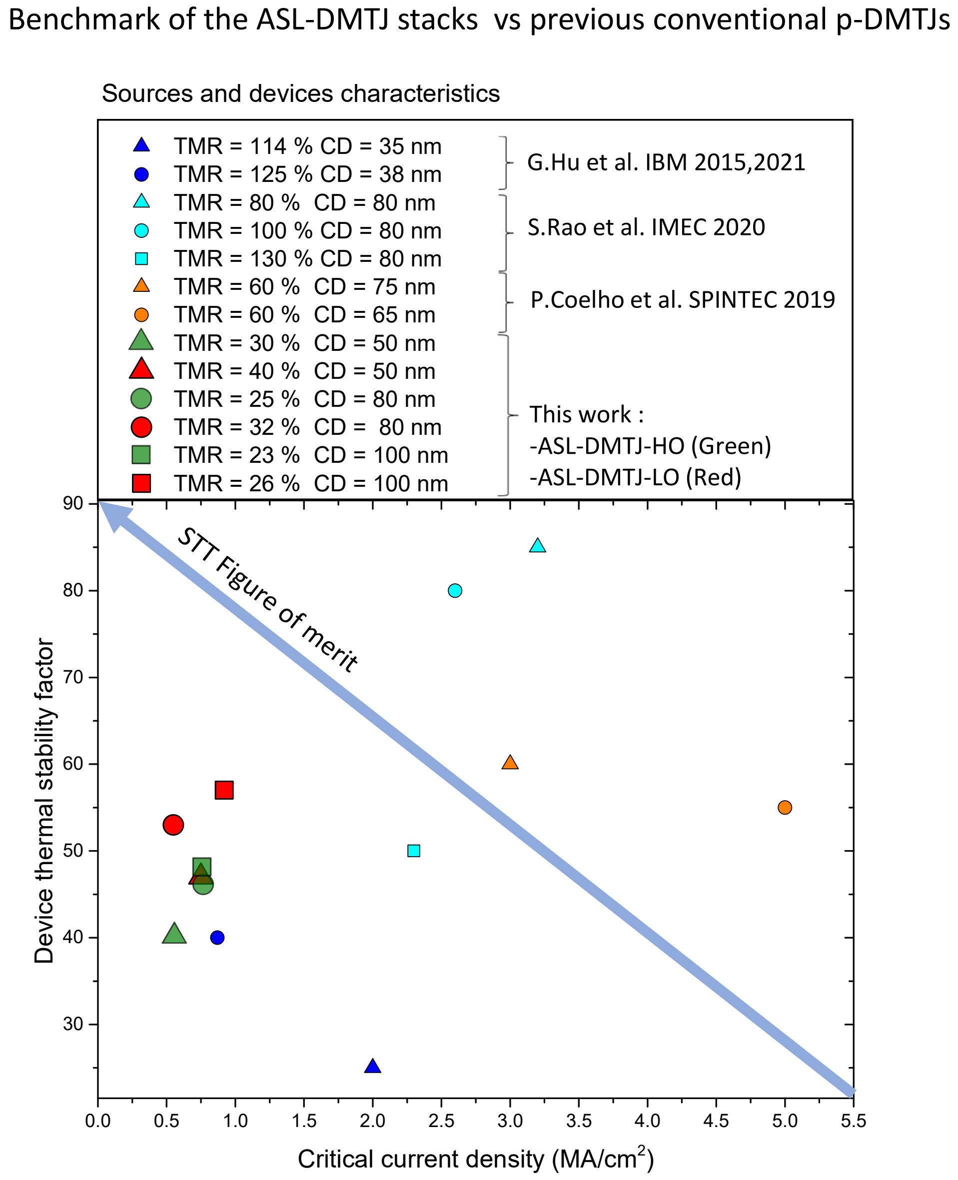

Figure. 5.10: Benchmarking of the ASL-DMTJ stacks developed during this work with respect to previous publications in conventional p-DMTJ designs

Chapter 6

Conclusions and perspectives

The main objective of this thesis was to design and evaluate a new stack design based on a simpler and thinner perpendicular double magnetic tunnel junction with a switchable top polarizer. Called ASL-DMTJ, it relies on the interaction of mutual magnetic coupling and spin-transfer torque between the switchable top polarizer (i.e., the assistance layer) and the storage layer to break the p-STT-MRAM dilemma between increasing data retention and decreasing critical current for switching. As in conventional p-DMTJ structures, the critical switching current is reduced by additive spin-transfer torques acting on the magnetization of the storage layer when the top and bottom polarizers are set in anti-parallel configuration. In contrast, the ASL-DMTJ relies on the suppression of the SAF-multilayer used to fix the magnetization of the top polarizer. This allows the magnetization of the assistance layer to be switched by the incoming spin-polarized current from the storage layer. When the magnetization of the two layers (ASL-SL) is aligned in a parallel configuration, the retention of the SL is further enhanced due to its ferromagnetic coupling. To achieve these properties, the layer coupling and relative thermal stability factors are controlled to meet all requirements for the highest memory cell efficiency.

In Chapter 2, the main theoretical principles of operation of our proposed device are discussed numerically. First, magnetostatic energy calculations show the origins of the thermal stability improvements and their dependence on the magnetic coupling amplitude between the layers. The adapted transport model of a DMTJ with a switchable polarizer is presented indicating the voltage drops across each tunnel barrier in the structure. The magnetic configurations of the ASL-DMTJ result in four possible resistance states, which can be stabilized by an external perpendicular field or voltage pulses. These resistance states are identified by providing an asymmetry between the TMR amplitude of the two tunnel barriers and the resistance area product. The magnetization dynamics of the coupled ASL/SL system was modeled by two coupled LLGS equations, considering in each layer the magnetic coupling and mutual spin transfer damping-like torques. From this first theoretical study it is concluded that for a correct operation an assistance layer with a thermal stability factor lower than that of the storage layer is required ($\Delta_{SL} > \Delta_{ASL}$). This condition ensures the specific reversal orders needed to exert a secondary STT contribution on the SL magnetization during the application of the voltage pulse, while the device always ends up in a parallel alignment between the ASL and SL magnetization, so that the thermal stability factor of the SL is also strengthened independently of the writing direction. Thanks to this first theoretical study, a description of the switching dynamics and STT contributions exerted on each layer comprised in the ASL-DMTJ is fully detailed, determining the specific magnetic properties of each layer to be experimentally optimized for the first proof-of-concept of this device.

In chapter 4, all materials optimization concerning the Assistance layer and Storage layer coupled system are described in order to achieve the conditions $\Delta_{SL} > \Delta_{ASL}$ experimentally. We first optimized independently the perpendicular anisotropy of each layer at thin film level by the use of either single-interface based Assistance layer and a composite double-interface based Storage layer. These first optimizations summarize the main strategies utilized in this thesis to modulate the perpendicular anisotropy of each layer. The three main varied materials parameters are the thickness of the layers, the oxidation conditions of the MgO/FM interfaces and the nature of the boron absorber during the annealing (either Ta or W). The origins of the interlayer exchange coupling through the low oxidation tunnel barriers are also discussed at thin film level. This coupling is found to be ferromagnetic and it decreases with the tunnel barrier thickness and stronger natural oxidation parameters. The most probable origin of this coupling in the ASL/MgO/SL MTJ is from localized dipolar interactions between the ferromagnetic electrodes caused by the MgO interfacial roughness (a.k.a Néel coupling). As the main source of SL thermal stability enhancement is the ferromagnetic coupling with the Assistance layer in the parallel alignments, this indirect exchange-like coupling is employed to increase the amplitude of the coupling for the SL/MgO/ASL system. The materials optimizations at thin film are then applied for the first proof of concept of our proposed stack design in patterned devices. The chosen stack composition is based on a single-interface ASL in the limits of PMA with an FeCoB thickness of 1.5 nm and a composite storage layer with a gradient of thickness. The purpose of this study was to evaluate the coupling influence between the layers in parallel alignments to stabilize the SL in the perpendicular direction. The coercivity values extracted from these ASL-DMTJ devices in comparison with those from a sample with the ASL as a dead magnetic layer indicate a successful stabilization of the SL in the out-of-plane direction for SL thicknesses in which its PMA is not sufficient. On the other hand, this stack composition showed important asymmetries in the critical voltages to switch by spin transfer torque. The origin behind these voltage asymmetries is identified thanks to temperature-dependent macrospin simulations with a good correlation with experimental voltage-field stability diagrams. These simulations point out that in structures with more than one tunnel barrier, the self-heating effects can have a strong impact on the magnetic properties of the layers. It is determined, that at a certain voltage threshold, the Joule heating produced during the application of the voltage pulses causes the ASL to become superparamagnetic. In this superparamagnetic state any STT or magnetic coupling influence from the ASL acting on the SL vanishes, giving rise to the important asymmetries between the critical voltage required for each writing operation. From these simulations, it is also concluded that an ASL with a higher blocking temperature will solve the self-heating issues. The following materials optimization at the patterned device level is thus based on the use of a composite ASL with a tungsten spacer in order to increase the volume of the layer while maintaining a positive effective anisotropy (still with enough PMA). Once again, a good correlation with the numerical voltage-field diagrams verifies that the ASL with a higher volume is acting as a magnetically stable top polarizer. At this moment, the composite-based ASL presented higher thermal stability than the storage layer, presenting the same response versus voltage pulse amplitudes than in the numerical simulations for $\Delta_{ASL} > \Delta_{SL}$. To reduce the ASL thermal stability while maintaining the layer thickness, the oxidation conditions of its MgO capping are varied. This causes the depletion of oxygen at one of the MgO/ASL interfaces reducing its final PMA. The verification of the conditions $\Delta_{SL} > \Delta_{ASL}$ are performed by observing the R-V cycles and comparing them to the same response from the numerical simulations.

Finally, in chapter 5, the ASL-DMTJ optimized stack composition is evaluated in terms of STT writing efficiency with a control sample without the Assistance layer. In this last study, two ASL-DMTJ samples are utilized with a variation on the natural oxidation conditions in the second MTJ (between the ASL and the SL). The variations in this tunnel barrier natural oxidation conditions between the ASL-DMTJ samples allow for the evaluation of both, the amplitude of the indirect coupling of the devices and the introduced serial resistance associated with this barrier. Both ASL-DMTJ samples present reduced values of TMR with respect to the amplitudes obtained with the control samples devices (Single-MTJ). This TMR reduction is minimized for the sample with the lowest oxidation conditions, ascribed to the reduced RA of these barriers. Moreover, is also observed that oxidation parameters of the barrier also influence the final reachable thermal stability of the ASL-DMTJ. While the single-MTJ presented median thermal stability values around 40, the ASL-DMTJ with the lowest oxidation parameters (maximizing the indirect coupling through the barrier) presents median thermal stability of 50 reaching a maximum of 80. The ASL-DMTJ with stronger oxidation conditions achieves only median thermal stability of 45 due to the reduction of the coupling amplitude through the barrier. The enhancements in thermal stability that the ASL-DMTJ presents are then from 5 to 10 points with respect to the single-MTJ with the same SL thickness. The dual free layer system switching sequences were validated by real-time measurements of the device's resistance state during the write operation, confirming that the double STT from the polarizers is acting in both transitions on the Storage layer magnetization. The experimental switching sequences are only observed for the ASL-DMTJ stack with a higher TMR ratio and sensitivity to the SL/ASL reversal orders from the second MTJ (higher natural oxidation parameters in the second barrier). However, in terms of critical switching current, both ASL-DMTJ samples present an average 30% reduction in J_c to switch for the P⟶AP transition and conservation or 50% reduction for the AP⟶P transition, despite the enhancements in thermal stability and pointing out to an enhanced STT writing efficiency of the memory cell switching. As a final conclusion to this work, taking into account the increase in thermal stability and reduction of the critical switching current, the ASL-DMTJ can reach a 2x increase in figure of merit ($\Delta_{SL} > \Delta_{ASL}$) with respect to a single-MTJ with only one spin transfer torque contribution and which SL thermal stability is only base in the PMA arising from the metallic/oxide interfaces. Benchmarking our proposed devices with previous performance metrics obtained for conventional p-DMTJ structures also highlights that the proposed device design is able to reach similar performances with a simplified version of the stack and suppress the complicated SAF multilayer structure required for a top pinned polarizer.

The general perspective for this kind of structure can be oriented in two directions. First, understanding the limits in the size of the proposed mechanism to increase the thermal stability. In fact, following the figure of merit trend with diameter sizes, scaling down the devices it might result in higher efficiencies at much higher memory densities. In addition, as this enhancement in retention is based on the magnetic coupling between the Assistance layer and the Storage layer, it could serve to stabilize the memories out-of-plane at reduced cell nodes within the limits of the surface anisotropy. Second, in terms of readability, in this work, we saw that our proposed stack design presents an intrinsic reduction of the main barrier TMR signal. This is a common flaw from double barrier based magnetic tunnel junctions stacks, but now with the ASL MgO capping is increased. We evidenced that this serial resistance can be minimized by reducing the RxA of the second barrier (between the ASL and the SL). This task should be easily achieved by following the same procedure and optimizing the barrier's crystal quality to maximize the TMR amplitude of the main barrier (between the RL and the SL) so regardless of any intrinsic serial resistances, the final device TMR amplitude is enough for real applications. Finally, in this thesis, we focused on the first experimental proof of concept of an ASL-DMTJ device. From the theoretical working principles to its experimental realization and the first observation of its specific switching sequences. The time resolved experiments showed that the switching speed for the full layers reversal is higher than 20 ns. These switching times should be reduced if maximizing the TMR amplitudes of both barriers and applying higher currents to switch the memory cells (as the critical current is already reduced). Moreover, future investigations in write error rate at decreasing voltage pulse lengths should give a more general idea of the minimum switching times required for the full reversal as well as the power consumption of the proposed device.

List of Figures

Bibliography

[1] John Shalf. "The future of computing beyond Moore’s Law". In: *Philosophical Transactions of the Royal Society A: Mathematical, Physical and Engineering Sciences* 378.2166 (2020), p. 20190061. DOI: 10.1098/rsta.2019.0061.

[2] Ethan Mollick. "Establishing Moore's Law". In: *Annals of the History of Computing, IEEE* 28 (Aug. 2006), pp. 62–75. DOI: 10.1109/MAHC.2006.45.

[3] Chris Mack. "Fifty Years of Moore's Law". In: *Semiconductor Manufacturing, IEEE Transactions on* 24 (June 2011), pp. 202–207. DOI: 10.1109/TSM.2010.2096437.

[4] Prashanth Barla, Vinod Joshi, and Somashekara Bhat. "Spintronic devices: a promising alternative to CMOS devices". In: *Journal of Computational Electronics* 20 (Apr. 2021). DOI: 10.1007/s10825-020-01648-6.

[5] Bernard Dieny et al. "Opportunities and challenges for spintronics in the microelectronic industry". In: (Aug. 2019).

[6] Jagan Meena et al. "Overview of Emerging Non-volatile Memory Technologies". In: *Nanoscale Research Letters* 9 (Sept. 2014), pp. 1–33. DOI: 10.1186/1556-276X-9-526.

[7] Ching Tsang et al. "Design, fabrication and testing of spin-valve read heads for high density recording". In: *IEEE Transactions on Magnetics* 30.6 (1994), pp. 3801–3806. DOI: 10.1109/20.333909.

[8] G. Binasch et al. "Enhanced magnetoresistance in layered magnetic structures with antiferromagnetic interlayer exchange". In: *Phys. Rev. B* 39 (7 Mar. 1989), pp. 4828–4830. DOI: 10.1103/PhysRevB.39.4828.

[9] M. N. Baibich et al. "Giant Magnetoresistance of (001)Fe/(001)Cr Magnetic Superlattices". In: *Phys. Rev. Lett.* 61 (21 Nov. 1988), pp. 2472–2475. DOI: 10.1103/PhysRevLett.61.2472.

[10] Shinji Yuasa. "Magnetic Properties of Materials for MRAM". In: *Introduction to Magnetic Random-Access Memory*. John Wiley Sons, Ltd, 2017. Chap. 2, pp. 29–54. ISBN: 9781119079415. DOI: https://doi.org/10.1002/9781119079415.ch2.

[11] M. Julliere. "Tunneling between Ferromagnetic Films". In: *Physics Letters A* 54 (1975), pp. 225–226. DOI: 10.1016/0375-9601(75)90174-7.

[12] T. Miyazaki and N. Tezuka. "Giant Magnetic Tunneling Effect in Fe/Al2O3/Fe Junction". In: *Journal of Magnetism and Magnetic Materials* 139 (1995), pp. L231–L234. DOI: 10.1016/0304-8853(95)90001-2.

[13] J. S. Moodera et al. "Large Magnetoresistance at Room Temperature in Ferromagnetic Thin Film Tunnel Junctions". In: *Physical Review Letters* 74 (1995), pp. 3273–3276. DOI: 10.1103/PhysRevLett.74.3273.

[14] W. H. Butler et al. "Spin-Dependent Tunneling Conductance of Fe/MgO/Fe Sandwiches". In: *Physical Review B* 63 (2001), p. 054416. DOI: 10.1103/PhysRevB.63.054416.

[15] J. Mathon and A. Umerski. "Theory of Tunneling Magnetoresistance in a Junction with a Nonmagnetic Metallic Interlayer". In: *Physical Review B* 60 (1999), pp. 1117–1121. DOI: 10.1103/PhysRevB.60.1117.

[16] M. Bowen et al. “Nearly Total Spin Polarization in La2/3Sr1/3MnO3 from Tunneling Experiments”. In: *Applied Physics Letters* 82 (2003), pp. 233–235. DOI: 10.1063/1.1534619.

[17] J. Faure-Vincent et al. “High Tunnel Magnetoresistance in Epitaxial Fe/MgO/Fe Tunnel Junctions”. In: *Applied Physics Letters* 82 (2003), pp. 4507–4509. DOI: 10.1063/1.1586785.

[18] Stuart S. P. Parkin et al. “Giant Tunnelling Magnetoresistance at Room Temperature with MgO (100) Tunnel Barriers”. In: *Nature Materials* 3 (2004), pp. 862–867. DOI: 10.1038/nmat1256.

[19] S. Ikeda et al. “Tunnel Magnetoresistance of 604% at 300 K by Suppression of Ta Diffusion in CoFeB/MgO/CoFeB Pseudo-Spin-Valves Annealed at High Temperature”. In: *Applied Physics Letters* 93 (Aug. 2008), pp. 082508–082508. DOI: 10.1063/1.2976435.

[20] S. Tehrani et al. “Magnetoresistive Random Access Memory Using Magnetic Tunnel Junctions”. In: *Proceedings of the IEEE* 91 (2003), pp. 703–714. DOI: 10.1109/JPROC.2003.811804.

[21] Leonid Savtchenko et al. “Method of Writing to Scalable Magnetoresistance Random Access Memory Element”. 2003.

[22] D. Worledge et al. “Spin torque switching of perpendicular Ta—CoFeB—MgO-based magnetic tunnel junctions”. In: *Applied Physics Letters* 98 (Feb. 2011), pp. 022501–022501. DOI: 10.1063/1.3536482.

[23] H Honjo et al. “28.5 First Demonstration of Field-Free SOT-MRAM with 0.35 Ns Write Speed and 70 Thermal Stability under 400°C Thermal Tolerance by Canted SOT Structure and Its Advanced Patterning/SOT Channel Technology”. In: (), p. 4.

[24] William Fuller Brown. “Criterion for Uniform Micromagnetization”. In: *Physical Review* 105 (1957), pp. 1479–1482. DOI: 10.1103/PhysRev.105.1479.

[25] W. Heisenberg. “Mehrkörperproblem und Resonanz in der Quantenmechanik”. In: *Zeitschrift für Physik* 38 (1926), pp. 411–426. DOI: 10.1007/BF01397160.

[26] N. Nakajima et al. “Perpendicular Magnetic Anisotropy Caused by Interfacial Hybridization via Enhanced Orbital Moment in Co/Pt Multilayers: Magnetic Circular X-Ray Dichroism Study”. In: *Phys. Rev. Lett.* 81 (23 Dec. 1998), pp. 5229–5232. DOI: 10.1103/PhysRevLett.81.5229.

[27] D. Weller et al. “Orbital magnetic moments of Co in multilayers with perpendicular magnetic anisotropy”. In: *Phys. Rev. B* 49 (18 May 1994), pp. 12888–12896. DOI: 10.1103/PhysRevB.49.12888.

[28] S. H. Liang et al. “Large and robust electrical spin injection into GaAs at zero magnetic field using an ultrathin CoFeB/MgO injector”. In: *Phys. Rev. B* 90 (8 Aug. 2014), p. 085310. DOI: 10.1103/PhysRevB.90.085310.

[29] B. Rodmacq et al. “Influence of thermal annealing on the perpendicular magnetic anisotropy of Pt/Co/AlOx trilayers”. In: *Phys. Rev. B* 79 (2 Jan. 2009), p. 024423. DOI: 10.1103/PhysRevB.79.024423.

[30] P. Bruno and C. Chappert. “Ruderman-Kittel theory of oscillatory interlayer exchange coupling”. In: *Phys. Rev. B* 46 (1 July 1992), pp. 261–270. DOI: 10.1103/PhysRevB.46.261.

[31] P. Bruno and C. Chappert. “Oscillatory coupling between ferromagnetic layers separated by a nonmagnetic metal spacer”. In: *Phys. Rev. Lett.* 67 (12 Sept. 1991), pp. 1602–1605. DOI: 10.1103/PhysRevLett.67.1602.

[32] S. S. P. Parkin and D. Mauri. “Spin engineering: Direct determination of the Ruderman-Kittel-Kasuya-Yosida far-field range function in ruthenium”. In: *Phys. Rev. B* 44 (13 Oct. 1991), pp. 7131–7134. DOI: 10.1103/PhysRevB.44.7131.

[33] S Ikeda et al. “A Perpendicular-Anisotropy CoFeB–MgO Magnetic Tunnel Junction”. In: *Nature materials* 9 (Sept. 2010), pp. 721–4. DOI: 10.1038/nmat2804.

[34] A V Khvalkovskiy et al. “Basic principles of STT-MRAM cell operation in memory arrays”. In: *Journal of Physics D: Applied Physics* 46.7 (Feb. 2013), p. 074001. DOI: `10.1088/0022-3727/46/7/074001`. URL: `https://doi.org/10.1088/0022-3727/46/7/074001`.

[35] Paul Bouquin et al. “Stochastic Processes in Magnetization Reversal Involving Domain-Wall Motion in Magnetic Memory Elements”. In: *Phys. Rev. Applied* 15 (2 Feb. 2021), p. 024037. DOI: `10.1103/PhysRevApplied.15.024037`.

[36] Paul Bouquin et al. “Size dependence of spin-torque switching in perpendicular magnetic tunnel junctions”. In: *Applied Physics Letters* 113.22 (2018), p. 222408. DOI: `10.1063/1.5055741`. eprint: `https://doi.org/10.1063/1.5055741`. URL: `https://doi.org/10.1063/1.5055741`.

[37] J. Z. Sun et al. “Effect of subvolume excitation and spin-torque efficiency on magnetic switching”. In: *Phys. Rev. B* 84 (6 Aug. 2011), p. 064413. DOI: `10.1103/PhysRevB.84.064413`.

[38] H. Sato et al. “CoFeB Thickness Dependence of Thermal Stability Factor in CoFeB/MgO Perpendicular Magnetic Tunnel Junctions”. In: *IEEE Magnetics Letters* 3 (2012), pp. 3000204–3000204. DOI: `10.1109/LMAG.2012.2190722`.

[39] Edmund Clifton Stoner and E. P. Wohlfarth. “A mechanism of magnetic hysteresis in heterogeneous alloys”. In: *Philosophical Transactions of the Royal Society of London. Series A, Mathematical and Physical Sciences* 240.826 (1948), pp. 599–642. DOI: `10.1098/rsta.1948.0007`.

[40] C Tannous and J Gieraltowski. “The Stoner–Wohlfarth model of ferromagnetism”. In: *European Journal of Physics* 29.3 (Mar. 2008), pp. 475–487. DOI: `10.1088/0143-0807/29/3/008`.

[41] J.C. Slonczewski. “Current-Driven Excitation of Magnetic Multilayers”. In: *Journal of Magnetism and Magnetic Materials* 159 (1996), pp. L1–L7. DOI: `10.1016/0304-8853(96)00062-5`.

[42] L. Berger. “Emission of Spin Waves by a Magnetic Multilayer Traversed by a Current”. In: *Physical Review B* 54 (1996), pp. 9353–9358. DOI: `10.1103/PhysRevB.54.9353`.

[43] Nicolas Locatelli and Vincent Cros. “Basic Spintronic Transport Phenomena”. In: *Introduction to Magnetic Random-Access Memory*. John Wiley Sons, Ltd, 2017. Chap. 1, pp. 1–28. ISBN: 9781119079415. DOI: `https://doi.org/10.1002/9781119079415.ch1`.

[44] A. A. Timopheev et al. “Respective Influence of In-Plane and out-of-Plane Spin-Transfer Torques in Magnetization Switching of Perpendicular Magnetic Tunnel Junctions”. In: *Physical Review B* 92 (2015), p. 104430. DOI: `10.1103/PhysRevB.92.104430`.

[45] D. M. Apalkov and P. B. Visscher. “Spin-Torque Switching: Fokker-Planck Rate Calculation”. In: *Physical Review B* 72 (2005), p. 180405. DOI: `10.1103/PhysRevB.72.180405`.

[46] Liliana D. Buda-Prejbeanu. “Micromagnetism Applied to Magnetic Nanostructures”. In: *Introduction to Magnetic Random-Access Memory*. John Wiley Sons, Ltd, 2017. Chap. 3, pp. 55–78. ISBN: 9781119079415. DOI: `https://doi.org/10.1002/9781119079415.ch3`.

[47] Lev Davidovich Landau and Evgenii Mikhailovich Lifshitz. “ON THE THEORY OF THE DISPERSION OF MAGNETIC PERMEABILITY IN FERROMAGNETIC BODIES”. In: 1935.

[48] Thomas L. Gilbert. “A phenomenological theory of damping in ferromagnetic materials”. In: *IEEE Transactions on Magnetics* 40 (2004), pp. 3443–3449.

[49] S. Azzawi, A. T. Hindmarch, and Del Atkinson. “Magnetic damping phenomena in ferromagnetic thin-films and multilayers”. In: *Journal of Physics D* 50 (2017), p. 473001.

[50] William E. Bailey. “Magnetization Dynamics”. In: *Introduction to Magnetic Random-Access Memory*. John Wiley Sons, Ltd, 2017. Chap. 4, pp. 79–100. ISBN: 9781119079415. DOI: `https://doi.org/10.1002/9781119079415.ch4`.

[51] Z. Li et al. “Perpendicular Spin Torques in Magnetic Tunnel Junctions”. In: *Physical Review Letters* 100 (2008), p. 246602. DOI: 10.1103/PhysRevLett.100.246602.

[52] Sumio Ikegawa et al. “Magnetoresistive Random Access Memory: Present and Future”. In: *IEEE Transactions on Electron Devices* 67.4 (2020), pp. 1407–1419. DOI: 10.1109/TED.2020.2965403.

[53] Michael Gaidis. “Magnetoresistive Random Access Memory”. In: July 2010. ISBN: 3527628150. DOI: 10.1002/9783527628155.nanotech033.

[54] Dmytro Apalkov, Bernard Dieny, and J. M. Slaughter. “Magnetoresistive Random Access Memory”. In: *Proceedings of the IEEE* 104.10 (2016), pp. 1796–1830. DOI: 10.1109/JPROC.2016.2590142.

[55] Shunsuke Fukami et al. “Magnetization Switching by Spin–Orbit Torque in an Antiferromagnet–Ferromagnet Bilayer System”. In: *Nature Materials* 15 (2016), pp. 535–541. DOI: 10.1038/nmat4566.

[56] Kevin Garello et al. *SOT-MRAM 300mm Integration for Low Power and Ultrafast Embedded Memories*. 2018.

[57] W Wang and Chia-Ling Chien. “Voltage-induced switching in magnetic tunnel junctions with perpendicular magnetic anisotropy”. In: *Journal of Physics D: Applied Physics* 46 (Jan. 2013), p. 074004. DOI: 10.1088/0022-3727/46/7/074004.

[58] Butsurin Jinnai et al. “Scaling magnetic tunnel junction down to single-digit nanometers—Challenges and prospects”. In: *Applied Physics Letters* 116 (Apr. 2020), p. 160501. DOI: 10.1063/5.0004434.

[59] J. Z. Sun et al. “Spin-torque switching efficiency in CoFeB-MgO based tunnel junctions”. In: *Phys. Rev. B* 88 (10 Sept. 2013), p. 104426. DOI: 10.1103/PhysRevB.88.104426.

[60] Luc Thomas et al. “Perpendicular spin transfer torque magnetic random access memories with high spin torque efficiency and thermal stability for embedded applications (invited)”. In: *Journal of Applied Physics* 115.17 (2014), p. 172615. DOI: 10.1063/1.4870917.

[61] Hiromori Sato et al. “Comprehensive study of CoFeB-MgO magnetic tunnel junction characteristics with single- and double-interface scaling down to 1X nm”. In: Dec. 2013, pp. 3.2.1–3.2.4. ISBN: 978-1-4799-2306-9. DOI: 10.1109/IEDM.2013.6724550.

[62] Hideo Sato et al. “MgO/CoFeB/Ta/CoFeB/MgO recording structure in magnetic tunnel junctions with perpendicular easy axis”. In: *IEEE Transactions on Magnetics* 49 (July 2013), pp. 4437–4440. DOI: 10.1109/TMAG.2013.2251326.

[63] Shivam Verma, Anant Kulkarni, and Brajesh Kumar Kaushik. “Spintronics-Based Devices to Circuits: Perspectives and Challenges”. In: *IEEE Nanotechnology Magazine* 10 (Oct. 2016). DOI: 10.1109/MNANO.2016.2606683.

[64] Rachid Sbiaa et al. “Spin transfer switching enhancement in perpendicular anisotropy magnetic tunnel junctions with a canted in-plane spin polarizer”. In: *Journal of Applied Physics* 105.1 (2009), p. 013910. DOI: 10.1063/1.3055373.

[65] Chun-Yeol You. “Reduced spin transfer torque switching current density with non-collinear polarizer layer magnetization in magnetic multilayer systems”. In: *Applied Physics Letters* 100 (June 2012). DOI: 10.1063/1.4730376.

[66] Georg Wolf et al. “Perpendicular Magnetized Magnetic Random-Access Memory Cells Utilizing the Precessional Spin-Current Structure: Benefits for Modern Memory Applications”. In: *IEEE Magnetics Letters* 11 (2020), pp. 1–4. DOI: 10.1109/LMAG.2020.3001487.

[67] Abir Shadman and Jian-Gang Zhu. “High-speed STT MRAM incorporating antiferromagnetic layer”. In: *Applied Physics Letters* 114 (Jan. 2019), p. 022403. DOI: 10.1063/1.5078525.

[68] Jian-Gang Zhu and Abir Shadman. "Resonant Spin-Transfer Torque Magnetoresistive Memory". In: *IEEE Transactions on Magnetics* PP (Oct. 2018), pp. 1–7. DOI: `10.1109/TMAG.2018.2871774`.

[69] G. Hu et al. "STT-MRAM with double magnetic tunnel junctions". In: (2015), pp. 26.3.1–26.3.4. DOI: `10.1109/IEDM.2015.7409772`.

[70] Daniel C. Worledge. "Theory of Spin Torque Switching Current for the Double Magnetic Tunnel Junction". In: *IEEE Magnetics Letters* 8 (2017), pp. 1–5. DOI: `10.1109/LMAG.2017.2707331`.

[71] Antoine Chavent et al. "Spin torque efficiency modulation in a double-barrier magnetic tunnel junction with a read/write mode control layer". In: *ACS Applied Electronic Materials* 3.6 (June 2021), pp. 2607–2613. DOI: `10.1021/acsaelm.1c00198`.

[72] Paulo Coelho. "Engineering of magnetic tunnel junction stacks for improved STT-MRAM performance and development of novel and cost-effective nano-patterning techniques". PhD thesis. Oct. 2018. Micro and nanotechnologies/Microelectronics. Université Grenoble Alpes.

[73] G. Hu et al. "2X reduction of STT-MRAM switching current using double spin-torque magnetic tunnel junction". In: *2021 IEEE International Electron Devices Meeting (IEDM)*. 2021. DOI: `10.1109/IEDM19574.2021.9720691`.

[74] S. Rao et al. "BEOL-compatible double magnetic tunnel junction pSTT-MRAM devices for IoT and edge computing". In: *2020 IEEE International Electron Devices Meeting (IEDM)* (2020).

[75] Léa Cuchet et al. "Perpendicular magnetic tunnel junctions with double barrier and single or synthetic antiferromagnetic storage layer". In: *Journal of Applied Physics* 117.23 (2015), p. 233901. DOI: `10.1063/1.4922630`.

[76] P.-Y. Clément et al. "Double barrier magnetic tunnel junctions with write/read mode select layer". In: *2014 IEEE 6th International Memory Workshop (IMW)*. 2014, pp. 1–4. DOI: `10.1109/IMW.2014.6849366`.

[77] Rodmacq et al. "Magnetic device, and method for reading from and writing to said device". 2013. US Patent 8513944 B2.

[78] Zhitao Diao et al. "Spin transfer switching in dual MgO magnetic tunnel junctions". In: *Applied Physics Letters* 90.13 (2007), p. 132508. DOI: `10.1063/1.2717556`.

[79] B.Dieny. *Magnetic device with magnetic tunnel junction, memory array and read/write methods using same*. 2005. US 0002228 A1.

[80] G. Hu et al. "Key parameters affecting STT-MRAM switching efficiency and improved device performance of 400°C-compatible p-MTJs". In: *2017 IEEE International Electron Devices Meeting (IEDM)*. 2017, pp. 38.3.1–38.3.4. DOI: `10.1109/IEDM.2017.8268515`.

[81] J. Swerts et al. "Solving the BEOL compatibility challenge of top-pinned magnetic tunnel junction stacks". In: (2017), pp. 38.6.1–38.6.4. DOI: `10.1109/IEDM.2017.8268518`.

[82] Zhai Zhonghai et al. "Perpendicular exchange bias of (Pt/Co)n/FeMn multilayers". In: *Journal of University of Science and Technology Beijing, Mineral, Metallurgy, Material* 14.6 (2007), pp. 543–546. ISSN: 1005-8850. DOI: `https://doi.org/10.1016/S1005-8850(07)60125-X`.

[83] F. Garcia et al. "Exchange bias in (Pt/Co0.9Fe0.1)n/FeMn multilayers with perpendicular magnetic anisotropy". In: *Journal of Applied Physics* 91.10 (2002), pp. 6905–6907. DOI: `10.1063/1.1447870`.

[84] Hideo Sato et al. "Co/Pt multilayer based reference layers in magnetic tunnel junctions for nonvolatile spintronics VLSIs". In: *Japanese Journal of Applied Physics* 53.4S (Jan. 2014), 04EM02. DOI: `10.7567/jjap.53.04em02`.

[85] Jyotirmoy Chatterjee. “Double barrier magnetic tunnel junctions for innovative spintronic devices”. PhD thesis. Nov. 2018.

[86] Jin-Young Choi et al. “Double MgO-based Perpendicular Magnetic-Tunnel-Junction Spin-valve Structure with a Top Co2Fe6B2 Free Layer using a Single SyAF [Co/Pt]n Layer”. In: *Scientific Reports* 8 (Feb. 2018). DOI: 10.1038/s41598-018-20626-4.

[87] Enlong Liu et al. “Seed Layer Impact on Structural and Magnetic Properties of [Co/Ni] Multilayers with Perpendicular Magnetic Anisotropy”. In: *Journal of Applied Physics* 121 (Jan. 2017), p. 043905. DOI: 10.1063/1.4974885.

[88] Jyotirmoy Chatterjee et al. “Impact of seed layer on post-annealing behavior of transport and magnetic properties of Co/Pt multilayer-based bottom-pinned perpendicular magnetic tunnel junctions”. In: *Applied Physics Express* 8 (2015), p. 063002.

[89] Sze Ter Lim et al. “Effect of different seed layers with varying Co and Pt thicknesses on the magnetic properties of Co/Pt multilayers”. In: *Journal of Applied Physics* 117.17 (2015), 17A731. DOI: 10.1063/1.4916295.

[90] Yuichi Ohsawa et al. “Precise Damage Observation in Ion-Beam Etched MTJ”. In: *IEEE Transactions on Magnetics* 52 (July 2016), pp. 1–1. DOI: 10.1109/TMAG.2015.2512588.

[91] Tomonori Mukai et al. “Plasma irradiation damages to magnetic tunneling junction devices”. In: *Journal of Applied Physics* 102.7 (2007), p. 073303. DOI: 10.1063/1.2785849.

[92] Yuichi Ohsawa, Kiyoshi Yamakawa, and Hiroaki Muraoka. “In situ magnetoresistance measurements of ion-beam-etched Fe-Co thin films”. In: *Journal of Applied Physics* 109.7 (2011), 07B736. DOI: 10.1063/1.3556927.

[93] Daniel Sanchez Hazen et al. “Double magnetic tunnel junctions with a switchable assistance layer for improved spin transfer torque magnetic memory performance”. In: *Nanoscale* 13 (33 2021), pp. 14096–14109. DOI: 10.1039/D1NR01656C.

[94] B.Dieny. *Memory and magnetic logic gate using such an element.* 2014. US 8811073 B2.

[95] Han-Sol Jun et al. “Multi-level resistance uniformity of double pinned perpendicular magnetic-tunnel-junction spin-valve depending on top MgO barrier thickness”. In: *AIP Advances* 10.6 (2020), p. 065126. DOI: 10.1063/5.0007064.

[96] B. Dieny and M. Chshiev. “Perpendicular magnetic anisotropy at transition metal/oxide interfaces and applications”. In: *Rev. Mod. Phys.* 89 (2 June 2017), p. 025008. DOI: 10.1103/RevModPhys.89.025008.

[97] K. Nishioka et al. “Effect of Magnetic Coupling Between Two CoFeB Layers on Thermal Stability in Perpendicular Magnetic Tunnel Junctions With MgO/CoFeB/Insertion Layer/CoFeB/MgO Free Layer”. In: *IEEE Transactions on Magnetics* 58.2 (2022), pp. 1–6. DOI: 10.1109/TMAG.2021.3083575.

[98] John Slonczewski. “Conductance and exchange coupling of two ferromagnets separated by a tunneling barrier”. In: *Physical review. B, Condensed matter* 39 (May 1989), pp. 6995–7002. DOI: 10.1103/PhysRevB.39.6995.

[99] M. Julliere. “Tunneling between ferromagnetic films”. In: *Physics Letters A* 54.3 (1975), pp. 225–226. ISSN: 0375-9601. DOI: https://doi.org/10.1016/0375-9601(75)90174-7.

[100] Kerem Y. Camsari et al. “Double-Free-Layer Magnetic Tunnel Junctions for Probabilistic Bits”. In: *Phys. Rev. Applied* 15 (4 Apr. 2021), p. 044049. DOI: 10.1103/PhysRevApplied.15.044049.

[101] A. Timopheev et al. “Respective influence of in-plane and out-of-plane spin-transfer torques in magnetization switching of perpendicular magnetic tunnel junctions”. In: *Physical Review B* 92 (June 2015), p. 104430. DOI: 10.1103/PhysRevB.92.104430.

[102] J.C. Slonczewski. “Current-driven excitation of magnetic multilayers”. In: *Journal of Magnetism and Magnetic Materials* 159.1 (1996), pp. L1–L7. ISSN: 0304-8853. DOI: `https://doi.org/10.1016/0304-8853(96)00062-5`.

[103] W. C. Nunes et al. “Temperature dependence of the coercive field in single-domain particle systems”. In: *Phys. Rev. B* 70 (1 July 2004), p. 014419. DOI: `10.1103/PhysRevB.70.014419`.

[104] I L Prejbeanu et al. “Thermally assisted MRAM”. In: *Journal of Physics: Condensed Matter* 19.16 (Apr. 2007), p. 165218. DOI: `10.1088/0953-8984/19/16/165218`.

[105] N. Strelkov et al. “Impact of Joule heating on the stability phase diagrams of perpendicular magnetic tunnel junctions”. In: *Phys. Rev. B* 98 (21 Dec. 2018), p. 214410. DOI: `10.1103/PhysRevB.98.214410`.

[106] E. Gapihan et al. “Heating asymmetry induced by tunneling current flow in magnetic tunnel junctions”. In: *Applied Physics Letters* 100.20 (2012), p. 202410. DOI: `10.1063/1.4719663`.

[107] Juan G. Alzate et al. “Temperature dependence of the voltage-controlled perpendicular anisotropy in nanoscale MgO—CoFeB—Ta magnetic tunnel junctions”. In: *Applied Physics Letters* 104.11 (2014), p. 112410. DOI: `10.1063/1.4869152`.

[108] Y. Lu et al. “Spin-Polarized Inelastic Tunneling through Insulating Barriers”. In: *Phys. Rev. Lett.* 102 (17 Apr. 2009), p. 176801. DOI: `10.1103/PhysRevLett.102.176801`.

[109] A. V. Khvalkovskiy et al. “Magnetic memory with a switchable reference layer”. In: *Journal of Applied Physics* 124.13 (2018), p. 133902. DOI: `10.1063/1.5045554`.

[110] P.J Kelly and R.D Arnell. “Magnetron sputtering: a review of recent developments and applications”. In: *Vacuum* 56.3 (2000), pp. 159–172. ISSN: 0042-207X. DOI: `https://doi.org/10.1016/S0042-207X(99)00189-X`.

[111] Jyotirmoy Chatterjee. “Engineering of magnetic tunnel junction stacks for improved STT-MRAM performance and development of novel and cost-effective nano-patterning techniques”. Theses. Université Grenoble Alpes, Mar. 2018.

[112] Marco Mansueto. “Memristive magnetic memory for spintronic synapses”. Theses. Université Grenoble Alpes [2020-....], Dec. 2020.

[113] Luc Tillie. “Study and optimization of thermal stability and temperature dependence of P-STT-MRAM for industrial applications”. Theses. Université Grenoble Alpes, Dec. 2018.

[114] Lea Cuchet. “Magnetic and transport properties of single and double perpendicular magnetic tunnel junctions”. Theses. Université Grenoble Alpes, Nov. 2015.

[115] Michael A. Johnson et al. “Dissociation of Water at the MgO(100)Water Interface: Comparison of Theory with Experiment”. In: *The Journal of Physical Chemistry B* 103.17 (1999), pp. 3391–3398. DOI: `10.1021/jp983729r`.

[116] Yoshinori Nagamine et al. “Ultralow resistance-area product of 0.4Ω(μm)2 and high magnetoresistance above 50% in CoFeBMgOCoFeB magnetic tunnel junctions”. In: *Applied Physics Letters* 89.16 (2006), p. 162507. DOI: `10.1063/1.2352046`.

[117] Du-Yeong Lee, Hyung-Tak Seo, and Jea-Gun Park. “Effects of the radio-frequency sputtering power of an MgO tunneling barrier on the tunneling magneto-resistance ratio for Co2Fe6B2/MgO-based perpendicular-magnetic tunnel junctions”. In: *J. Mater. Chem. C* 4 (1 2016), pp. 135–141. DOI: `10.1039/C5TC03669K`.

[118] D. C. Worledge and P. L. Trouilloud. “Magnetoresistance measurement of unpatterned magnetic tunnel junction wafers by current-in-plane tunneling”. In: *Applied Physics Letters* 83.1 (2003), pp. 84–86. DOI: `10.1063/1.1590740`.

[119] Shinji Yuasa et al. “Giant Room-Temperature Magnetoresistance in Single-Crystal Fe/MgO/Fe Magnetic Tunnel Junctions”. In: *Nature materials* 3 (Jan. 2005), pp. 868–71. DOI: `10.1038/nmat1257`.

[120] F. Bonell et al. “Spin-Polarized Electron Tunneling in bcc FeCo/MgO/FeCo(001) Magnetic Tunnel Junctions”. In: *Phys. Rev. Lett.* 108 (17 Apr. 2012), p. 176602. DOI: 10.1103/PhysRevLett.108.176602.

[121] Bernard Dieny and Mairbek Chshiev. “Perpendicular magnetic anisotropy at transition metal/oxide interfaces and applications”. In: *Review of Modern Physics* 89 (June 2017), p. 025008. DOI: 10.1103/RevModPhys.89.025008.

[122] Henning Schuhmann et al. “Controlling boron redistribution in CoFeB/MgO magnetic tunnel junctions during annealing by variation of cap layer materials and MgO deposition methods”. In: *preprint, arXiv:1405.1907* (May 2014).

[123] Daniel Schreiber et al. “Effects of elemental distributions on the behavior of MgO-based magnetic tunnel junctions”. In: *Journal of Applied Physics* 109 (May 2011), pp. 103909–103909. DOI: 10.1063/1.3583569.

[124] Y. Choi et al. “Effect of Ta getter on the quality of MgO tunnel barrier in the polycrystalline CoFeB/MgO/CoFeB magnetic tunnel junction”. In: *Applied Physics Letters* 90 (Feb. 2007), pp. 012505–012505. DOI: 10.1063/1.2426902.

[125] Hiroaki Honjo et al. “Impact of Tungsten Sputtering Condition on Magnetic and Transport Properties of Double-MgO Magnetic Tunneling Junction With CoFeB/W/CoFeB Free Layer”. In: *IEEE Transactions on Magnetics* PP (May 2017), pp. 1–1. DOI: 10.1109/TMAG.2017.2701838.

[126] Du-Yeong Lee et al. “Dependency of Tunneling-Magnetoresistance Ratio on Nanoscale Spacer Thickness and Material for Double MgO Based Perpendicular-Magnetic-Tunneling-Junction”. In: *Scientific Reports* 6 (Dec. 2016), p. 38125. DOI: 10.1038/srep38125.

[127] Tao Liu et al. “Thermally robust Mo/CoFeB/MgO trilayers with strong perpendicular magnetic anisotropy”. In: *Scientific reports* 4 (July 2014), p. 5895. DOI: 10.1038/srep05895.

[128] M.R. Parker. “The Kerr magneto-optic effect (1876–1976)”. In: *Physica B+C* 86-88 (1977), pp. 1171–1176. ISSN: 0378-4363. DOI: https://doi.org/10.1016/0378-4363(77)90836-1.

[129] J. C. Suits. “Magneto-Optical Rotation and Ellipticity Measurements with a Spinning Analyzer”. In: *Review of Scientific Instruments* 42.1 (1971), pp. 19–22. DOI: 10.1063/1.1684868.

[130] James Erskine and E. Stern. “Magneto-optic Kerr Effect in Ni, Co, and Fe”. In: *Physical Review Letters - PHYS REV LETT* 30 (June 1973), pp. 1329–1332. DOI: 10.1103/PhysRevLett.30.1329.

[131] M.P. Sharrock. “Measurement and interpretation of magnetic time effects in recording media”. In: *IEEE Transactions on Magnetics* 35.6 (1999), pp. 4414–4422. DOI: 10.1109/20.809133.

[132] L. Tillie et al. “Data retention extraction methodology for perpendicular STT-MRAM”. In: *Electron Devices Meeting (IEDM), 2016 IEEE International*. San Francisco, United States, Dec. 2016. DOI: 10.1109/IEDM.2016.7838492.

[133] Kumar Srinivasan, B. Ramamurthy Acharya, and Gerardo Bertero. “Thermal effects on the magnetization reversal process and its interpretation in perpendicular magnetic recording media”. In: *Journal of Applied Physics* 107 (July 2010), pp. 113912–113912. DOI: 10.1063/1.3436583.

[134] Witold Skowroński et al. “Understanding stability diagram of perpendicular magnetic tunnel junctions”. In: *Scientific Reports* 7 (Jan. 2017). DOI: 10.1038/s41598-017-10706-2.

[135] S. Monso et al. “Crossover from in-plane to perpendicular anisotropy in Pt/CoFe/AlOx sandwiches as a function of Al oxidation: A very accurate control of the oxidation of tunnel barriers”. In: *Applied Physics Letters* 80 (June 2002), pp. 4157–4159. DOI: 10.1063/1.1483122.

[136] Houyi Cheng et al. “Giant Perpendicular Magnetic Anisotropy in Mo-Based Double-Interface Free Layer Structure for Advanced Magnetic Tunnel Junctions”. In: *Advanced Electronic Materials* (July 2020). DOI: 10.1002/aelm.202000271.

[137] K. Nishioka et al. “Novel Quad Interface MTJ Technology and Its First Demonstration with High Thermal Stability and Switching Efficiency for STT-MRAM Beyond 2Xnm”. In: June 2019. DOI: 10.23919/VLSIT.2019.8776499.

[138] Luc Tillie et al. “Temperature Limits of Single and Composite Storage Layer with Different Thicknesses and Capping Materials for p-STT-MRAM Applications”. In: May 2018, pp. 1–4. DOI: 10.1109/IMW.2018.8388854.

[139] Lavinia Nistor et al. “Correlation Between Perpendicular Anisotropy and Magnetoresistance in Magnetic Tunnel Junctions”. In: *IEEE Transactions on Magnetics* 46 (July 2010), p. 1412. DOI: 10.1109/TMAG.2010.2045641.

[140] Naruto Miyakawa, D.C. Worledge, and Koji Kita. “Impact of Ta Diffusion on the Perpendicular Magnetic Anisotropy of Ta/CoFeB/MgO”. In: *Magnetics Letters, IEEE* 4 (Jan. 2013), pp. 1000104–1000104. DOI: 10.1109/LMAG.2013.2240266.

[141] Lea Cuchet et al. “Influence of magnetic electrodes thicknesses on the transport properties of magnetic tunnel junctions with perpendicular anisotropy”. In: *Applied Physics Letters* 105 (Aug. 2014), pp. 052408–052408. DOI: 10.1063/1.4892450.

[142] B. Rodmacq et al. “Influence of thermal annealing on the perpendicular magnetic anisotropy of Pt/Co/AlOx trilayers”. In: *Phys. Rev. B* 79 (Jan. 2009). DOI: 10.1103/PhysRevB.79.024423.

[143] Hitoshi Kubota et al. “Enhancement of perpendicular magnetic anisotropy in FeB free layers using a thin MgO cap layer”. In: *Journal of Applied Physics* 111 (Mar. 2012). DOI: 10.1063/1.3679393.

[144] Tao Liu, Jian-Wang Cai, and Li Sun. “Large enhanced perpendicular magnetic anisotropy in CoFeB/MgO system with the typical Ta buffer replaced by an Hf layer”. In: *AIP Advances* 2 (Aug. 2012). DOI: 10.1063/1.4748337.

[145] Jae-Hong Kim et al. “Ultrathin W space layer-enabled thermal stability enhancement in a perpendicular MgO/CoFeB/W/CoFeB/MgO recording frame”. In: *Scientific reports* 5 (Nov. 2015), p. 16903. DOI: 10.1038/srep16903.

[146] Vincent Sokalski et al. “Optimization of Ta thickness for perpendicular magnetic tunnel junction applications in the MgO-FeCoB-Ta system”. In: *Applied Physics Letters* 101 (Aug. 2012). DOI: 10.1063/1.4746426.

[147] S. Miura et al. “Insertion Layer Thickness Dependence of Magnetic and Electrical Properties for Double-CoFeB/MgO-Interface Magnetic Tunnel Junctions”. In: *IEEE Transactions on Magnetics* PP (Mar. 2019), pp. 1–4. DOI: 10.1109/TMAG.2019.2901841.

[148] Seung-Eun Lee, Yasutaka Takemura, and Jea-Gun Park. “Effect of double MgO tunneling barrier on thermal stability and TMR ratio for perpendicular MTJ spin-valve with tungsten layers”. In: *Applied Physics Letters* 109 (Oct. 2016), p. 182405. DOI: 10.1063/1.4967172.

[149] S. Couet et al. “Impact of Ta and W-based spacers in double MgO STT-MRAM free layers on perpendicular anisotropy and damping”. In: *Applied Physics Letters* 111 (Oct. 2017), p. 152406. DOI: 10.1063/1.5000992.

[150] J. S. Moodera et al. “Large Magnetoresistance at Room Temperature in Ferromagnetic Thin Film Tunnel Junctions”. In: *Phys. Rev. Lett.* 74 (16 Apr. 1995), pp. 3273–3276. DOI: 10.1103/PhysRevLett.74.3273.

[151] T. Miyazaki and N. Tezuka. “Giant magnetic tunneling effect in Fe/Al2O3/Fe junction”. In: *Journal of Magnetism and Magnetic Materials* 139.3 (1995), pp. L231–L234. ISSN: 0304-8853. DOI: https://doi.org/10.1016/0304-8853(95)90001-2.

[152] B. Schrag et al. “Néel “orange-peel” coupling in magnetic tunneling junction devices”. In: *Applied Physics Letters* 77 (Oct. 2000), pp. 2373–2375. DOI: 10.1063/1.1315633.

[153] J. Faure-Vincent et al. “Interlayer Magnetic Coupling Interactions of Two Ferromagnetic Layers by Spin Polarized Tunneling”. In: *Phys. Rev. Lett.* 89 (10 Aug. 2002), p. 107206. DOI: 10.1103/PhysRevLett.89.107206.

[154] Hongxin Yang et al. “Effect of structural relaxation and oxidation conditions on interlayer exchange coupling in FeMgOFe tunnel junctions”. In: *Applied Physics Letters* (July 2010).

[155] Elena Popova et al. “Temperature dependence of the interlayer exchange coupling in epitaxial Fe1/MgO/Fe2/Co tunnel junctions”. In: *Applied Physics Letters* 91 (Sept. 2007), pp. 112504–112504. DOI: 10.1063/1.2784942.

[156] J. C. Slonczewski. “Conductance and exchange coupling of two ferromagnets separated by a tunneling barrier”. In: *Phys. Rev. B* 39 (10 Apr. 1989), pp. 6995–7002. DOI: 10.1103/PhysRevB.39.6995.

[157] Patrick Bruno. “Oscillations of Interlayer Exchange Coupling vs. Ferromagnetic-Layers Thickness”. In: *EPL* 23 (1993), pp. 615–620.

[158] P. Bruno. “Theory of interlayer magnetic coupling”. In: *Phys. Rev. B* 52 (1 July 1995), pp. 411–439. DOI: 10.1103/PhysRevB.52.411.

[159] J. Moritz et al. “Orange peel coupling in multilayers with perpendicular magnetic anisotropy: Application to (Co/Pt)-based exchange-biased spin-valves”. In: *EPL (Europhysics Letters)* 65 (Jan. 2007), p. 123. DOI: 10.1209/epl/i2003-10063-9.

[160] Lavinia E. Nistor et al. “Oscillatory interlayer exchange coupling in MgO tunnel junctions with perpendicular magnetic anisotropy”. In: *Phys. Rev. B* 81 (22 June 2010), p. 220407. DOI: 10.1103/PhysRevB.81.220407.

[161] Lavinia Nistor. “Jonctions tunnel magnétiques à aimantation perpendiculaire : anisotropie, magnétorésistance, couplages magnétiques et renversement par couple de transfert de spin”. Theses. Université de Grenoble, Oct. 2011.

[162] Louis Néel. “Sur un nouveau mode de couplage entre les aimantations de deux couches minces ferromagnétiques”. In: *Comptes Rendus Hebdomadaires Des Seances De L Academie Des Sciences* 255.15 (1962), pp. 1676–1681.

[163] Hideto Yanagihara, Yuta Toyoda, and Eiji Kita. “Antiferromagnetic coupling between spinel ferrite and α-Fe layers in Fe3δO4/MgO/Fe(0 0 1) epitaxial films”. In: *Journal of Physics D: Applied Physics* 44 (Jan. 2011), p. 064011. DOI: 10.1088/0022-3727/44/6/064011.

[164] Hideo Sato et al. “MgO/CoFeB/Ta/CoFeB/MgO recording structure in magnetic tunnel junctions with perpendicular easy axis”. In: *IEEE Transactions on Magnetics* 49 (July 2013), pp. 4437–4440. DOI: 10.1109/TMAG.2013.2251326.

[165] Kyungjun Kim et al. “Time-dependent dielectric breakdown of MgO magnetic tunnel junctions and novel test method”. In: *Japanese Journal of Applied Physics* 56 (Apr. 2017), 04CN02. DOI: 10.7567/JJAP.56.04CN02.

[166] M. Tokaç. “Influence of tantalum concentrations on the magnetic properties of amorphous CoFeTaB thin-films”. In: *Journal of Non Crystalline Solids* 572, 121080 (Nov. 2021), p. 121080. DOI: 10.1016/j.jnoncrysol.2021.121080.

[167] Bruno Teixeira et al. “Stabilization of the easy-cone magnetic state in free layers of magnetic tunnel junctions”. In: *Physical review. B, Condensed matter* 100 (Nov. 2019), p. 184405. DOI: 10.1103/PhysRevB.100.184405.

[168] Louis Néel. “Théorie du traînage magnétique des substances massives dans le domaine de Rayleigh”. In: *J. Phys. Radium* 11.2 (1950), pp. 49–61. DOI: 10.1051/jphysrad:0195000110204900.

[169] Claus Schneider et al. "Curie temperature of ultrathin films of fcc-cobalt epitaxially grown on atomically flat Cu(100) surfaces". In: *Physical review letters* 64 (Mar. 1990), pp. 1059–1062. DOI: 10.1103/PhysRevLett.64.1059.

[170] M. Stampanoni et al. "Magnetism of Epitaxial bcc Iron on Ag(001) Observed by Spin-Polarized Photoemission". In: *Phys. Rev. Lett.* 59 (21 Nov. 1987), pp. 2483–2485. DOI: 10.1103/PhysRevLett.59.2483.

[171] H. Sato et al. "Temperature-dependent properties of CoFeB/MgO thin films: Experiments versus simulations". In: *Phys. Rev. B* 98 (21 Dec. 2018), p. 214428. DOI: 10.1103/PhysRevB.98.214428.

[172] D. Sanchez Hazen et al. "Real time investigation of double magnetic tunnel junction with a switchable assistance layer for high efficiency STT-MRAM". In: *APL Materials* 10.3 (2022), p. 031104. DOI: 10.1063/5.0080335.

[173] Fumitaka Iga et al. "Time-Resolved Switching Characteristic in Magnetic Tunnel Junction with Spin Transfer Torque Write Scheme". In: *Japanese Journal of Applied Physics* 51 (Feb. 2012). DOI: 10.1143/JJAP.51.02BM02.

[174] G. Hu et al. "2X reduction of STT-MRAM switching current using double spin-torque magnetic tunnel junction". In: *2021 IEEE International Electron Devices Meeting (IEDM)*. 2021, pp. 2.5.1–2.5.4. DOI: 10.1109/IEDM19574.2021.9720691.